Investigation of Laser Sintering of Pharmaceutical Excipients for Oral Solid Dosage Forms

Marina-Eirini Mitrousi

Doctoral Thesis

Submitted to the University of Nottingham for the

degree of Doctor of Philosophy

Faculty of Engineering

Centre for Additive Manufacturing

June 2021

Acknowledgements

I would like to thank a number of people, without whom I would have not been able to complete this thesis. Their help and support was invaluable during the course of my PhD.

My first and big appreciation goes to my principal supervisor, Professor Christopher Tuck, for his precious supervision, advice and encouragement, with a perfect blend of insight and humour. Thank you Chris, for your patience, guidance, and kind support. I am extremely grateful that you took me on as your student and continued to have faith in me over the years. Also, I greatly appreciate my additional supervisors, Professor Ruth Goodridge and Dr Laura Ruiz Cantu for their guidance and detailed feedback that was very important to me. Many thanks to the both of you.

My gratitude extends to the Engineering and Physical Sciences Research Council for the funding opportunity to undertake my studies at the Department of Mechanical, Materials and Manufacturing Engineering at the University of Nottingham. Additionally, I acknowledge the generous financial support from Pfizer, and I would like to express gratitude to Brian Henry and Martin Rowland for their support and great feedback, which was really influential in shaping my research.

I am fortunate to have been part of the CfAM group, a world leading centre for Additive Manufacturing that provided me with great opportunities to grow professionally. It has been a pleasure working with many brilliant people over the years. Their help in the laboratory will always be remembered.

I would like to thank my friends, lab mates, colleagues and all the CDT in Additive Manufacturing and 3D Printing team. I cherished the time that we spent together in the office. It is important to strike a balance with life outside of the monotony of the lab, and so, thank you to my colleagues for their company and lively conversations. Special thanks to my friends Han, Ian, Tom, Liz, Sam, Yazid, Richard, Katie, Alex, Carlo, Duncan, Hatim, Adam, Jing, Carlos and Leonidas, who helped me to find my footing when I started this process five years ago. Thank you for all the laughs, the unlimited support and your friendship. I miss you already.

Most importantly, I am grateful to my family and friends for their unconditional support and continuous encouragement. My accomplishments and success are because they believed in me and are always supportive of my adventures.

Abstract

Additive Manufacturing (AM) of medication has offered great potential to the pharmaceutical industry in recent years, specifically for its revolutionary potential for personalised medicine. The replacement of conventional drug manufacture and distribution could provide patients with customised drug dosages fabricated at the point of care to reduce cost and enhance therapy adherence. Laser Sintering is a powder-based AM technique with potential for use in pharmaceutical applications. It is a solvent-free process that does not require support structures compared to other AM processes, providing increased stability and productivity in comparison to other AM techniques such as extrusion. Laser Sintering relies on consolidation mechanisms achieving high mechanical properties, and further it offers unlimited design freedom and industrial scale opportunities. However, there are limitations that prevent rapid deployment of Laser Sintering in pharmaceutics mainly due to the narrow variety of applicable polymer based excipient materials, which results from the complex thermal processing conditions. Most materials do not make it through the development stages in Laser Sintering, which makes it necessary to understand the most important factors that influence processing and part properties to enable design and development of drug dosage forms by this technology.

This PhD studied the potential of using Laser Sintering for the fabrication of oral solid dosage forms (tablets) using placebo formulations. To achieve this, characterisation and processing of several pharmaceutical grade polymers was performed to identify candidate materials. Primarily, Laser Sintering showed potential for processing pharmaceuticals, however all the investigated materials presented important incompatibilities that impacted their processability. Materials with high moisture content experienced dehydration, which led to degradation upon the application of the laser beam. Furthermore, increased moisture levels induced cohesiveness and prevented the deposition of uniform layers of powder. Processing materials consisting of large and irregular particles introduced porosity and shrinkage, while processing of fine particle grades generated high electrostatic forces causing agglomeration and limiting powder flow. However, among the tested materials, Eudragit L100-55, a methacrylic acid ethyl acrylate copolymer known for its use as a coating agent in drug dosage forms, although an amorphous polymer it exhibited acceptable sinter-ability due to its ideal particle morphology and distribution that resulted in high packing efficiency and part density.

Eudragit L100-55 and Avicel 101, a microcrystalline cellulose grade pharmaceutical popularly used as a diluent, were used for the development of preliminary formulations for the preliminary assessment on Laser Sintering of oral solid dosage forms. Avicel 101 demonstrated poor sinter-ability due to its unfavourable thermal characteristics, which resisted particle fusion and experienced degradation. Processing of the two materials together was proved viable by direct sintering of Eudragit L100-55 as a matrix to bind together the solid particles of Avicel 101. However, the presence of unmolten Avicel 101 particles increased the number of voids and promoted structural porosity. The increased porosity enhanced fragility of the parts, which impacted the mechanical properties resulting in poor strength, friability and stiffness. The poor mechanical performance significantly reduced the tablet integrity, which was translated in poor pharmaceutical functionality, demonstrating rapid disintegration.

To enhance the processability of the powders and enable the production of oral solid dosage forms with increased functionality, an alternative approach was taken to produce an optimal pharmaceutical material for Laser Sintering. Exploiting the pH-dependent solubility of Eudragit L100-55, polymer precipitation and evaporation methods were used in a simple cost-effective system to create a film coating on Avicel 101 particles. The methods proved suitable to produce a film on the surface of Avicel 101 particles and they were simple and easy to reproduce. The development of a coated cellulose-base material aimed at the production of parts with increased density and mechanical strength, compared to the powder blends. This coating approach could have wide implications for Laser Sintering providing a new route for materials development for Laser Sintering that can open the way for innovative opportunities in pharmaceutics and broader, enabling the selection of a greater list of materials for further adoption of Laser Sintering in a wider range of applications.

Table of Contents

List of Figures

List of Tables

List of Abbreviations

Al_2O_3	Aluminium oxide
AM	Additive Manufacturing
ASTM	American Society for Testing and Materials
BFE	Basic Flowability Energy
CAD	Computer-aided design
CO	Carbon monoxide
CO_2	Carbon dioxide
CSM	Continuous stiffness mode
DMA	Dynamic Mechanical Analysis
DoP	Drop-on-powder
DSC	Differential Scanning Calorimetry
E'	Storage modulus
E''	Loss modulus
ED	Energy density
E_r	Reduced elastic modulus
FDA	Food and Drug Administration
FDM	Fused Deposition Modelling
FEG-SEM	Field Emission Gun Scanning Electron Microscope
FRI	Flow Rate Index
FT4	Powder Flow Rheometer
FTIR	Fourier-Transform Infrared Spectroscopy
H	Hardness
HAp	Hydroxyapatite
HDPE	High-density polyethylene
h_{max}	Maximum depth
h_p	Plastic depth
HPC	Hydroxypropyl cellulose
HPMC	Hydroxypropyl methylcellulose
HPMC-AS	Hypromellose acetate succinate
ISO	International Organization for Standardization
KPI	Key performance indicators

LED	Light emitting diodes
LS	Laser Sintering
MCC	Microcrystalline cellulose
MeOH	Methanol
MgSt	Magnesium stearate
Mid-IR	Mid-Infrared
MW	Molecular weight
PA11	Polyamide 11
PA12 or Nylon	Polyamide 12
PA6	Polyamide 6
PAEK	Polyaryletherketones
PBF	Powder Bed Fusion
PBT	Polybutylene terephthalate
PC	Polycarbonate
PCL	Poly-ε-caprolactone
PE	Polyethylene
PEA	Ethyl acrylate unit
PEBA	Polyether block amide
PEEK	Poly (ether ether ketone)
PEG	Polyethylene glycol
PEO	Polyethylene oxide
PGA	Poly-glycolide
PHBV	Poly (3-hydroxybutyrate-co-3-hydroxyvalerate)
PLA	Poly (lactic acid)
PLGA	Poly (lactic-co-glycolic) acid
PLLA	Poly-l-lactic acid
PMA	Polymethacrylic acid unit
POM	Polyoxymethylene
PP	Polypropylene
PPS	Polyphenylene sulphide
PS	Polystyrene
PSD	Particle size distribution
PVA	Poly (vinyl alcohol)

SE	Specific Energy
SEM	Scanning Electron Microscopy
SI	Stability Index
SLA	Stereolithography
Tanδ	Loss tangent or damping factor
T_c	Crystallisation temperature
T_g	Glass transition temperature
TGA	Thermogravimetric Analysis
T_m	Melting temperature
ToF-SIMS	Time-of-Flight Secondary Ion Mass Spectrometry
T_{onset}	Weight loss onset temperature
TPE	Thermoplastic elastomers
TPU	Thermoplastic polyurethane
UHMWPE	Ultra-high molecular weight polyethylene
UV	Ultraviolet
VFR	Variable Flow Rate test
γ	Surface tension
η_0	Melting viscosity
ρ	Volume

CHAPTER 1   INTRODUCTION

1.1   Background

Additive Manufacturing (AM) technologies have revolutionary capabilities to produce 3D objects with extremely complex geometries in a fast and effective way. AM has the ability to produce fully functional parts without the need for moulds or tooling when compared to conventional manufacturing, which has pushed the boundaries of cost-efficiency, production lead-times, convenience and customisation. AM technologies have also proved valuable in the production of functional prototypes and rapid tooling, and are growing in interest in nearly all industrial sectors for the production of end-use parts. On-demand manufacturing and products with shapes that were impossible to produce by other means have now been introduced, which provided to researchers and engineers innovative opportunities that have already changed the future of many industrial applications. AM has already made a big impact in aerospace and automotive and is expanding rapidly in healthcare. The benefits that this technology introduced to the medical sector include the customisation of medical products and drugs with reduced costs. With great flexibility in the design and production of small volume units, AM has opened the way for the development of personalised healthcare towards the needs of each individual, targeting to increase therapeutic benefit. In parallel, pharmaceutical research has been transformed through the design of novel drug delivery concepts that demonstrate complex geometries for the control of local composition and drug release rate.

The AM technologies that have been involved in pharmaceutical research are Binder Jetting, Ink Jetting, Material Extrusion, Laser Sintering and Vat Photopolymerisation. The choice of technology depends on the required materials and the demands of the final product. Some of these methods (i.e. Extrusion) are simple and some are adaptable to using biocompatible polymers and ceramics (i.e. Sintering) and have been researched for the production of drug dosage forms and implantable drug delivery devices. The most commonly used technology for the fabrication of a wide range of pharmaceutical products is Binder Jetting, which deposits ink droplets on a powder bed to bind together powder particles to build a solid structure. Binder Jetting was used for the first commercial drug product ever made using AM, Spritam®, which is a fast-dispersing oral solid dosage form used to treat epilepsy [1]–[3]. However, there are major drawbacks in the use of this

method as of the degree of powder-binder wettability and droplet penetration, fluid leakage, toxicity and/or impurities, and additional intermediate steps (eg. solvent drying). Furthermore, solidification in this process relies only on the localised dissolution of the binder ink without any consolidation or compression forces, which introduces high structural porosity compared to other AM processes.

Recently, Laser Sintering gained interest from researchers and companies for the production of oral solid dosage forms and has already demonstrated substantial potential in the field. Laser Sintering is a Powder Bed Fusion process presenting a set of advantageous features when compared to other AM processes that can enable new opportunities in pharmaceutics. In particular, Laser Sintering is a single-step and solvent-free process that can provide increased stability, manufacturing speed and mechanical properties, compared to other AM techniques. Some of the biggest benefits is that Laser Sintering does not require the use of support structures and potentially additional post processing steps, compared to Material Extrusion and Vat Photopolymerisation. Moreover, Laser Sintering offers high degrees of design freedom and more importantly, control over the microstructure, which can enhance the production of complex drug delivery systems with multiple functionality. Finally, of greater importance is that Laser Sintering is one of few AM processes with the ability of large production and industrial scale opportunities. Although the many advantages Laser Sintering has to offer, there is a significant limitation that has prevented the use of this technology in pharmaceutics and this is mainly due to the small number of materials that demonstrate compatibility with the process. There are complex physical mechanisms related to processing that generate high material requirements, and for this reason powders must present a very specific combination of material properties. In order for Laser Sintering to become a widespread manufacturing tool, processing of a greater number of materials is necessary to create a database of the various influences related to material properties, on the sintering performance.

1.2 Aims and Objectives of Thesis

As AM has become a popular research theme in recent years for the development of modern medicines, this PhD aims to explore the processability of pharmaceutical grade materials by Laser Sintering to produce oral solid dosage forms that may be subsequently

designed for tailored release properties. The development of a comprehensive understanding of the performance capabilities and limitations of materials can expand the Laser Sintering material portfolio in pharmaceutics and allow further adoption of AM techniques. The following objectives that need to be achieved to complete this research are listed:

1. Identify and understand the relationship between the feedstock material properties and Laser Sintering (EOS P100) processing parameters to find an ideal combination for optimal sintering quality.

2. Investigate the thermal and physical properties of common pharmaceutical powders to select candidate materials and assess their suitability for Laser Sintering.

3. Investigate the effects of Laser Sintering conditions on selected powders based on key performance indicators for acceptable density, surface finish and mechanical integrity.

4. Investigate strategies to modify the selected Laser Sintering materials morphology and constitution to account for sintering requirements which affect the critical factors related to the tablet quality.

Through these objectives this thesis provides novelty to the subject area through provision of an investigation of the production of oral solid dosage forms by commercial (infrared) based Laser Sintering system using common pharmaceutical grade excipients for oral applications.

1.3 Thesis Structure

Each chapter of the thesis is addressing a different research objective. The structure is as follows:

Chapter 2 Literature Review: This chapter focuses on common aspects related to Additive Manufacturing and then concentrates on the area of pharmaceuticals and Laser Sintering. A review of the methods and materials used in pharmaceutical research is provided, which targets to identify the gap in literature. Further, Laser Sintering technical features, materials and processing considerations, are being discussed extensively to

provide an overview of the technology, the advantages and drawbacks involved. Finally, literature regarding the properties and uses of the pharmaceutical materials involved in this PhD is been given.

Chapter 3 Materials and Methods: The selected pharmaceutical material grades used in this PhD are presented in this chapter. Details on the established methodology and equipment used for the characterisation of raw materials, Laser Sintering, and mechanical analysis of the fabricated parts are provided. Furthermore, the process methodology followed to develop an optimal pharmaceutical material is discussed, with all the relevant equipment used to analyse the quality of the samples.

Chapter 4 Characterisation of Pharmaceutical Ingredients: In this chapter the work related to the characterisation of the raw material properties prior to sintering is presented. Analysis of the thermal, physical and rheological characteristics of the powders is provided with a link to the processing requirements to identify candidate materials for processing with Laser Sintering.

Chapter 5 Laser Sintering of Pharmaceutical Ingredients: This chapter explores the sinter-ability of raw pharmaceutical materials. Initial investigation on the processing of raw powders and the issues encountered are presented. Analysis of the factors related to material properties and processing conditions influencing the sintering performance is provided. Potential modifications on the powders for improvements in their processability are addressed.

Chapter 6 Laser Sintering of Pharmaceutical Ingredient Blends: Material blends are developed in this chapter to produce oral solid dosage forms. A variety of laser parameters is investigated to achieve optimal sintering. Limitations on the sinter-ability of the blends related to the process conditions and material composition are discussed.

Chapter 7 Quality Analysis of Laser Sintered Parts: This chapter provides an analysis of the microstructure characteristics and the mechanical behaviour of the fabricated oral solid dosage forms. The key factors that affected the quality of the parts are identified. An extensive discussion related to the density, the uniformity, the surface roughness, the elasticity and the stiffness of the parts is provided with important correlations to the processing parameters and the materials composition in the blends.

Chapter 8 Formulation of Coated Particles for Laser Sintering: A new approach of blending polymer powders to enhance their processability in Laser Sintering is presented in this chapter. Three methods based on precipitation and emulsion-solvent evaporation principles are developed for the production of a polymer film coating. The various mechanisms that influenced the coating quality and discussed.

Chapter 9 Concluding Remarks and Future Recommendations: This chapter highlights the most important findings of this PhD and provides a short discussion of the main conclusions. Areas of improvement are outlined and future research ideas are recommended.

CHAPTER 2   LITERATURE REVIEW

2.1   Additive Manufacturing – An Overview

Additive manufacturing (AM) is the general term for a set of technologies that use a 3D computer aided design (CAD) to create physical objects by successive addition of material [4]–[6]. During the development of AM various terms and definitions have been used, often referring to specific applications and trademarks, such as automated fabrication, solid freeform fabrication, layer-based manufacturing, stereolithography or 3D printing, and rapid prototyping [4], [7]. AM is the formalised term defined by the International Organization for Standardization (ISO), for the process of joining materials to make parts from 3D model data, usually layer upon layer, as opposed to subtractive manufacturing and formative manufacturing methodologies (ISO/ASTM DIS 52900:2018) [4]. Originally, AM was introduced by Charles Hull in 1986 in a process known as stereolithography, which used resins to create models and prototypes, and since then many developments have followed including methods, materials and equipment [7]– [11]. According to the ISO/ASTM standard, AM technologies can be classified into seven categories: Vat Photopolymerisation, Powder Bed Fusion, Material Extrusion, Material Jetting, Binder Jetting, Sheet Lamination, and Direct Energy Deposition [12]. These technologies are classified based on the printing concept (eg. lasers, print heads, extrusion, etc.) that gives each of them unique characteristics for unique applications [1], [7]. These categories are further divided into subgroups based on the equipment, the raw material input or the layer binding mechanism [1], [7], [13]. Depending on the process and the materials used each one of the techniques has both strong and weak points, but the principal advantage of all AM technologies is the freedom of design [5], [6], [14].

AM technologies use a computer generated model to directly fabricate components using plastics, metals or ceramics [7], [15]. Processing involves the deposition or fusion or binding of materials to produce a 3D object by building it layer by layer [14]. At first a 3D design model in CAD software containing information of the external geometry of the object is converted to STL format, which is a triangular mesh of the object. Then the file is sliced into 2D profile layers, the thickness of which depends on the equipment used. The file is finally transferred to the AM machine where each sliced layer of the model is

deposited on a build platform and bonded to the previous layer until the 3D object is complete [7], [10], [14].

The main advantage of AM technologies is the ability to produce fully functional parts with significant complex geometries, without the need for moulds or tooling, compared to conventional manufacturing [5], [6], [14], [16], [17]. Geometries that are difficult or impossible to fabricate with traditional processes can be produced easily and at similar costs as simple shapes [6], [14], [15]. Furthermore, as tooling is no longer required the cost of product development at early stages can also be reduced (Figure 2.1) [2], [5], [6], [10], [14], [17]. Moreover, parts can be modified fast and easily changing the design, which significantly reduces the lead-times for a product and also enables flexible production and even customised products [5], [6], [14], [15], [17]. AM has introduced on-demand manufacturing, products with shapes that were impossible to produce by other means, and has proved valuable in the manufacturing of high value low volume parts in a cost-efficient way, compared to the current mass manufacturing [15].

In the early days of AM, the technology was used for the production of functional and technical models and patterns for rapid cost-effective prototypes [2], [5], [10], [14], [17]. However, the driving force from industry contributed in the expansion of AM to develop rapid tooling and rapid manufacturing of functional end-use products [9], [17]. The technology has experienced a number of significant changes through the years that led to improvements in accuracy, mechanical performance, reductions in costs of machines and production that have increased the volume of manufacturing and applications [6], [7], [9], [10]. AM has come into its forth decade and is already used in various applications in engineering industry showing high promises, as well as in other areas of everyday life, including medicine, education, architecture, entertainment, etc. [6], [7], [9], [15]. The key industries currently driving innovation is the aerospace, automotive and medical industries, mainly because of the high complexity of the geometry of the fabricated parts, the low density achieved using lattices and introducing cut-outs to develop lightweight structures and the customised solutions found, in combination of saving time, tooling and process planning during the development of products [6], [7], [15], [17]. Many companies in the aerospace industry have started producing high-performance, lightweight and complex AM parts for satellites, helicopters and aircrafts, for better cooling pathways and support. Boeing installed parts on their military and commercial jets and airliners, GE started a large production of gas turbine engine components, such as blades and nozzles,

Airbus developed and installed hinge brackets saving up to 40% in weight, and various F1 components, such as gearboxes, suspension parts and engine parts with lattice structures, are already been used in racing cars [5]–[7], [9], [17].
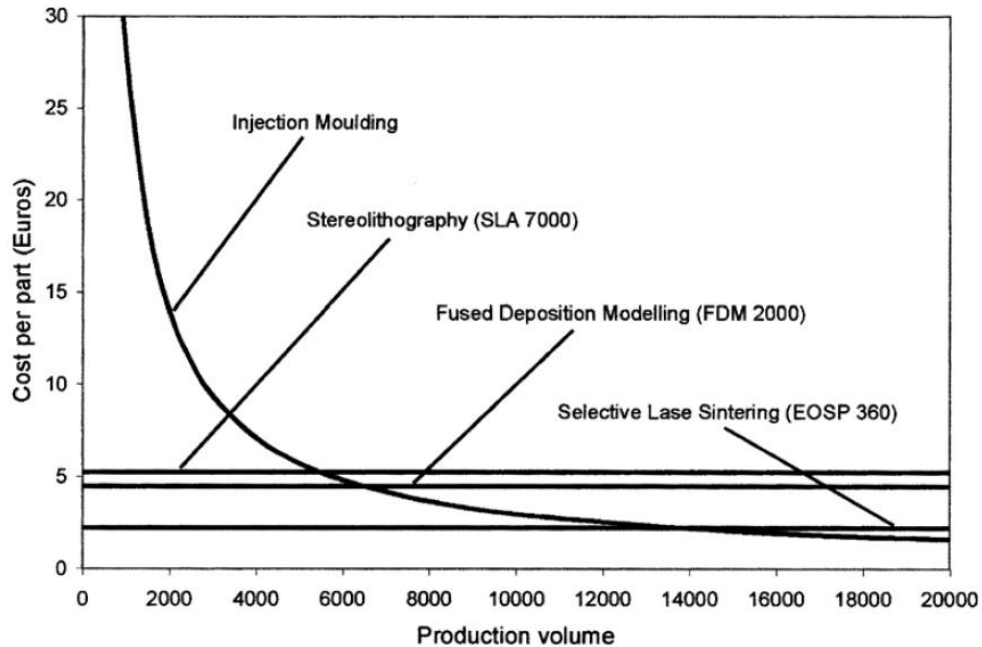
Figure 2.1: Cost comparison through the years using different processes for the production of a lever [5]

2.2 AM in Pharmaceutics

AM has offered great potential to the pharmaceutical industry that is expected to change the future manufacturing of drug delivery systems [9], [18]. Conventional manufacturing of drug delivery systems has evolved into using multi-step processing, such as granulation, extrusion and coating, which introduces limitations to practical flexibility and complex design, but also generates problems related to drug degradation, formulation or batch failures [2], [8]. The high cost and risk of mass manufacturing has turned the interest towards AM [2], [3], [15]. Recent advances in AM provided with new opportunities in pharmaceutical research and early stage development reducing both time and cost [2], [8], [15]. AM can be a valuable tool in pre-formulation as for the validation of novel drug delivery concepts, and therefore can reduce the inherent risk of scale-up and time to market [2]. The high potential of AM opened the way to the design and production of small volume units and novel drug devices, which further allowed the

development of personalised medicines [1]–[3], [18], [19]. Freedom of design changed the microarchitecture of drug dosage forms through the years developing novel delivery systems, a few examples of which are microcapsules, antibiotic micro-patterns, synthetic extracellular matrices, nano-suspensions, doughnut-shaped designs and rings for controlled-release systems, etc. that can demonstrate controlled local composition [8], [9], [20], [21]. Personalised medicines on-demand target to increase efficacy and reduce adverse reactions, through the development of new formulations and devices, drug combinations and multi-component dosage forms with complex release profiles [8], [22], [23]. Based on the age, race or gender and the pharmacogenomics profile, a targeted therapeutic treatment can be designed to address the needs of each individual and deliver the drug safely and effectively [2], [3], [8], [9], [22].

A variety of AM processes have been introduced in pharmaceutical industry depending on the materials and the demands of the final product, which fall into the categories of Binder Jetting, Material Jetting, Material Extrusion, Powder Bed Fusion (PBF) and Vat Photopolymerisation [1]–[3], [8], [19], [20], [22]–[25]. Some of these techniques are simple (i.e. Extrusion) and some are adaptable to using natural and synthetic polymers, but also bioceramics (i.e. Sintering) and they have been employed for the production of drug dosage forms, implantable and topical drug delivery systems, such as scaffolds, tissues and films [8], [9], [15], [17], [26]. The most commonly used materials are cellulose, collagen, natural rubber, poly(lactic acid) (PLA), poly-l-lactic acid (PLLA), polyethylene glycol (PEG), polyethylene oxide (PEO), poly-ε-caprolactone (PCL), poly-glycolide (PGA), poly(lactic-co-glycolic)acid (PLGA), poly(vinyl alcohol) (PVA), polymethacrylates (Eudragit®), hydroxyapatite (HAp), bio-glass, bio-resins, and others [2], [8], [17], [26], [27].

The first time that AM was used in pharmaceutics was in 1996 when a powder bed process was employed to fabricate oral solid dosage forms (tablets) [2], [25]. Wu et al. [28], demonstrated the ability to produce AM drug delivery systems developing core-shell dosage forms containing the drug within the core to control the release, using the TheriForm™ process. The core was consisted by PEO, which was the main filler material and the outer walls were made with PCL, however the printed dosage forms exhibited high porosity due to limitations of the process, which led to an immediate drug release profile [2], [28]. The process used is a drop-on-powder (DoP) licensed application, which covers the use of AM in medical products and is widely known nowadays as Binder

Jetting [2]. The method uses a liquid material across the powder bed to bind the powder particles together through the localised dissolution of the liquid binder, which results in the solidification of the layers [2], [3], [7], [9]. However, the absence of external force and deformation mechanisms introduces porosity within the structure, compared to other AM processes, which can reduce the product performance [2], [3]. In 2016 the first FDA-approved AM drug product was released in the market using Binder Jetting technology [2], [3], [25]. In fact, Spritam® (Aprecia Pharmaceuticals) exhibits rapid dispersion properties due to the manufactured increased porosity, which made it the first fast-dispersing drug product that has been ever developed [2], [3]. Recently, researchers have been trying to develop more drug products using alternative AM methods, such as Ink Jetting, Fused Deposition Modelling (FDM), and Stereolithography (SLA). However, there are major drawbacks in the use of these technologies in pharmaceutics, in terms of powder-binder wettability, droplet penetration, nozzle clogging, fluid leakage, toxicity, additional intermediate steps (eg. solvent drying), impurities, resolution finish, etc. [2], [3], [18], [25], [29]. Furthermore, these methods present considerable limitations in scaling-up the manufacturing process and complicated evaluation steps of the developed products [2], [5], [9], [15]. Therefore, an AM technique that does not require the use of solvents or filaments, able to produce larger volumes, could potentially push the boundaries of mass production of functional drug delivery systems [1], [2], [20], [25].

Laser Sintering (LS) is another PBF process presenting a set of advantageous features, compared to other processes, enabling new opportunities in pharmaceutics [1], [6], [20], [29]–[31]. LS is applicable to powder-based biocompatible material systems, which opens the way for the development of various dosage forms, since most of the materials for pharmaceutical applications are in powder form [1], [6], [9], [20], [25], [32]. LS is a single-step, solvent-free process, which provides with increased stability, manufacturing speed and mechanical properties, compared to other AM techniques [1], [2], [15], [21], [25], [29], [33]. LS does not require prior production of filaments or support structures and potentially additional post processing steps, compared to FDM and SLA, and moreover achieves high resolution and part functionality due to the laser precision [1], [6], [8], [9], [17], [18], [25], [21], [29], [33], [34]. LS offers high degrees of design freedom and more importantly, control over the microstructure, which can enhance the production of complex drug delivery systems with increased functionality [1], [24], [26], [31], [33], [35], [36]. Furthermore, LS has the ability to manufacture different

components during a single build and has a high build platform capacity, which reduces the processing time and cost compared to other processes, and can lead to scale-up opportunities and mass production [1], [5], [6], [9], [20], [33].

Although LS has many advantages to offer, there are limitations that have limited the use of this technology mostly to biomedical scaffolds [1], [8], [15], [25], [27], [31], [37], [38]. The primary reason is the harsh conditions that occur during the sintering process, which can compromise the stability of the powder and the drug due to high energy input of the laser [1], [6], [15], [20], [25]. In that event, there are no pharmaceutically approved materials to date for LS, which reveals the need to develop new biocompatible/biodegradable material systems and benefit from this technology in pharmaceutics [1], [2], [25], [30]. Initial LS research in pharmaceutics has demonstrated the use of a variety of pharmaceutical polymeric powders to fabricate implants and scaffolds, including PCL, high-density polyethylene (HDPE), PVA, PLLA, PEG, and cellulose acetate [25], [39]–[42]. First, attempt to incorporate the drug within the polymer mixture prior to sintering, was in 2007 when Leong et al. produced drug delivery systems with immediate release in a 3D Systems LS machine, using PCL and Methylene Blue as a model drug [1], [24]. Later in 2017, Fina et al. used a LED laser diode desktop LS machine to produce modified-release profile oral dosages, using two thermoplastic pharmaceutical grade polymers, Eudragit L100-55 and Kollicoat IR, containing paracetamol in the powder mixture [25]. Their results showed that the process was completed without degradation of the drug, however sintering could not be achieved without the use of additives in the mixture to enhance the absorption of the laser [1], [25]. Since then, a few researchers have conducted studies to understand the effects of the formulation on the sintering process, and additionally the effects of the process variables on the final quality, in order to explore the feasibility of producing LS oral dosage forms [21], [29], [36], [43]. A range of new pharmaceutical materials for LS were successfully employed, such as hydroxypropyl methylcellulose (HPMC), ethyl cellulose, mannitol, lactose monohydrate, PEO, vinylpyrrolidone-vinyl acetate copolymer (Kollidon®), and Eudragit RL. However, most of the studies have been limited in the use of PCL or Eudragit L100-55, since both the materials presented a preferred set of characteristics that found to result in enhanced sintering performance [25], [36], [43], [44]. Furthermore, it has been reported that the laser energy input needed to sinter pharmaceutical powders had to remain low, in order to avoid degradation of the materials and the drug [20], [44].

Therefore, it was observed that sintering led to reduced part density, which has restricted the use of LS to the production of immediate or fast release oral dosage forms, due to the manufacturing induced overall porosity that facilitates the penetration of liquids in the structure [1], [20], [25], [29], [43], [44]. This highlights the need to investigate further the behaviour of powders and drugs under various processing parameters, towards the development of new materials and formulations with enhanced properties. This could enable the production of LS multi-material systems with complex release profiles that can be patient specific and offer innovative opportunities to modern medicines.

2.3   Laser Sintering

Laser Sintering was the first commercialised Powder Bed Fusion process, which was originally employed for the production of plastic prototypes, using a laser scanning approach [7]. All PBF processes use a thermal source to locally induce fusion between the particles contained within a powder bed to create a 3D object [6], [7], [13], [35]. A range of radiation sources including LED, lasers and broadband light have been employed over the years that extended the application of PBF processes to metals and ceramics, which increased their use worldwide [7], [15]. The most popular industrial radiation sources for PBF are lasers, a powerful source of heat that provides with high level of control and precision, and therefore with finer resolutions [7]–[9], [15]. One of the biggest advantages of PBF processes is that they do not require support structures, since the parts are supported by the surrounding unfused powder within the bed, which leads to greater design freedom [6], [9], [13], [27], [45]. Furthermore, the unfused powder can be recycled and reused, which is highly beneficial, as the cost and the material wastage can be reduced [1], [5]–[7], [10], [21], [33], [35], [46], [47].

LS is reported as the second most important process of AM technologies [9]. Since the first time LS was introduced, it has gone through many developments and the technology has evolved from prototyping to the manufacturing of end-use parts [6], [45], [48]–[50]. LS has reached a high technical level showing great improvements in build repeatability, dimensional accuracy, surface finish and mechanical properties compared to engineering-grade materials [7], [33], [48], [50], [51]. This technological advances have further improved the times and costs of production, but also the energy uses, which reduced the environmental impact of the process [1], [5], [15], [51]. Nowadays, LS can provide a

viable alternative to established manufacturing processes by moving to the mass production of integrated products and by introducing on-demand manufacturing of individual parts [7], [15], [33].

LS is the only AM process that is applicable in a great variety of materials, such as waxes, food, polymers, polymer composites, metals, ceramics and combinations of materials, which has made it very popular, since is the most common and widely accepted AM process [6]–[10], [15], [17], [26], [45],[52]–[54]. The versatility of LS has increased the use for direct manufacturing of products in a vast number of fields, while many industrial companies have already adopted the technology in a number of their operations [7], [15], [51], [55]. Typical applications for LS include, high-performance components for aerospace, automotive and sports, but also electronic and medical devices, consumer goods, toys, and cosmetics [1], [7], [9], [13], [15], [17], [35], [56].

The LS technique uses a focused laser beam to selectively fuse together successive layers of a powder in order to create a 3D object [7], [24], [57], [58]. The layer thickness is usually between 100 to 150μm. Initially, the powdered material is spread across a building area with a blade or a roller in a chamber filled with nitrogen, to minimise oxidation and further degradation of the material. Before the process begins, a warm-up phase of approximately 1 to 2h is taking place, where the powder bed is slowly heated up to a selected temperature. During processing, the temperature raises just below the melting point of the material and the laser beam scans the surface in specific locations to form layers of fused powder. The selected areas correspond to a cross-section of a 3D part according to the prescribed geometry in the CAD model. Once a layer is formed the build platform is lowered by one layer thickness and a new layer of powder is spread. The laser beam scans the subsequent cross-section and the process is repeated until the entire part is built. When the part is complete, a cooling period of several hours is required before the part is exposed to ambient conditions, in order to avoid oxidation and distortion due to thermal stress. After the cool-down phase, the part is removed from the powder bed and the loose powder is cleaned from the surfaces using a brush or a high pressure bead blast [1], [6], [7], [10], [13], [17], [45], [49], [53], [59]. A schematic of the LS process is shown in Figure 2.2.

Sintering is the process of powder fusion without complete melting [7]. The process relies on the coalescence between adjacent particles, which is induced by the thermal energy transferred from the laser to the scanned regions [9], [31], [51]. The mechanism is

activated by the reduction of the surface free energy, which results from the decrease of the total surface area caused by the diffusion between powder particles [7], [31]. The fusion mechanisms vary depending on the nature of the material composition and the powder properties [7], [51], [53]. Partial melting is the most common fusion mechanism in LS applied to sinter polymer powders, such as single phase material or a mixture of different polymers [6], [7], [53]. Considering that sintering does not occur in full melting of the particles, this binding mechanism involves the formation of necks between the particles, which results from the molten outer shell, while the core of the particles remains solid [6], [7], [53]. The second most important fusion mechanism is the liquid phase sintering, where a binder is used to bring together solid particles of powder [38], [53]. In particular, the process temperature targets to liquefy a low melting point polymer, which disperses between the solid particles of a high melting point material that is difficult to sinter [7], [30], [53]. This binding mechanism occurs during sintering of metal and ceramic powders, where a polymer is used to serve as the binder in a simple powder blend or a composite mixture, or even as a coating [7], [17], [30], [38], [53].

The first commercial LS system was the DTM Sinterstation 2000, which entered the market in 1992, developed by DTM Corporation, which later merged with 3D Systems. Thirty years later the two largest manufacturers of commercial LS systems, 3D Systems (USA) and EOS (Germany), have developed a series of machines that meet the standards of industrial manufacturing [6], [7], [49], [52], [60]. The machines are equipped with CO_2 gas lasers, which have a wavelength of 10.6μm that makes them highly suitable to sinter polymeric materials, since polymers exhibit increased absorption rates at far infrared [1], [7], [53], [61]. Recently, EOS announced the development of CO laser system with an ultra-fine laser beam, which is half the diameter of the current CO_2 laser, and is designed to achieve increased precision, high surface finish, and the fabrication of smaller geometries [1]. Another two key commercial suppliers for LS are ASPECT (Japan) and Farsoon (China) [45], [49]. Farsoon has replaced the standard CO_2 laser with a fibre laser that has a smaller laser beam, which applies high power density to the powder bed, in combination with the use of a scanning system operating at higher speeds, which reduces the production times [1], [7]. More recently, desktop LS systems entered the market, which made it more affordable for smaller companies to employ LS in their operations and extend its use to a wider range of industries and applications. Furthermore, the small build volume of these systems and the lower costs of materials and equipment, promoted

the research towards the development of new materials for LS. The manufacturing companies are Sharebot (Italy), Sintratec (Switzerland), Sinterit (Poland) and Formlabs (USA). Sintratec and Sinterit machines are designed to use diode lasers, which are much cheaper, however they are lower intensity lasers absorbing in the optical spectrum, and therefore require additives to achieve sintering of the powders [1], [6], [25]. Recent advances include the launch of high-temperature processing LS systems from EOS, which are optimised to sinter a broader range of engineering thermoplastic materials (eg. poly ether ketone (PEEK)) and composites (eg. carbon-fibre reinforced PEKK) that require high temperature conditions to be successfully processed, since most commercial systems are able to heat up the chamber to approximately 180°C, which is limiting their use to a small variety of thermoplastic polymers [6], [45]. Furthermore, a start-up company from Belgium, Aerosint, is developing a LS machine that will use a double-material system, one for the fabrication of the components and one for the surrounding support powder, which in fact will enable the consecutive powder recycling, and thus, the reduction of the overall manufacturing costs.
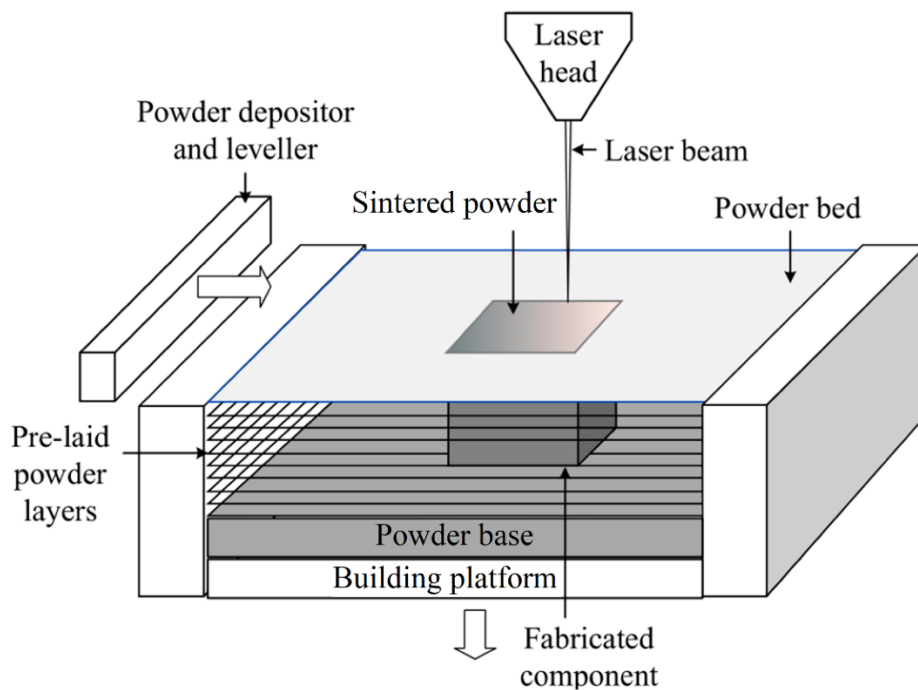
Figure 2.2: Schematic of Laser Sintering process [59]

2.4   Materials for Laser Sintering

The most common materials processed with LS are polymers [51], [53]. LS systems are designed to directly process polymeric materials and to indirectly process metals and ceramics [7], [17], [38]. Polymers have been very popular in AM in general, due to their chemical stability and their increased functionality in a variety of applications [15]. The range of polymers for LS falls in the category of thermoplastic polymers, since they exhibit relatively low melting temperature and high melting viscosity, low thermal conductivity and low tendency for balling, which makes them highly suitable for processing with this technology [1], [7], [15], [51]. Thermosetting polymers are not normally processed, as they tend to harden at elevated temperatures, rather than melt to achieve particle coalescence [7]. However, thermosets can be used for indirect processing as an infiltrant, which penetrates the structure filling in the pores that leads to increased part density, strength and precision [33], [53].

The most common powdered material used in LS is polyamide 12 (PA12 or Nylon); a thermoplastic semi-crystalline polymer presenting excellent thermal characteristics, which are aligned with the LS requirements, and enable the powder to be processed reliably. Mechanical properties of LS parts produced using Nylon 12 powder approach those of injection moulded components, showing unique microstructures, however they exhibit significantly reduced elongation at break due to the nature of layered manufacturing [6], [7], [24], [39], [54], [62]–[64]. Other commercially available materials for LS include PA 11, PA 6, polypropylene (PP) and various reinforced polyamides (fibre or metal fillers), high-temperature engineering plastics, such as polyaryletherketones (PAEK), polybutylene terephthalate (PBT) and polyphenylene sulphide (PPS), which are flame retardant and chemically resistant ideal for high performance applications, and finally thermoplastic elastomers (TPE), such as polyurethane (TPU) and polyether block amide (PEBA), which are rubber-like suitable for shape-memory applications [6], [7], [9], [10], [13], [15], [33], [45], [48], [53], [54], [58]. The majority of LS materials are semi-crystalline thermoplastic polymers with relatively high crystallinity, which allows for a well-defined transition from the rubbery state to the melt that is favourable in LS [6], [7], [30], [34], [52], [53]. On the contrary, amorphous thermoplastic polymers present a random polymer chain structure and therefore do not exhibit a distinct melting point. These materials gradually soften above their glass transition in a wide range of temperatures, however they stay in a much more viscous state compared to semi-

crystalline that transform quickly to viscous liquids. For this reason, amorphous polymers present a lower degree of fusion between particles, and consequently higher degree of porosity, which results in parts with lower strength [6], [7], [52], [53], [65]. Despite this, amorphous materials require longer cooling times compared to semi-crystalline, which in fact results in lower shrinkage and hence, higher dimensional accuracy [6], [7], [53], [55], [60]. Polystyrene (PS) is a successful example of amorphous commercial material for LS that is used for investment casting, to produce patterns or moulds with increased precision for high surface finish [6], [7], [45], [53], [55].

Research within the universities and research institutes has demonstrated the ability to process more polymers with LS, however the number of materials explored is limited [6]. Among the materials that have been referred in literature are polyethylene (PE), HDPE, ultra-high molecular weight polyethylene (UHMWPE), polyoxymethylene (POM), and polycarbonate (PC) [42], [48], [55], [65]–[70]. Furthermore, several biodegradable polymers have been investigated, including PCL, PLA, PLLA, PLGA, PVA, and poly(3-hydroxybutyrate-co-3-hydroxyvalerate) (PHBV) [17], [31], [62], [71]. Although optimisation procedures have been followed based on the polymer physical properties that led to some remarkable part end-properties, these new materials continue to have limited achievement due to moderate success, in terms of precision and mechanical performance [13], [15], [31], [42], [48], [55], [65], [70]. Further research, has focused on the possibility of using nanofillers, such as carbon and glass fibres, graphite, quartz, aluminium, silica, HAp and talk, as reinforcement in LS powders (PAs, PC, PP, PEEK, PCL) that could lead to the improvement of their mechanical, physical or electrical properties and the potential use to a wider range of AM applications [7], [13], [15], [17], [26], [35], [42], [48], [53], [68], [72], [73]. Another method to reinforce LS powders is to prepare core-shell composite particles by coating the filler material with the base LS polymer. This approach was developed as an alternative to simple mechanical mixing for indirect processing of metal and ceramic powders, to ensure good dispersion and stability of the filler material within the polymer matrix. In addition, the absorption of the laser beam radiation increases, which further improves the sintering performance and therefore the mechanical behaviour, since the laser beam simply fuses the polymeric shell of the particles [53], [72]. Some researchers have attempted to coat nanofillers to improve the processability of LS powders and have achieved some success. Zheng et al., developed nano-Al_2O_3/PS coated particles with a core-shell structure by emulsion polymerisation.

Their results demonstrated improvements in the filler/matrix interface adhesion and the laser beam absorption, compared to simple mixing of materials, which led to the production of parts with enhanced mechanical response [74]. Yan et al. adopted a similar approach, to coat nanosilica particles with PA12 using a dissolution-precipitation method. They found that the dispersion of the nanosilica was uniform in the polymer matrix avoiding the formation of agglomerates occurred in the conventional material mixing powder, and furthermore the absorption of the laser beam was increased by the powder. It was demonstrated that the coating improved the physical characteristics of the powder, which eventually offered better sintering conditions, resulting in an increase in the tensile strength and modulus, impact strength and elongation at break [75].

However, although advances have been made from researchers towards processing of new materials with LS, Nylon 12 makes up to more than 90-95% of the current market, while there are thousands of injection moulding polymer grade materials commercially available [6], [48], [58], [65]. One of the reasons is that Nylon 12 possesses physical properties that are compatible with LS and this makes the material easy to process [6], [48], [60]. Another reason is the relatively low cost of Nylon 12 compared to the other LS polymers [6], [45], [48]. Commercially available polymers were developed for injection moulding applications, where the processing conditions considerably differ from LS, which puts restrictions in finding polymers in powder form that meet the requirements of LS [7], [48]. Although Nylon 12 parts present properties similar to injection moulding components, some of the mechanical properties, such as impact strength and elongation at break are significantly inferior [6], [53], [65], [75]. Furthermore, the increased demand for new high-performance materials and highly flexible polymers towards the spread of AM industrial applications, highlights the need for developing and processing a greater variety of new materials with LS [6], [15], [45], [55], [65], [72]. Hence, focus must be made on the complex LS processing conditions and the required material properties, in order to understand the criteria for successful sintering [48], [54], [65]. Addressing the challenge of processing alternative materials, while monitoring the various influences on the sintering behaviour, can contribute to the improvement of the process capability of current and new materials and eventually exploit the greater design freedom and rest of the benefits that LS can offer throughout many industries [6], [45], [48], [65].

2.5 Material and Processing Considerations

Processing of polymeric powders with LS requires specific material and process characteristics in order to achieve high quality functional parts [48], [55], [57]. Quality can be defined in terms of precision, mainly for dimensional accuracy and surface finish, and in terms of mechanical performance, mainly for strength, stiffness, surface hardness and density [6], [52], [55], [57]. The ability to process a given material in LS is strongly influenced by the properties of the powder and the process parameters used during sintering [45], [52], [55]. According to researchers there are four criteria: 1) the physical properties of the material (eg. particle size, particle shape and flowability), 2) the thermal properties of the material (eg. glass transition, melting and crystallisation temperatures), 3) the LS processing parameters (eg. laser parameters and build parameters), and 4) the behaviour of the material during processing (eg. melt flow and viscosity) [6], [15], [52], [57], [58], [76].

Although in theory any powder should be able to be processed with LS, the harsh conditions applied with the use of a laser beam, the complexity of the process and the mechanisms of polymer consolidation, have limited the choices of suitable materials for use [53], [58], [72]. In order to process successfully a polymer, the powder must present a specific set of thermal and physical characteristics, which are discussed in the following sections. Furthermore, the process parameters must be adjusted according to the material properties to achieve optimal sintering and avoid part failure or material degradation [6], [52], [54], [58], [66], [76]–[78]. An increased understanding of the relationship between the powder properties and the process parameters is crucial for the evolution from fabrication of parts with good properties to the production of parts that will satisfy the requirements of end-use applications [45], [52], [58], [65], [78].

2.5.1 Thermal processing window

During LS the powdered material is raised to temperatures close to their melt points in order for the laser to apply the minimum energy needed to induce fusion of the particles [45], [49], [55]. It is necessary for the material to achieve a molten state in order to achieve the highest part density and mechanical properties [6], [7], [49], [55]. However, the complexity of the process introduces many challenges in the consolidation mechanism for many polymers [6], [65]. In order to address the challenges of the thermal

requirements it is necessary to understand that in the LS process the particles of the polymer are selectively fused or melted changing state from a solid to a viscous flowing liquid for the subsequent creation of layers [45], [52], [55], [58]. However, the laser scans the selected area and the polymer exceeds the point of phase transition for a short period of time, where solidification depends only on the temperature induced degree of particle coalescence, since the process does not involve any mechanical pressure [45], [48], [54], [55], [66]. Afterwards, the produced parts are cooled slowly, whereas in injection moulding parts are cooled and solidified in a few seconds [7], [45]. Therefore, to achieve full coalescence of the particles in the top powder layer and increase adhesion with the previous sintered layers, it is necessary to have a large difference between the melting (T_m) and crystallisation (T_c) points of the polymer. This difference defines the thermal processing window of the polymer, which ideally will allow the material to stay in liquid state for a longer period of time during the cooling stage, preventing shrinkage and warping, but also reducing the accumulation of residual stresses in the part structure, and thus it will be less likely to distort or curl [6], [7], [45], [48], [49], [54], [57], [58], [64], [65], [79]. Besides the thermal processing window, it is important to have a narrow melt temperature range so that the laser transfers enough thermal energy for the polymer to fully melt. Furthermore, the polymer can be heated up to just below the melting point allowing the power of the laser to be minimised to lower running costs [6], [31], [45], [49], [53], [55], [65]. The thermal processing window is that which makes polyamides perfect for LS, as the polymers present a relatively sharp melting peak with a super-cooling window, which provides more leeway towards optimisation for successful sintering, and hence, superior mechanical properties [7], [26], [31], [45], [64]. Most commercial polymers present a small processing window or an overlap of the melting and crystallisation peak. A schematic representation of a Differential Scanning Calorimetry (DSC) curve showing a wide sintering window is displayed in Figure 2.3 representing the desirable type of thermal characteristics of a LS polymer. It is possible to sinter materials showing a smaller sintering window with more control over the different processing parameters, however it is more difficult, and more likely to result in shrinkage due to premature crystallisation [7], [45], [55], [58], [65].
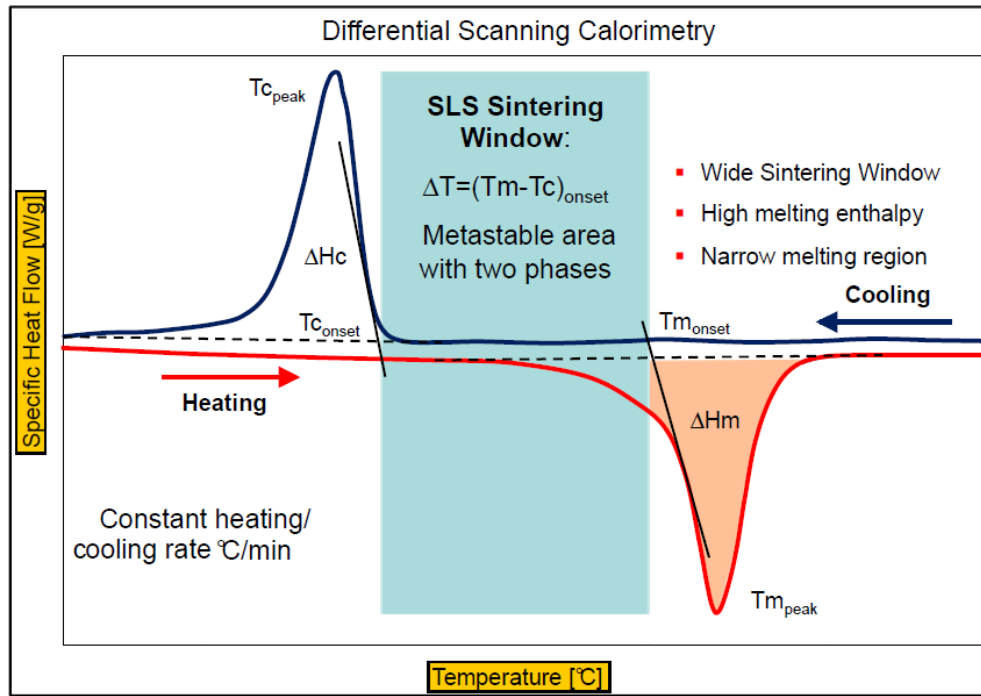
Figure 2.3: The nature of the sintering window in a typical DSC thermogram for LS [58]

2.5.2 Rheology of powders

Besides the wide thermal sintering window, polymers undergo changes in the chemical structure upon heating, which leads to important changes in the physical properties, such as the molecular weight (MW) that relate to the sintering process [6], [45], [57], [64], [65]. As described earlier, successful sintering is dependent on the particle coalescence, since no additional mechanical pressure is applied. To achieve high coalescence rates it is necessary for the polymer to present low melting viscosity (η_0) and high surface tension (γ) [6], [7], [45], [54], [57], [58], [64], [65]. In particular, the melting viscosity should be low enough to allow complete consolidation during the process, which involves good interfusion of the polymer chains to induce particle necking and layer to layer adhesion in order to obtain high part density [48], [53], [54], [58], [64], [65]. However, significant low melting viscosity can lead to high shrinkage during cooling and recrystallisation of the polymer, which results in poor part dimensional accuracy [49], [53]. A good way to prevent shrinkage is by controlling the rate of recrystallisation, through the preheating of the powder at a temperature slightly below the melting point of the material before processing. Maintaining this temperature for a certain time after consolidation, slows down the recrystallisation that can lead to the production of parts with improved dimensional accuracy and lower risk of distortion and warping [6], [31], [34], [53], [57].

On the other hand, the melting viscosity is linearly related to the MW of the polymer; low MW associates with low melting viscosity and high MW is linked to high melting viscosity. When the melting viscosity is quite high it brings difficulties in processing the powder due to poor consolidation [53], [57], [58], [64]. Therefore, there seems to be an optimum MW range for processing polymers with LS, however it is very difficult to control, since the MW of polymeric materials increases in every thermal cycle during the build process due to ageing phenomena [6], [7], [45], [53], [64]. A good practise is to mix virgin and used powder together, which in fact has been reported to improve ductility, and hence elongation at break [6], [64].

2.5.3   Particle size and shape

The morphology of the single particles highly determine the behaviour of the powder during processing, which is linked to the properties of the final sintered part. In case of LS powders, the size distribution and geometry of the particles directly influence the performance of the process, in terms of powder spreading, part density and precision, and consequently, the final mechanical performance [6], [45], [57], [58], [76]. Since the process does not involve any additional compaction, it is very important to achieve high powder bed density during the deposition of powder layers over the build platform [6], [45], [58]. Therefore, particles are preferred to be as spherical as possible as shown in Figure 2.4, in order to achieve a high packing density and induce an almost free flow, as the powder is distributed on the bed by the blade system [6], [45], [49], [54], [58], [76]. Angular and irregular shapes of particles result in poor packing efficiency due to their tendency to interlock with each other, which leads to increased part porosity and thus, inferior mechanical properties [45], [49], [58], [77], [80]–[82]. In addition, there is an optimum particle size for LS powders between 45 and 90μm, with a relatively narrow size distribution of 50 to 60μm, which are considered key parameters for high part density, high surface quality and accuracy [6], [45], [49], [65]. Larger particles can be processed, however the core of the particles may not melt completely, which results in porosity and rough surfaces [7], [45], [49], [57], [65]. On the other hand, very small particles have negative effects on the deposition of uniform powder layers, due to high electrostatic forces and inter-particle friction that cause agglomeration and powder stickiness [6], [7], [54], [57], [58], [76], [77]. It is quite challenging to find powders with the optimum particle requirements, however, researchers have reported the use of

multimodal powders that consist of a range of particle sizes that could lead to optimal sintering [6], [45]. A mixture of different particle size fractions increases the packing density since the smaller particles fill in the gaps between the larger particles, leading to less particle interactions. Ideally these particles should have a high sphericity to further improve the powder flow, which will increase the density, the accuracy, the surface finish and the mechanical performance of the final part [6], [7], [57], [81].
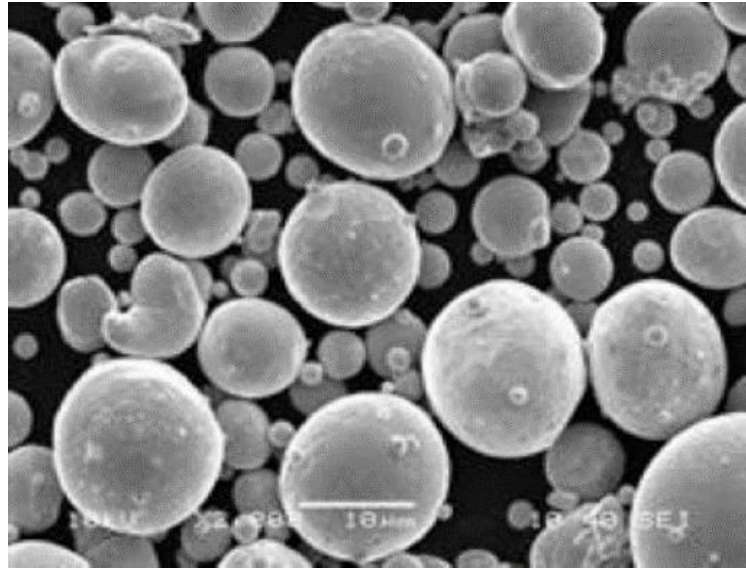
Figure 2.4: Typical powder for LS process [83]

2.5.4   Flowability

Flowability is the property related to the materials dynamic flow characteristics, which are crucial during the application of the powder across the LS build platform [80]. As it was mentioned in the previous section, the packing density of the powder bed is a key requirement for high quality LS parts. High flowability increases the packing efficiency and allows the deposition of thin, homogeneous layers of powder, which results in increased density and precision of the final parts [6], [54], [76], [77]. Flowability is strongly influenced by the cohesive characteristics of the powder that can significantly impact the flow efficiency. Low flowability results in the poor distribution of the powder into layers, and therefore, a lack of homogeneity that leads to high porosity and low mechanical properties [76], [77], [80], [81]. Flowability is dependent on the physical properties of the powder itself (particle size and shape) as was described earlier in 2.5.3, on the environmental conditions (temperature, humidity), but also on the test conditions

[6], [45], [54], [77], [80], [81], [84]. Researchers have remarked that humidity affects the flowability of powders causing electrostatic charges between the particles that lead to agglomeration due to cohesion [6], [77], [81], [84]. Furthermore, electrostatic forces may be generated from impurities into the powder, crystalline defects, absorption of gas molecules in the polymeric crystals or even during handling of the powders (eg. sieving or milling) [6], [84]. The use of inorganic powdered additives, such as hydrated silicas, glassy oxides, fluoroplastics and metallic stearates has been reported in literature to improve the powder flow and enhance the LS process [6], [54]. An example of a non-cohesive powder and a cohesive one is given in Figure 2.5.

Figure 2.5: Particles of a non-cohesive powder spread evenly and particles of a cohesive powder clump together [85]

2.5.5   Process parameters

When preparing a build in LS many process parameters need to be adjusted in order to achieve the optimum quality of the sintered parts. These parameters differ according to the properties of the powder and the specific requirements of each application [1], [6], [7], [52], [57]. A typical LS system includes a scanner that enables the laser to move across the powder bed in two dimensions in order to sinter specific areas of material. Laser and powder interactions are fundamental and depend on the three most influential parameters related to the laser system, which are the laser power, the scan speed and the scan spacing. The laser power is the rate of change of thermal energy that the laser applies on the powder as it scans; the scan spacing is the distance between two parallel laser scan lines; and the scan speed is the velocity at which the laser travels along the surface of each layer. These parameters form the equation of the energy density (ED) as proposed by Nelson et al. (Equation 2.1) [86], which describes the energy transferred from the laser

to the powder. The laser energy density should be set by adjusting these three parameters to provide adequate heat to melt the materials [1], [6], [7], [45], [48], [52], [67], [87].

$$Energy\ Density = \frac{Laser\ Power}{Hatching\ Spacing\ x\ Laser\ Speed}\ J\ /\ mm^2$$

(2.1)

The ideal ED needed for each material is different and varies between different LS systems, although, there are some generalities that apply to all powders and systems [6]. As such, higher ED typically yields parts with increased density and therefore strength, due to the increased heat that is been transferred to the powder, which causes the viscosity of the melted material to be reduced and leads to improved particle fusion [1], [6], [7], [30], [34], [38], [45], [87]. However, if the laser power is been increased over a certain point, may form shear stresses between the layers as a result of the increased liquid flow, which leads to curling and distortion. Furthermore, the polymer may experience material degradation, further affecting the physical and mechanical properties. The required laser power depends on the degree of absorptivity of each material and the powder bed temperature, which needs to be set as close as possible to the melting point of the polymer. This way the effect of the laser increases by operating at the minimum of power required for particle consolidation, and furthermore the thermal gradients are minimised between melting and recrystallisation, which prevents part shrinkage [6], [7], [31], [45], [49], [52], [79]. In addition, studies have shown that by decreasing the scan speed and the scan spacing boosts the rate of energy delivered to the powder bed due to extended period of interaction between the powder and the laser beam. In general, when using higher scan speed decreases the effect of sintering on the powder and leads to higher structural porosity[1], [6], [7], [30], [45], [52]. Apart from the parameters related to the energy input, there are also other important factors that influence processing with respect to the properties of the final sintered parts and should be taken under consideration for increased efficiency. As such is the layer thickness, the laser spot size, the beam offset, the delay time, and the part build orientation and placement [1], [6], [7], [30], [45], [49], [52], [67], [79].

2.6 Pharmaceutical Excipients

Drug substances are typically combined with non-medicinal agents in order to be delivered in the body [88]. Drug delivery refers to those systems (formulation, technology and approach) developed to transport a drug substance safely and efficiently to deliver its desired therapeutic effect [2]. Over the years, drug delivery has progressively evolved from traditional immediate-release systems towards novel concepts of formulation, such as personalised medicine for targeted treatment, to optimise the product's efficacy and safety, and increase the compliance of the patients [2], [21], [43].

Oral drug delivery is the most common route of administration for many drugs mainly because of ease of application, since is non-invasive and convenient to handle, which increases the patient's compliance, and moreover it does not require sterilisation [21], [89], [90]. However, there are a few disadvantages when compared to alternate routes, which include slow response or irregular absorption of the drug, unpleasant taste, frequent doses, and drug degradation by stomach acids. Nevertheless, the oral route still remains the most natural, uncomplicated, convenient, and safe for administering drugs. Examples of common oral delivery systems include tablets, capsules, beads, oromucosal preparations, sprays, and lozenges [88]–[90].

The well-known tablet, is the unit solid dosage form that contains medicinal substances and is mainly prepared by compaction processes [88], [89], [91], [92]. Tablets are to date the most preferred oral solid dosage form consisting more than 80% of all dosage forms administered to patients. The principle reasons for their popularity is the convenience of dosing, their accurate dose of delivery, the flexibility in design, and their production with great precision and minimal variation. Tablets are manufactured, handled and packaged more easily, under lower costs than other oral dosage forms. And moreover, they present increased chemical, physical, and microbiological stability compared to liquid and semi-solid systems [89], [92]. The most significant attribute of a tablet is that it is made of powder or granules [91]. The drug substance is mixed with pharmaceutical agents in powder form, commonly known as excipients, to facilitate the administration of the drug and improve patient's acceptance [88], [89], [92]. Excipients are referred to as any components in the formulation other than the drug, and are mainly powdered polymers that are included to impart functionality. Excipients' functionality is broad and qualitative and describes the general role they serve in a formulation, based on the physical and chemical attributes of each excipient towards a specialised pharmaceutical application

[89], [93], [94]. Based on these properties excipients used in oral solid dosage forms have been classified into groups, such as fillers, diluents, disintegrants, binders, glidants, lubricants, stabilisers, coating agents, plasticisers, surfactants, colorants, sweeteners, and flavours [88], [89], [94]–[96].

Excipients have been appropriately evaluated for safety and are in general pharmacologically inert [95]. The selection of excipients is vital in the design of a drug product and is based not only on their functionality, but also on the compatibility with the drug, the method of manufacture, and the container or closure system [89], [94]. These substances give advantageous physical properties, which enhance the quality of the tablet, the volume or size, they facilitate the manufacturing process, the binding or lubrication of particles, and they modify the drug release. Furthermore, they improve the product performance, stability and bioavailability, they assist in product identification, and enhance the overall safety and effectiveness of the drug delivery system. Excipients are also used to prevent drug degradation in the acid stomach environment, to protect the drug from moisture, light and atmosphere during storage, and to provide the desired colour and taste ensuring consistent appearance and patient compliance. Excipients' performance influences the finished product, which makes each pharmaceutical preparation unique in its physical and pharmaceutical characteristics [88], [89], [93], [95]–[98].

In this PhD a selection of commonly used pharmaceutical excipients suitable for oral solid dosage forms has been investigated, for the potential production of tablets through Laser Sintering technologies. The excipients chosen and their relative characteristics are been discussed in the following sections.

2.6.1   Microcrystalline Cellulose

Microcrystalline cellulose (MCC) is a natural plastic material [93]. Is widely recognised to be one of the most important excipients for large-scale manufacture of tablets, and there is a variability in its tableting functionality depending on the particle size, the porosity and the moisture content [93], [99], [100]. Several grades are commercially available, which are produced with different manufacturing methods and therefore provide with a range of physical properties, depending on the flow, the moisture sorption, and others. For example, commercial MCC with a large particle size generally exhibits

high flowability, compared to other grades, which is important for direct compression processes [94], [99]. Furthermore, low moisture commercial grades are being used for the degradation of moisture-sensitive drug compounds, and higher density grades for further improvement of the powder flow properties [89], [94].

Microcrystalline cellulose is primarily used in pharmaceuticals as a diluent in concentrations up to 90%, to increase the volume in oral tablet and capsule systems [93], [101]. It is an excipient used in a variety of tablet manufacturing processes, including dry-granulation, wet-granulation, and direct-compression [102]. MCC is generally considered as the diluent with the greatest binding properties and is widely recognised as one of the most preferred direct compression binders [93]. The exceptional binding properties that MCC exhibits derive from its superior plasticity [92], [93], [102]. MCC may also be used to reduce friction during tablet ejection and facilitate the disintegration process [92]–[94]. Furthermore, MCC offers a broad compatibility with many drug substances and may be combined with nanoparticles and nanogels for sustained drug release [93], [103]. Certain grades that consist of spherical particles are suitable for drug layering as well [104]. Other advantages include physical inertness, ease of handling, and security of supply [93], [102].

Properties

MCC is a purified, partially depolymerised cellulose in a white, odourless, tasteless powder form that consists of porous particles [92]. Its chemical formula is $(C_6H_{10}O_5)_n$ and its structure is presented in Figure 2.6. MCC is physically and chemically stable in ambient conditions, presenting a melting point at between 260-270°C. The bulk material is hygroscopic due to the presence of abundant hydroxyl groups in the cellulose molecular chain, and therefore it requires controlled storage conditions in a cool, dry environment. MCC at 25 °C and 50% relative humidity, normally exhibits approximately 5% w/w in moisture levels, however different grades contain different levels of water. The particle size depends on the grade, however all MCC grades present a typical needle-like shape of microcrystals, which is shown in Figure 2.7. MCC is insoluble in water, in dilute acids and most organic solvents, but it has been reported to be slightly soluble in 5% w/v sodium hydroxide solution. Furthermore, MCC is incompatible with strong oxidising agents [93], [98].
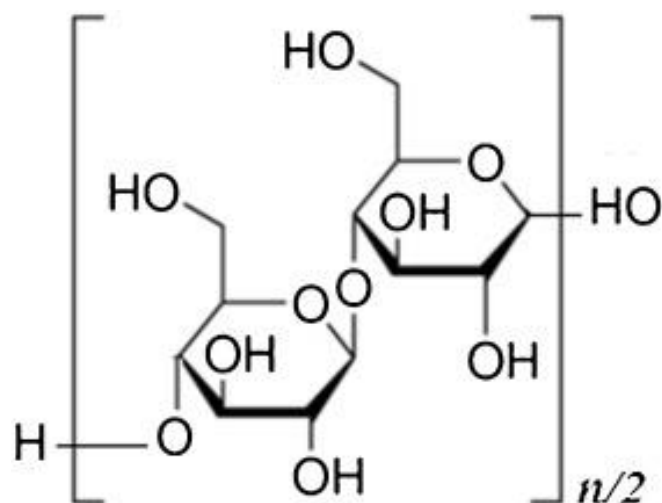
Figure 2.6: Chemical structure of microcrystalline cellulose
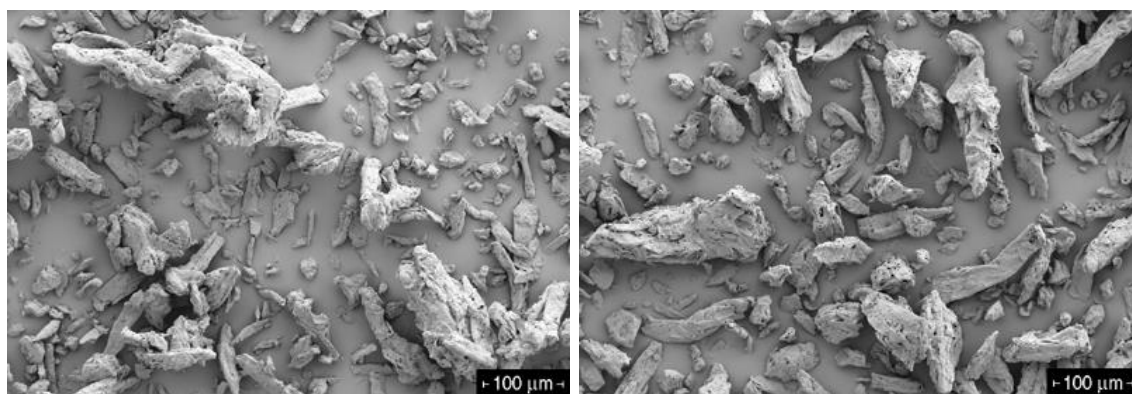
Figure 2.7: Particle shape and size of MCC Avicel 101 (left) and MCC Avicel 102 (right) [FCC Biopolymer]

Pharmaceutical MCC is derived from natural wood, which structure mainly consists from cellulose molecular chains packed in layers that are bound with strong hydrogen bonds. That makes cellulose the most abundant natural polymer on earth [93]. Cellulose is a polysaccharide consisting of a linear chain of several 100 to over 10.000 $\beta(1\rightarrow4)$ linked d-glucose units. These linear cellulose molecular chains are bundled together resulting in high crystalline regions forming MCC [96]. MCC is typically produced by controlled hydrolysis of the α-cellulose in dilute mineral acid solutions, which is obtained as a pulp from fibrous plant materials. Following the hydrolysis step, the hydrocellulose is washed with water and filtered, and then the aqueous slurry is spray-dried to form a dry powder [93], [94]. However, the amorphous regions of MCC are susceptible to hydrolysis, and therefore under partial depolymerisation it can lead to shorter crystalline fragments [93].

MCC is generally a non-toxic and non-irritant material and apart from drug delivery applications, it is also widely used in cosmetic and food industry [91], [98], [100].

2.6.2   Polyethylene Oxide

Polyethylene oxide (PEO) is a polyether compound used in several applications including medicine, cosmetics, and personal care preparations [96], [105]. It is also known as polyethylene glycol (PEG). PEG comes in liquid form and PEO as a low-melting solid and both are available in different molecular weights. The variety of applications is based on the polymer chain length, therefore PEG is normally referred to oligomers and lower molecular weight polymers below 20.000 g/mol, and PEO refers to higher molecular weight polymers above 20.000 g/mol [98], [105].

Polyethylene oxide is primarily used as a tablet binder at various concentrations between 5-85% [96], [102]. The higher molecular mass grades are used for prolonged drug release in hydrophilic matrices [106]. PEO has also proved to facilitate coarse extrusion manufacturing processes for tableting, but also hot-melt extrusion [106], [107]. Furthermore, low levels of PEO can be used as effective thickeners providing with improved viscosity stability [108]. PEO has also been utilised in the development of coatings for medical devices, since it demonstrates good lubricity as a film [96], [108]. Moreover, it can be cross-linked via radiation in aqueous solutions for the production of hydrogels for wound care applications [106].

Properties

PEO is a non-ionic homopolymer of ethylene oxide with the chemical formula $(CH_2CH_2O)_n$, where n is the average number of monomer ethylene groups. Its chemical structure is shown in Figure 2.8. It may contain up to 3% of silicon dioxide or other suitable antioxidants and is incompatible with strong oxidising agents. PEO is a white to off-white, free-flowing powder with a light ammoniacal odour. It is a semi-crystalline polymer presenting a melting point at approximately 65-70°C and the moisture content level is less than 1%. Typical particle size and shape of PEO are displayed in Figure 2.9. Furthermore, PEO is highly soluble in water and many other popular organic solvents, including methanol, ethanol, benzene, acetonitrile, chloroform, and methylene chloride. It is insoluble in aliphatic hydrocarbons, ethylene glycol, diethylether and hexane. The

excellent water solubility properties allow the use of aqueous ingredients into formulations, preventing them of becoming rancid or have a nutritional value to support microbial growth [96], [98], [106], [108], [109].
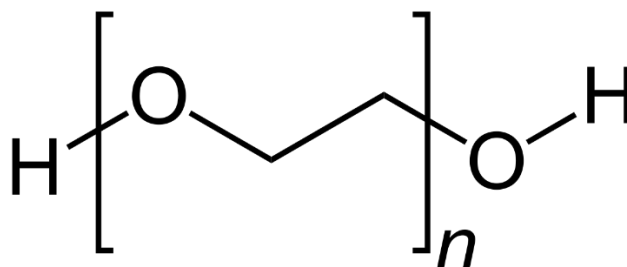
Figure 2.8: Chemical structure of polyethylene oxide
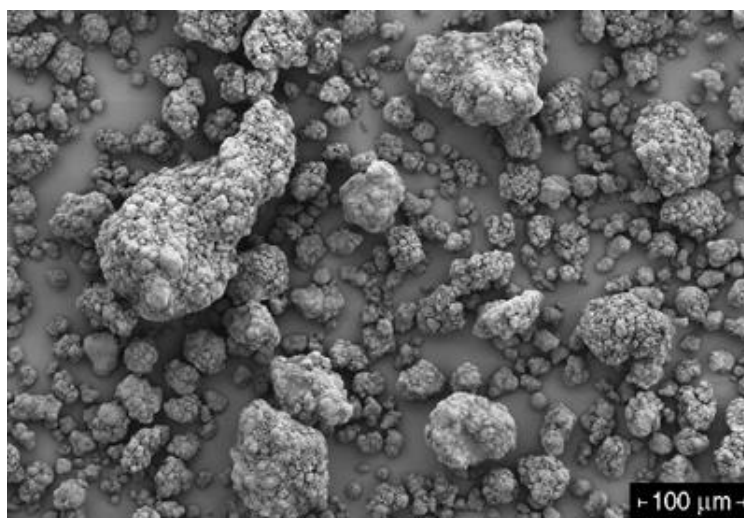
Figure 2.9: Particle shape and size of PEO N80 [Dow Chemicals]

Polyethylene oxide is synthesised by suspension polymerisation processes using ethylene oxide and a suitable metallic catalyst, such as magnesium, aluminium or calcium organic elements. The chain-growth formation is very important to occur in solution during the polycondensation step. PEO has a low level of toxicity and is poorly absorbed from the gastrointestinal tract, although it appears to be completely and rapidly dissolved [96], [98], [106], [108].

2.6.3   Polymethacrylates

Polymethacrylates are synthetic cationic and anionic polymers of dimethylaminoethyl methacrylates, methacrylic acid and methacrylic acid esters that are commercially available in varying ratios and can be found in a form of dry powder, or aqueous dispersion or organic solution [110]. Polymethacrylates are marketed under the trade name Eudragit®, and are popular types of film coating polymers [89]. Depending on the ratio of each type of polymethacrylates, films with different solubility characteristics can be produced. These acrylate polymers are non-toxic, non-biodegradable, and non-absorbable. Various grades can be produced depending on the chemical composition for several different applications. With a use of a plasticiser, such as dibutyl sebacate, dibutyl phthalate, glyceryl triacetate or polyethylene glycol, the polymer properties can be enhanced for special requirements. For use in spray coating solutions and dispersions, polymethacrylates should be diluted with suitable solvents [89], [90], [111], [112].

Polymethacrylates are widely used for controlled drug release applications as film coating agents in oral tablets and capsules. At the same time they serve another important function that is to prevent drug degradation from the gastric environment and deliver the drug to the intestine for local action [89], [90], [111], [112]. Larger quantities up to 20% of dry powder are used to control the release of drug substances from a tablet matrix. Furthermore, polymethacrylates are suitable binders for both aqueous and organic wet-granulation processes. Solid powders in concentrations of 10-50% are used in direct-compression processes or even in hot melt extrusion, since several types of polymethacrylates present a low glass transition temperature (T_g) of about 50 °C [112]–[114]. These polymers may also be used for the formation of matrix layers in transdermal delivery systems and novel gel formulations for rectal administration [89].

Properties

The average molecular weight currently reported for commercial polymethacrylates is typically above 30.000 g/mol. Their chemical structure is presented in Figure 2.10, where the R' side groups in the molecular chain differ depending on the type of the copolymer formed [98]. The methacrylic acid content (typically up to 50% wt) controls their solubility that makes them either freely soluble in ethanol either water soluble or insoluble. Polymethacrylates are amorphous thermoplastic polymers, in white,

colourless, free-flowing, fine granular powder form [111]. Dry powder grades are generally stable in environmental conditions, however in higher temperatures some grades tend to form lumps, although this has no influence on quality [101]. Certain polymethacrylate dispersions develop incompatibilities that depend on the physical and ionic properties of the polymer and solvent, which include coagulation induced by soluble electrolytes, or pH changes, or extreme temperatures. Some interactions with certain drugs may occur, but generally they are considered as non-toxic and non-irritant materials [98], [110].
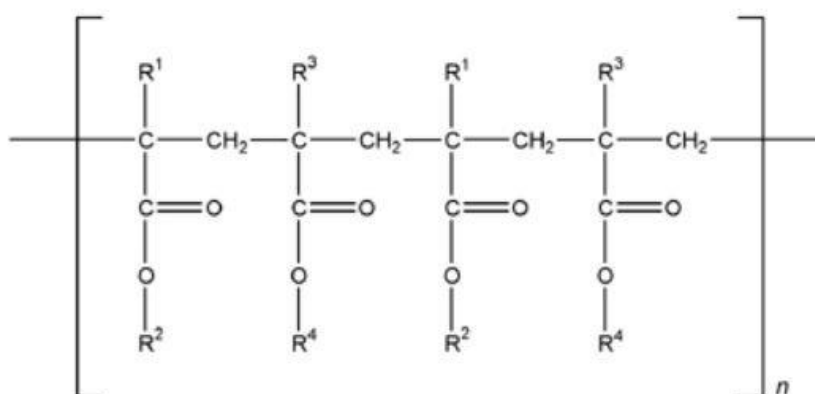
Figure 2.10: Chemical structure of polymethacrylates

2.6.4 Hydroxypropyl Cellulose

Hydroxypropyl cellulose (HPC) is a popular thermoplastic polymer that can be processed through mostly all methods of production for plastics. It can be described as a partially substituted poly(hydroxypropyl) ether of cellulose [91], [96]. It may contain less than 0.6% of silica or other suitable anticaking agents [98]. HPC can be produced in a variety of solution viscosities that result in varied molecular chain mass, and for this there are various grades commercially available. The molecular chain mass is dependent on the degree of substitution. The propylene oxide chain contains a reactive hydroxyl group, which can be further polymerised in a higher degree of molecular substitution [91].

Hydroxypropyl cellulose is commonly used in oral and topical drug delivery systems. In tablet formulations it is primarily used as a binder and a film former. Furthermore, high molecular weight grades (high viscosity) are effective thickeners and low molecular weight grades can be used as disintegrants [89], [96], [115]. Concentrations of 2-6% w/w

are used as binders in immediate-release tablets in wet- or dry-granulation and direct-compression processes. Concentrations of 15-35% w/w are used to produce tablets with a sustained drug release profile. The drug release increases with decreasing viscosity of HPC depending on the molecular weight [98], [115]. The varied solubility of HPC in water and polar organic solvents, can be used for the preparation of different solutions for either casting films or for coating purposes. Furthermore, it is also used in hot-melt extruded films for topical use [98], [116].

Properties

HPC is a white to off-white or light yellow-coloured powder, which is odourless and tasteless. It is a non-toxic and non-irritant material, which is further broadly used in cosmetics and food products [98], [116]. It starts to soften at 130ºC and chars at 260-275°C. It absorbs moisture from the atmosphere depending on the temperature and relative humidity of the surrounding environment [64]. The typical equilibrium moisture content at room temperature is 4% w/w under 50% of relative humidity and raises at 12% w/w under higher levels of relative humidity of 84%. The molecular weight and particle shape and size vary between the different commercial grades of HPC [98]. In Figure 2.11 a larger particle size grade from Nippon Soda is displayed.

HPC is freely soluble in water below 38°C, which forms a smooth, clear, colloidal solution. Also it is soluble in many cold or hot polar organic solvents, including dimethyl sulfoxide, ethanol (95%), methanol, polyethylene glycol and propylene glycol [96], [117]. The water solubility makes it prone to chemical and biological degradation, which may result in the reduction of the molecular weight and decrease the viscosity of the solution. On the other hand, it is insoluble in aliphatic hydrocarbons, aromatic hydrocarbons, carbon tetrachloride, petroleum distillates, glycerine and oils [98].
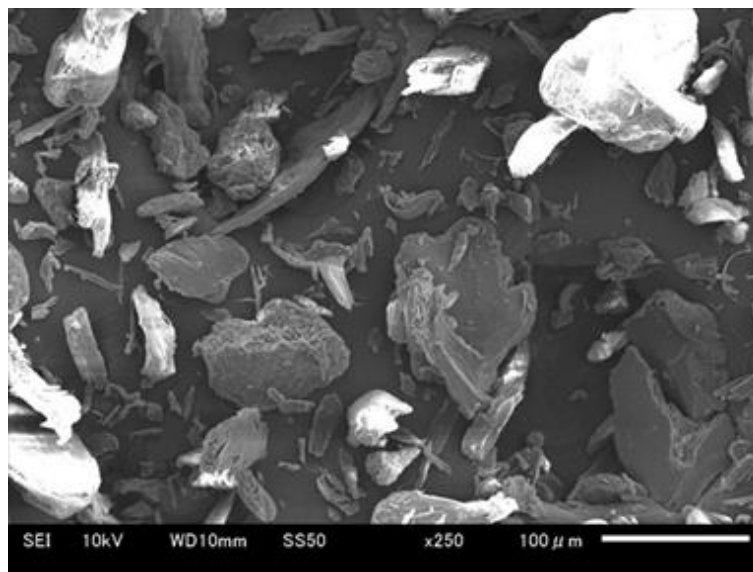
Figure 2.11: Particle shape and size of HPC SL [Nippon Soda]

HPC is derived from a purified form of cellulose upon the reaction with sodium hydroxide, which forms a swollen alkali cellulose that is chemically more reactive compared to untreated cellulose. The alkali cellulose is further reacted with propylene oxide at elevated temperature and pressure [98]. The propylene oxide is been substituted in the cellulose via an ether linkage present at the reactive hydroxyl groups in each unit of the cellulose chain. The etherification step produces secondary hydroxyls in the hydroxypropyl substituent groups, which further react with the propylene oxide. The final polymerisation results in the formation of molecular chains that contain more than 1 mole of combined propylene oxide [91], [98], [115].

2.6.5 Lactose Monohydrate

Lactose is a natural sugar, which makes it an ideal excipient [118]. It demonstrates chemical and physical stability, and thus is highly compatible with other excipients and drug compounds. Lactose is a double sugar consisting of glucose and galactose, which is obtained from the whey fraction of bovine milk [94]. It can be produced in two crystalline types, monohydrate or anhydrous, depending on the manufacturing process. It is an all-natural product with low cost of production, commercially available in several grades with varying physical properties, and easy to store [92], [102], [119].

Lactose is widely used in tablets and capsules as a diluent (commonly known as filler), but it can also be used in lyophilised products and baby food formulas, or in dry-powder inhaled drugs. Furthermore, lactose is known as a taste masking excipient used in sugar-coating preparations to improve the taste. For tablets produced by wet-granulation processes, fine or milled crystalline lactose grades are typically used and for those prepared by direct compression, spray dried forms are preferred. Figure 2.12 presents particles of lactose monohydrate in the form of granulates; this is a commercial lactose monohydrate grade that contains low levels of anhydrous lactose and is available for direct compression [92], [98], [102], [120].
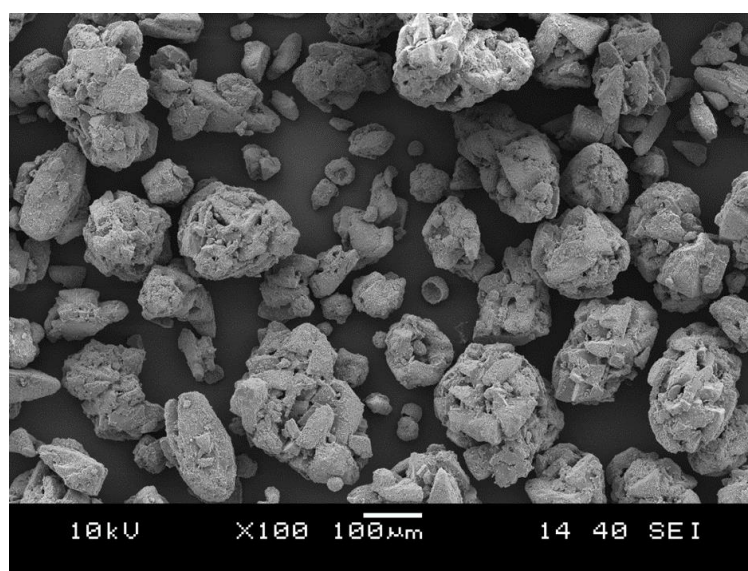
Figure 2.12: Particle shape and size of α-lactose monohydrate [Foremost Farms]
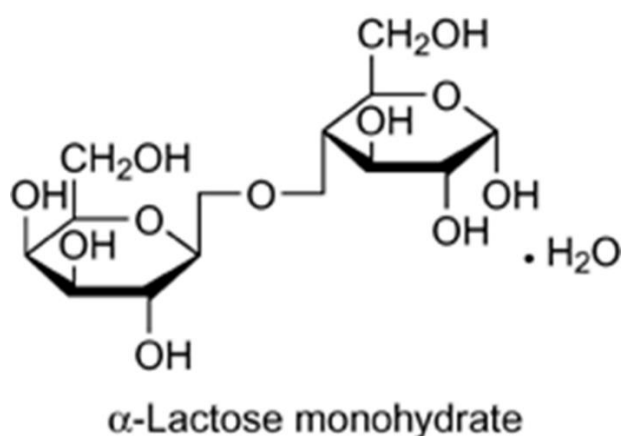
Figure 2.13: Chemical structure of α-lactose monohydrate

Properties

Lactose is a white to creamy white, free-flowing and non-hygroscopic powder, which is odourless, with a light sweet taste and free of sediment [121]. Lactose is a disaccharide composed of the two sugar molecules of galactose and glucose. Depending on the crystallisation and drying conditions, lactose disaccharide has the ability to form two stable isomers known as α-lactose and β-lactose [94], [98], [120]. These two isomers present a different orientation of the hydroxyl group in the glucose moiety [121]. The monohydrate crystal mainly consists of lactose α-form, whereas the anhydrous crystal is mainly lactose β-form [92], [120]. There are three crystalline forms of lactose in the solid state, which are the α-lactose monohydrate, the β-lactose anhydrous, and the α-lactose anhydrous. The chemical structure of α-lactose monohydrate is presented in Figure 2.13. α-lactose monohydrate is a very popular grade prepared by exothermic crystallisation in supersaturated solutions in temperatures below 93.5°C. The geometry of the lactose crystal depends on the precipitation method used for crystallisation and exists in various shapes, such as pyramids, prisms, monoclinic sphenoid or 'tomahawk' [98].

2.6.6   Hypromellose Acetate Succinate

Hypromellose acetate succinate (HPMC-AS) is another cellulose derivative [89], [122]. It is among the most popular film coating polymers used in enteric applications, due to increased chemical and physical stability [123]. HPMC-AS is hygroscopic in nature and insoluble in gastric fluid, however it swells and completely dissolves in the upper intestine [89]. HPMC-AS consists of a mixture of acetic acid and monosuccinic acid esters of hydroxypropylmethyl cellulose. Depending on the content of acetic and succinic acid, different grades are commercially available that vary in particle size (fine or granular) and dissolve at different pH values [89], [122]–[124]. The free succinic and acetic acid chain groups may react with drugs that contain hydroxyl groups to form esters, and therefore the use of HPMC-AS is avoided [89], [98].

Hypromellose acetate succinate is a versatile polymer and can be used in various solid dosage pharmaceuticals, ranging from enteric film coatings for tablets, capsules and granules, to amorphous solid dispersions via spray drying that enhance the solubility of poorly soluble drugs [124], [125]. HPMC-AS is also increasing its potential applications in hot melt extrusion processes [125]. HPMC-AS granulated grades are used for modified

drug release, alone or in combination with other binders. The release rate depends on the pH. For film-forming processes, HPMC-AS is dissolved in organic solvents to form a film coating [123]. On the other hand, dry coating process are used to prepare enteric coated pellets and enteric coated soft gelatine capsules [98].

Properties

Hypromellose acetate succinate occurs as a white to off-white powder or granules, with a faint acetic acid-like odour and almost undetectable taste. Depending on the extent of substitution, the molecular weight can range from 55.000 to 160.000 [122]. HPMC-AS is an amorphous polymer with unique properties, such relatively high T_g, solubility in volatile organic solvents (methanol, acetone), and high melting viscosity, suitable for use in various manufacturing processes [125]. HMPC-AS is incompatible with strong acids or bases, oxidising agents, and increased levels of humidity [98], [124]. HMPC-AS is commercially available in several grades, low L, medium M, and high H, according to the pH at which it dissolves, and also in fine powder F or granules G, according to the particle size (Figure 2.14) [122], [123].
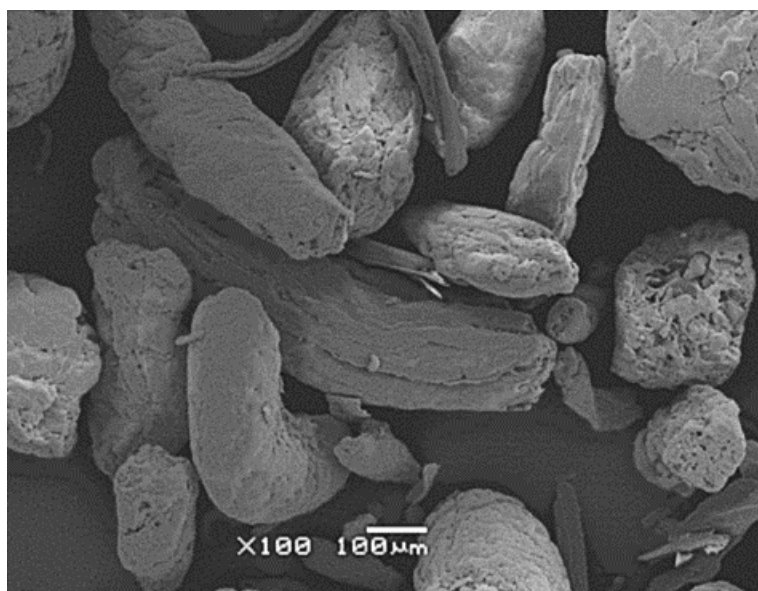
Figure 2.14: Particle shape and size of HPMC-AS MG [Shin-Etsu Chemical]

HPMC-AS is produced by the esterification of hypromellose in a carboxylic acid solution by adding acetic anhydride and succinic anhydride, in the presence of a strong acid catalyst, such as sodium acetate. The reaction is taking place in a large volume of an aqueous medium to obtain a fibrous product. The product is purified by thorough washing with water [122], [124]. The precipitation method results in granulates that can be further pulverised to obtain fine particles if required. HPMC-AS is generally an inert, non-ionic, and non-toxic polymer, which also makes it safe for use in cosmetics and personal care products [98].

2.7   Gap in the Knowledge

The challenge of this PhD is in the processing of commercial pharmaceutical excipients for oral applications within a commercial LS system. LS is one of the most established and widely used AM techniques with scale-up opportunities for mass production. The reviewed literature has covered the common aspects related to AM and then concentrated on the area of Laser Sintering and materials development for pharmaceutical applications. Therefore, a review of pharmaceutical materials used for oral applications was made to investigate the potential use of commercial LS equipment for the production of oral solid dosage forms. The development of materials for LS is well established, but there are limited guidelines for the development of new materials, particularly those that are not semi-crystalline in nature.

Although, there are authors [20], [21], [25], [29], [44] that have begun to develop LS of oral solid dosage forms, they have mainly studied fast dissolving tablets and further they have not used commercially available "mainframe" LS systems, they have relied on those that are lab-based and therefore not suitable for scaled production. The lab-based systems (UV/Blue light based) rely on a different energy coupling mechanism to induce sintering to those based on infrared radiation, which is more commonly available in commercial LS production machines. As such, their material development centres on coupling of light through additives, rather than directly into the powdered material. Further, literature has shown little work in the development of multi-material pharmaceutical formulations for LS of oral solid dosage forms. This leads to gap in the knowledge for commercial LS of oral solid dosage forms, in that there has been no work on the use of pharmaceutical grade material systems for oral applications in infrared-based LS machines.

This thesis attempts to address the gap through the following work which, attempted to process pharmaceutical blends and explore the sinter-ability of preliminary formulations in order to increase the level of scientific understanding and develop a bridge between LS and pharmaceutics. The various influences on the sintering behaviour of the blends were examined thoroughly, to fully understand the key requirements for successful processing of pharmaceuticals towards the design of functional LS oral solid dosage forms. This work outlines the necessity to design novel material systems that can enable the control of the microstructure and the production of oral pharmaceuticals with multiple release profiles. In the event that new concepts and ideas are proposed for the improvement of the process capability of matrix-forming powder formulations that could potentially push the boundaries of mass production of functional LS oral pharmaceuticals. The key areas of novelty of this PhD are the following:

1. Process of pharmaceutical excipients in an industrial LS system able to produce large volumes reducing the processing time and cost per tablet that can lead to scale-up production of AM oral solid dosage forms.

2. Provide a systematic way to test excipients for use in LS and a guideline for the selection of potential candidates towards the development of LS oral solid dosage forms.

3. Process of preliminary placebo formulations consisting of excipient blends that can simulate the design criteria of oral solid dosage forms.

4. Provide a systematic understanding of all the critical factors that affect the mechanical properties of LS oral solid dosage forms to enable the design of material systems that can increase versatility in functionality.

5. Develop a core-shell polymer powder system to enhance processability of materials that are incompatible with LS and enable the use of a larger number of materials with LS.

CHAPTER 3   MATERIALS AND METHODS

3.1   Introduction

This thesis investigated polymer blends consisting of common pharmaceutical excipients for the manufacture of LS drug dosage forms. Prior to the development of the blends, it was important to understand individual material properties and their link to the LS process parameters, as material aspects strongly influence the LS process and consequently the final properties of the sintered parts, as discussed in Chapter 2. Therefore, the right choice of materials was the main determining factor of this study; each excipient was chosen in order to contribute to the enhancement of sintering and further allow the design of a drug dosage form towards the demands of pharmaceutical applications. In the following sections the standard equipment, the materials and the methods used, are described.

The first step in this study, was the screening of common pharmaceutical excipients in terms of their thermal, physical and rheological characteristics to reveal their level of compatibility with LS. The level of compatibility reflected on the sinter-ability of each material. Excipients with high sinter-ability would allow the control and optimisation of the LS scanning strategy that could lead to the production of robust parts. For this purpose, a number of analytical techniques was employed to characterise the selected powders in order to determine their processing window, the size and shape of their particles, and their flow properties. These characteristics were related to level of consolidation and powder bed density, and hence the LS outcome and final part quality.

Candidate materials were subjected to LS trials in order to explore their in-process behaviour and the final quality of sintering. Trials were performed using sets of laser parameters to investigate the best scanning strategy for each powder. Observations during the trials meant to develop a deeper understanding of the process conditions and lead to the selection of materials for blending towards the design of a preliminary pharmaceutical formulation. Further LS trials on the blended excipients aimed to identify the key performance indicators (KPI), such as density, uniformity, surface roughness, and stiffness of the final parts, in order to understand the requirements for sintering tablets and further improve the design of the formulation and subsequently the LS conditions for optimal results.

The next step was to evaluate the quality of the laser sintered tablets, investigating the factors that influenced their final mechanical performance and pharmaceutical functionality. Mechanical testing and analysis of their microstructure aimed to introduce important correlations between the bulk powder characteristics and the properties of the sintered parts, such as strength, hardness and elasticity. The analysis of the effect of all the elements involved and all the underlying mechanisms was meant to increase the understanding of the formulation design criteria necessary to develop robust and functional LS oral solid dosage forms.

The information and knowledge gathered through testing of the materials and the sintered tablets, led to the development and implementation of a method of blending polymer powders that may enhance processability of pharmaceutical formulations on the LS system. The principles of precipitation and emulsion-solvent evaporation methods were used to produce a polymer coating aiming at the development of an improved LS powder feedstock. The selection of materials was based on their physical and chemical characteristics compatible with the LS process and the needs of the intended application.

A simple flow chart is presented below in Figure 3.1 to show the experimental design employed through the thesis.
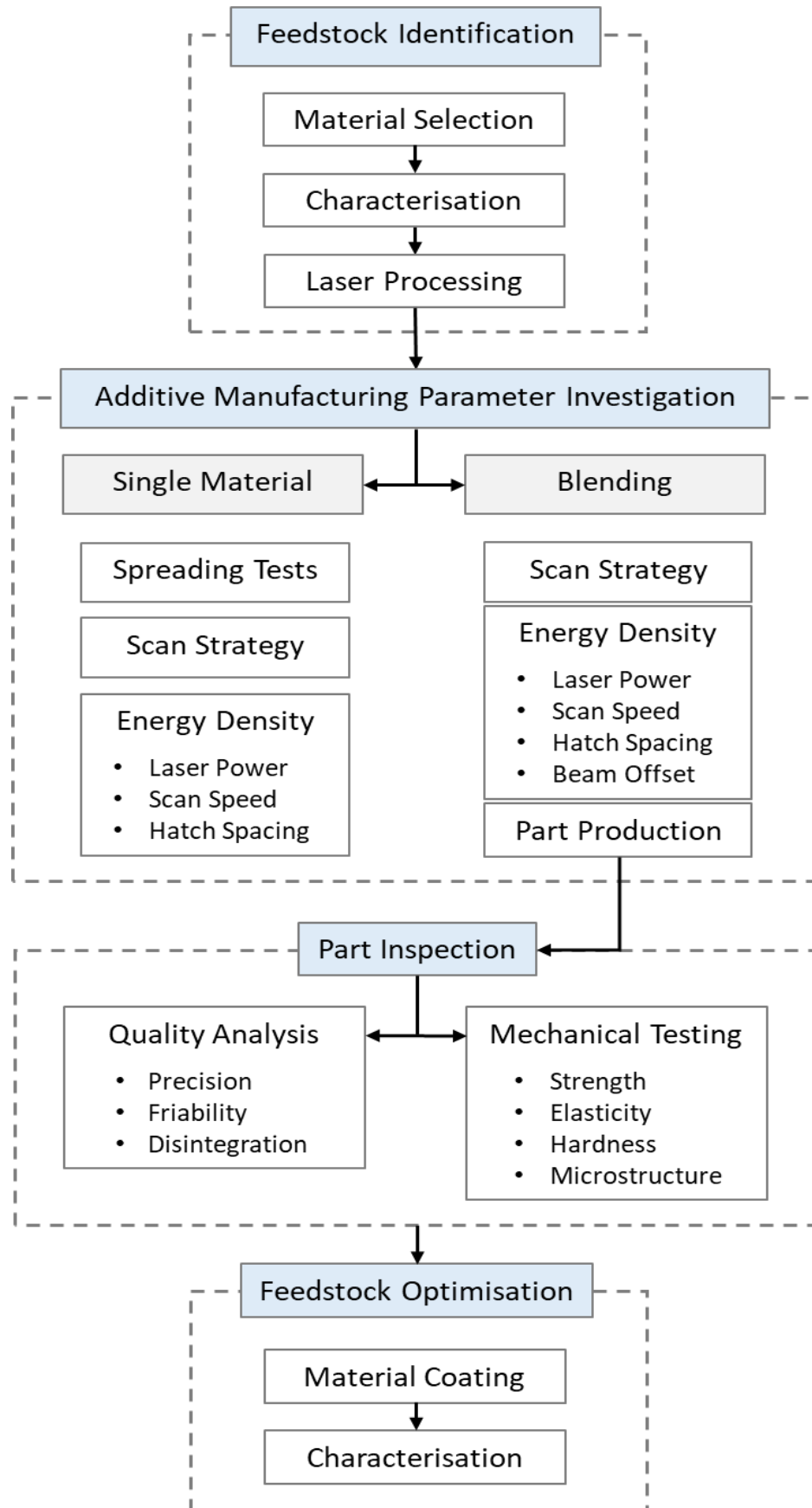
Figure 3.1: Flowchart of key stages in order to achieve AM parts for oral pharmaceutics

3.2   Materials

Six common pharmaceutical polymer excipients in powder form and in different grades were mapped in terms of their thermal, physical and rheological properties, in order to assess their compatibility with LS process. The materials present an increased industrial interest as they are widely used for the production of tablets due to their physical characteristics and low cost. Focus was also given to the amorphous/crystallinity levels of the materials since semi-crystalline polymers are preferred for LS. The materials were provided by Pfizer and were: 1) microcrystalline cellulose (Avicel 101 and 102); 2) polyethylene oxide (PolyOx N80); 3) methacrylic acid ethyl acrylate copolymer (Eudragit L100-55 and FS100); 4) hydroxypropyl cellulose (HPC SL, SSL and SSL SFP); 5) lactose monohydrate (Foremost 316); and 6) hypromellose acetate succinate (AQOAT LMP, MMP and HMP). The main characteristics of the excipients are shown in Table 3.1. The level of suitability of these materials will determined the outcome of this PhD related to successful material processing and to the development of solid parts.

Table 3.1: Basic summary of common pharmaceutical excipients

Trade Name	Grade	Polymer	Use	Functionality	Manufacturer
Avicel PH 101	Fine powder type	Microcrystalline Cellulose (MCC)	Disintegrant/ Diluent/Binder/ Adsorbent	Increase the bulk volume, impart cohesion, enhance flow	FMC BioPolymer
Avicel PH 102	Regular powder type	Microcrystalline Cellulose (MCC)	Disintegrant/ Diluent/Binder/ Adsorbent	Increase the bulk volume, impart cohesion, enhance flow	FMC BioPolymer
PolyOx N80	Low molecular weight	Polyethylene Oxide (PEO)	Plasticiser/ Thickener/ Binder/ Lubricant/ Glidant	Improve elasticity and flexibility, facilitate ejection, enhance flow, control release	DOW Chemical Company
Eudragit L100-55	Soluble powder in intestinal fluid	Polymethacrylate	Coating agent/ Binder/ Adsorbent	Prevent degradation, control release, enhance flow	EVONIK Industries
Eudragit FS100	Soluble powder in intestinal fluid	Polymethacrylate	Coating agent/ Binder/ Adsorbent	Prevent degradation, control release, enhance flow	EVONIK Industries
HPC SL	Regular powder type	Hydroxypropyl Cellulose (HPC)	Coating agent/Binder	Prevent degradation, control release, enhance flow, improve appearance	NIPPON SODA
HPC SSL	Fine powder type	Hydroxypropyl Cellulose (HPC)	Coating agent/Binder	Prevent degradation, control release, enhance flow, improve appearance	NIPPON SODA
HPC SSL SFP	Super fine powder	Hydroxypropyl Cellulose (HPC)	Coating agent/Binder	Prevent degradation, control release, enhance flow, improve appearance	NIPPON SODA
Foremost 316	Crystalline powder	Lactose Monohydrate	Diluent/Filler/ Binder	Increase the bulk volume, impart cohesion, enhance flow, aid drug degradation	Foremost Farms
AQOAT-AS LMP	Soluble in low PH	Hypromellose Acetate Succinate (HPMC)	Coating agent/ Binder	Prevent degradation, control release, enhance flow	ShinEtsu Chemical
AQOAT-AS MMP	Soluble in medium PH	Hypromellose Acetate Succinate (HPMC)	Coating agent/ Binder	Prevent degradation, control release, enhance flow	ShinEtsu Chemical
AQOAT-AS HMP	Fine powder soluble in high PH	Hypromellose Acetate Succinate (HPMC)	Coating agent/ Binder	Prevent degradation, control release, enhance flow	ShinEtsu Chemical

3.3   Methods of Characterisation of Powders

As discussed in Chapter 2, materials play an important role in LS technology before and during the printing process. Finding suitable materials with compatible physical and morphological characteristics still remains a challenge for the development of LS, as powder properties and LS parameters are strongly interdependent and are mutually interacting [34], [126]. Therefore, in this section a number of characterisation techniques were employed to investigate the powder properties of each selected material and their suitability for LS. Specifically, thermal analysis using Differential Scanning Calorimetry and Thermogravimetric Analysis estimated the thermal processing window of each of the powders. Flowability tests revealed whether the powders are going to spread evenly to the bed. Finally, particle size distribution analysis and electron microscopy determined the morphological characteristics of the powders that were related to the packing density.

3.3.1   Differential Scanning Calorimetry (DSC)

Thermal analysis was performed using a DSC 8000 (Perkin Elmer, Inc., MA, USA) in order to investigate the phase transitions and the melting range of the powders, which were necessary for the specification and control of the LS processing parameters. For the DSC measurements samples of mass ~10 mg were accurately weighed into aluminium tzero pans (P/N 901683.901) and sealed using aluminium tzero lids (P/N 901671.901). The instrument's furnace was purged with nitrogen (20 ml/min) and the samples were heated from room temperature to 200-350 °C depending on the material properties. The melting temperature was obtained at a heating rate of 10 °C/min for semi-crystalline materials and the glass transition temperature using a higher rate of 30 °C/min, required to detect the transition from the glassy state to the rubbery for amorphous materials [127]. The DSC scans were repeated twice for each material. The analysis of the thermograms and all the reported values calculated were obtained through the PerkinElmer Pyris software v13.3.

3.3.2   Thermogravimetric analysis (TGA)

TGA analysis was performed to collect information about the thermal decomposition and the absorption levels of the materials and set the limits of a safe sintering region within the LS system. The equipment used was a TGA 4000 (Perkin Elmer, Inc., MA, USA).

For the TGA measurements samples of mass ~15 mg were placed onto a 250 micro litre alumina pan (N5200040), which had been previously tared. The instrument's furnace was purged with nitrogen (25 ml/min) and the samples were heated at 20 °C/min up to 600 °C, to undergo thorough decomposition. All materials were scanned twice and analysed using the Pyris software v13.3.

3.3.3 Flowability

The dynamic flow properties of the powders were investigated using a FT4 Powder Rheometer (Freeman Technology, Ltd, Tewkesbury, UK). In general, the sensitivity of a powder to flow rate is an important parameter that reveals how stable and viscous the material is. Cohesive powders strongly influence the packing efficiency of the particles, thus the flow efficiency during the application of the powder on the bed platform [54], [80]. It is common that cohesive powders are more sensitive to changes in flow rate, mainly as a result of the high air content contained [128].

The test method followed was the Stability and Variable Flow Rate test (VFR) [80], using a 25 mm x 25 mL vessel assembly. The materials were measured 2 or 3 times depending on the repeatability of the resulted flow pattern. The method used is a combination of the seven conditioning and test cycles of the Stability test (blade tip speed 100 mm/s) and the four conditioning and test cycles of the Variable Flow Rate Test (blade tip speed 100 >70 > 40 > 10 mm/s). The structure of the VFR test program is defined below in Figure 3.2, where C is the conditioning cycle, T is the test cycle, the blade tip speed during the test cycle is mentioned into the brackets in mm/s and "Split" defines the splitting of vessel to provide precise volume of powder for measurement. Blade tip speed is 100 mm/s, where not defined in brackets.
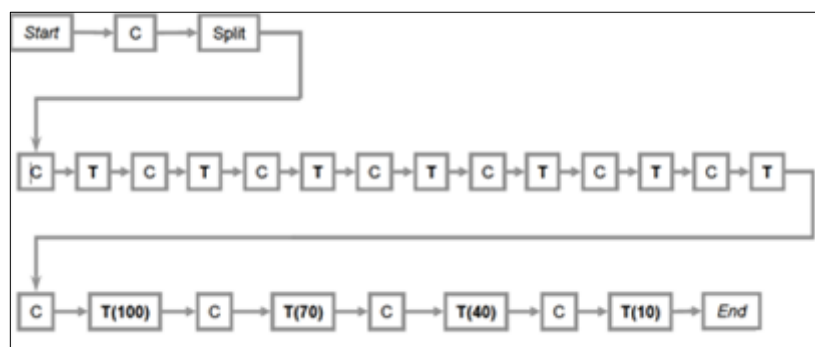
Figure 3.2: Structure of the VFR test program [129]

This method measured several parameters among which the Basic Flowability Energy (BFE), Stability Index (SI), Specific Energy (SE), and Flow Rate Index (FRI). The BFE is the energy (mJ) required to establish a flow pattern in a conditioned volume of powder at a given flow pattern and flow rate, typically at 100 mm/s blade tip speed. This flow pattern generated a compressive, relatively high stress flow mode in the powder that gave an estimation of the ease to spread the powder. The lower the energy required, the easier is to spread. The SI is a factor that indicated the changes to the flow energy during repeat testing. The closer the SI value is to 1, the more stable the material behaves and is a desirable attribute. The increase in density and particle size results in increased energy and an SI value above 1. It is closely linked to how cohesive one material is, which is better represented by the SE and the FRI. The SE defined the flowability of a powder in a low stress environment and it is particularly sensitive to cohesion. It was calculated from the energy required to establish a flow pattern in a precise volume of powder. Generally, SE values below 5 mJ/g suggest low cohesion, while values above 10 mJ/g are related to high cohesion, which can lead to increased agglomeration. The FRI is more sensitive to high flow rates and for most materials falls in the range of 1.5 to 3.0. An FRI typically higher than 3.0 is exhibited by very cohesive materials [80], [129].

3.3.4 Particle size analysis

For LS powders, a certain particle size distribution is necessary to be processable [6], [76]. The EOS patent [130] suggests that ideal particles should have a D_{50} in the range of 40 to 70 µm and a distribution curve as narrow as possible to guarantee the optimal powder flow during spreading of the successive layers. To reveal information about the particle size and distribution of materials laser diffraction systems are typically used, which measure the intensity of light scattered as the laser beam passes through the dispersed powders [58]. For the purpose of this study a Mastersizer 3000 (Malvern Instruments Ltd, Malvern, UK) was employed configured in dry dispersion mode with the Aero S unit. The bulk material was thoroughly stirred using a spatula to ensure homogeneity of the samples. For most of the powders, particles were reported as a volume equivalent to non-spherical diameter. Measurements were carried out 10 times for each material and were repeated 3 times. The size of the particles was calculated by the scattering pattern created, using the Mie theory of light scattering through the Mastersizer

software [131]. Results were obtained for D_{10}, D_{50} and D_{90}, which represented the 10%, 50% and 90% of the total volume of the particles respectively.

3.3.5 Microstructure

Further examination of the shape and particle surface morphology of the powders was performed using Scanning Electron Microscopy (SEM). Samples were sputtered with a gold, Au, coater to be viewed in a secondary electron mode using a JEOL 6060LV SEM instrument. High magnification images at 50x, 100x and 500x, were captured for each powder.

3.4 Laser Sintering

As previously discussed, evaluation of the effect of sintering on the individual materials was necessary for the selection of excipients for blending and the development of a preliminary formulation. In this section, some initial LS builds took place, where a range of different combinations of process parameters were used to explore the processing ability of the excipients, aiming to gain a better understanding of the link between the material properties and the process parameters. Based on the observations of processing the individual materials, the printing process was adjusted to sinter blends of selected materials aiming to develop a robust printing strategy to increase repeatability and consequently to potentially produce robust parts.

3.4.1 Laser Sintering system

Processing of materials was performed in a commercial laser sintering system the EOS Formiga P100 (EOS Gmbh, Germany). The P100 uses a CO_2 laser beam (wavelength 10.2 to 10.8 μm) to thermally fuse the material onto the powder bed to form successive layers. The diameter of the focussed beam or laser spot size was 420 μm and the nominal laser power was 30 W. The building volume was 200 x 250 x 330 mm. The powder was spread across the building area by a recoating blade. The blade can be adjusted at different heights to achieve various layer thickness. The minimum layer thickness of the P100 was 100 μm. The P100 can achieve a maximum powder bed surface temperature of 182ºC.

The scanning of the layers in the P100 can use both a contour pattern and a filling pattern (hatching). The contour is the outline of each layer, which is typically used for accuracy and surface finish around the perimeter. The rest of the layer is scanned inside the contour using the filling pattern. The hatching scans the layers in the X or Y direction changing the direction of the exposure from layer to layer (single scan mode) or expose each layer in both directions (double scan mode). The maximum scan velocity was 5000 mm/s. Furthermore, the P100 is able to adjust the process parameters (bed temperature, laser power, scan speed, scan spacing, beam offset, etc.) towards the needs of different materials, to determine the necessary energy input to improve particle fusion and achieve the desired part properties.

3.4.2   Processing conditions

Prior to the application of the laser, evaluation of powder deposition by the blade was necessary to assess the processability of the excipients during the application of a new powder layer. All powders were subjected to spreading tests under varied bed temperatures to examine their ability to flow under sintering conditions. To achieve better results in some cases, additives were used to improve the flow. After that step, the laser scanned on the surface of the last layer spread to initiate sintering. For the tests, square parts of 20 x 20 x 2 mm were designed to be built flat (x-y orientation) at fixed places in the middle of the build area, to minimise anisotropy [6], [48], [52], [67], [132].

For the experiments the temperature range and the scanning pattern were balanced to provide optimal sintering for each material/blend and achieve the maximum performance avoiding degradation. The main laser parameters that were adjusted during the trials were the laser power, the scan speed, and the hatch distance. In particular, the laser power was adjusted to force coalescence of the particles; variations on the scanning speed controlled the energy input transferred from the laser beam, allowing enough heat to fuse the powders and at the same time prevent degradation; the hatching distance permitted layer bonding by adjusting the overlapping percentage coverage [6], [7], [30], [38], [55], [66], [87], [133]. These three parameters determined the energy input needed for sintering the excipients based on the ED equation presented in Chapter 2 (Eq. 2.1). Higher ED typically achieved increased density and part strength, however, it was found that there was a maximum energy that could be applied, as high shear stresses induced by thermal

gradients can be formed between the layers and possibly lead to distortion [6], [7], [31], [55], [65], [87].

The scan patterns that were used for the sintering trials were varied between single scans and double scans, with or without contouring. The scan pattern was chosen based on the material properties to achieve the best sintering results. Single scan strategy was applied for the first series of tests to determine the minimum energy necessary to achieve consolidation of the layers. In single scan mode the laser scanned along the X and Y axis alternating between the layers. In most cases, an increase in the ED was needed to achieve adequate fusion of the powders, therefore double scan mode was applied. In that case, the laser scanned in both the X and Y axis on each layer and created further overlap increasing layer bonding. It was further found that the use of contouring in the beginning and ending of the scan lines increased precision of the parts' boundaries [79].

To simply evaluate the effect of the laser exposure and scanning pattern on the individual layers and qualify the potential parts formed, a custom scale was used. The format of the scale was using five ordered response levels, which allowed a qualitative comparison between the different sintering results and materials, as seen in Figure 3.3. An example of the scale is given in Table 3.2 to deliver a better understanding of the sintering profiles expected when processing powders under different conditions.
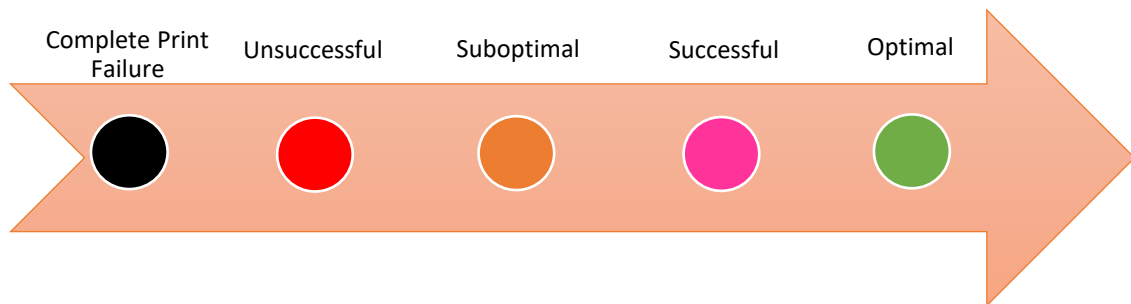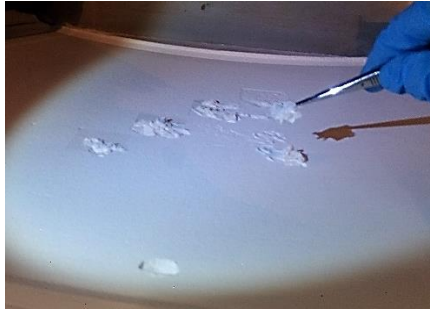
Figure 3.3: Five level scale of sintering

Table 3.2: Description of the different sintering profiles

Level	Description	Example
Print failure	decomposition, no fusion, fuming	
Unsuccessful	some fusion, partial consolidation	
Suboptimal	evidence of layers	
Successful	multilayers, solid parts, low adhesion, low precision	
Optimal	robust parts, high density, high strength, high precision	

3.5   Quality Testing of Laser Sintered Parts

In this section, the effect on the surface quality and density of the laser sintered tablets and consequently their mechanical properties, was investigated in relation to the particle morphology, flowability, packing density and consolidation phenomena. It was necessary to explore the strength of the produced parts that would be required to resist the mechanical impact on the tablets during packaging, shipping and distribution [89]. Therefore, a number of experimental techniques was used to determine the sustainability of the tablets, such as tablet hardness test, friability and disintegration. Furthermore, in order to evaluate the deformation properties of the tablets, such as hardness and elasticity, Dynamic Mechanical Analysis and nanoindentation tests were carried out. A generic comparison was performed between the blends that were developed in the previous section, to evaluate the effect of the corresponding powders on the tablet properties.

3.5.1   Mass and Density

45 cubic parts for each blend composition were measured before mechanical testing. The density of the parts was defined as the ratio of weight to volume. The weight was accurately measured using a Kern ABT 100-5m balance. The volume (ρ) was calculated by the average dimensions on the top and bottom surfaces of the parts using a calliper. The average of the length, width and height was calculated from three locations for each dimension. The weight and volume were then used to determine the sintered density of the parts in a simple volumetric method [67], [76], using the equation below:

$$\rho = \frac{mass}{volume} \tag{3.1}$$

3.5.2   Crushing Strength

The crushing strength as described by the European Pharmacopoeia is the breaking force of a tablet, which is the force required to cause the tablet to fail in a specific plane. The crushing strength of the sintered parts was measured using a traditional tablet hardness tester TH3/500 (Copley Scientific, Ltd, Nottingham, UK). During this experiment the parts were subjected to simple diametrical compression tests to measure the resistance in breaking [108]. The parts were placed between the jaws in the perpendicular direction of

their axis, where they were subjected to an increasing force until fracture, as illustrated in Figure 3.4. The measurement was repeated for 10 samples of sizes of 20 x 20 x 2 mm for each blend, based on the Ph. Eur. 2.9.8 Standard.
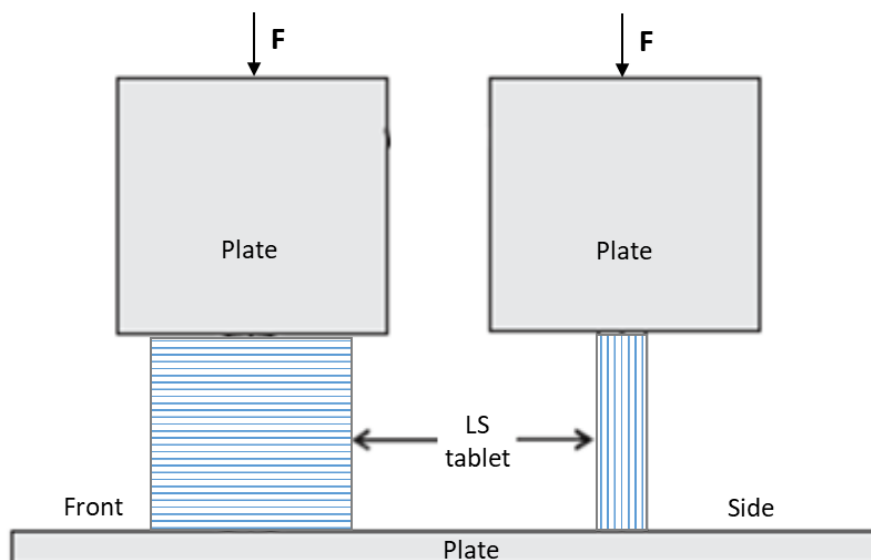
Figure 3.4: Schematic of the diametrical compression test

3.5.3 Friability

Friability is the tendency of a tablet to crumble or break during handling or subsequent storage. A friability tester FR(V) 1000/2000 (Copley Scientific, Ltd, Nottingham, UK) was used to show any evidence of damage or lamination of the sintered parts when subjected to mechanical shock. Ten parts of sizes of 20 x 20 x 2 mm for each blend were de-dusted, accurately weighed and placed in the drum (Figure 3.5). The drum then rotated 100 times at 25rpm according to the Ph. Eur. 2.9.7 Standard, and then the parts were de-dusted and re-weighed to determine the loss in weight caused by fracture or abrasion. Friability was evaluated from the percentage of mass loss, which was calculated using the values of the initial and final mass [108]. A maximum weight loss of 1 percent is considered to be acceptable for most tablets (Ph. Eur. 2.9.7 Standard).
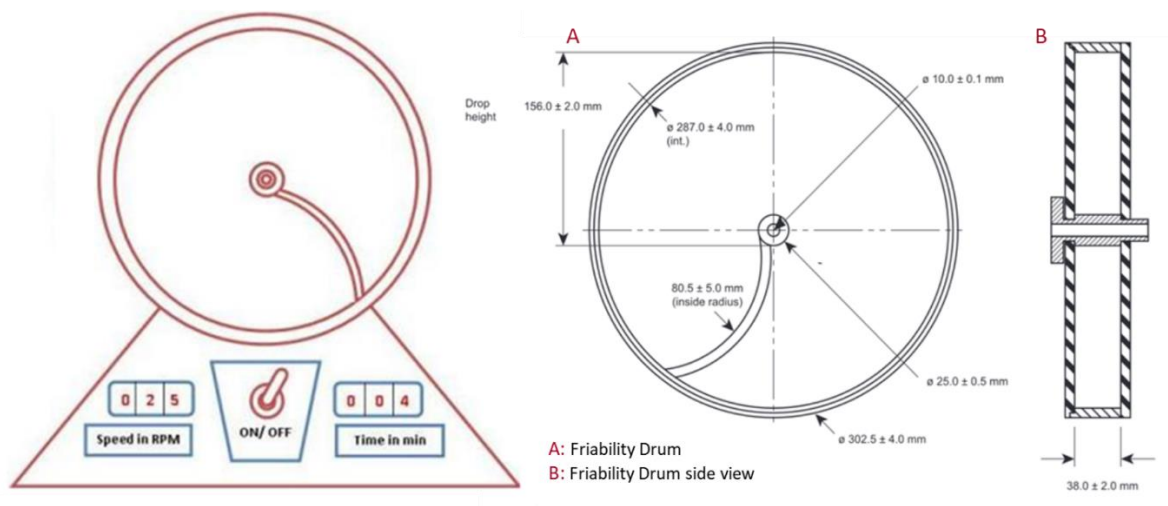
Figure 3.5: Tablet friability apparatus (Ph. Eur. 2.9.7 Standard)

3.5.4 Disintegration

The disintegration test aimed to investigate whether the parts would disintegrate when administered and determine the release of the laser sintered tablets. As there was no expected prescribed time for the sintered parts to disintegrate in this study, a simple way to examine the disintegration properties was to dissolve them into a neutral medium. Three parts of sizes of 20 x 20 x 2 mm were examined for each blend one at a time, placed into a beaker containing 50 ml of the medium, which was consisted of water at a temperature of 20 ℃ and were monitored, as illustrated in Figure 3.6. According to the Ph. Eur. 2.9.1 Standard, disintegration is to be achieved when no residue remains. Tablets were considered to have disintegrated when completely dispersed fragments were obtained.
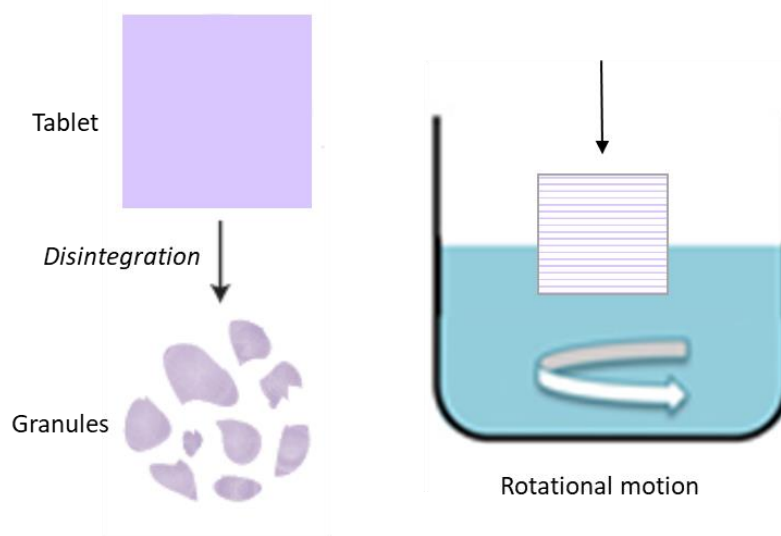
Figure 3.6: Disintegration method in aqueous medium

3.5.5 Dynamic Mechanical Analysis (DMA)

Dynamic Mechanical Analysis (DMA) was employed to determine the mechanical properties of the laser sintered tablets. The materials that were used in this study are viscoelastic polymers and therefore a constant value of the elastic modulus using universal testing machines would not accurately measure the stiffness of the parts [66]. Using DMA the time-dependent loss or storage of energy was measured under stress or deformation as heat/cycle, and then the dynamic (or complex) modulus was calculated giving an estimation of the stiffness of the laser sintered tablets [66], [134], [135]. The dynamic modulus E* is the instantaneous ratio of stress to strain (σ_0/ε_0) under vibratory conditions as seen in equation 3.2 [134]. The time dependent variables acquired through the analysis were the storage modulus E′ representing the in-phase or elastic response of the parts [E′= (σ_0/ε_0)cosδ], the loss modulus E″ representing the out-of-phase or viscous response [E″= (σ_0/ε_0)sinδ], and the tanδ, representing the energy dissipation. The angle δ is the phase angle between the applied stress and the resultant strain as demonstrated in Figure 3.7a. Therefore, tanδ or loss tangent or damping factor given by the ratio of loss to storage modulus, E″/E′, was used to express the parts' ability to store and dissipate energy [134], [135].

$$E^* = \left(\frac{\sigma_0}{\varepsilon_0}\right)\cos\delta + i\left(\frac{\sigma_0}{\varepsilon_0}\right)\sin\delta \qquad (3.2)$$

All the parts were tested by employing a DMA 8000 (Perkin Elmer, Inc., MA, USA) with a parallel plate geometry in compression mode according to the ISO/DIS 6721-12 as shown in Figure 3.7b [136]. For testing, each part was placed in the centre of the platform and the furnace was purged with nitrogen (20 ml/min). Dynamic scans were performed under a strain rate of 0.002 mm/min applying a static force of 2000 mN and a frequency of 1 Hz [134]. A temperature scan mode was employed between 20 ºC and 37 ºC to monitor any changes in the viscoelastic properties of the parts between room and body temperature. Through the dynamic scans many variables were measured; for the purpose of this study storage modulus and phase angle as a function of temperature are reported. Ten samples of sizes of 20 x 10 x 2 mm were tested for each blend to acquire a mean value of those parameters.
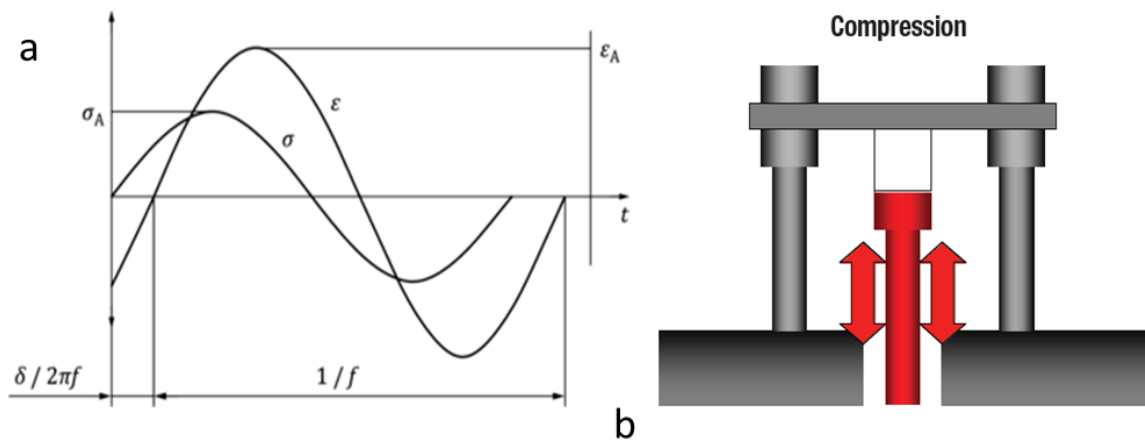
Figure 3.7: a) Phase shift $\delta/2\pi f$ between the stress σ and strain ε in a viscoelastic material subjected to sinusoidal oscillation (σ_A and ε_A are the respective amplitudes, f is the frequency) (ISO 6721-1:2019), b) Compression stress is applied by the motor; sample is sandwiched between a fixed plate and a plate mounted on the drive shaft [137]

3.5.6 Nanoindentation

Further mechanical analysis was performed using nanoindentation, where a spherical indenter was used to penetrate into the surface of the produced parts. The depth of penetration and the applied load were recorded to determine the contact area and therefore the hardness of the laser sintered tablets in accordance to ASTM E2546-07. Hardness describes the resistance to plastic deformation caused by a rigid body and is normally obtained by the ratio of the applied force to the residual indentation area, as defined in equation 3.3 [113], [138], [139].

$$H = \frac{P_{max}}{A_p}$$

(3.3)

Indentation experiments were performed using a NanoTest instrument (Micro Materials Ltd., Wrexham, UK) in continuous stiffness mode (CSM) with 20 μm indentation depth. In CSM the tip is forced into the material to the set maximum depth, while imposing a small harmonic oscillation in the force signal, providing a continuous measurement of the indentation depth [111], [140]. Thus, hardness was measured as a function of indentation depth in a single loading/unloading circle. Three samples of sizes of 20 x 10 x 2 mm were tested for each blend, with indentations at the centre and the edges of the sintered parts. Ten indentations were carried out per set of parameters at 10, 100, 250 and 500 mN of maximum load at a loading/unloading rate of 0.1, 0.5 and 1 mN/s. A 15 sec holding period (dwell time) was inserted at peak load to remove the time-dependent effects of the viscoelastic nature of the parts [141]. The elastic contact analysis developed by Hertz was used for contacting spheres ($H = P_{max}/A_p = P_{max}/\pi \alpha^2$) [142]–[144] to evaluate the load-displacement curves that were generated and calculate the experimental parameters, such as the hardness, but also the elastic modulus of the parts that was obtained through the slope of the unloading curve, as depicted in Figure 3.8.
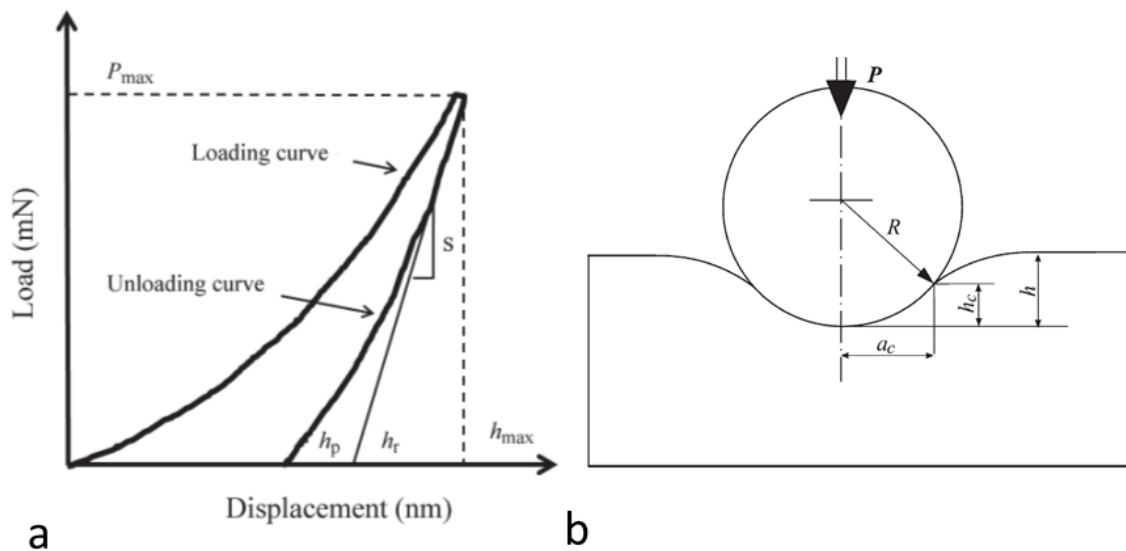
Figure 3.8: a) Load-displacement curve obtained in a nanoindentation experiment with maximum load P_{max} (h_p – permanent depth after removal of test force; h_r – intersection of the tangent to the first part of the unloading curve with the displacement axis; h_{max} – indenter displacement at peak load) [140], b) Schematic of the contact area between a spherical indenter with radius R and the flat surface of the specimen [145]

3.5.7 Surface analysis

In addition to the mechanical analysis, the surface morphology of the parts was observed in order to examine the surface finish after sintering. A Field Emission Gun Scanning Electron Microscope (JEOL 7100F FEG-SEM) was used due to its improved performance at lower accelerating voltages (< 5 kV), to investigate the consolidation phenomena and consequently the packing density during the process, and thus, detect any defects related to trapped powder, particle interlocking, etc. Iridium, Ir, was used to apply a fine coating on the samples to capture images of low and high magnification (100x – 8500x).

3.6 Methods of Development and Analysis of Coated Particles

The production of a polymer coating on the surface of the particles aiming to enhance processability in LS was developed and is demonstrated in this section. Two of the excipients were selected, Avicel 101 (microcrystalline cellulose) and Eudragit L100-55 (methacrylic acid-ethyl acrylate copolymer), based on their effect on sintering and their functionality in tablet formulation. Avicel 101 is purified cellulose and highly crystalline that is insoluble in common solvents and is typically used as a filler material in oral solid dosage forms [89], [93], [98]. Eudragit L100-55 is an acrylic copolymer that can be dissolved above pH 6 and it serves as a film coating, and therefore it was selected to coat Avicel 101 [89], [98], [104], [110], [146]–[149]. Exploiting the pH-dependent solubility of Eudragit L100-55, polymer precipitation and emulsion-evaporation methods were employed to produce a coated cellulose-based material [90]. The efficacy of the process, the material ratio and the solvent ratio were evaluated using Fourier-transform infrared Spectroscopy, Thermogravimetric Analysis and Scanning Electron Microscopy. Additionally, Time-of-Flight Secondary Ion Mass Spectrometry revealed information related to material concentration that allowed the development of an optimised formulation.

3.6.1 Precipitation of Eudragit L100-55 onto Avicel 101

In the first approach that was taken towards the development of the coating, 1gr of Eudragit L100-55 was dissolved in 10, 20, 30, 40 and 50 ml of methanol (MeOH) under sonication, to prepare solutions of different concentrations (10, 5, 3.3, 2.5 and 2wt%).

One gram of Avicel 101 was then dispersed in 100, 50, 30, 40 and 50 ml of water to prepare different concentrations (1, 2, 3.3, 2.5 and 2wt%) of the aqueous phase [150]–[152]. The organic phase containing the Eudragit L100-55 was added drop-wise to the suspension containing the Avicel 101 utilising high-speed homogenisation at ambient temperature with a stirring rate of 6000rpm, to form a stable emulsion (1:1 core/coat ratio) [153]. Particles of Avicel 101 coated with Eudragit L100-55 were isolated by centrifugation, before drying under reduced pressure at 50 °C [146], [153]. Details of the procedure and a schematic representation of the method are presented in Table 3.3 and Figure 3.9, respectively.

Table 3.3: Basic summary of the first coating method used

Eudragit L100-55 (gr)	Methanol (ml)	Organic phase wt%	Avicel 101 (gr)	Water (ml)	Aqueous phase wt%	Method
1	10	10	1	100	1	High speed mixer/ Centrifugation/ Drying
1	20	5	1	50	2	
1	30	3.3	1	30	3.3	
1	40	2.5	1	40	2.5	
1	50	2	1	50	2	
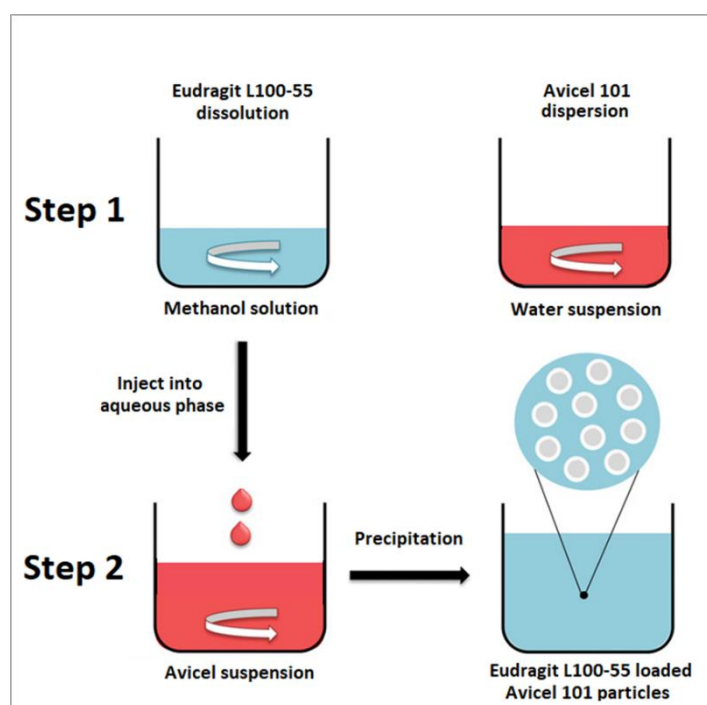
Figure 3.9: 1) Preparation of organic phase (Eudragit L100-55 in MeOH) and aqueous phase (Avicel 101 in water) separately, 2) Injection of organic phase into aqueous phase to force precipitation

A second approach was taken to mix both Eudragit L100-55 and Avicel 101 in methanol and then inject them into water. One gram of Eudragit L100-55 was dissolved in 10, 20, 30, 40 and 50 ml of MeOH under sonication, to make solutions of 10, 5, 3.3, 2.5 and 2wt%. One gram of Avicel 101 was then dispersed into the solution [150], [151], [154]. The organic phase was added drop-wise to the aqueous phase with a constant stirring rate of 600rpm on magnetic stirrer, to emulsify (1:1 core/coat ratio) [146], [150]. Particles of Avicel 101 coated with Eudragit L100-55 were recovered by centrifugation, before drying under reduced pressure at 50 °C [146], [153]. Details of the procedure and a schematic representation of the method are presented in Table 3.4 and Figure 3.10, respectively.

An alternative method to facilitate the precipitation of the particles, was to maintain the concentration of Eudragit L100-55 low in the organic phase and gradually decrease the concentration of the aqueous phase [153], [154]. One gram of each component was dispersed in 50 ml of MeOH (20wt%) and then injected with increasing amounts of water (20, 30, 40 and 50 ml). Details are summarised in Table 3.4.

Table 3.4: Basic summary of the second coating method used

Eudragit L100-55 (gr)	Methanol (ml)	Organic phase wt%	Avicel 101 (gr)	Water (ml)	Aqueous phase wt%	Method
1	10	10	1	10	20	
1	20	5	1	10	20	
1	30	3.3	1	10	20	
1	40	2.5	1	10	20	High speed mixer/ Centrifugation/ Drying
1	50	2	1	10	20	
1	50	2	1	20	10	
1	50	2	1	30	6.66	
1	50	2	1	40	5	
1	50	2	1	50	4	
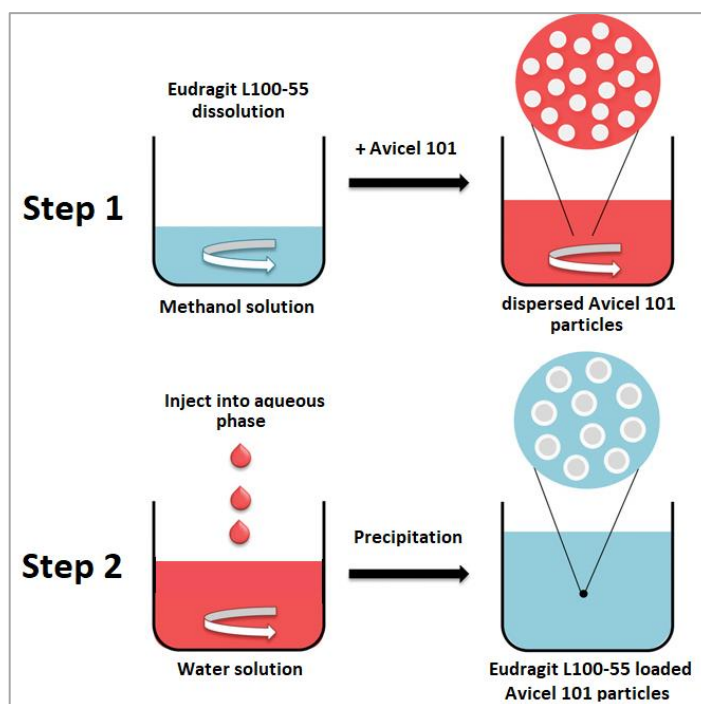
Figure 3.10: 1) Preparation of organic phase (Eudragit L100-55 in MeOH) and disperse Avicel 101 into solution, 2) Injection of organic phase into aqueous phase to force precipitation

In the third and final approach to the method used, different amounts of Avicel 101 were dispersed in MeOH instead of water, preparing the suspension phase [146]. Briefly, 200mg of Eudragit L100-55 were dissolved in 10ml of MeOH (2wt%) under sonication. Avicel 101 was then dispersed in 40ml of MeOH at different concentrations (2, 1, 0.5wt%) [146], [154]. The organic phase containing the Eudragit L100-55 was added drop-wise to the suspension containing the Avicel 101 at a constant stirring rate of 600rpm on magnetic stirrer at ambient temperature, to form a stable emulsion (4:1, 2:1, 1:1 core/coat ratio) [146], [151]. The emulsion formulated was left overnight in a petri dish at room temperature to evaporate the solvent (MeOH). After evaporation of the solvent, particles of Avicel 101 coated with Eudragit L100-55 were collected. Details of the procedure and a schematic representation of the method are presented in Table 3.5 and Figure 3.11, respectively.

Table 3.5: Basic summary of the third coating method used

Eudragit L100-55 (gr)	Methanol (ml)	Organic phase wt%	Avicel 101 (gr)	Methanol (ml)	Suspension phase wt%	Method
0.2	10	2	0.8	40	2	Magnetic stirrer/ Evaporation
0.2	10	2	0.4	40	1	
0.2	10	2	0.2	40	0.5	
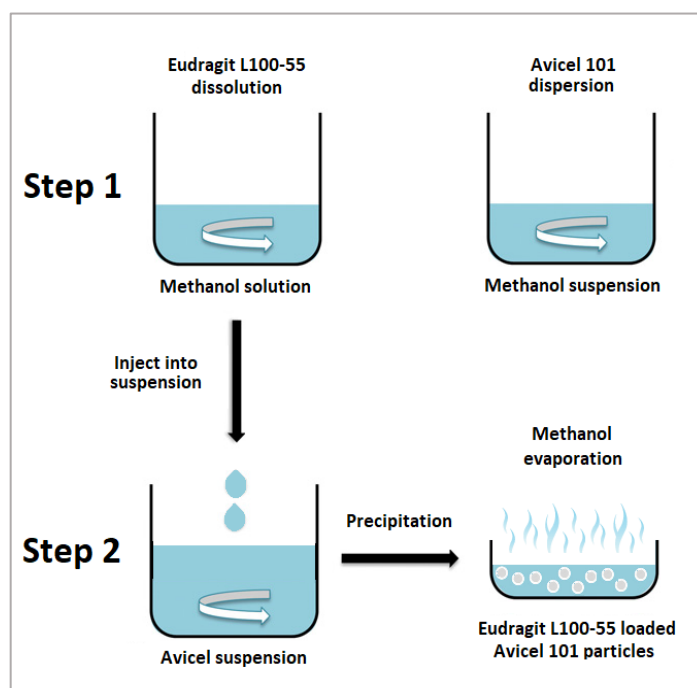
Figure 3.11: 1) Preparation of organic phase (Eudragit L100-55 in MeOH) and suspension phase (Avicel 101 in water) separately, 2) Injection of organic phase into suspension phase to force precipitation

3.6.2 Fourier Transform Infrared Spectroscopy (FTIR)

In order to investigate any chemical interaction between the Eudragit L100-55 and the Avicel 101 after the coating process, a spectroscopic analysis was performed to identify the characteristic bands of the two components before and after the coating. Mid-IR spectra were obtained to identify the band positions and intensities of the important polymer functional groups with the use of an FTIR (Fourier-transform infrared) spectrometer (Frontier MIR/NIR Spectrometer, PerkinElmer, Inc., MA, USA), equipped with a diamond-based ATR accessory (brand). All Mid-IR spectra were acquired through the PerkinElmer Spectrum software v10.4, from an average of 30 scans for each sample

in the range of 4000-700cm^{-1}. Eudragit L100-55 and Avicel 101 spectra were used as a reference in order to be compared with the unknown spectra of the coated samples.

3.6.3   Thermogravimetric Analysis (TGA)

To gain complementary information about the effectiveness of the coating process, TGA analysis was performed to monitor the change in mass and the physical transitions of the samples. The weight loss percentage and the decomposition temperature were measured using a Discovery Thermogravimetric Analyser Q500 (TA Instruments). Samples of mass ~15 mg were placed onto 100 micro litre platinum pans (P/N 957207.904), which had been previously tared. The instrument's furnace was purged with nitrogen (25 ml/min) and the samples were heated between 30°C and 600°C at a heating rate of 10°C/min to undergo thorough decomposition. All coated samples were scanned twice and analysed using the TA Trios software v4.1.

3.6.4   Time-of-Flight Secondary Ion Mass Spectrometry (ToF-SIMS)

Time-of-Flight Secondary Ion Mass Spectrometry (ToF-SIMS) is a surface-sensitive analytical method useful for the molecular chemical identification of the samples [119]. FTIR and TGA provided information about the chemical structure and physical transitions of the coated samples, however these techniques provided no information about the distribution of the different components over the surface of the coated samples. Therefore, ToF-SIMS was employed to elementally and chemically map the surface of the coated particles on a sub-micron scale and estimate the efficacy of the coating.

ToF-SIMS analysis of positively and negatively charged secondary ions was conducted using a Hybrid SIMS system (ION-ToF GmbH, Münster, Germany). The instrument employed a 30 keV Bi_3^+ as primary ion beam operated in the high current bunched mode delivering 0.3 pA with 200 µs cycle time. For surface imaging, the whole area (500 x 500 µm^2, 256 x 256 pixels) was scanned (30 scans) in the raster mode with one shot per pixel, ensuring static conditions. A low-energy, 20 eV, electron flood was used to neutralise charge build-up on the samples surface. ToF V measurements gave high mass resolution spectrometry (11.000 amu) and high spatial resolution chemical images. Depth profiles were conducted in a non-interlaced mode with Bi_3^+ (30 keV) as primary ion species and Ar_{1460}^+ (10 keV) for sputtering. The surface was flooded with low-energy electrons for 1

sec for charge compensation. The analysis area was (150×150) μm^2 and placed in the center of the (400×400) μm^2 sputter crater [119].

3.6.5   Scanning Electron Microscopy (SEM)

A FEG-SEM (JEOL 7100F FEG-SEM) was employed to study the type and the quality of the coating obtained, due to its improved performance at lower accelerating voltages (< 5 kV), to achieve the highest resolution possible. The coated samples were sputtered with Iridium, Ir, to capture surface images of high spacial resolution, 2000x - 27000x.

CHAPTER 4 CHARACTERISATION OF PHARMACEUTICAL INGREDIENTS

4.1 Introduction

This study aims at developing oral pharmaceuticals using LS technologies, therefore the selection of materials will strongly influence the outcome of this PhD. As has been discussed in Chapter 2, LS powders should possess a set of physical and morphological characteristics compatible with the LS process [53], [58], [66], [80], [81], [155], which makes necessary to identify the key material properties that are related to the LS process and predict the behaviour of the powders during processing. Therefore, this chapter focuses on the thorough characterisation of regular pharmaceutical polymers using a number of analytical techniques to investigate their thermal, physical and rheological properties. The materials were microcrystalline cellulose (Avicel 101 and 102), polyethylene oxide (PolyOx N80), methacrylic acid ethyl acrylate copolymer (Eudragit L100-55, FS100), hydroxypropyl cellulose (HPC SL, SSL and SSL SFP), lactose monohydrate (Foremost 316) and hypromellose acetate succinate (AQOAT LMP, MMP and HMP), and were presented in Chapter 3.

It has been discussed previously that during LS the materials are raised to high temperatures in order to change from a solid to a more viscous state, and therefore, a wide thermal processing window is necessary to allow full consolidation of the polymer particles and achieve the highest part density and mechanical performance[6], [48], [52]–[54], [58], [156]. For this reason, the materials were subjected to DSC and TGA measurements to identify their thermal transitions and estimate their thermal processing window. Additionally, the flow properties of the materials it has been noted previously that are related to the efficient application of the polymer powders to the LS bed. Consequently, FT4 measurements were conducted to explore the flowability of each powder and estimate their behaviour during spreading and sintering, which is further related to the particle morphology [54], [80], [81]. The preferred particle size for LS is in the range of 45-90μm, with a particle shape near as spherical in order to achieve high part density, therefore, using particle size distribution and SEM, the size and shape of the particles for each of the excipients were measured, to estimate the packing efficiency of the powders [6], [48], [80], [81]. The resulted combination of all the properties measured,

gave an estimation of the powder performance during processing and determined the suitability of the selected materials for LS.

4.2   Thermal analysis

This section investigates the thermal transitions of the excipients mentioned above. DSC and TGA thermograms are displayed in Figure 4.1 - Figure 4.12 as a function of temperature. The experimental procedure is described in sections 3.3.1 and 3.3.2 for DSC and TGA, respectively. From the resultant thermograms, phase transitions were monitored, such as, the melting temperature (T_m), which is the temperature that semi-crystalline polymers pass from the rubbery phase to the melt; the glass transition temperature (T_g), which is the temperature that polymers pass from the glassy state to the rubbery; and the weight loss onset temperature (T_{onset}), at which oxidation begins and the polymer decomposes [30], [52], [53], [157]. It should be noted that the materials can be heated up to 182°C in the P100 laser sintering system, which is the maximum powder bed surface temperature that can be achieved. Ideally, the excipients should possess a melting point lower than this temperature [34], [54], [58]. Therefore, DSC and TGA experiments aimed to ensure that the excipients would undergo melting below 182°C, and very importantly that they would not decompose during the process. The values for the phase transitions that were identified for each excipient are presented in Table 4.1. The range of temperatures were very similar to those given by the manufacturers for all the excipients.

Table 4.1: Thermal properties of the pharmaceutical excipients tested

Sample	T_g (°C)	T_m (°C)	T_{onset} (°C)	Weight loss (%)
Avicel 101	106.96	254.47	270	4.15
Avicel 102	106.54	-	270	3.63
PolyOx N80	-	67.67	> 300	Negligible
Eudragit L100-55	93.21	-	200	5.83
Eudragit FS100	55.56	-	> 250	Negligible
HPC SL	92.82	-	250	1.80
HPC SSL	88.94	-	250	1.67
HPC SSL SFP	91.99	-	250	1.71
Foremost 316	-	219.30	230	4.56
AQOAT LMP	91.65	-	> 250	Negligible
AQOAT MMP	83.69	-	> 250	Negligible
AQOAT HMP	82.50	-	> 250	Negligible

DSC curves in Figure 4.1 revealed two endotherm peaks for Avicel 101 and 102. The first peak corresponded to the T_g at about 106°C and the second peak to the T_m at 254°C [158], [159]. The difference between the two transitions could provide a wide processing window for LS, which can be used to delay the onset of crystallisation until the end of the printing process. The sharp melting peak revealed the semi-crystalline nature of Avicel [160], which is preferable in LS [39], [57]. However, the melting of the material occurred significantly higher than the maximum bed temperature of P100, limiting the ability of sintering Avicel successfully. Additionally, this would create a large temperature variation between successive layers, the new layer before sintering and the already consolidated one that would strongly affect dimensional stability, due to warping, curling and other deformations [34], [48], [54], [58], [161].

In addition to the DSC results, TGA curves for Avicel 101 and 102 in Figure 4.2, revealed an extensive mass reduction of approximately 4% up to 150°C, which was associated with a water bound [93], [135], [162]–[165]. This initial water loss continued to decrease at a slow rate until the initiation of the final decomposition of Avicel at ~270°C [135], [165]–[167]. The decomposition of the material, meaning the pyrolysis of the polymer

chain backbone, presented a sharp rate just above the T_m, which denoted that Avicel would possibly cake during sintering [7], [39], [49].
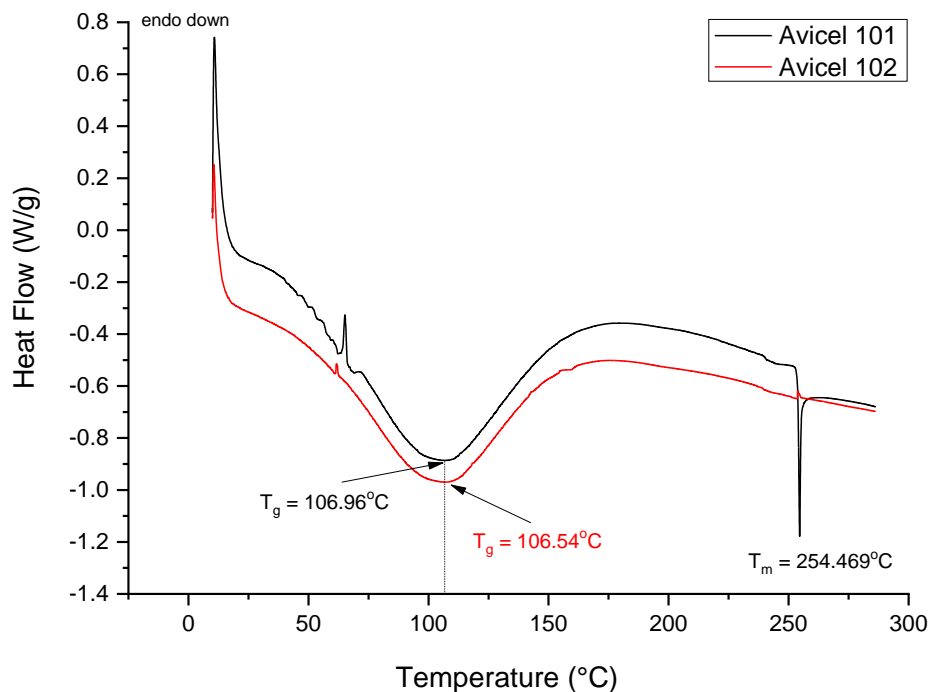
Figure 4.1: DSC thermograms as a function of temperature for Avicel 101 and 102
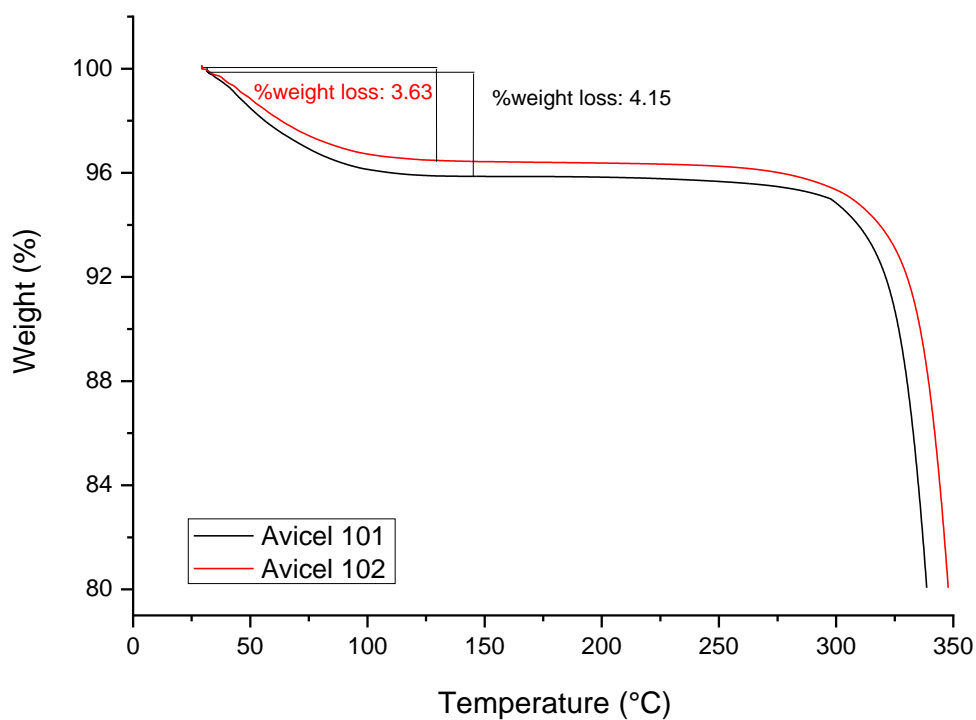
Figure 4.2: TGA thermograms as a function of temperature for Avicel 101 and 102

In Figure 4.3, DSC curves for Polyox N80 showed a very distinct melting point at 67.67°C with a sharp peak, revealing that the material was highly crystalline [69], [105], [109], [168]. Phase transitions occurred lower than the P100 bed temperature limit. Moreover, TGA curves in Figure 4.4 did not show any significant degradation when PolyOx N80 was subjected to extensive heating. The mass decreased 0.05% roughly up to 100°C, followed by 0.5% until 300°C [105], [169], [170], which implied that zero material property degradation would occur during sintering.

DSC curves for Eudragit L100-55 and FS100 in Figure 4.5, revealed that the material was amorphous, showing only one phase transition, which corresponded to the T_g. The L100-55 grade presented a wide peak, as with most amorphous polymers, at 93.21°C [147], [171], [172]. Amorphous materials do not exhibit a clear and fast transition to the melt like crystalline polymers [6], [7], [30], [53], [157], which suggested that sintering of L100-55 may become more challenging [6], [7], [34], [58]. Specifically, small percentages of the material would start flowing in a range of temperatures, which could possibly inhibit powder flow across the powder bed due to the temperature sensitivity of the thermal and viscous characteristics of the material [34], [53]. On the contrary, the FS100 grade presented a sharp glass transition at 55.56°C [112], [166]. The melt-like glass transition is known to be similar to other amorphous Eudragit polymers, such as Eudragit E [173]. This melt-like glass transition would be expected to facilitate the sintering process, as the material would become softer quickly above the T_g, like crystalline materials. Although, L100-55 and FS100 had a similar chemical structure, the variation in their T_g resulted from the different monomer ratio between methacrylic acid and ethyl acrylate [172].

In Figure 4.6, TGA curves for Eudragit L100-55 revealed a reduction of mass of about 5.83%. The first mass loss was attributed to surface water release and can be observed up to 100°C, and the second mass loss was associated to crystal water release due to the conversion of methacrylic acid to anhydrites, between 150-200°C [172], [174], [175]. It was noticed that the material continued reducing the mass at a slow rate above 200°C, leading to the last and main decomposition of the polymer [89], [172], [174], which indicated that L100-55 would not decompose during processing in the P100. In contrast, Eudragit FS100 did not show any similar behaviour. The mass decreased by approximately 1% up to 250°C, which suggested minimal material degradation [176].
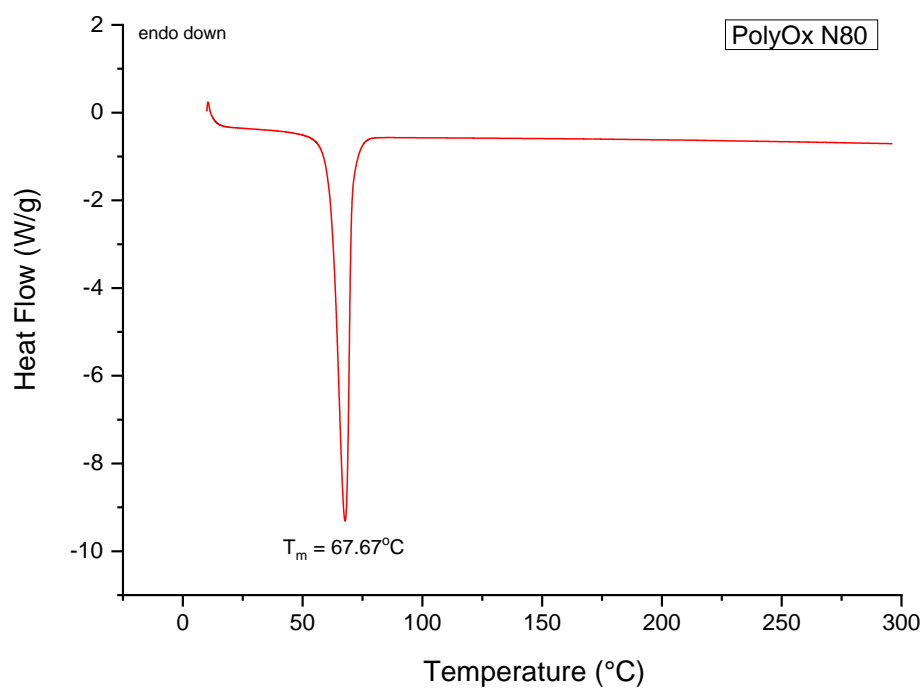
Figure 4.3: DSC thermogram as a function of temperature for PolyOx N80
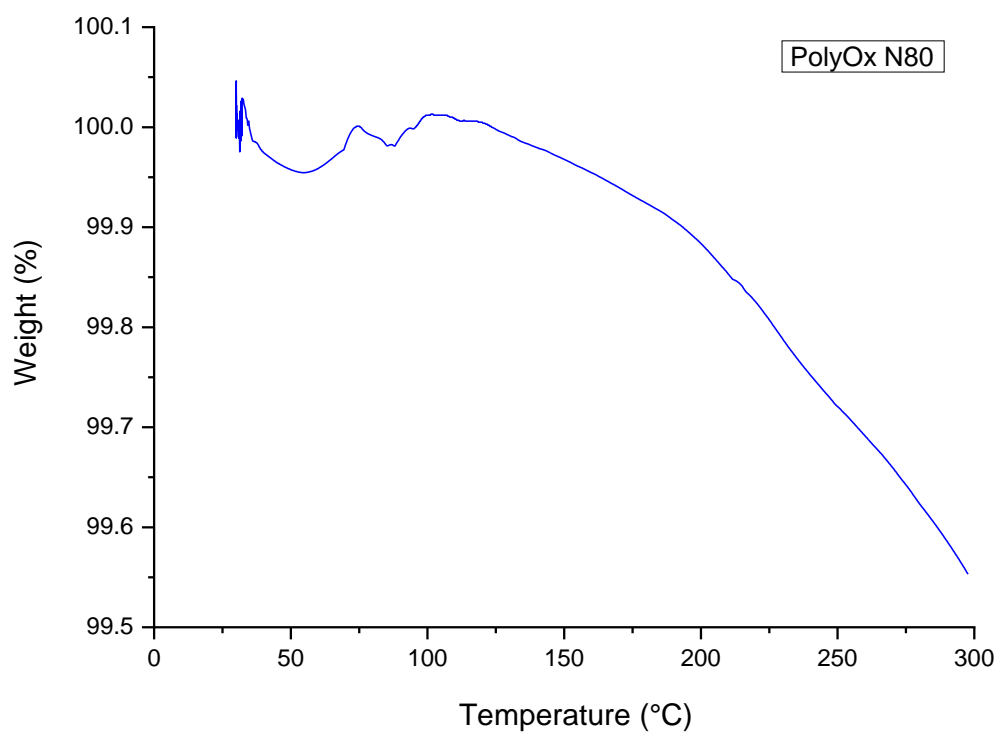
Figure 4.4: TGA thermogram as a function of temperature for PolyOx N80
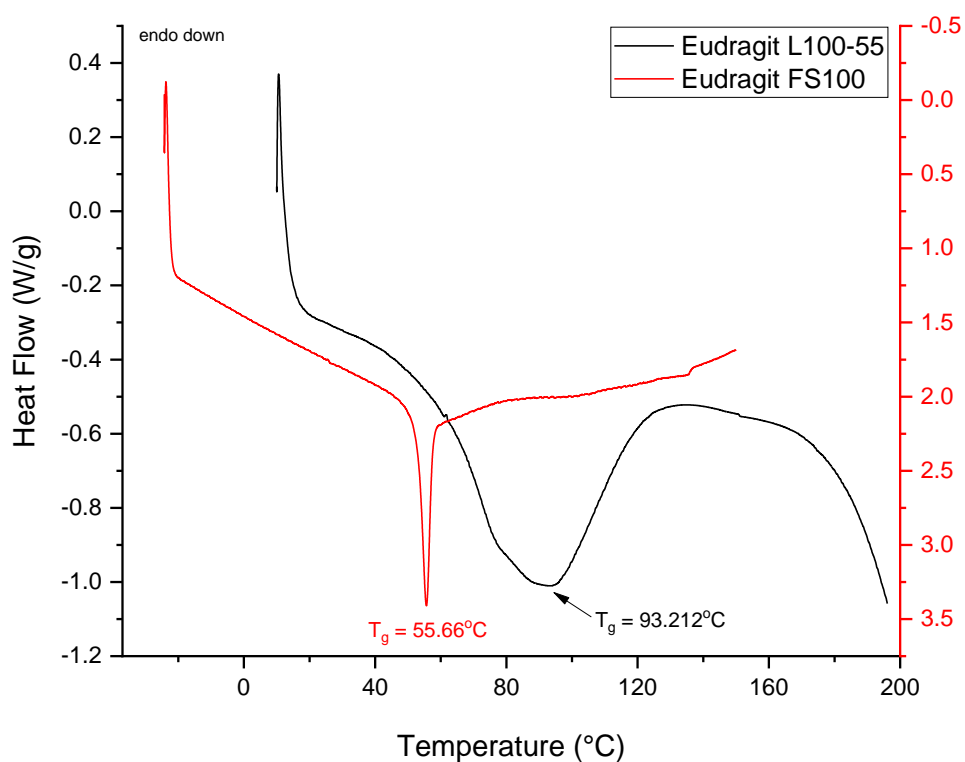
Figure 4.5: DSC thermograms as a function of temperature for Eudragit L100-55 and FS100
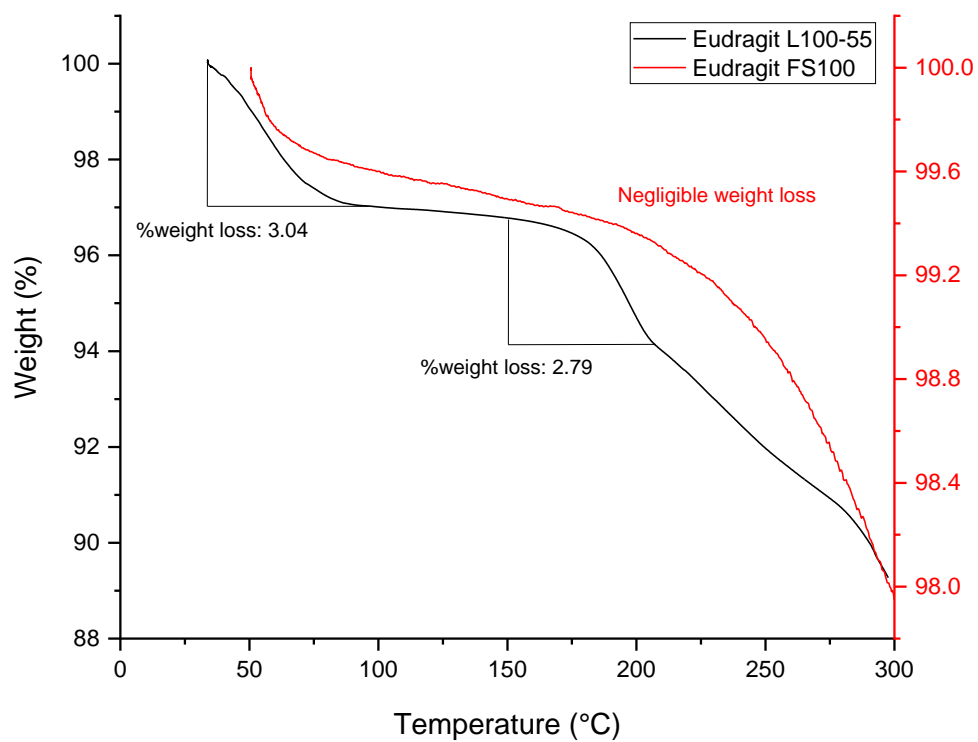
Figure 4.6: TGA thermograms as a function of temperature for Eudragit L100-55 and FS100

DSC curves in Figure 4.7 for HPC SL, SSL, and SSL SFP were similar to those of Avicel 101 and 102, except that only one phase transition was observed around 90°C, which corresponded to the T_g. This T_g resembled the typical glass transition of cellulose as can be observed in the DSC thermogram of Avicel (Figure 4.1) [177]. It is important to note that a melt transition for HPC has been reported to occur in the range of 160-220°C [115], [177], [178]. HPC is a semi-crystalline cellulose ether derivative, obtained from the chemical reaction of hydroxyl groups of cellulose [177], [179]. Introducing hydroxypropyl groups increased the amorphous content of the polymer and therefore the molecular mobility and plasticity, which in this case resulted in a decline of T_g (~90°C) compared to Avicel (~106°C) [115], [177]–[179]. While this is not unusual for HPC, a more prominent melt transition would be expected. At this point, it has been considered that the degree of crystallinity was relatively low, hence the small change in the associated heat capacity could not be detected [177], [178].

Similar to the TGA results of Avicel 101 and 102 (Figure 4.2), TGA curves for HPC SL, SSL, and SSL SFP can be divided in two steps, as shown in Figure 4.8. An initial mass reduction of about 1.75% corresponded to water loss before 100°C, which was attributed to the high moisture content of HPC, likewise Avicel [115], [163], [180], [181]. As the temperature increased, the material slowly reduced mass up to 250°C, above which the main decomposition was observed to initiate [180], [182]. TGA curves of HPC were more stable compared to Avicel, showing that the material presented improved thermal stability, thus it would be safer to be processed in the P100 [180], [182].
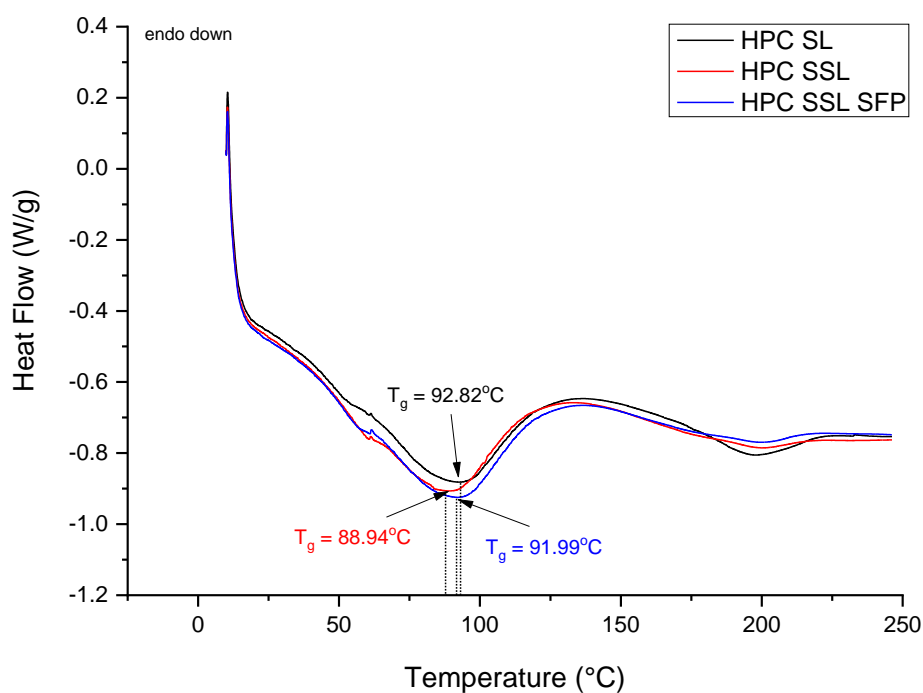
Figure 4.7: DSC thermograms as a function of temperature for HPC SL, SSL, and SSL SFP
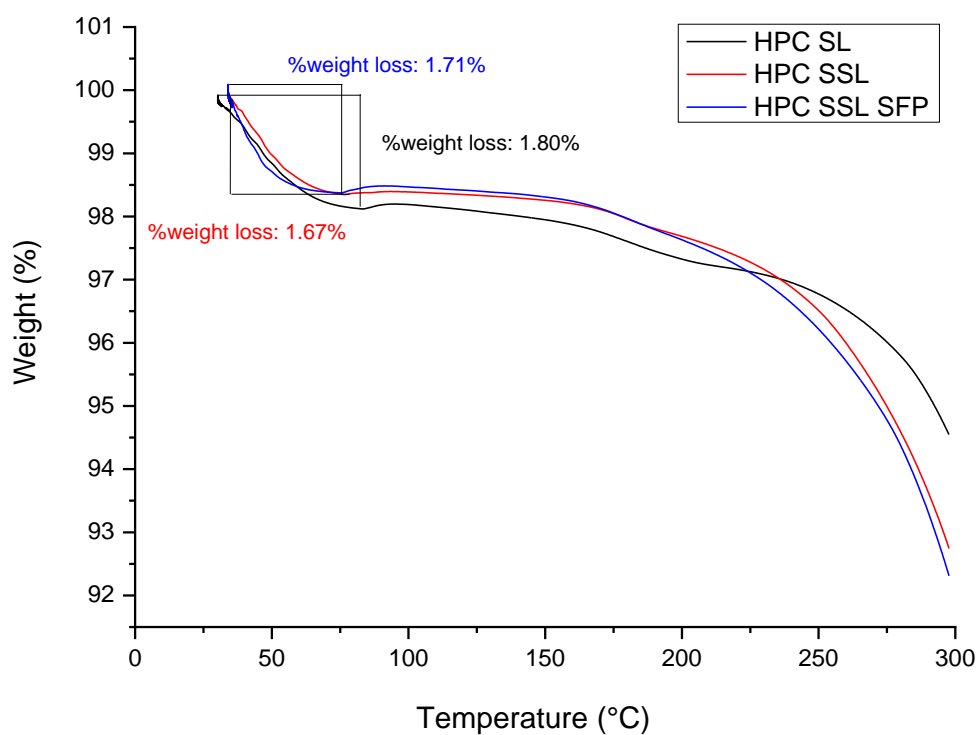
Figure 4.8: TGA thermograms as a function of temperature for HPC SL, SSL, and SSL SFP

In Figure 4.9, DSC curves for Foremost 316 revealed two sharp endotherm peaks. The first peak corresponded to the dehydration of the to the α-anhydrous form, at about 144°C, according to literature [118], [183]. The second peak was related to the melting of the lactose crystal at 219.3°C, which indicated that the material was semi-crystalline [118], [183], [184]. Additionally, TGA analysis revealed three distinctive areas of mass loss, as presented in Figure 4.10. The first loss of mass can be observed up to 130°C, presumably due to the loss of surface free water molecules [183], [184]. The second mass reduction of 4% occurred between 130 and 170°C, related to the release of water of crystallisation trapped in the crystal lattice structure [184]. The third and final mass loss observed at 230°C was the dominant decomposition of lactose, which according to the DSC results, it took place shortly after the T_m implying that Foremost 316 would char when sintered [7], [39], [49], [183], [184].

DSC curves in Figure 4.11 for AQOAT LMP, MMP and HMP, presented a single glass transition at around 85°C [185]. AQOAT is an amorphous synthetic polymer derived from the reaction of cellulose with methyl chloride and propylene oxide to produce hydroxypropylmethyl cellulose (HPMC), which is then reacted with acetic and succinic anhydride [122], [124]. Similarly described for HPC, the presence of the methyl groups correlated with the amorphous domain of this cellulosic polymer, therefore the decrease of the T_g that was noticed [186], [187]. Furthermore, the presence of the methyl and acetate constituents make AQOAT relatively hydrophobic [163], [186], which was confirmed through the minimum mass loss observed in the TGA curves, in Figure 4.12. The evolution of mass reduction when the polymer subjected to heating was 1% up to 250°C, which would maintain the stability of AQOAT during processing in the P100 [125], [187].
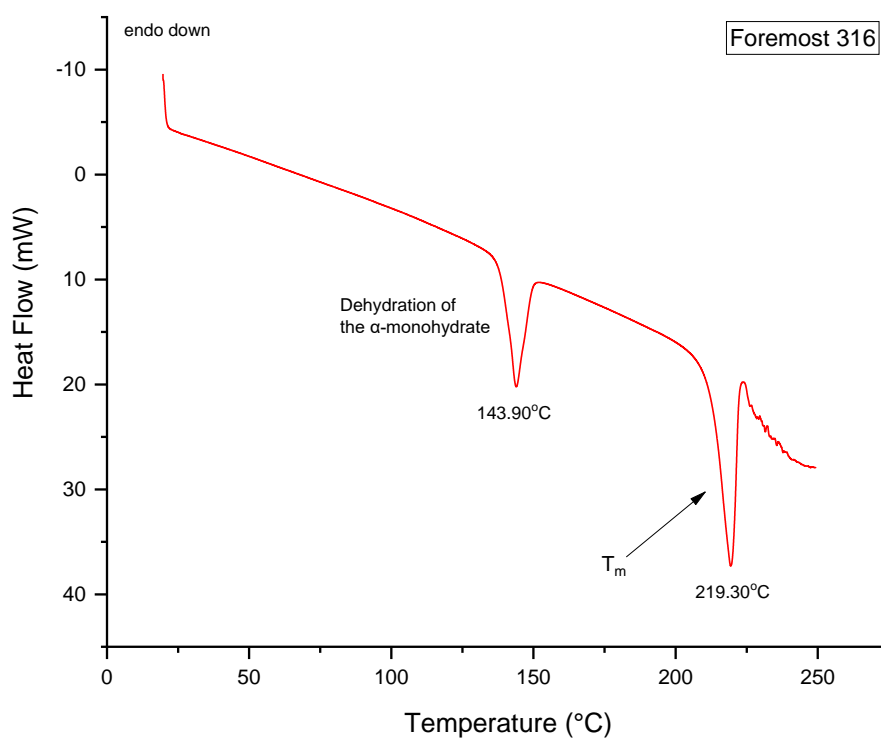
Figure 4.9: DSC thermogram as a function of temperature for Foremost 316
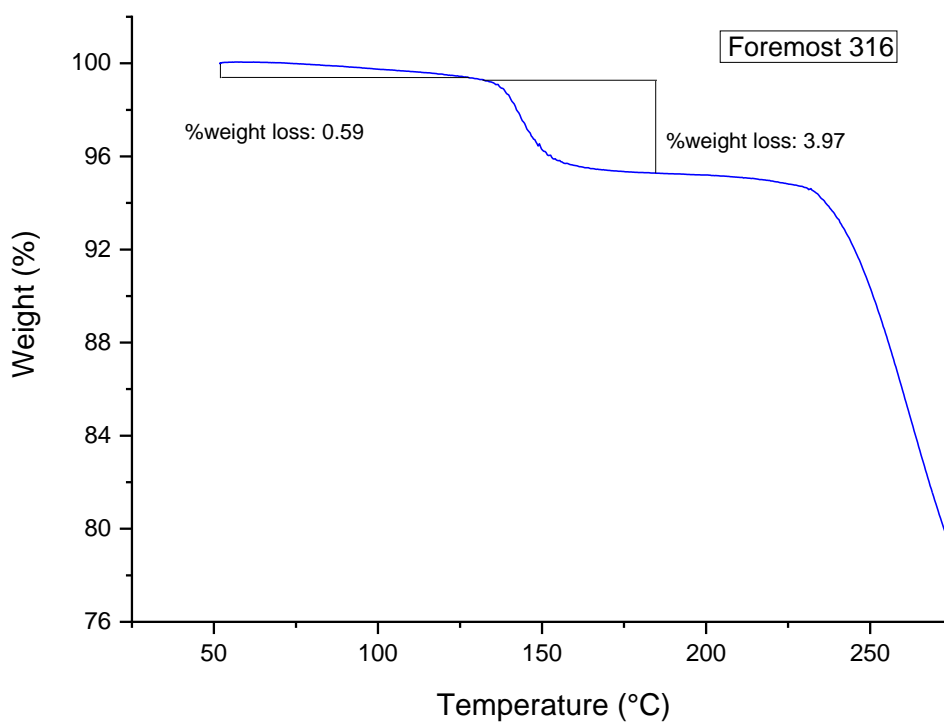
Figure 4.10: TGA thermogram as a function of temperature for Foremost 316
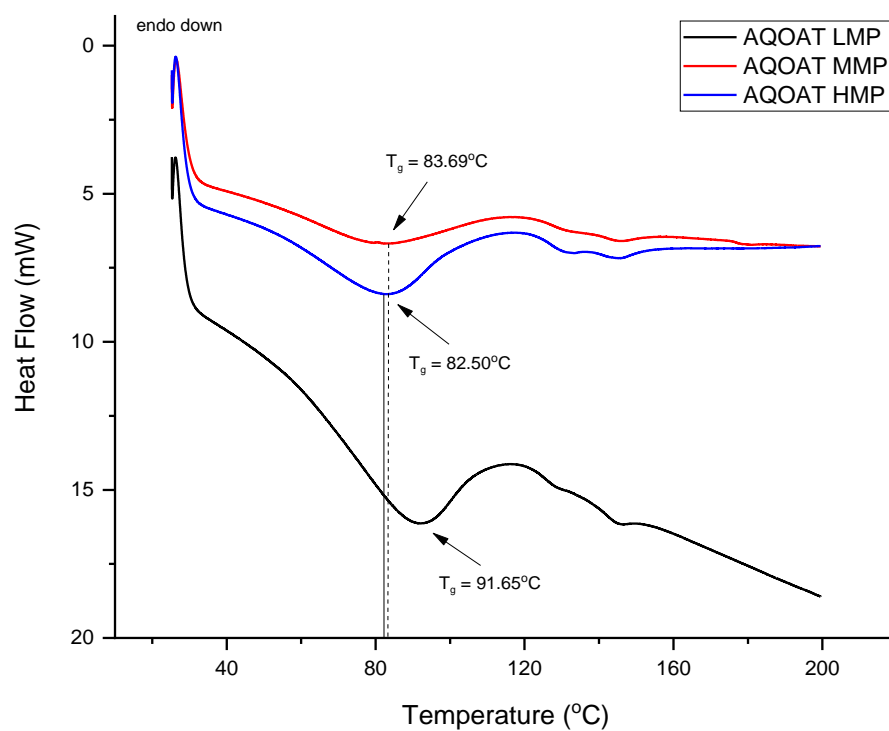
Figure 4.11: DSC thermograms as a function of temperature for AQOAT LMP, MMP and HMP
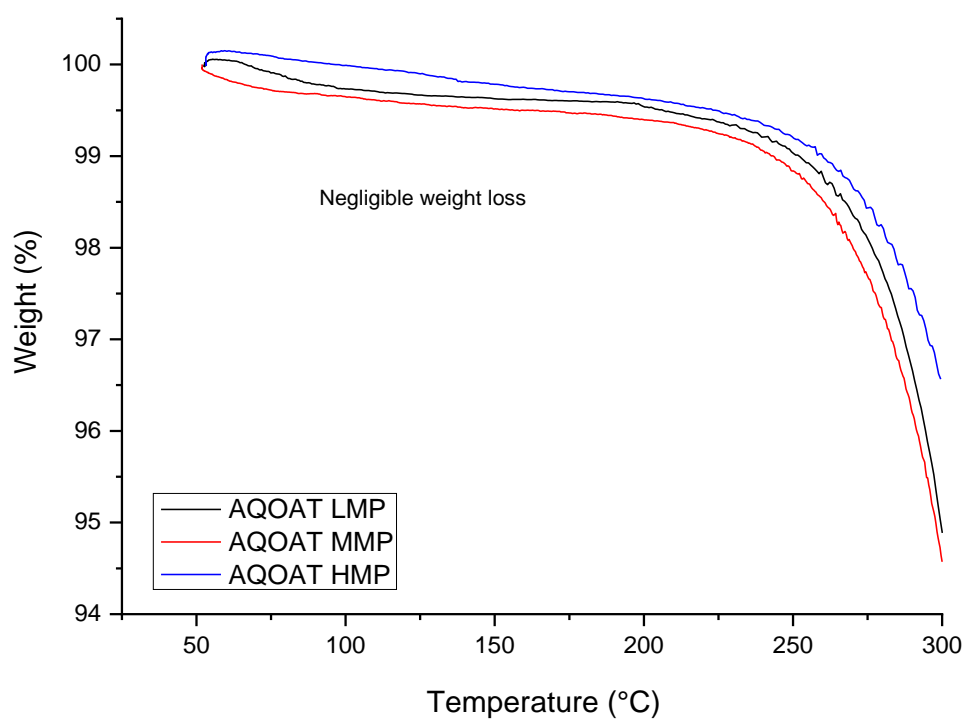
Figure 4.12: TGA thermograms as a function of temperature for AQOAT LMP, MMP and HMP

4.3 Flowability analysis

This section describes the dynamic flow and bulk properties of the excipients. An FT4 Powder Rheometer operating under the stability and variable flow rate method (for details see section 3.3.3), was used to create dynamic flow patterns, as shown in Figure 4.13. The standard material for the P100, PA2200 (EOS), was used as a benchmark material for its proven high flow efficiency [80], [81]. Several variables were calculated in order to assess the materials' ability to change their bulk and flow properties when forced to flow, such as the energy required, BFE, the stability of the flow, SI, and the SE and FRI, which were linked to cohesion [80], [129]. Their average values are presented in Table 4.2.
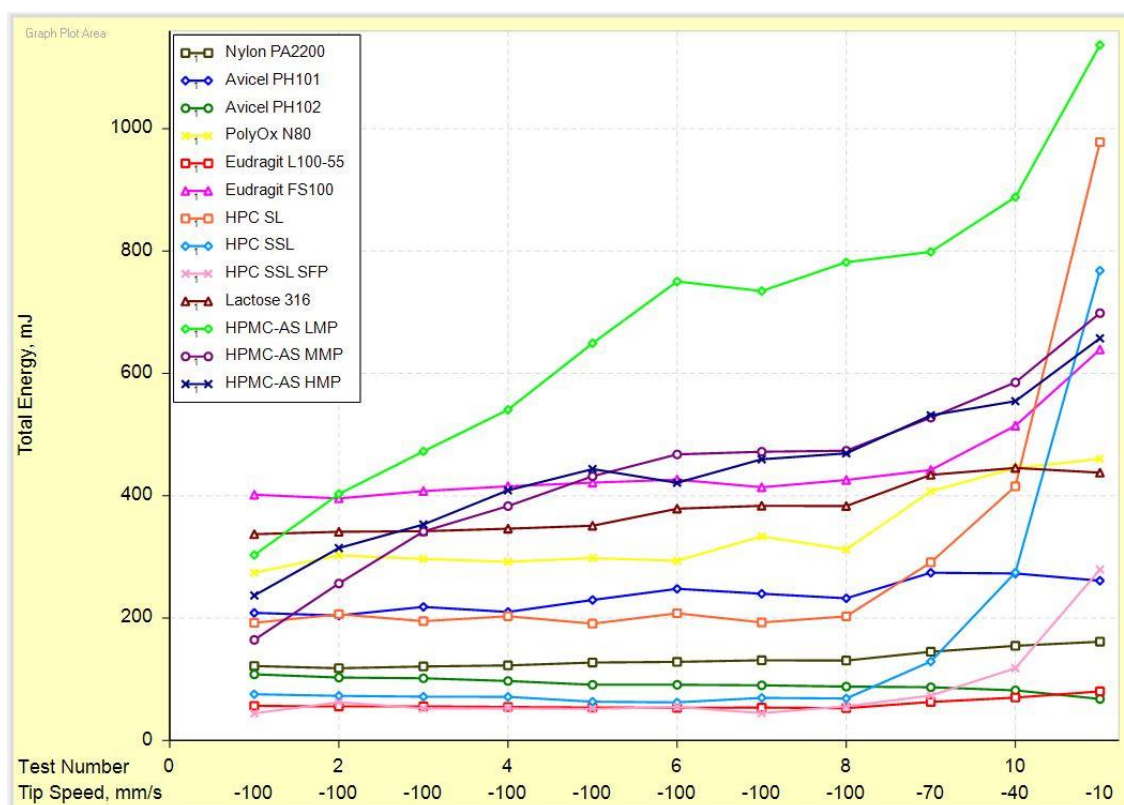
Figure 4.13: Flow patterns of the excipients compared to PA2200

Table 4.2: Powder flow properties of the pharmaceutical excipients tested

Sample	BFE (± 5mJ)	SI	FRI	SE (± 0.02mJ/g)
PA2200	126.0	1.04	1.23	4.93
Avicel 101	259.0	1.17	1.22	6.53
Avicel 102	84.3	0.80	0.79	3.27
PolyOx N80	339.0	1.14	1.41	4.58
Foremost 316	384.0	0.97	1.03	4.60
Eudragit L100-55	52.8	0.96	1.52	2.48
Eudragit FS100	410.0	1.09	1.43	249
HPC SL	200.0	1.03	5.12	7.39
HPC SSL	68.0	0.80	12.60	8.85
HPC SSL SFP	46.6	1.02	5.80	14.20
AQOAT LMP	735.0	2.42	1.56	10.45
AQOAT MMP	472.0	2.23	1.48	12.40
AQOAT HMP	460.0	1.94	1.40	12.20

Avicel 101 and 102 presented a rather stable flow pattern, showing values for SI and FRI close to 1. This result was expected as it has been extensively reported in literature that microcrystalline cellulose has excellent flow properties and thereby is used to facilitate tablet manufacture [93], [99], [102]. The flow pattern for Avicel 102 was similar to that of PA2200, which is a commercial LS powder, showing that Avicel 102 exhibited high flowability [6], [54], [163]. On the contrary, Avicel 101 required higher amounts of energy to flow than Avicel 102, which may be related to differences in the particle size and distribution. This behaviour was further confirmed by the increased BFE and SE values recorded for Avicel 101, at 259 mJ and 6.53 mJ/g respectively, compared to Avicel 102 that were at 84.3 mJ and 3.27 mJ/g.

PolyOx N80 and Foremost 316 presented similar flow patterns. Particularly, the flow pattern was considered borderline unstable for PolyOx N80, showing high values of 339 mJ and 4.58 mJ/g, for BFE and SE respectively. Foremost 316 even though presented a relatively linear flow pattern compared to PolyOx N80, showing a SI value at 1.03, the energy recorded for the powder to flow was at 384 mJ, which was considered high

compared to the standard PA2200, which was at 126 mJ. According to these results, it would be highly possible that Foremost 316 and PolyOx N80 may present an average particle size that is higher than the preferred one for LS, explaining the excess in energy needed for the powders to flow [69].

Eudragit L100-55 exhibited the best flowability results, showing a flow pattern better and more stable than the standard PA2200. The BFE needed for the powder to flow was 52.8 mJ, the SE was 2.48 mJ/g, SI and FRI values were at 0.96 and 1.52 respectively. These values revealed impressive flow properties with minimum cohesion for L100-55 that may be related to the presence of spherical and smooth particles showing increased packing efficiency [6], [54], [80]. In contrast, Eudragit FS100 showed high cohesive values compared to the L100-55 grade. BFE and SE presented values of 410 mJ and 259 mJ/g, respectively. As the material showed limited weight loss during TGA tests, this behaviour could be linked to particle irregularities that resulted in poor flow [76], [80], [188].

All three grades of HPC exhibited significantly high values for SE and FRI, presenting a flow pattern very sensitive to lower speed. The FRI values for HPC SL, SSL and SSL SFP were 5.12, 12.60 and 5.80, respectively, which typically correspond to materials with very cohesive characteristics [80], [129]. HPC has been characterised as a highly plastic binder material, which generally exhibits high cohesive and adhesive forces, explaining the observed poor flowability of the powder in high flow rates [3], [97], [115], [181], [189]. According to the TGA results in section 4.2, HPC presented high concentration of moisture, which in fact acted as a plasticiser for the amorphous phase of the polymer chain and increased plasticity [3], [89], [115], [163], [181], [190]. This explained the enhanced cohesion of the powder, due to condensed water on the surface of the particles that formed strong liquid bridges, inducing capillary forces between the particles, and therefore decreasing flowability [115], [163], [181], [191], [192]. The obtained SE values certified the cohesive nature of the HPC materials; 7.39, 8.85 and 14.20 mJ/g for SL, SSL and SSL SFP, respectively. It was noticed that SSL SFP grade presented a value above 10 mJ/g, which was strongly related to high cohesion and significant increase in agglomeration [80], [129]. This intense cohesive behaviour may be explained by the presence of super fine particles [76], [80], [188].

Finally, AQOAT LMP, MMP and HMP presented very unstable flow patterns in low and high flow rates, further proved by the high value of SI, which was above 2 and above 10 mJ/g for the SE. The BFE was 735.0 mJ, 472.0 mJ and 460.0 mJ for LMP, MMP and

HMP, respectively, which revealed that the powders needed excessive energy amounts in order to flow (noted that 126 mJ was for PA2200). These results indicated a low flowability and a relative cohesive nature for AQOAT. This behaviour could be related to a broad PSD consisting of fairly large particles with varying sizes and shapes for all AQOAT grades, which inhibited free flow. Moreover, the BFE for MMP and HMP grades was an order of about 300 mJ lower compared to LMP. These two powders could possibly consist of smaller particles, which was believed to perhaps filled in the voids between the larger ones, resulting in a slight increase in flow efficiency [80].

To provide an overview among the different flow properties of the excipients and assess their reliability, two additional graphs were constructed, which depicted the most influential flow variables. Figure 4.14 illustrated the BFE and SI, which were linked to the stability of the powders during flow, and Figure 4.15 illustrated the FRI in addition to the SE, which were related to cohesive characteristics.
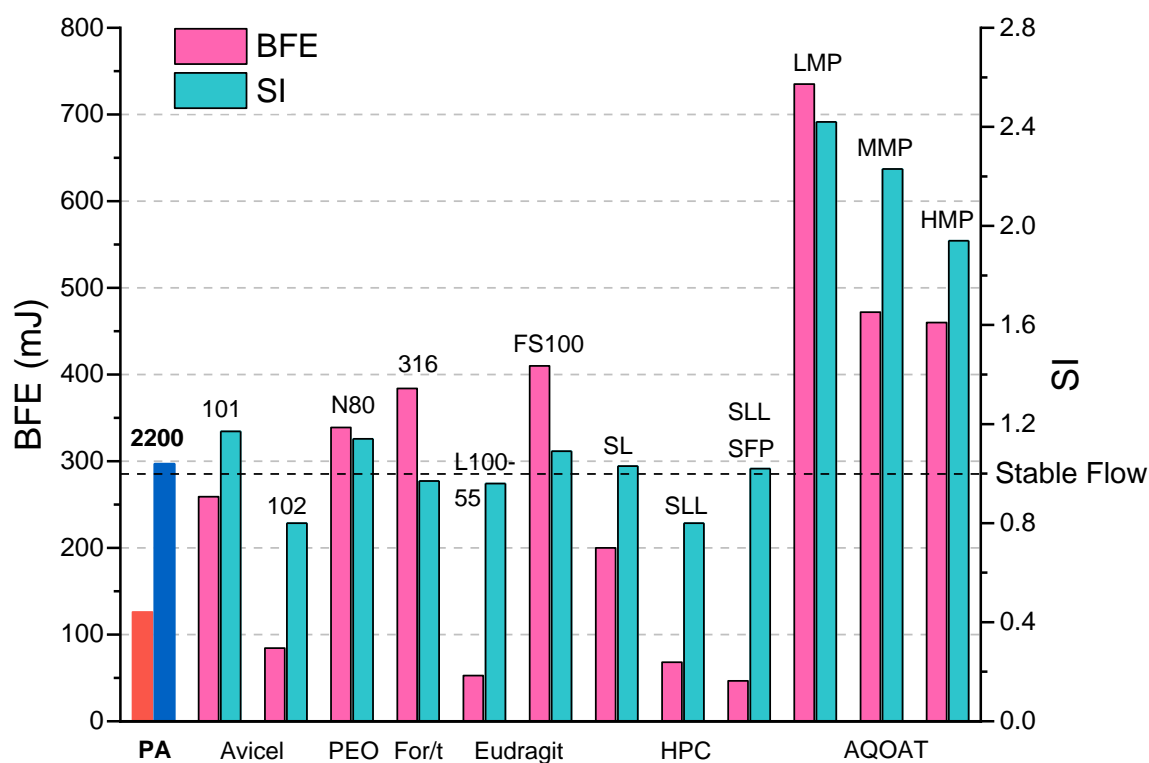
Figure 4.14: Basic Flowability Energy (BFE) and Stability Index (SI) of the excipients compared to PA2200
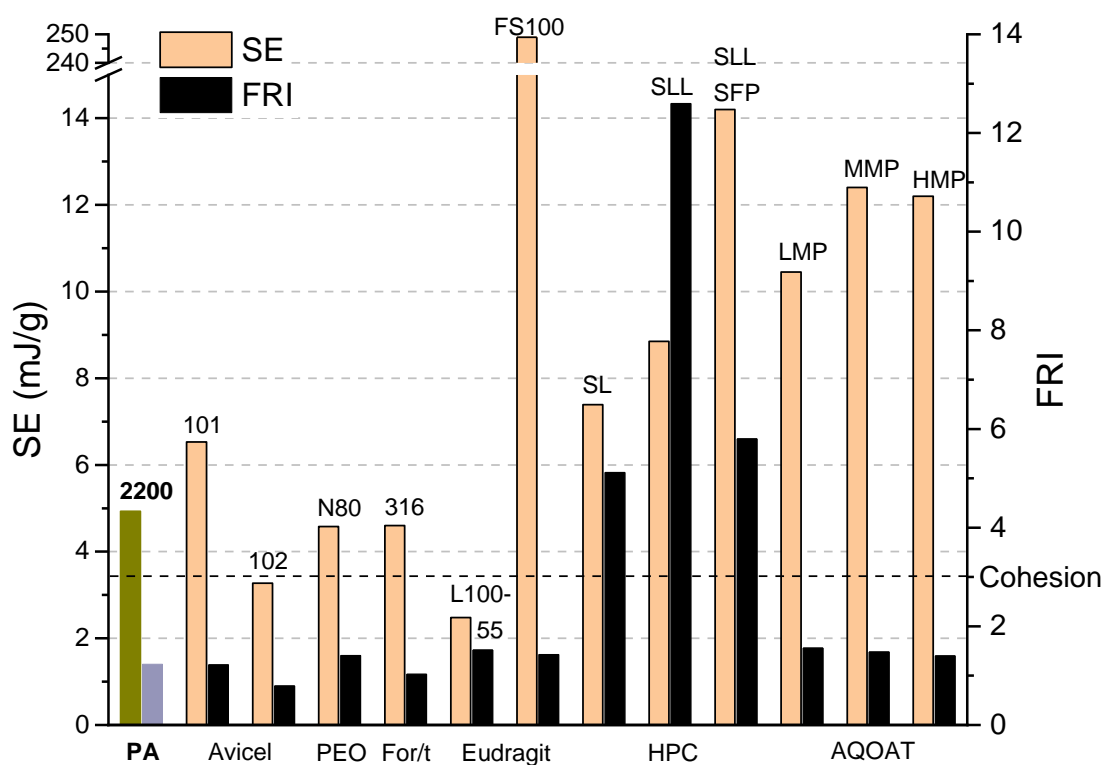
Figure 4.15: Specific Energy (SE), and Flow Rate Index (FRI) of the excipients compared to PA2200

4.4 Particle size and distribution analysis

In this section analysis of the particle size and size distribution was performed, using the methodology described in section 3.3.4. The distribution curves of the excipients are shown in Figure 4.16 to Figure 4.20, while the statistical data of the average values of D_{10}, D_{50} and D_{90} are presented in Table 4.3. According to literature, commercially available powders for LS consist of particles with a narrow PSD around 50μm or 60μm and a volumetrically small population of fine particles with sizes around 10μm [58], [76], [188]. It has been discussed in Chapter 2 that a distribution of particle sizes in the range of 45 to 90μm is generally preferable, to ensure layer thickness of 100-150μm. Therefore, to achieve the standard layer thickness and increase density, particles should approximately be half that size to provide parts with increased dimensional accuracy and good surface finish [6], [34], [54], [76], [188]. The relationship between particle size and part density is known to be proportional [57]. Large particles typically increase porosity and surface roughness, while small particles typically increase precision and part density [6], [30], [39], [57], [66], [76], [188]. However, as it was described earlier, super fine particles

could hinder free flow and consequently bring difficulties in spreading the powders onto the LS bed [57], [188].

Table 4.3: Particle size distribution of the pharmaceutical excipients tested

Sample	D_{10} (μm)	D_{50} (μm)	D_{90} (μm)	PSD (μm)
Avicel 101	22.3	70.2	171.7	149.4
Avicel 102	40.8	128.2	264.9	224.1
PolyOx N80	28.3	109.6	352.8	324.5
Foremost 316	62.0	118.0	205.0	143.0
Eudragit L100-55	18.5	50.3	97.1	78.6
Eudragit FS100	76.4	162.7	324.4	248.0
HPC SL	28.7	102.5	228.7	199.9
HPC SSL	10.8	50.9	140.1	129.3
HPC SSL SFP	3.1	16.5	35.4	32.3
AQOAT LMP	81.0	269.2	590.6	509.6
AQOAT MMP	78.3	258.6	538.4	460.1
AQOAT HMP	44.1	208.4	527.8	482.7

Avicel's 101 average particle size was at 70.2μm, which fell in the range of commercial LS powders. Avicel 102 possessed an average particle of 128.2μm, which was higher than recommended, although, previous studies have reported processing of powders with particles ranging from 100 to 150μm, achieving high quality parts [54], [76], [188]. However, Avicel 102 showed increased flowability compared to Avicel 101. PSD for both grades was relatively broad, as can be seen in Figure 4.16, with a volume of D_{10} 22.3μm to D_{90} 171.7μm for Avicel 101, and of D_{10} 40.8μm to D_{90} 264.9μm for Avicel 102. Therefore, it was obvious that PSD for Avicel 101 was broader than Avicel's 102 and also revealed a large population of smaller particles. Fine particles could have enhanced mechanical interlocking, according to other reports and resisted free flow, explaining the decreased flow efficiency of Avicel 101 [76], [80], [188]. Despite the relatively broad PSD, both the powders exhibited good flowability as described in section

4.3, which in combination to their average particle size, which fell into the acceptable range for LS, it should be expected to result in a reasonable processing behaviour.
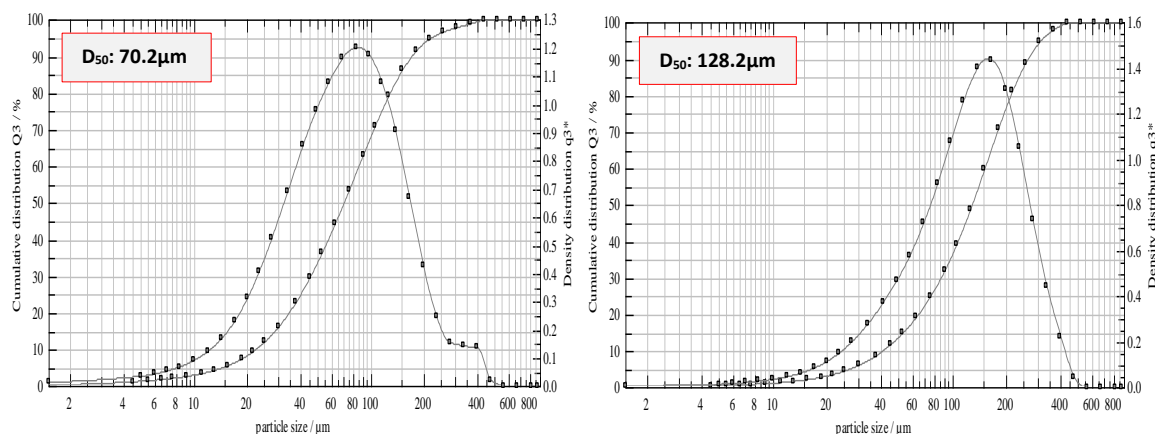
Figure 4.16: Particle size distribution of Avicel 101 (left), and 102 (right)

PolyOx N80 presented a wide PSD shown in Figure 4.17, which revealed a bulk consisting of broad varying sizes: D_{10} 28.3μm, D_{50} 109.6μm, D_{90} 352.8μm. The PSD curve showed high fractions of particles larger than 200μm. These results correlated well with the relative unstable flow pattern of PolyOx N80 that was presented earlier in section 4.3, explaining the high BFE [69]. Furthermore, the lowest 10% of the bulk volume consisted of small particles, however, given the numbers for FRI and SE, the flow properties of the powder showed low cohesion. Smaller particles more likely acted like fillers/additives, which filled in the voids between the larger particles and resulted in more compact formations than expected [6], [76], [80], [188], further explaining the stable value of SI, considering that the PSD of PolyOx N80 was fairly broad.

In a similar way, Foremost 316 distribution curve had a broad shape, presenting particles with an average diameter of 118μm, higher than the preferred one for LS, and the highest 10% of the volume of the population above 205μm (Figure 4.17). As a result, the powder required higher energy in order to flow, as discussed in section 4.3. However, it exhibited a rather stable flow pattern, and therefore, Foremost 316, would perhaps be spread evenly on the LS powder bed. Although, it should be taken into account that the large amount of bigger particles present in the PSD curve, would possibly increase porosity and surface roughness of the sintered parts [30], [34], [38], [57], [76], [188].
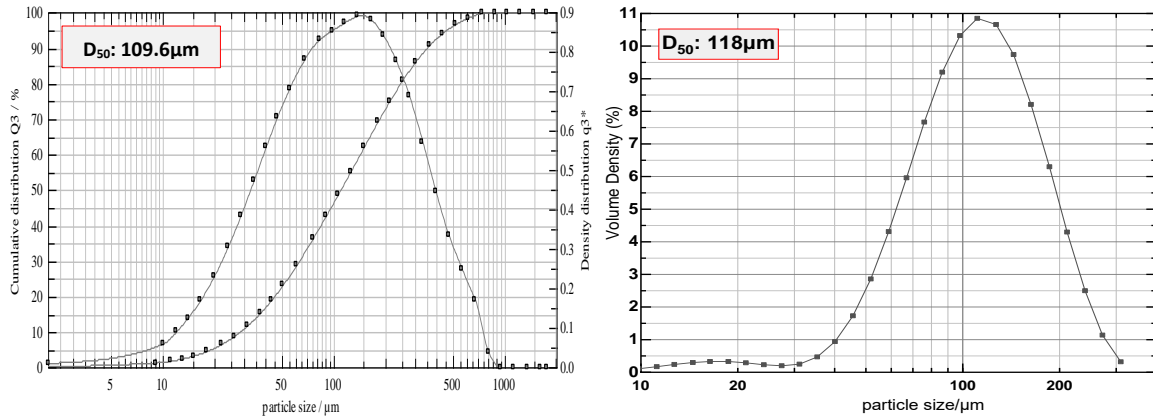
Figure 4.17: Particle size distribution of PolyOx N80 (left), and Foremost 316 (right)

PSD results for Eudragit L100-55 were very close to the PA2200 standard LS material. The powder exhibited the narrowest distribution of 78.6μm (Figure 4.18), which aligned well to the PSD of commercially available materials. The volume of the particles' sizes was D_{10} 18.5μm, D_{50} 50.3μm, and D_{90} 97.1μm, which revealed an ideal average particle size, as well as the presence of a favourable small fraction of fine particles. This was not surprising, considering the enhanced flow efficiency of the L100-55 described earlier in section 4.3. On the other hand, statistical data for the FS100 grade, presented an average particle size of 162.7μm and a large amount of particles above 300μm that resulted in a least preferred broad PSD. This result explained the unstable flow pattern of the powder observed in the previous section. Furthermore, the powder exhibited high cohesive behaviour, which could have implied the presence of small particles [76], [188], however, the lower 10% of the volume of the particles was at 76.4μm. The cohesion of FS100 at this point, was expected to be related to shape irregularities of the particles, as was briefly described in section 4.3.
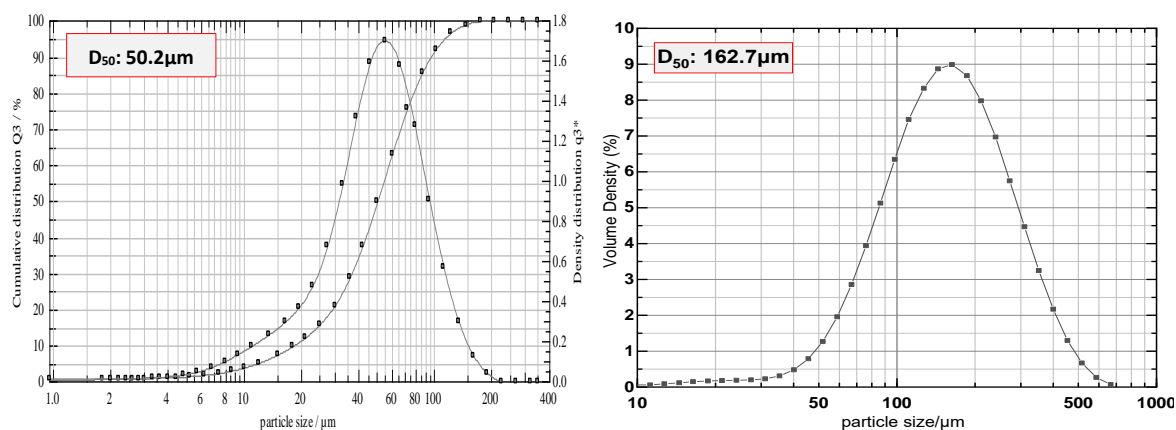
Figure 4.18: Particle size distribution of Eudragit L100-55 (left), and FS100 (right)

HPC grades presented differences regarding their PSD. Particle sizes for the SL were at lowest volume of 10% at 28.7μm, an average size at 102.5μm, and highest volume of 90% at 228.7μm. In Figure 4.19 it was observed that the PSD of the powder was quite broad, which was not favourable. The SSL grade presented a decrease in the particle size, with D_{10} 10.8μm, D_{50} 50.9μm and D_{90} 140.1μm, and a less broad PSD curve. The SSL SFP grade exhibited a significant decrease in the particle diameter, with average sizes at 3.1μm for D_{10} volume, 16.5μm for D_{50}, and 35.4μm for D_{90}, which resulted in a quite narrow PSD of 32.3μm. The particle characteristics of the three powders would be expected to have completely different packing behaviour based on the statistical data, and hence varied flowability. On the contrary, the flow pattern of the powders was very similar and exhibited dominant cohesive characteristics, as described in section 4.3. This behaviour was explained through the PSD curves that revealed half the population of the powders was consisted of small and fine particles, which is known to increase inter-particle adhesive forces and therefore increase the packing density [6], [54], [76], [80], [81]. It has been outlined in other reports that the smaller the size of the particles the larger the specific surface area, which introduced van der Waals interactions and forced the particles to pack in bigger formations to reduce surface energy [6], [30], [54], [76], [80], [188]. The ability of small/fine particles to pack tight to each other eventually led to the formation of agglomerates due to friction, and enhanced the cohesive behaviour of the HPC powders, especially SSL SFP. The SSL SFP grade presented a value above 10 mJ/g for SE, which strongly indicated high cohesion related to significant increase in agglomeration [80], [129]. This intense cohesive behaviour was explained through the narrowest PSD consisting of particles with sizes of 3 - 35μm. Although, the positive effect

86

of fine particles described above to fill in the gaps between the large particles, as was observed in the case of Eudragit L100-55, in this case the powder consisted exclusively of super fine particles [76], [80], [188].
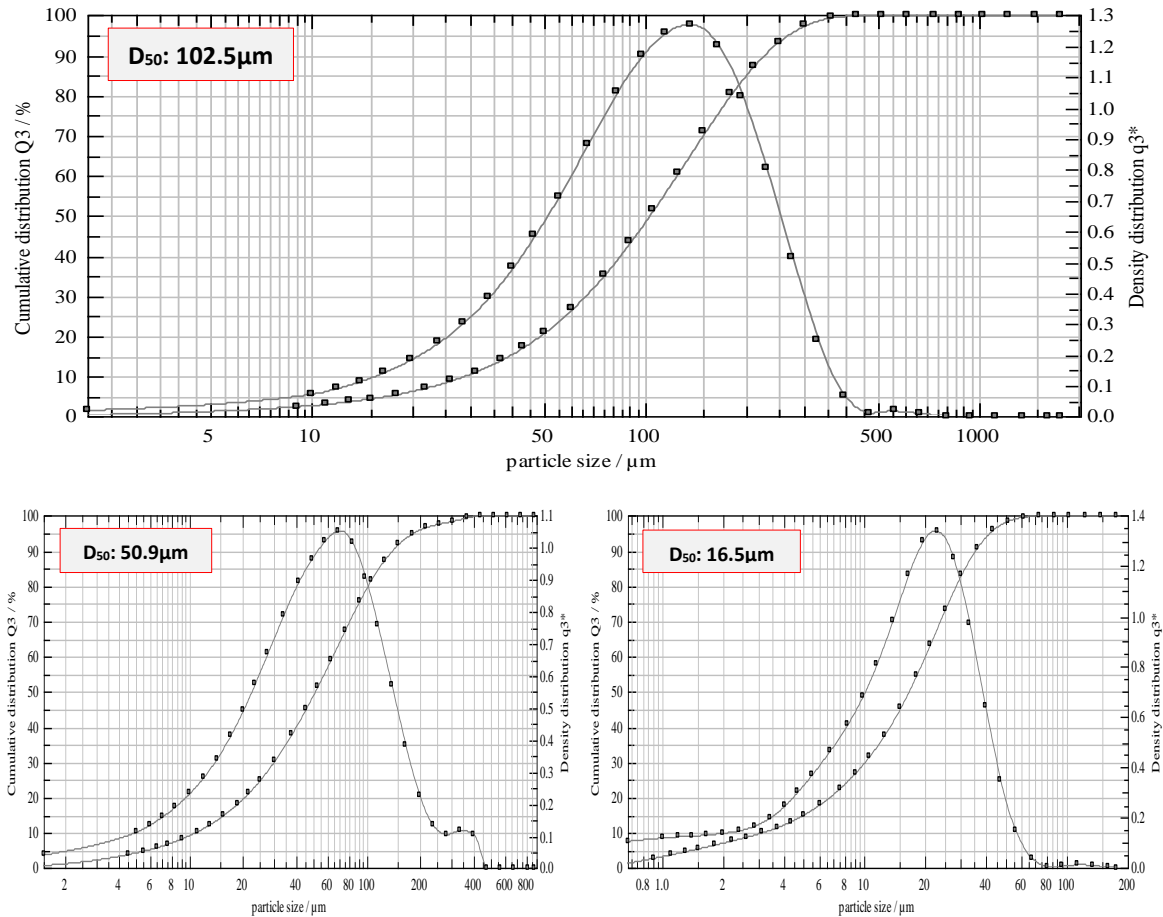
Figure 4.19: Particle size distribution of HPC SL (top), SSL (bottom left), and SSL SFP (bottom right)

The D_{50} for the AQOAT grades was 269.2μm, 258.6μm and 208.4μm, for LMP, MMP and HMP, respectively. Furthermore, the highest 10% of the volume of the particles was at 590.6μm, 538.4μm and 527.8μm, which resulted in an extended PSD for all three grades, as can be seen in Figure 4.20. The AQOAT powders predominantly consisted of larger particles, which explained the significant poor flowability properties described earlier in section 4.3. Most of the population of the particles fell far above the acceptable diameter range for LS materials and it exceeded the limit of the standard layer thickness of 100-150μm [6], [34], [54], [76], [188]. AQOAT powders consisted of very large particles that would affect the spreading by the blade and most likely inhibit the

deposition of homogeneous layers on the LS platform increasing the voids in the powder bed volume and eventually leading to increased porosity and surface roughness [6], [30], [38], [53], [57], [66], [76], [188].
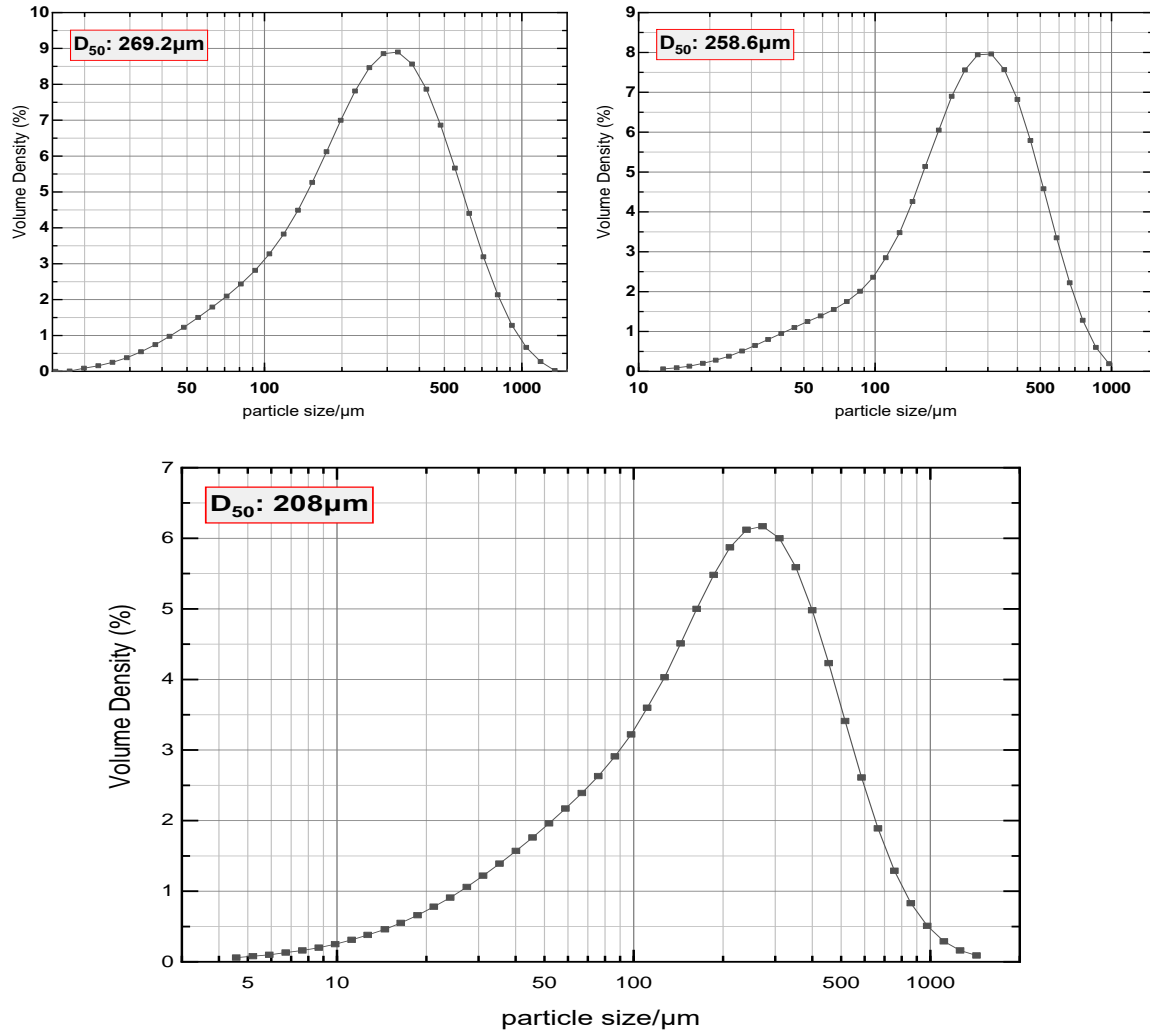
Figure 4.20: Particle size distribution of AQOAT LMP (top left), MMP (top right), and HMP (bottom)

4.5 Particle shape and morphology analysis

In this section the morphology of the particles was examined thoroughly, as the importance of the particles shape and surface characteristics in LS has already been demonstrated in Chapter 2, and could directly influence the performance of the process, in terms of spreading, precision, density, and consequently, the mechanical behaviour of the sintered parts [6], [30], [34], [38], [39], [53], [54], [57], [58], [66], [76], [81]. For the

analysis, 50x, 100x and 500x resolution SEM pictures were captured to investigate the shape variations of the bulk of the particles and the surface texture characteristics. Particle images of all the excipients are displayed in Figure 4.21 to Figure 4.25.
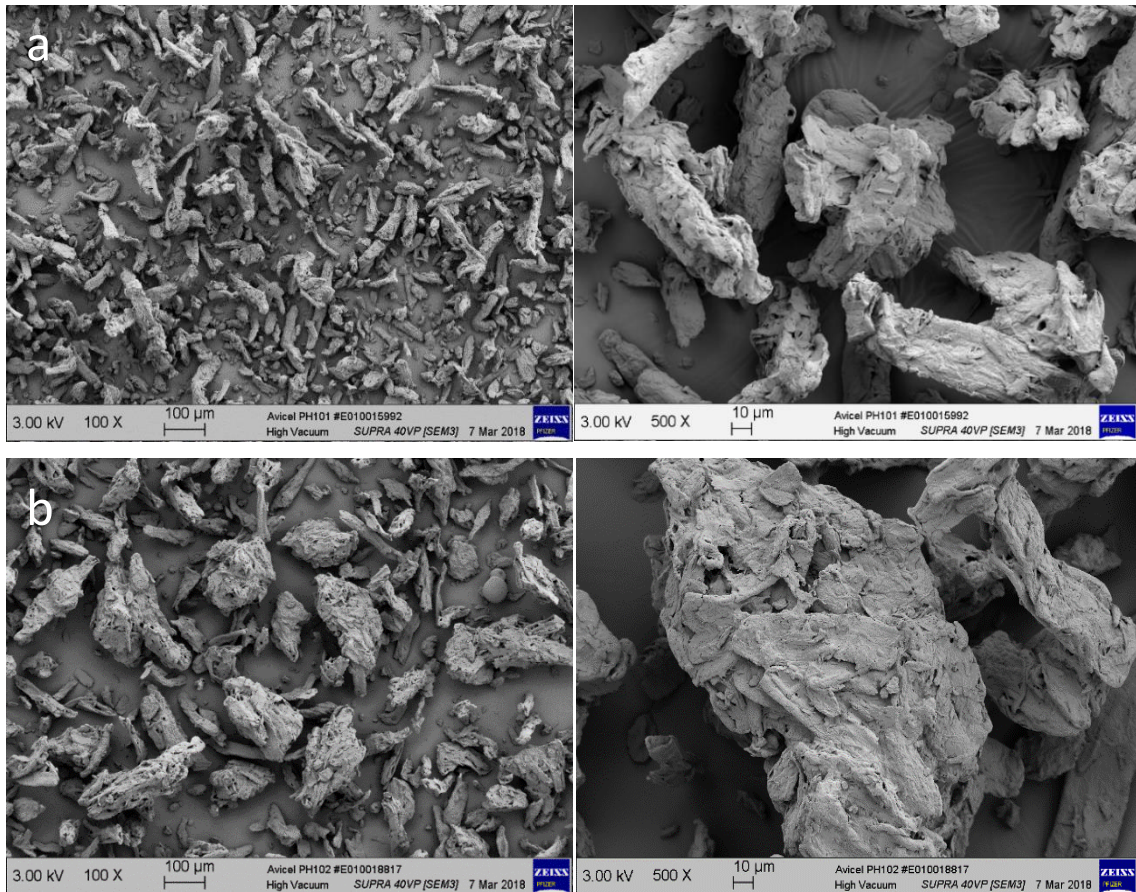
Figure 4.21: SEM images in 100x, 500x magnification representing the particle morphology of a) Avicel 101, and b) Avicel 102

SEM images revealed similarities regarding the particle shape of Avicel grades, as shown in Figure 4.21 above. Particles consisted of both fibrous and elongated shapes with asymmetrical porous surface texture [93], [99], [159]. Particles of Avicel 102 were longer and thicker than those of Avicel 101. In addition, smaller particles could clearly be detected in the Avicel 101 bulk powder, aligned with the PSD results in the previous section that revealed a smaller average diameter and the presence of fine particles. Although, it has been highlighted that irregular and edgy particles have the tendency to interlock to each other, both the Avicel grades exhibited good flowability. Similar behaviour has been described in other reports, where it was demonstrated that irregular particles with wider PSD, could perfectly be used in LS, as long as the distribution and

the average particle size are tuned to achieve high density and prevent agglomeration [54], [188].
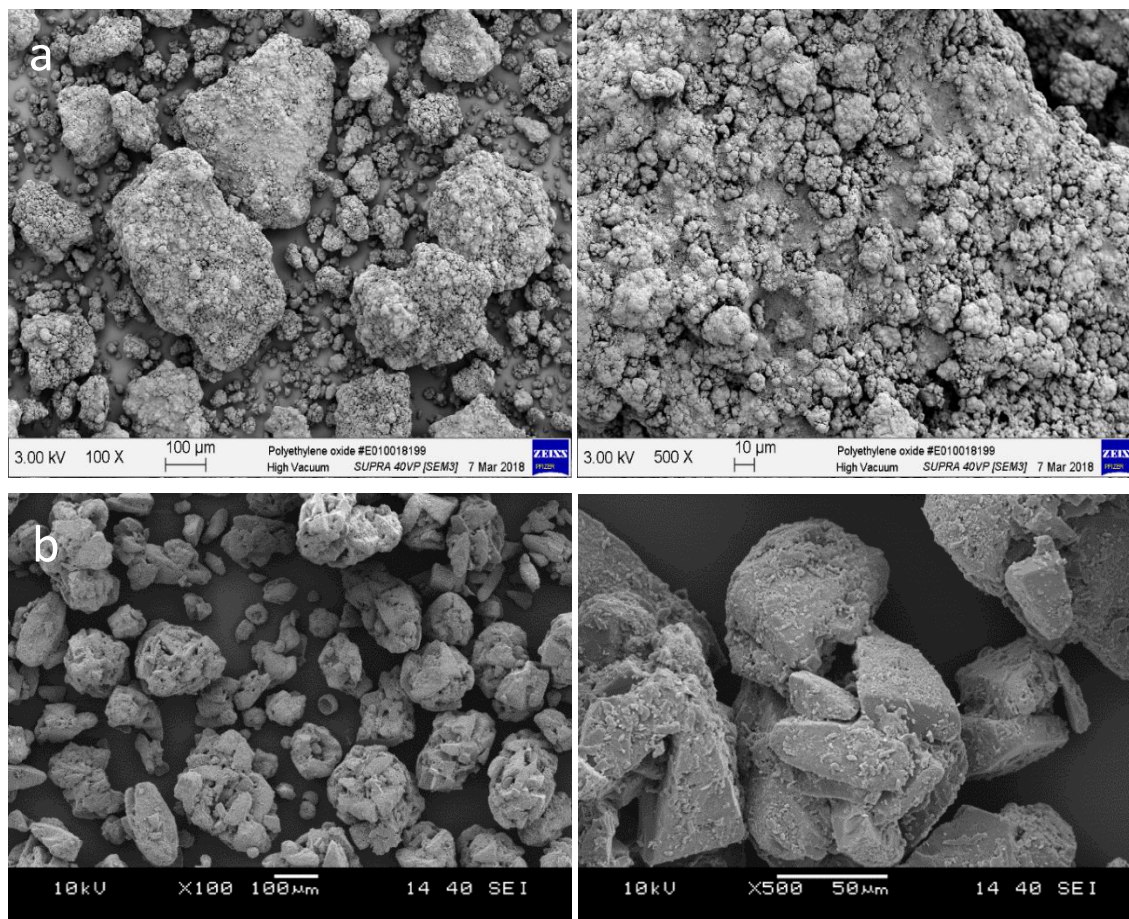
Figure 4.22: SEM images in 100x, 500x magnification representing the particle morphology of a) PolyOx N80, and b) Foremost 316

PolyOx N80 presented particles of varying shapes and sizes that can be observed in Figure 4.22 above. SEM revealed a cauliflower surface texture that introduced irregularities, such as lumps [109], [168]. Moreover, particles seemed to have a very large or very small diameter, which correlated well with the PSD analysis in section 4.4, explaining further the relatively unstable flow properties.

As Foremost 316 showed resemblance in flowability and PSD results to PolyOx N80, it made it interesting to put together the SEM images of the two materials, in Figure 4.22. In fact, the bulk powder of Foremost 316 appeared to consist of cauliflower-shaped particles in a range of different sizes and the surface of the particles displayed irregularities in the form of flakes and short fibrils.

Both the powders consisted of non-spherical particles, however presented relatively small shape angularity, which suggested to prevent mechanical interlocking. Indeed, it was considered in section 4.4 that the population of small particles present in both powders, had positively contributed to their packing efficiency. Existing materials for LS present similar structures with high irregularities according to other reports [54], [76], [80], [81], [188], [191]. However, it has been outlined that a large amount of bigger particles, which has been already detected in these powders, could potentially introduce layer defects [30], [34], [38], [57], [81].
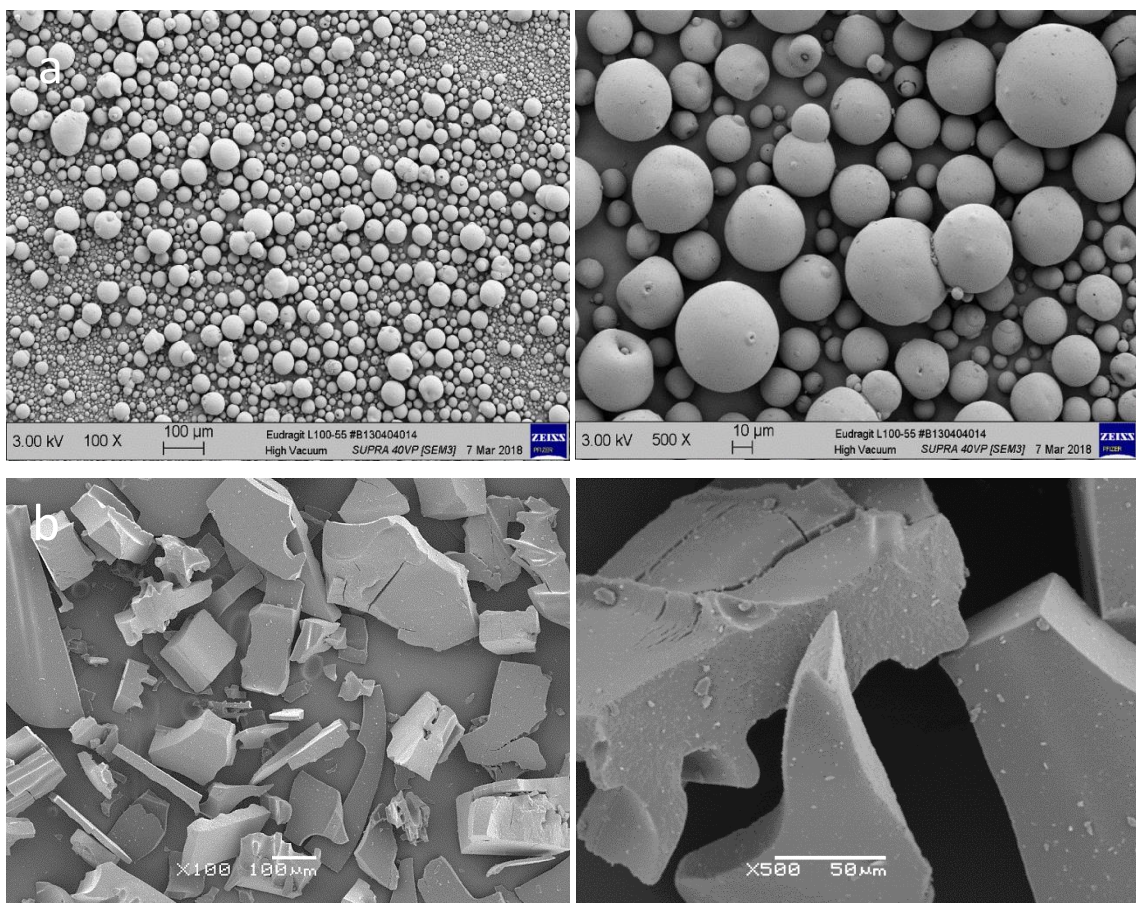
Figure 4.23: SEM images in 100x, 500x magnification representing the particle morphology of a) Eudragit L100-55, and b) Eudragit FS100

Figure 4.23 demonstrated the particle and surface morphology of Eudragit grades. SEM for the L100-55, portrayed images of round particles with ideal sphericity and very smooth surface texture, indicating the use of co-extrusion processes for the preparation of this powder [6], [34], [58]. Spherical and smooth particles increased the packing efficiency and hence, the flowability of the powder as was observed in section 4.3 [6],

[54], [80]. This smooth surface morphology allowed particles to roll over one another ensuring minimal contact, which reduced friction forces and subsequently the resistance to flow [54], [76], [81], [188]. In contrast, FS100 grade presented a large diversity in shapes and sizes. SEM revealed that the bulk powder consisted entirely from angular edged particles in random formations with cracked surface morphology, presumably resulting from a cryogenic milling step [54], [58], [76], [80]. The rough texture of the particles was connected to their natural orientation to interlock; high irregularities enhanced the particle mechanical interlocking and inter-particulate friction forces resulting in poor flow, as has been already demonstrated in sections 4.3 and 4.4 [76], [80], [188]. The sharp edges hooked on to each other and twisted together increasing intramolecular shear stresses that led to high cohesion, and prevented FS100 to flow [6], [80], [81], [188].

SEM images for HPC in Figure 4.24, revealed the same type of particles for all three grades, which consisted of both irregular and elongated shaped particles with relative fluffy surface morphology [115]. When comparing the three grades, it was obvious that the SL presented the larger average particle diameter, while the SSL SFP consisted entirely of fine particles, which agreed with the size distribution results in section 4.4. Furthermore, SEM analysis confirmed the presence of a large amount of fine particles in the bulk of the SL and SSL powder, which was connected to their cohesive behaviour similar to that of SSL SFP, as was observed in section 4.3. It was obvious through the SEM images that the three HPC powders presented a large specific surface area due to the relatively small average particle diameter, which in fact, resulted in extended van der Waals adhesive forces between the contacting particles. These interactions most likely were enhanced by the elongated shape of the particles and therefore, dominated within the bulk of the powders leading to the macroscopic poor flow behaviour of HPC [54], [76], [80], [81], [188], [191].
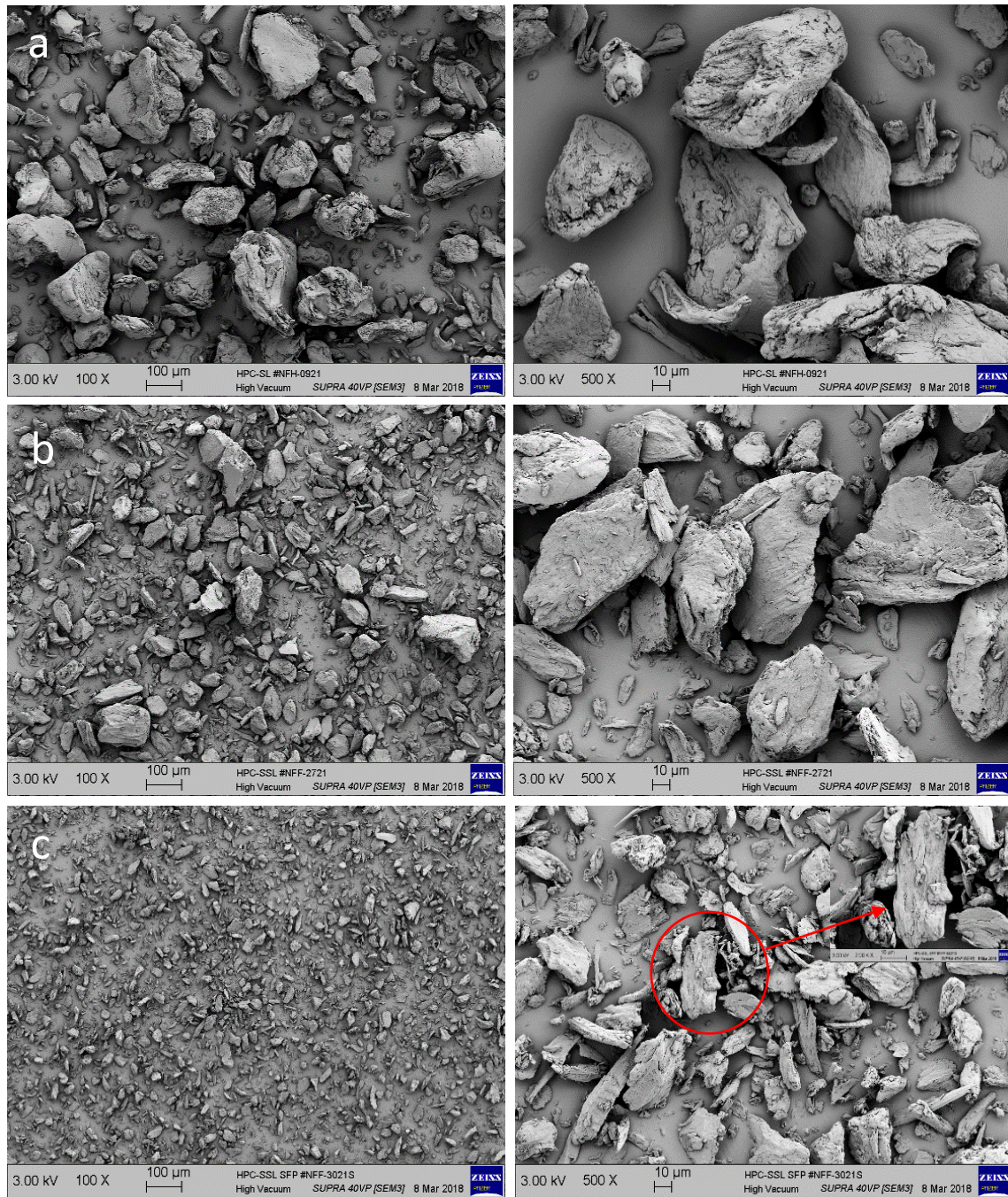
Figure 4.24: SEM images in 100x, 500x magnification representing the particle morphology of a) HPC SL, b) HPC SSL, and c) HPC SSL SFP

The particle morphology for all AQOAT powders was similar, based on the SEM analysis in Figure 4.25. AQOAT featured large rough and irregular particles with asymmetrical porous surface. Particles appeared in a variety of shapes and sizes, mainly cylindrical-shaped, with traces of near-ellipsoidal shapes and sharp fibrils [193]. LMP and MMP grades exhibited fairly the same particle diameter range, while HMP presented a slight decrease in particle size. The results were aligned to the PSD analysis in the previous

section, which also revealed that the majority of the population in AQOAT was primarily consisted of particles above the maximum acceptable range of diameter for LS powders. Essentially, these large irregular particles formed a loose bulk packing with trapped air and voids, which induced the free flow of the powders, and were responsible for the unstable flow patterns presented in section 4.3 [38], [53], [76], [81].
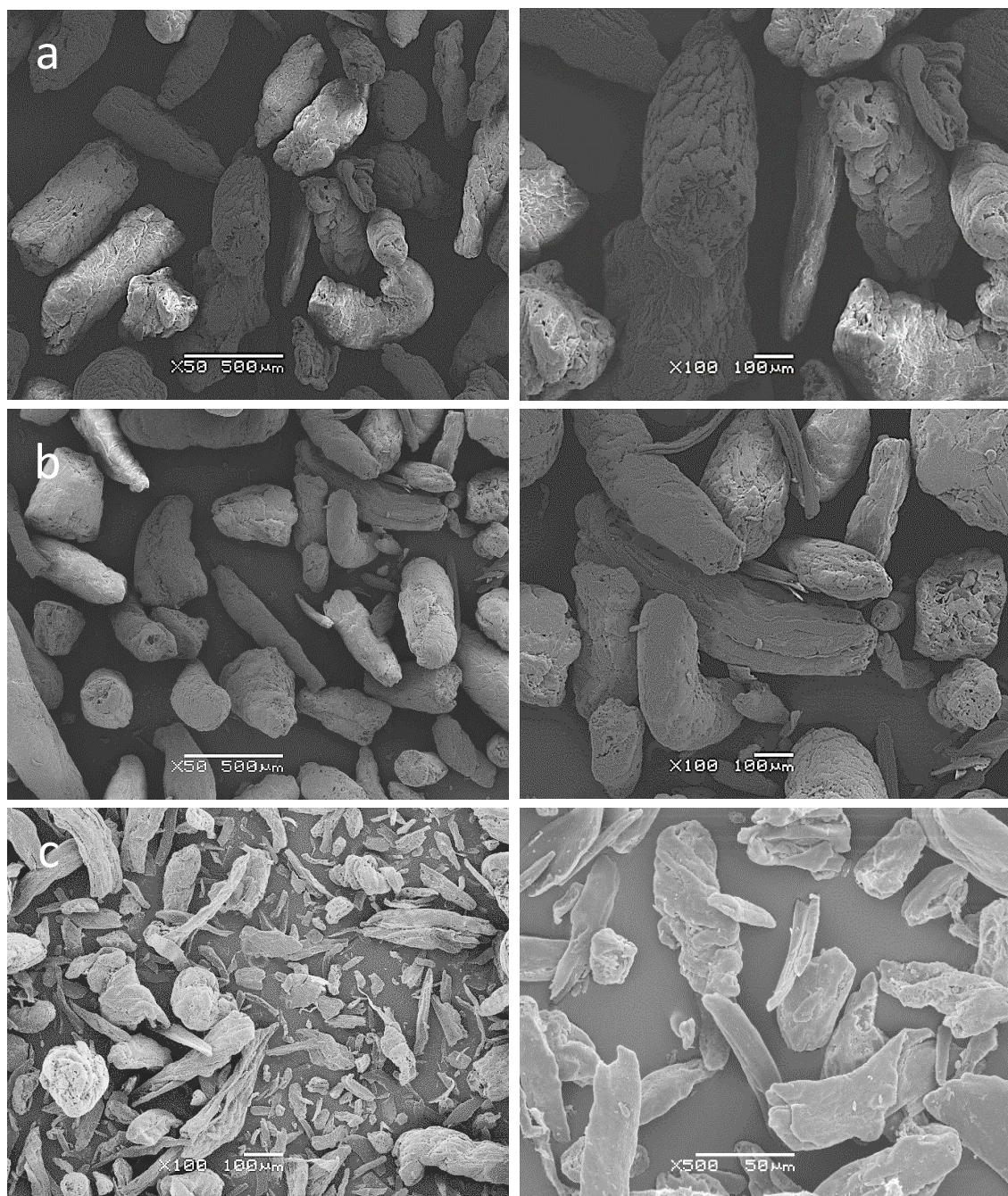
Figure 4.25: SEM images in 50x, 100x and 500x magnification representing the particles morphology of a) AQOAT LMP, b) AQOAT MMP, and c) AQOAT HMP

4.6   Summary

The most influential material characteristics related to the LS process were extensively investigated in this chapter. Each powder was analysed thoroughly, providing important information that contributed to the final selection of materials for processing. Specifically, DSC measurements allowed the identification of the thermal transitions and molecular structure of the excipients, for the specification and control of the processing parameters to achieve the optimum sintering result. Further thermal analysis through TGA measurements monitored the moisture levels and degradation kinetics, which set the limits of a safe sintering region. Powder flowability measurements using FT4 predicted the behaviour of the powders during spreading on the bed platform, which directly related to the application of thin homogeneous layers. SEM and particle size distribution analysis revealed the type and morphology of the particles that were related to the packing efficiency of the powders, influencing the part density.

The analysis revealed that the level of crystallinity of the polymers that allowed complete melting transitions in the P100 processing window, is desirable to achieve full consolidation. Furthermore, it was described that high flowability is preferable for uniform spreading. In parallel, it was discovered that the particle morphology strongly influenced the packing efficiency, which directly impacted on the flowability. Based on these observations, a basic comparison was made between the different materials tested, and is presented in Table 4.4, outlining the reasons for material selection in the next steps of this PhD.

Table 4.4: Suitability of the pharmaceutical excipients with LS

	Crystallinity	$T_m/T_g < 182°C$	Round Particle	PSD	Good Flow
Nylon 12	✓	✓	✓	✓	✓
Avicel 101	✓	✗	✗	✓	—
Avicel 102	✓	✗	✗	✗	✓
Foremost 316	✓	✗	—	✓	—
PolyOx N80	✓	✓	—	✗	—
Eudragit 100-55	✗	✓	✓	✓	✓
Eudragit FS100	—	✓	✗	✗	✗
HPC SL	✗	✓	✗	✗	✗
HPC SSL	✗	✓	✗	✓	✗
HPC SSL-SFP	✗	✓	✗	—	✗
HPMC-AS LMP	✗	✓	✗	✗	✗
HPMC-AS MMP	✗	✓	✗	✗	✗
HPMC-AS HMP	✗	✓	✗	✗	✗

Table 4.4 shows that all the materials presented incompatibilities, however some of the excipients hold a set of properties that could be processed with the right combination of LS parameters. Avicel 101 and Avicel 102 presented high crystallinity and flowability, which is favourable for LS. However Avicel 101 presented a better particle size distribution and was chosen over Avicel 102. Similarly, Foremost 316 and PolyOx N80 exhibited high crystallinity, relatively good flowability and an almost round particle. On the other hand, the Eudragits were amorphous, however the L100-55 possessed and ideal particle morphology with an excellent flowability, compared to the FS100. Similarly, HPC SSL was chosen over other HPC grades for its desired average particle size and narrow distribution, favourable for LS. Finally, HPMC-AS grades presented important incompatibilities that made them unsuitable for LS.

CHAPTER 5   LASER SINTERING OF PHARMACEUTICAL INGREDIENTS

5.1   Introduction

In Chapter 2 LS was introduced and the fact that it uses laser light to selectively fuse polymer powder particles together to create parts layer by layer [6], [7], [64], [66], [67], [76], therefore, any polymer in powder form should be able to be processed using LS. However, as mentioned previously, the limited availability in commercial polymers has proven that this is not so simple [6], [72]. It was demonstrated in the previous chapter that LS materials should melt or soften to achieve coalescence of the particles towards the formation of layers when the laser scans over the powder. In addition, the particle size and morphology should enhance the free flow of the powder for the application of homogeneous layers, to achieve maximum densification and thus, enhance microstructural features within the part. The decision on materials for the next step of this study was based on these findings. Specifically, Avicel 101 and Foremost 316 were selected for their semi-crystalline properties, since they exhibited clear melting transitions, and presented an acceptable particle size distribution for LS and relatively good flowability. PolyOx N80 presented a low and sharp melting point, which is favourable for LS, and further consisted of relatively round particles. Finally, Eudragit L100-55 and HPC SSL demonstrated amorphous characteristics, however they were chosen for their ideal particle size distribution. Furthermore, these materials are fillers, binders and coating agents, which can be used to formulate a mixture of ingredients for the development of oral solid dosage forms that may present a tailored release profile.

Although the selected excipients demonstrated characteristics that are compatible with LS, they also presented incompatibilities. However, it was discussed in Chapter 2 that during LS the process parameters can be adjusted according to the material characteristics in order to optimise the sintering conditions and potentially increase densification and mechanical response of the printed parts [6], [39], [52], [66], [69], [194]. Therefore, in this chapter, research focuses on processing the selected materials in order to gain a full understanding of the key material properties and their link to key process parameters, needed for sintering pharmaceuticals. Specifically, this work aimed to connect the observations made in Chapter 4 with in-process laser sintering, to study the influence of

the exposure parameters on the material properties and their effect on the final performance of the parts. The development of optimised sintering conditions was attempted for each of the excipients to ensure the production of uniform solid parts through a stable sintering route.

5.2 Processing of Avicel 101

Avicel 101 presented an average particle size of 70.22μm and a stable flow pattern, as described in Chapter 4. Despite the non-spherical particle shape found, the packing efficiency of the powder allowed the homogenous spreading of layers on the bed platform, as can be seen in Figure 5.1. The powder was evenly spread by the blade at room temperature and also at 170°C, which was the maximum chamber temperature reached before the sintering process begun. The bed temperature was set at 182°C, the maximum operating temperature of the P100, which was the closest possible to the melting point of Avicel 101, found at 254°C in section 4.2. Ideally the material should heat up close to the T_m to develop low viscosity and facilitate consolidation of the particles. However, the T_g was found to occur at 106.96°C, which indicated the powder would go through its glass transition and soften during the preheating step at 170°C. The decreased viscosity of the polymer in combination with the right scanning strategy aimed to result in partial consolidation [6], [7], [52], [53].

Figure 5.1: Homogeneous spreading of Avicel 101 powder at 25°C (left) and 170°C (right)

Considering that the bed temperature was relatively low to melt Avicel 101, sintering started in single scan mode and high ED rate, using laser power of 21W in order to induce particle fusion. The powder showed no evidence of consolidation and furthermore, fuming was observed upon the application of the laser beam, which led to the change of colour from white to brown, indicating degradation of the polymer. For the next set of tests the laser power was kept lower from 6W to 15W to avoid degradation, however it was observed that the powder was still brownish, except only at the lowest power applied, and resulted in zero fusion. At this point double scan mode was applied in order to increase the energy input transferred to the powder. A number of different sets of parameters, varying the laser power and scan speed, were used in an attempt to reduce the fuming and degradation observed, and induce fusion. The rest of laser parameters were kept at the standard values following the manufacturer's guide. A map of the scanning strategy for Avicel 101 was produced (Figure 5.2). The laser parameters used for all the tests are presented in Table 5.1 and Table 5.2. A summary of the observations during sintering of Avicel 101 under double scan mode, is listed below:

- The laser power was varied from 4W to 7W and the scan speed was set at 2000mm/s and 2500mm/s aimed to explore a range of ED that could potentially sinter the powder. The results showed no evidence of particle fusion; meanwhile there was fuming and clear degradation of the material as it turned brown.

- A decrease of the total ED was attempted in the next tests to prevent material degradation. Laser powder varied from 3W to 6W and scan speed from 3000mm/s to 4500mm/s. No fuming and material degradation were observed, however the scanning strategy did not result in powder consolidation.

- Increase of the ED was applied during the final trials. Scan speed was set at 1500mm/s and 1800mm/s as laser power was kept at 3-6W. The powder caked severely, which is presented in Figure 5.3, resulting in fuming and deterioration. There was no evidence of layer formation or consolidation of the powder.

Sintering of Avicel 101 using the P100 was not possible. It was clear that the window of the energy input applied was very narrow to avoid degradation of the material. This behaviour limited the options to explore a path of fusing the powder and eventually sinter Avicel 101. Unsuccessful sintering was related to the dehydration of the polymer. It was demonstrated in section 4.2 that Avicel 101 contained high moisture content of 4% of the

total mass, which was progressively reduced up to 150°C. When the material was processed at 182°C the water was eliminated, forming solid bridges between the particles. The fact that the laser raised further the temperature locally over the scanned area, resulted in caking of the bridges that was eventually linked to the severe degradation of the powder [3], [7], [48], [55], [68], [135], [164].

Table 5.1: Process parameters investigated for sintering tests of Avicel 101

Process Parameters	Constant	Varied	
Layer thickness	0.10 mm		
Bed temperature	182°C ($T_m = 254$°C)		
Hatching power		3 - 21 W	
Scan speed		1500 - 4500 mm/s	
Contour power / speed		- (0-2) W lower than hatching power - (0-500) mm/s lower than scanning speed	
Hatching distance	0.25 mm		
Beam offset	0.15 mm		
Scan pattern		Single	Double

Table 5.2: Detailed scanning strategy for sintering Avicel 101

Test / material	Sample	Layer Scan	Hatching P (W)	Hatching S (mm/s)	Contour P	Contour S	PC P	PC S	Comments
Test 1 Avicel 101	A		21	1500	21	2500	21	2500	• Fumes everywhere • Too much power • Powder turned brown
	B			2000					
	C			2500					
	D			3000					
Test 2 Avicel 101	A		6	2000	5	1500	5	1500	• No sintering • Except A the rest fumed and turned brown
	B		9		8		8		
	C		12		10		10		
	D		15		13		13		
	A1		6	2500	5	2000	5	2000	• Less fuming due to higher speed but the powder turned brown and did not melt • Powder in the whole chamber turned yellow due to degradation
	B1		9		8		8		
	C1		12		10		10		
	D1		15		13		13		

Test	Sample								Notes
Test 3 Avicel 101	A		4	2000	3	1500	3	1500	• No sintering • Cs and Ds fumed and turned brown
	B		5		4		4		
	C		6		5		5		
	D		7		5		5		
	A1		4	2500	3	2000	3	2000	
	B1		5		4		4		
	C1		6		5		5		
	D1		7		5		5		
Test 4 Avicel 101	A		3	4000	3	3500	3	3500	• No sintering • No fuming • Scanning was not visible, speed was too high
	B		4		4		4		
	C		5		5		5		
	D		6		5		5		
	A1		3	4500	3	4000	3	4000	
	B1		4		4		4		
	C1		5		5		5		
	D1		6		5		5		
Test 5 Avicel 101	A		3	3000	3	2500	3	2500	• No sintering • Scanning was not visible • Powder remained white
	B		4		4		4		
	C		5		5		5		
	D		6		5		5		
	A1		3	3500	3	3000	3	3000	
	B1		4		4		4		
	C1		5		5		5		
	D		6		5		5		
Test 6 Avicel 101	A		3	1500	3	1500	3	1500	• Fuming • No sintering • All turned brown, mostly D • Powder in the chamber turned dark yellow due to degradation
	B		4		4		4		
	C		5		5		5		
	D		6		6		6		
	A1		3	1800	3	1800	3	1800	• No sintering • Higher speed resulted in light brown colour • Powder in the chamber turned dark yellow due to degradation
	B1		4		4		4		
	C1		5		5		5		
	D1		6		6		6		

Figure 5.2: Processing map of Avicel 101; plot power against speed; constant parameters: bed temperature 182°C, layer thickness 0.10mm, hatching distance 0.25mm, beam offset 0.15mm

Figure 5.3: Double scanning in Test 6 at low speed resulted in fuming and degradation of Avicel 101

5.3   Processing of Foremost 316

Foremost 316 presented an average particle size of 118μm with surface irregularities that was believed to result in a relative unstable flow pattern, as discussed in Chapter 4. The poor flowability of the material limited the ability of spreading evenly the powder on the bed platform. Foremost 316 has been considered as a temperature-sensitive lactose sugar, which features stickiness and caking problems due to the moisture content of the powder, and has been broadly described in other reports [89], [184], [195]–[200]. In Figure 5.4 it can be observed that the powder compacted in bigger lumps at 70°C and resulted in very poor spreading. The cohesive behaviour of Foremost 316 observed, was overlooked in the previous chapter. Based on the TGA analysis in section 4.2, the material presented loss of surface water up to 130°C. It has been described in literature that the high moisture content of the material promoted the formation of a porous network in the structure of the polymer [120], [195]–[199], [201], [202]. Therefore, it was further believed that as the temperature was increased in the chamber, the number of pores formed from the water molecules decreased, leading to the formation of solid bridges between the particles. Consequently, the stickiness of the powder was enhanced, resulting in compaction at elevated temperatures as observed during the spreading tests [163], [192], [195]–[197], [199].

In order to improve the processability of Foremost 316 a common pharmaceutical lubricant was added to prevent the stickiness of the powder. Glyceryl dibehenate is a fatty acid widely used in pharmaceutical industry to improve the powder flow by reducing the inter-particle friction and thus, the wear resistance. The additive was known to be compatible with Foremost 316 in an optimum concentration range of 1-3% (w/w), without any detected compromise of the mechanical performance of the powder. Therefore, 2% of glyceryl dibehenate was blended with Foremost 316 for 15 min, using a conventional tumbling mixer [89], [197], [200], [201]. The mixed powder was subjected to spreading tests up to 150°C to investigate the resulted flow efficiency. Figure 5.5 demonstrates the improvement in the flowability of Foremost 316 by the addition of the flow-aid glyceryl dibehenate, showing the homogeneous application of the excipient by the blade on the bed platform.

Figure 5.4: Formation of lumps of Foremost 316 powder during spreading at 50°C (left) and 70°C (right)

Figure 5.5: Demonstration of improved flow of Foremost 316 powder at 120°C (left) and 150°C (right) by the addition of 2% of Glyceryl Dibehenate

The scanning strategy of Foremost 316 was structured based on the observations made when sintering Avicel 101, as it was expected to behave similarly, having a melting point at 219°C. Therefore, the bed temperature was set at 182°C, at the operating maximum of the P100, in order to be at the closest possible to the T_m of the material. The powder was observed to spread evenly at 170°C during the preheating step, prior to sintering. Double scanning mode was applied to increase the heat transferred to the powder and facilitate coalescence between the particles, under lower temperature conditions than the ones needed to melt. Laser power was the only parameter varied as a starting point, to identify a possible fusion space for the powder in a range of ED. Five, 10, 15 and 20W were chosen, keeping the rest of the parameters constant at default values, all presented in Table 5.3. A summary of the observations during the sintering trials of Foremost 316 is listed below:

- At the lowest laser power of 5W, the powder turned yellow with no evidence of consolidation. The ED was insufficient to fuse the particles together, and showed signs of degradation.

- The next laser power used at 10W, resulted in crystallisation of the powder, however none layer formation was present.

- An increase in the ED at 15W of power, induced fuming and degradation, as the powder changed to brown colour. Meanwhile, the material formed sugar crystals, however there was no evidence of layers or fusion.

- At the highest laser power of 20W, the powder caked severely, resulting in fuming, which indicated acute deterioration. Crystal formation was obvious and yet the ED applied was insufficient to fuse the sugar crystals together.

All of the above observations can be seen in Figure 5.6. In addition to the crystal formation and the fuming, there was an intense sugar smell during scanning of the powder bed, and furthermore, fogging was noticed on the optics and heating elements. This result indicated charring of the polymer through dehydration. As mentioned earlier, lactose has been reported to experience caking problems, resulting from the loss of water. It was described in the TGA analysis in section 4.2 that the α-monohydrate dehydrates at 143.90°C, which reduced the crystallisation water within the lattice structure to 4% of the total mass. As it was observed during the sintering process, which occurred above the dehydration temperature at 170°C, the polymer had the tendency to crystallise [89], [183], [184], [195]. The application of the laser increased locally the energy input, which damaged the powder by abrupt vaporisation of the liquid bridges [53], [68], [118], [195], [196], [198]. The liquid bridges were crystallised as part of a continual process and Foremost 316 powder resulted in caking upon sintering.

The poor performance of Foremost 316, prevented the use of further adjusted exposure parameters in order to explore a sintering route for the powder. The behaviour of the material during initial tests, indicated degradation starting at the lowest ED and further dehydration and crystallisation of the powder at increased energy input. Sintering of Foremost 316 was prevented since the potential of lactose to cake was very high, due to the main dehydration mechanism occurring 80°C below the melting of the polymer.

Table 5.3: Process parameters investigated for sintering tests of Foremost 316

Process Parameters	Constant	Varied
Layer thickness	0.10 mm	
Bed temperature	182°C (T_m = 219°C)	
Hatching power		5/ 10/ 15/ 20 W
Scan speed	2500 mm/s	
Contour power / speed	2500 mm/s	5/ 8/ 13/ 18 W
Hatching distance	0.25 mm	
Beam offset	0.15 mm	
Scan pattern	Double	
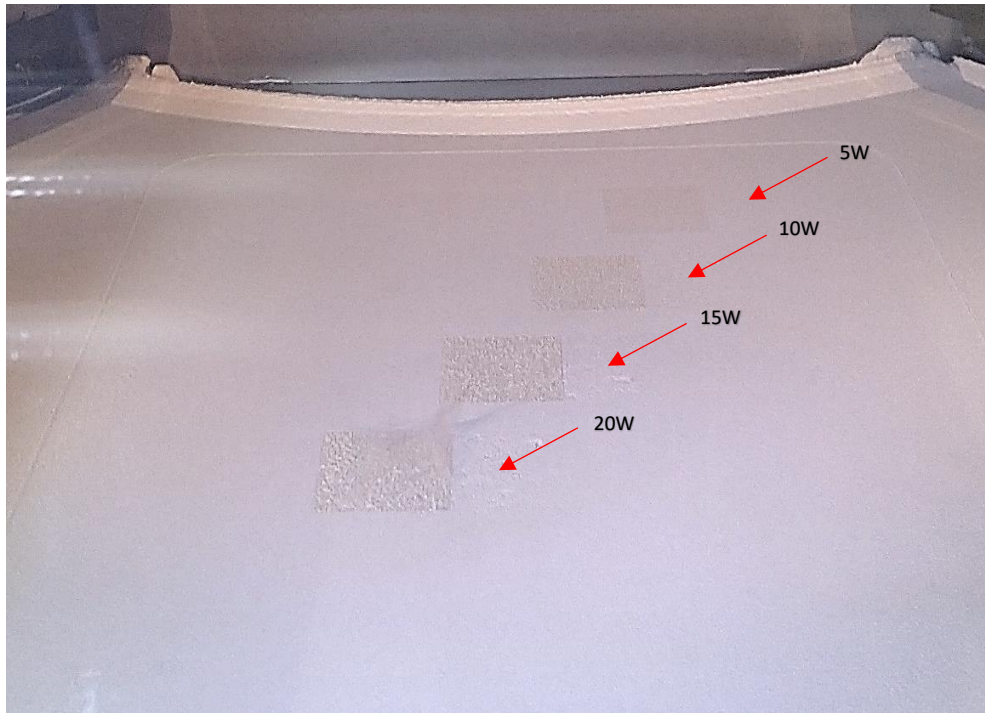
Figure 5.6: Double scanning mode in 5, 10, 15 and 20W resulted in crystallisation of Foremost 316

5.4   Processing of HPC SSL

HPC SSL was discovered to possess an average particle size of 50.29μm, which was favourable for LS process. Additionally, the material behaved like amorphous, starting softening above 90°C, which should result in lower viscosity within the temperature range of the P100, in contrast with Avicel 101 and Foremost 316. However, the powder was

found to be extremely cohesive. As it was demonstrated in section 4.3, the increased moisture content in the amorphous phase of the polymer acted like a plasticiser, which increased compaction and led to poor flow efficiency. Figure 5.7 illustrates the influence of the cohesion of HPC SSL on the application of the powder on the bed platform. It can be observed that the blade failed to spread the powder at 30°C, resulting in an inhomogeneous layer deposition over the build area. As the temperature increased to 60°C the powder further agglomerated and formed clumps over the bed. In further increase of the temperature to 80°C the powder compacted between the blade and the walls of the machine. This behaviour was highly expected as the material demonstrated a reduction of surface water up to 80°C, monitored during TGA. Therefore, the progressive vaporisation of the condensed surface water trapped in the lattice during preheating, enhanced the interaction of inter-particle capillary forces and eventually the particles formed strong solid bridges upon drying [3], [53], [192].
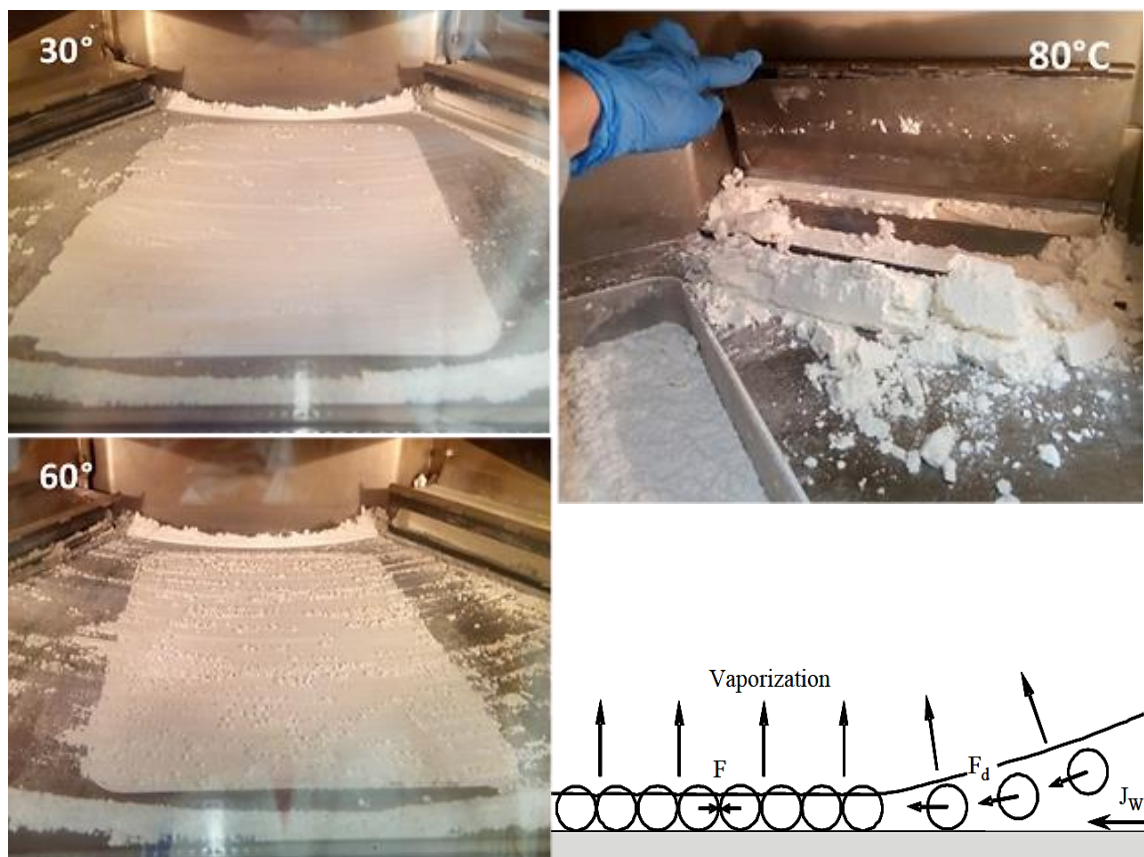
Figure 5.7: Spreading failure of HPC SSL powder below the glass transition. Inhomogeneous spreading at 30°C, formation of agglomerates at 60°C, and high compaction at 80°C. Image at the bottom right explains the mechanism of progressing compaction with increasing temperature due to the self-orientation of the particles by capillary forces upon vaporisation of surface water [53]

In order to improve flowability of HPC SSL a flow control additive was necessary to be added in the powder to achieve uniformity in the deposition of the layers. Magnesium Stearate (MgSt) is a fatty acid salt well known to behave as a boundary lubricant of cohesive pharmaceutical powders. MgSt in small concentrations of 0.5-1% (w/w) has been reported to reduce adhesion at the interface of the particles, facilitating them to roll over one another, resulting in the improvement of the flow [89], [200]. Therefore, 0.5% and 1% of MgSt was mixed with HPC SSL for 15min to modify the flowability [3], [189], [203]. The two mixtures of powder were subjected to FT4 tests before spreading, to monitor any enhancement on their flow properties. Figure 5.8 presents the resulted flow diagrams compared to pure HPC SSL and PA2200. The addition of MgSt positively affected flowability of HPC SSL, creating a narrower flow pattern. However, the total energy needed for the powders to flow, increased at lower rates exhibiting cohesive characteristics. Meanwhile, the addition of a higher amount of MgSt was not considered, as a higher concentration could impact the mechanical behaviour of the bulk material [6], [200], [203]–[205]. In Figure 5.9 the difficulty to spread the powder across the build area after the addition of 0.5% MgSt was observed. The material tended to agglomerate every time the blade spread a new layer of powder. The surface looked patchy and the spreading of a second layer was prohibited due to high cohesion forces. The addition of 1% MgSt allowed the application of consecutive layers on the bed platform, indicating noticeable improvement of the flow efficiency. However, the characteristics of the top surface of the layers presented irregularities, which resulted in increased roughness, as shown in Figure 5.10.
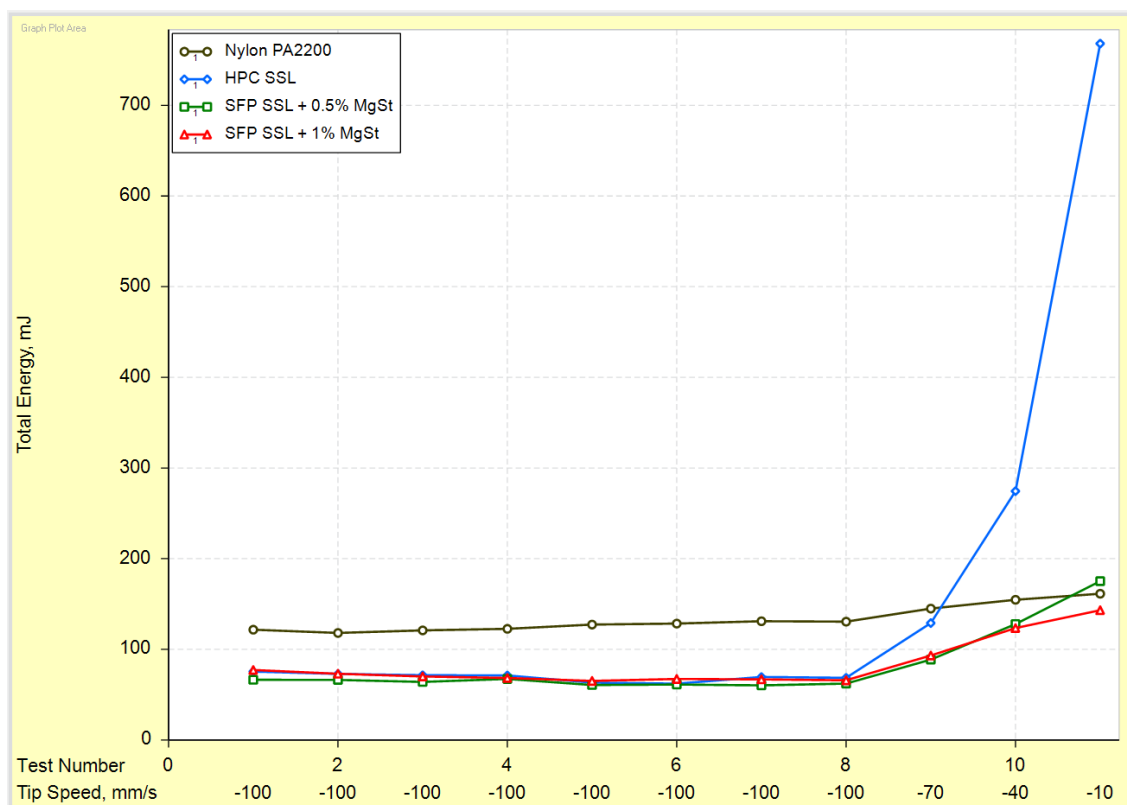
Figure 5.8: Flow patterns of HPC SSL powder after the addition of small percentages of MgSt compared to pure HPC SSL and PA2200

Figure 5.9: Non-uniform spreading of HPC SSL powder at 30°C after the addition of 0.5% MgSt

Figure 5.10: Spreading of HPC SSL powder with 1% MgSt at 30°C resulted in high surface roughness

An increase in the temperature within the chamber was made to evaluate the ability of the reinforced HPC SSL with 1% of MgSt to spread, as an attempt to reach the glass transition of the material. As the polymer remained below the T_g the mobility of the chains was frozen, which enhanced the interaction of capillary forces and hence cohesion characteristics. If the T_g could be reached, the polymer chain mobility would increase, minimising the effect of adhesion and eventually lead to partial consolidation at elevated temperatures [6], [7], [30], [52], [53], [196]. Nonetheless, when the temperature was raised to 50°C, the powder agglomerated and the surface looked quite patchy, as demonstrated in Figure 5.11. Afterwards, the temperature was increased to 75°C at which the powder formed bigger lumps across the build area and was compacted around the rotating paddle in the powder well on the sides.

The glass transition of HPC SSL could not be reached. The strong adhesion forces dominating the bulk of the powder prevented homogeneous spreading across the build area. Flowability of the powder was very poor despite of the addition of 1% of MgSt in an effort to decrease surface particles charges. Apparently, the distribution of inter-particulate forces was broadly extended in the structure of HPC SSL that inhibited further improvement on the flow at the bulk level. It was noted that the particles were charged with capillary forces due to the critical amount of water coverage on the surface of the

particles, along with van der Waals forces attracted by their small geometry. Treatment of the powder with MgSt failed to minimise contact of the particles due to the strong charges. It was assumed that the fine particles of MgSt were trapped in the electrostatic network; if the grains had a weight larger than the attractive forces, it may have resulted in significant reduction of the van der Waals [163], [191], [192]. It was evident that HPC SSL could not be processed using LS without further modification of the powder. The powder could possibly result in uniform spreading of separate layers close to the T_g, after targeted chemical treatment aiming to prevent moisture absorbance by the powder and thus, the formation of bonds between particles.

Figure 5.11: Formation of agglomerates and failure to spread HPC SSL with 1% of MgSt added, at 50°C (left) and 75°C (right)

5.5   Processing of Eudragit L100-55

Eudragit L100-55 was found to possess an ideal spherical particle with an average diameter of 50.29µm that enhanced flowability of the powder, as was demonstrated in Chapter 4. These powder characteristics were fitted for an optimal sintering. However, the material presented an amorphous thermal behaviour without a defined melting point that could be used to control particle fusion. Meanwhile, the glass transition was found at 93°C; the viscosity of amorphous polymers has been well known to decrease gradually when the temperature rises. Therefore, following guidance from other reports, the bed temperature was set 30°C above the T_g, to induce higher mobility of polymer chains and ultimately allow sintering of Eudragit L100-55 in the P100 [6], [30], [52]. The powder had an excellent spreading performance at elevated temperatures, resulting in the application of smooth, repeatable layers on the build area. Sintering started using a basic single scan strategy, varying only the build temperature and the laser power, aimed to

establish a set of suitable energy input for sintering the powder and acquiring structurally stable parts. The rest of the parameters were kept under default values. Details of the laser parameters applied on the first attempt to sinter Eudragit L100-55 are presented in Table 5.4 and Table 5.5. A brief description of the sintering result using the single scan pattern, is listed below:

- At a low laser power of 5W, the resulted parts turned out weak implying limited sintering effect. On the contrary, sintering under high laser power >15W, induced excessive fuming across the scanned area. No more than 2 layers were managed to be built in this first attempt, as the blade dislodged the parts from their position due to warped edges. Warping prevented the deposition of subsequent layers, as can be observed in Figure 5.12. In addition to these observations, it was also noticed that the powder started sticking at 122°C on the metal surfaces in the chamber and on the rotating paddle in the powder well. This would most likely block the recoating mechanism during continuing processing.

- The processing temperature was set to 115°C to prevent powder from sticking. Laser power was varied between 11W and 14W to explore a narrower range of ED that could sinter the powder without introducing fuming and curling. The build was successful, however, sintering did result in fuming, especially for 13W and 14W, at which parts experienced small degrees of curling. Nonetheless, delamination was observed in all the scanned parts due to poor intra-layer bonding, as demonstrated in Figure 5.13.

- Based on the previous observations the temperature increased at 116°C, which aimed to improve consolidation of the particles and consequently layer bonding. Furthermore, a decrease in laser power at the range of 7-10W aimed to decrease the total ED applied to reduce fuming and curling. However, the energy input was very low at 7W and the resulted part was very weak. 9W and 10W exhibited insignificant difference from the previous test. Meanwhile delamination evolved gradually during the build in all parts.

- In the final trials, laser power was set between 7W and 8.5W and scan speed was lowered at 2500mm/s to improve layer bonding. Indeed, the produced parts were stronger, however 7W resulted in a noticeable lower strength, while above 8W slight warping occurred. Nevertheless, the latter scanning strategy showed promising results producing parts in high precision, as presented in Figure 5.13.

Table 5.4: Process parameters investigated for initial sintering tests of Eudragit L100-55

Process Parameters	Constant	Varied
Layer thickness	0.10 mm	
Bed temperature		115 - 122°C ($T_g = 93$°C)
Hatching power		5 - 20 W
Scan speed		2500 / 2800 mm/s
Contour power / speed	16 W / 2500 mm/s	
Hatching distance	0.25 mm	
Beam offset	0.15 mm	
Scan pattern	Single	

Table 5.5: Detailed scanning strategy for initial sintering tests of Eudragit L100-55

Test / material	Temp (°C)	Sample	Hatching P (W)	Hatching S (mm/s)	Contour P	Contour S	PC P	PC S	Comments
Test 1 Eudragit L100-55	122	A	5	2800	16	2500	16	2500	• 2 layers • A was friable. Low power resulted in poor sintering • C, D were stable but they fumed and warped
		B	10						
		C	15						
		D	20						
Test 2 Eudragit L100-55	115	A	11	2800	16	2500	16	2500	• All layers • Fuming • Delamination of layers due to low bed temperature • C and D curled
		B	12						
		C	13						
		D	14						
Test 3 Eudragit L100-55	116	A	7	2800	16	2500	16	2500	• All layers • Delamination • A disintegrated • C and D fumed and curled
		B	8						
		C	9						
		D	10						
Test 4 Eudragit L100-55	116	A	7	2500	16	2500	16	2500	• All layers • Lower speed increased layer bonding • A was weak • C, D curled and fumed
		B	7.5						
		C	8						
		D	8.5						

Figure 5.12: Build failure of Eudragit L100-55 due to warping of the layers occurring at 15W and 20W in test 1
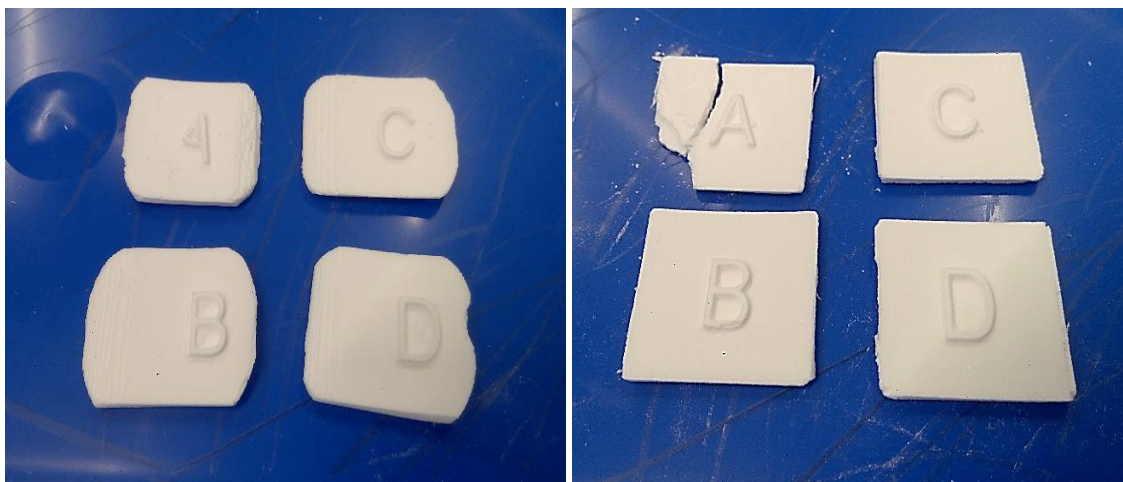
Figure 5.13: Delamination of Eudragit L100-55 parts due to weak layer bonding at 115°C (Test 2 left); high precision at 116°C under lower scan speed (Test 4 right)

Initial tests on Eudragit L100-55 powder resulted in parts with low stiffness and low precision. The observations indicated that when the temperature of the powder bed was kept low the consolidation of the particles was low, leading to weak intra-layer bonding and distortion of the finished part [6], [7], [30], [49], [52], [65], [66], [132], [194], [204], [206]. Upon the application of high laser power attempting to impart sufficient energy to

the powder, the parts experienced fuming and higher curling [6], [67], [68], [194], [205]. A combination of decreased power and speed increased precision, meanwhile the finished parts exhibited low stiffness [6], [7], [65], [67], [68], [71], [205]. In order to induce a sufficient degree of consolidation of the powder and produce denser parts with increased dimensional accuracy and mechanical performance, double scanning mode was applied in the next series of tests. This strategy was followed to increase the heat transferred to the powder, consequently the depth of fusion upon the application of the laser, and hence, improve adhesion between the layers [6], [7], [52], [53], [65], [67], [78], [205], [207]. A number of different sets of parameters, varying the temperature, the laser power and scan speed, in the filling pattern but also in the contour, were focused on determining the building parameters that permit complete layer bonding, while minimising the fuming and curling effect. A map of the scanning strategy followed is displayed in Figure 5.15. The detailed laser parameters investigated for the optimisation tests of Eudragit L100-55 are presented in Table 5.6 and Table 5.7. A brief summary of the sintering performance under double scan mode, is listed below:

- The temperature was raised to 117°C as a starting point. Meanwhile, the contour parameters were set low in order to decrease the ED applied at the edges and minimise warping. Laser power was explored between 5W and 7.5W to eliminate any degradation effects due to excess in the energy input transferred using double scans. The part exposed to 5W was very weak, and parts exposed above 7W exhibited increased density and stiffness, while they curled as displayed in Figure 5.14.

- To improve consolidation and increase density, strength and precision, temperature was raised by another degree of Celsius. In addition, post contour settings were removed to minimise the ED at the perimeter of the parts. However, the absence of post contour enhanced warping and resulted in delamination, as the edges opened up. Although, it was noticed that at 5-6W the parts exhibited the minimum effect. A repeated build at 118°C using 5-6W of laser power was designed using the settings for post contour, which resulted in finished parts with clear and flat edges; nonetheless stiffness remained low.

- In order to increase the density and therefore the stiffness at low laser power, speed was decreased to allow a longer laser scan time to ensure proper particle

fusion. It was observed in 1750mm/s and 2000mm/s that parts resulted in increased thickness and lack of precision.

- Towards the optimisation of the process, the temperature was further increased at 119°C and the speed was set at an optimal range between 2100mm/s and 2700mm/s. Except the part exposed at the highest speed that was weak due to the insufficient ED applied, the rest of the finished parts exhibited increased density and strength, while dimensional accuracy was very high. The results of the total energy input applied were very satisfying, producing uniform robust parts.

During the second part of this investigation the successful production of fully-dense parts with increased precision was demonstrated. The process parameters were optimised to maximise the strength and dimensional accuracy, while keeping the ED as low as possible to prevent fuming/degradation of the powder. The two most influential parameters during sintering of Eudragit L100-55 were the process temperature and the laser power. The bed temperature needed to be set at the highest possible to increase the melt viscosity of the amorphous polymer, before reaching a critical point at which the powder would stick on the accessories of the P100. The combination of temperature, scan pattern, low laser power and relative high speed, resulted in an optimum sintering performance that inhibited distortion of the final parts. It was noted that double scanning created a layer overlap of the two parallel consecutive laser scans, improving adhesion; scan speed determined thickness, which increased at lower rates; and contouring determined dimensional stability, forming a barrier at the boundaries of the parts [6], [7], [52], [55], [65]–[67], [87], [204], [205].

Table 5.6: Process parameters investigated for optimised sintering of Eudragit L100-55

Process Parameters	Constant	Varied
Layer thickness	0.10 mm	
Bed temperature		117 - 119°C ($T_g = 93$°C)
Hatching power		5 - 8 W
Scan speed		1750 - 2700 mm/s
Contour power /speed	2500 mm/s	5 - 7 W
Hatching distance	0.25 mm	
Beam offset	0.15 mm	
Scan pattern	Double	

Table 5.7: Detailed scanning strategy for the optimisation of Eudragit L100-55

Test / material	Temp (°C)	Sample	Hatching		Contour		PC		Comments
			P (W)	S (mm/s)	P	S	P	S	
Test 5 Eudragit L100-55	117	A	5	2500	5	2500	5	2500	• All layers • A disintegrated • B looked uniform but weak • C, D were stiff but curled
		B	7		5		5		
		C	7.5		5		5		
		D	7		7		7		
Test 6 Eudragit L100-55	118	A	5	2500	5	2500	/	/	• All layers • A, B small curling • C, D curled • Parts were weak due to the absence of contour
		B	6						
		C	7						
		D	8						
Test 7 Eudragit L100-55	118	A	5	2500	5	2500	5	2500	• All layers • A, B showed clear and flat edges, but low stiffness • C, D were denser but thicker and curled
		B	6		6		6		
		C	5	2500	5	2500	/	/	
		D	6		6				
Test 8 Eudragit L100-55	118	A	6	2500	6	2500	6	2500	• All layers • C, D were stiff and dense, but thicker due to lower speed
		B		2250					
		C		2000					
		D		1750					
Test 9 Eudragit L100-55	119	A	6	2100	6	2500	6	2500	• All layers • D was weak • A, B, C were stiffer and denser • Parts look uniform
		B		2300					
		C		2500					
		D		2700					

Figure 5.14: Structurally stable Eudragit L100-55 parts scanned at 117°C, showing fragility and curling in low and high laser power, respectively (Test 5)
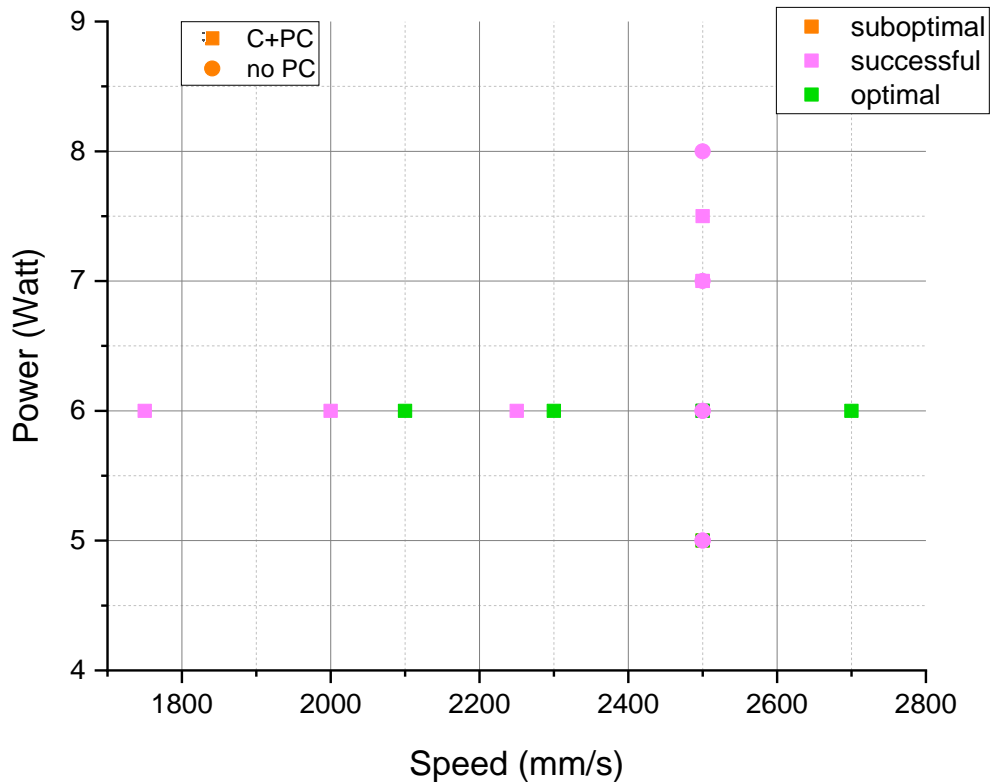
Figure 5.15: Processing map of Eudragit L100-55 under double scanning mode; plot power against speed; constant parameters: layer thickness 0.10mm, hatching distance 0.25mm, beam offset 0.15mm

5.6 Processing of PolyOx N80

PolyOx N80 presented a narrow and fast transition to the melt at 67°C found in section 4.2, as is a highly crystalline polymer. This thermal behaviour was suitable for the P100 that was capable of processing PolyOx N80 at low temperatures. Meanwhile, previous tests revealed poor flowability resulting from the wide size and shape distribution of the particles with 10% of the volume above 352.8μm. Considering that the large particles would strongly affect the packing efficiency of the powder and influence the density of the produced parts, the powder was sieved at 250μm to remove the bigger particles and create a narrower PSD. Additionally, the layer thickness was set at the maximum of 150μm to spread the bigger particles. After these few adjustments, the blade deposited evenly the sieved powder across the build area, close to the melting point during the preheating step, as illustrated in Figure 5.16.

Sintering tests were performed to explore the processing temperatures for PolyOx N80 and define a stable sintering region. Initially, a broad range of exposure parameters were used varying the laser power and scan speed, both in the hatching and the contouring. During the first layer scan it was observed that the edges were undergoing acute warping in-build. An increase in bed temperature was applied in combination with a decrease in laser power to investigate whether this resulted due to shrinkage or super-cooling phenomena. It was found that the total energy input was significantly low to fully fuse the powder, while the layers formed were very fragile to manually handle, which can be observed in Figure 5.17. To correct this, an increase in the ED was attempted using higher laser power and lower speed, which resulted once again in immediate warping, meanwhile the powder locally fumed. At this point it was considered that the layers cooled down very quickly due to the surrounding powder kept at low temperature, which induced thermal distortion [6], [7], [49], [52], [66], [194], [204]. The range of exposure parameters used at the various temperatures can be studied in Table 5.8 and Table 5.9. The map of the scanning strategy in Figure 5.18 was meant to identify a potential sintering region as a starting point for the trials following.

Figure 5.16: Uniform spreading of PolyOx N80 powder at 25°C (left) and 50°C (right)

Table 5.8: Process parameters investigated for initial sintering tests of PolyOx N80

Process Parameters	Constant	Varied
Layer thickness	0.15 mm	
Bed temperature		58 - 62°C ($T_m = 67$°C)
Hatching power		4 - 21 W
Scan speed		1500 - 3000 mm/s
Contour power / speed		- (0-6) W lower than hatching power Same as scanning speed
Hatching distance	0.25 mm	
Beam offset	0.15 mm	
Scan pattern	Single	

Table 5.9: Detailed scanning strategy for initial sintering tests of PolyOx N80

Test / material	Temp (°C)	Sample	Hatching P (W)	Hatching S (mm/s)	Contour P	Contour S	PC P	PC S	Comments
Test 1 PolyOx N80	58	A	4	2500	4	2500	4	2500	• 1 layer • Parts warped and dislodged
		B	6		5		5		
		C	8		7		7		
		D	10		9		9		
Test 2 PolyOx N80	60	A	4	2500	3	2500	3	2500	• 1 layer • Low power • Powder was poorly sintered • Layers were sticky
		B	4	3000	3	3000	3	3000	
		C	6	2500	5	2500	5	2500	
		D	6	3000	5	3000	5	3000	
Test 3 PolyOx N80	60	A	6	1500	4	1500	4	1500	• 1 layer • A, B warped in low speed • C, D formed sticky membranes due to partial sintering
		B		2000		2000		2000	
		C		2500		2500		2500	
		D		3000		3000		3000	
Test 4 PolyOx N80	62	A	15	1500	15	1500	15	1500	• 1 layer • Fuming • Ductile and stable layers • Layers fumed and warped due to high ED
		B	17						
		C	19						
		D	21						
Test 5 PolyOx N80	62	A	14	2000	14	2000	14	2000	• 1 layer • Fuming • Warping of the edges
		B	15						
		C	16						
		D	17						

Figure 5.17: Poor consolidation of PolyOx N80 powder due to low ED at 60°C (Test 2 left); layer warping at high ED at 62°C (Test 5 right)
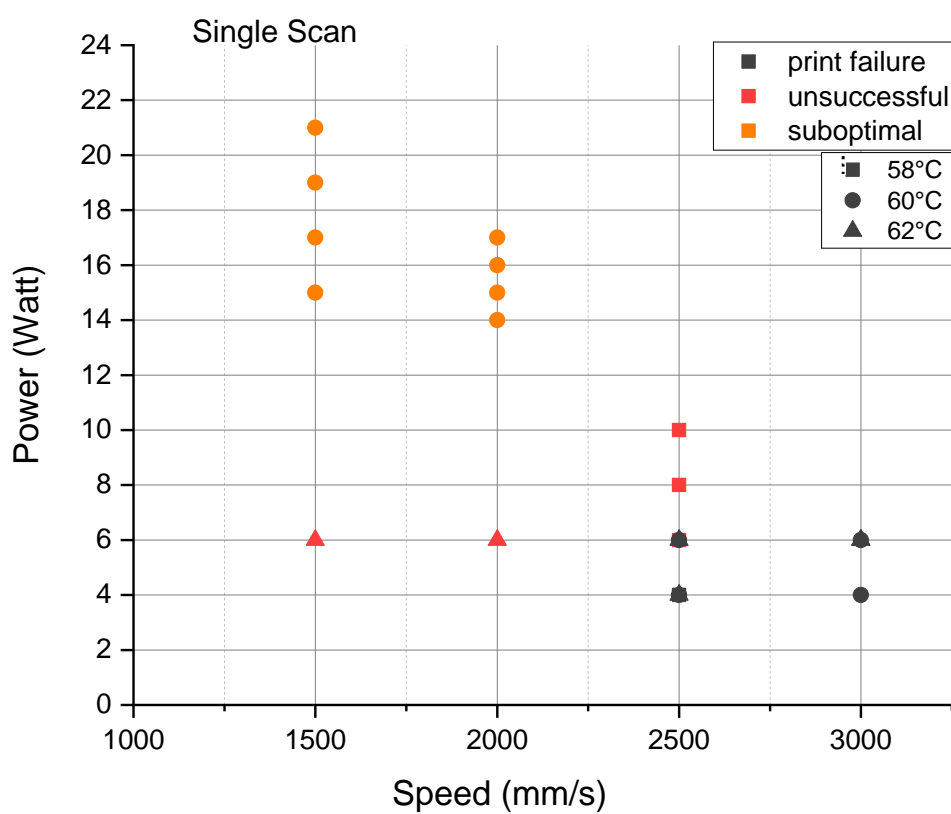
Figure 5.18: Processing map of PolyOx N80 under single scanning mode; plot power against speed; constant parameters: layer thickness 0.15mm, hatching distance 0.25mm, beam offset 0.15mm

To improve processability of PolyOx N80, the bed temperature was maintained as close as possible to the T_m of the polymer. It has been discussed in previous reports that preferred temperature for semi-crystalline materials was 3-4°C below the melting point, so that upon the application of the laser the temperature was raised above the melting point and allowed full consolidation of the particles [49], [52]. However, this was material specific and presented variations between different polymers. Nevertheless, a critical temperature was discovered for every polymer, below which residual stresses can be induced and lead to curling, and above which degradation of the sintered powder may occur [6], [7], [49], [65], [204], [206]. In that event, the processing temperature was set at 63°C, 63.5°C and 64°C and the laser power was kept low, between 7W and 10W, to prevent fuming. Double scanning mode was chosen in order to transfer adequate heat to the powder and ensure fusion at decreased laser power applied, compared to the previous tests. The detailed scanning strategy can be found in Table 5.10 and Table 5.11, while the scanning map is illustrated in Figure 5.19. Briefly:

- At 64°C the resulting viscosity of PolyOx N80 was very low that found to sinking of the molten phase into the supporting powder bed. The best sintering result was observed at the combination of 10W at 63.5°C. At the same time fuming was not observed in any of the trials, indicating that the material can be safely processed in that sintering region.

- In spite of the promising result, the build resulted in the formation of only 3 layers, as there was lack of layer adhesion, despite the double scan pattern used and the increased temperature.

- A range of scan speeds was chosen aiming to identify a region that can result in better fusion, and hence, increased adhesion and stiffness. The speed was varied between 1800mm/s and 2800mm/s, however there was no significant variance on the sintering result. The layers formed exhibited high porosity, weak bonding and warped edges as presented in Figure 5.20.

Table 5.10: Process parameters investigated for the second phase of sintering PolyOx N80

Process Parameters	Constant	Varied
Layer thickness	0.15 mm	
Bed temperature		63 - 64°C ($T_m = 67$°C)
Hatching power		7 - 10 W
Scan speed		1800 - 2800 mm/s
Contour power / speed	7 W	2000 / 2200 mm/s
Hatching distance	0.25 mm	
Beam offset	0.15 mm	
Scan pattern	Double	

Table 5.11: Detailed scanning strategy for the second phase of sintering PolyOx N80

Test / material	Temp (°C)	Sample	Hatching P (W)	S (mm/s)	C P	C S	PC P	PC S	Comments
Test 6 1/2/19	64	A	7	2000	7	2000	7	2000	• 1 layers • Build failure • Sinkhole
		B	8						
		C	9						
		D	10						
Test 7 1/2/19	63.5	A	7	2000	7	2000	7	2000	• 2 layers • No fumes • Warping • D formed 3 layers
		B	8						
		C	9						
		D	10						
Test 8 1/2/19	63	A	7	2000	7	2000	7	2000	• 2 layers • Warping • Weak layer bonding
		B	8						
		C	9						
		D	10						
Test 9 4/2/19	63.5	A	10	1800	7	2000	7	2000	• 2 layers • Warping • A, B stronger effect • Weak bonding
		B		2000					
		C		2200					
		D		2400					
Test 10 4/2/19	63.5	A	10	2200	7	2200	7	2200	• 2 layers • Warping • Weak bonding
		B		2400					
		C		2600					
		D		2800					
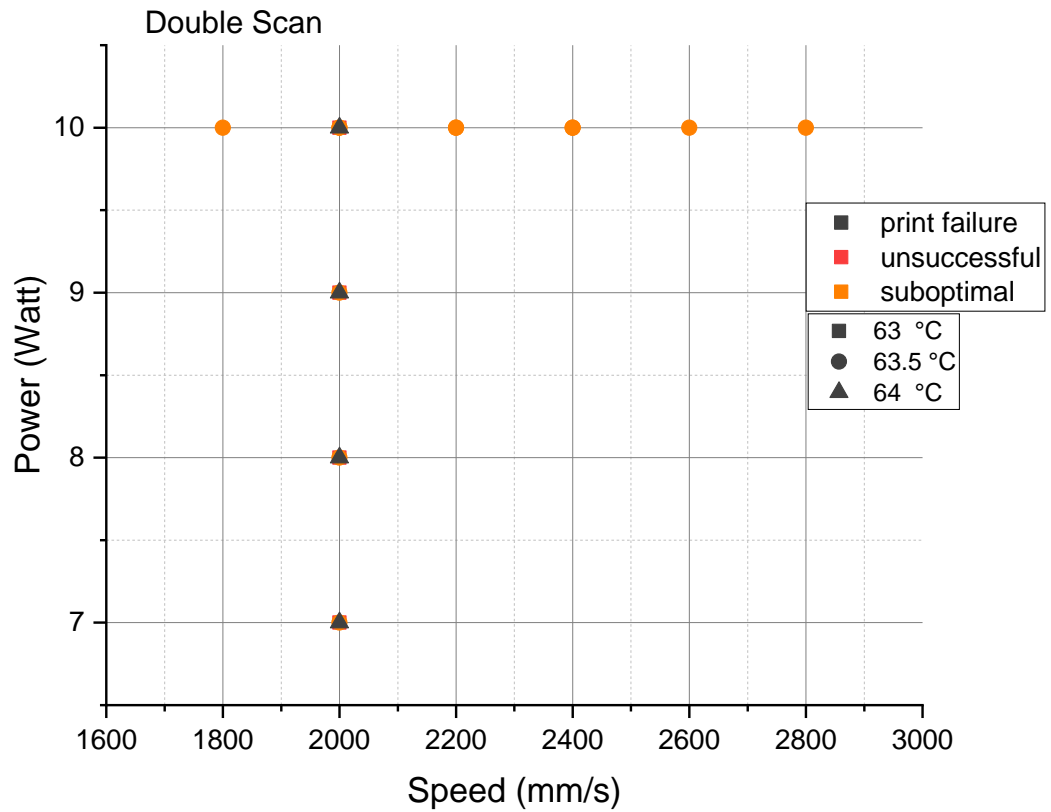
Figure 5.19: Processing map of PolyOx N80 under double scanning mode; plot power against speed; constant parameters: layer thickness 0.15mm, hatching distance 0.25mm, beam offset 0.15mm
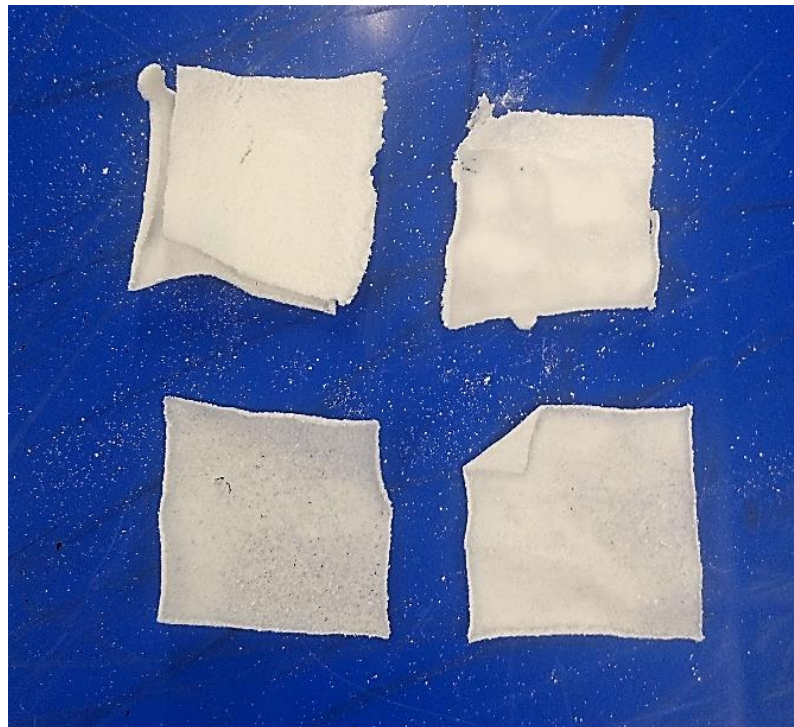
Figure 5.20: Warping and lack of adhesion between the two layers of PolyOx N80 formed in Test 10

So far, sintering of PolyOx N80 powder was unsuccessful. It was considered that the maximum layer thickness of 150μm used introduced thermal imbalances. The large and irregular particles present in the bulk of the powder resulted in inhomogeneous initial packing of the deposited layers. The increased thickness and porosity of the powder bed resulted in low bed thermal conductivity and poor consolidation of the larger particles. Consequently, failed to fill in inter-particle gaps and create sintering necks towards the formation of fully-dense multilayers [6], [7], [30], [49], [53], [66], [67], [69], [194], [204]. Therefore, to increase efficiency, lower scanning distance was selected in order to create an overlap between parallel scan lines and impart sufficient heat to the particles to increase necking. The rest of the parameters were kept the same as in the previous tests, found to result in minimum warping and degradation, except the scan speed, which was adjusted for the filling and contouring, to ensure the best sintering performance. The scanning strategy followed is presented in Table 5.12 and Table 5.13 and is illustrated in Figure 5.21. A summary of the findings is described below:

- Distance was set at 0.18-0.20mm which was half the laser spot size, thus the laser scanned over the same line twice. It was found that the smaller distance fairly reduced layer porosity, and thus inter-layer bonding was improved, as can be observed in Figure 5.22.

- Increased speed was applied at the contour line to further improve the effect of warping at the edges and resulted in the deposition of a few layers with increased stiffness. However, the smallest increase in ED using lower speed resulted in better strength but enhanced warping, and the smallest decrease in the ED due to higher speed, always resulted in poor fusion and unstable layers.

- Although the efforts made to explore different set of parameters, the sintering window of PolyOx N80 proved to be very narrow. The selected scanning strategy could not be considered to lead in the optimum sintering outcome.

Table 5.12: Process parameters investigated towards optimisation of PolyOx N80

Process Parameters	Constant	Varied
Layer thickness	0.15 mm	
Bed temperature	63.5°C (T_m = 67°C)	
Hatching power	10 W	
Scan speed		2200 - 2800 mm/s
Contour power / speed	7 W	2200 / 2500 mm/s
Hatching distance		0.18 / 0.20 mm
Beam offset	0.15 mm	
Scan pattern	Double	

Table 5.13: Detailed scanning strategy towards optimisation of PolyOx N80

Test / material	Sample	Hatching						Comments
		D (mm)	S (mm/s)	C P	C S	PC P	PC S	
Test 11 PolyOx N80	A	0.20	2200	7	2200	7	2200	• Better fusion due to overlapping • A warped a lot due to low speed • B formed 3 layers showing increased strength • D was sticky due to poor fusion
	B		2400					
	C		2600					
	D		2800					
Test 12 PolyOx N80	A	0.20	2300	7	2500	7	2500	• 3 layers • A warped and was dislodged • B, C, D showed increased adhesion and stiffness
	B		2400					
	C		2500					
	D		2600					
Test 13 PolyOx N80	A	0.18	2400	7	2500	7	2500	• 4 layers • A warped due to high ED • C was better than B
	B	0.18	2500					
	C	0.20						
	D	0.18	2600					
Test 14 PolyOx N80	A	0.18	2500	7	2500	7	2500	• 5 layers • Strong layers • D had less warping effect
	B		2600					
	C	0.20	2500					
	D		2600					

Figure 5.21: Processing map of PolyOx N80; plot distance against speed; constant parameters: bed temperature 63.5°C, layer thickness 0.15mm, laser power 10W, beam offset 0.15mm

Figure 5.22: Warping and lack of adhesion between layers of PolyOx N80 in Test 11 (left); improved fusion, adhesion and stiffness in Test 12 (right)

Laser sintering of PolyOx N80 proved to be quite challenging. The available options based on the behaviour of the material during processing had limited the ability to

optimise the powder's sintering performance. In the final attempt, the beam offset was varied aiming to explore any reductions on the warping effect, which remained the main failure mechanism. The beam offset is the distance between the contour line and the first hatching line, which can alternate the amount of energy input at the edges of the layers. The results were satisfactory as complete parts were obtained. The parts were scanned using an optimal set of laser parameters investigated in the previous trials in combination with a high beam offset of 0.26mm. It can be observed in Figure 5.23 that finished parts were fully-dense demonstrating increased plasticity and strength. However, high degrees of shrinkage were evident due to high distortion of the parts' morphology. Evidently, the increased powder bed porosity had a negative effect in shrinkage. Shrinkage resulting from the poor packing of the large particles explained the consistent warping occurring in all the investigated exposure parameters.

Meanwhile, it was decided after examining closely all the details in the previous tests, to use a "downskin" strategy to scan the first layers, completing the build process under a different scanning strategy. Downskin provided the option to scan the layers under two different sets of parameters for the top and bottom of the parts. Therefore, to ensure the creation of a support base, the laser parameters investigated at the last set of tests resulting in full consolidation of the powder were used to produce robust initial layers. The rest of the part was scanned under decreased ED, using lower laser power of 5-8W, in order to produce porous layers with reduced levels of shrinkage. The concept, assumed that the fully molten scanned base, could transfer heat, due to increased energy input used, to the newly deposited layers scanned under lower ED, in order to facilitate layer bonding of the top porous layers and produce parts with increased adhesion, while shrinkage could be minimised. Nevertheless, the layers scanned using lower laser power at the top, were poorly sintered resulting in tackiness, and were caught by the blade in the next pass, causing the build to fail. The complete scanning strategy can be viewed in Figure 5.24 and in Table 5.14 and Table 5.15.

To summarise, sintering of PolyOx N80 failed to produce finished parts with clear and flat edges due to extended shrinkage of the molten state induced upon cooling. The large particles introduced large inconsistencies in the powder bed density, which increased porosity within the structure, and hence, led to shrinkage after densification [6], [66], [67], [194], [204], [208].
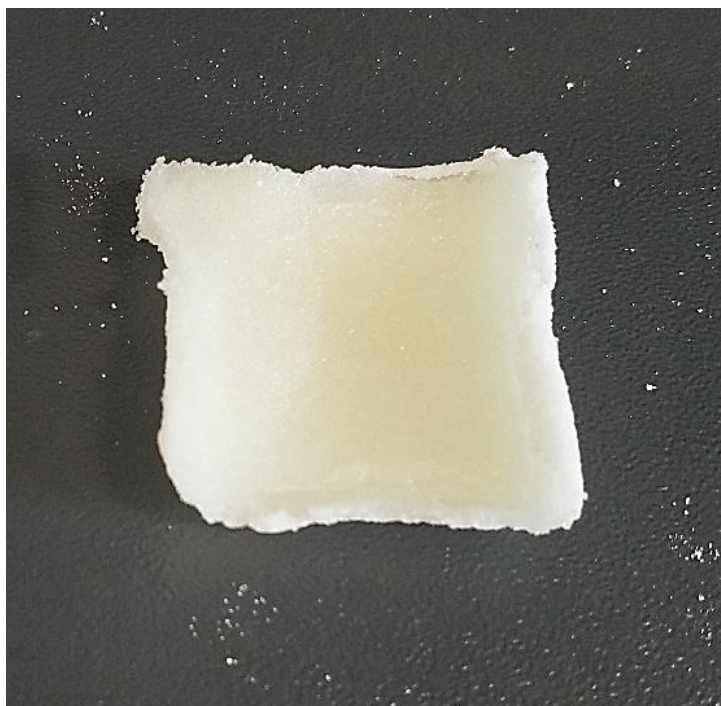
Figure 5.23: Successful sintering of a robust PolyOx N80 part using high values of beam offset (Test 17)

Table 5.14: Process parameters investigated for optimisation tests of PolyOx N80

Process Parameters	Constant	Varied
Layer thickness	0.15 mm	
Bed temperature	63.5°C ($T_m = 67$°C)	
Hatching power		5 - 10 W
Scan speed	2600 mm/s	
Contour power / speed		- (0-3) W lower than hatching power
Hatching distance	0.20 mm	
Beam offset		0.15 - 0.28 mm
Scan pattern	Double	
Downskin (P / S)	10 W / 2500 mm/s	

Table 5.15: Detailed scanning strategy for optimisation tests of PolyOx N80

Test / material	Sample	Beam Offset (mm)	P (W)	C P	C S	PC P	PC S	Comments
Test 15 PolyOx N80	A	0.15	10	7	2500	7	2500	• 4 layers • Higher the beam offset to apply less energy at the edges • A warped/dislodged • B, C & D warped
	B	0.18						
	C	0.20						
	D	0.22						
Test 16 PolyOx N80	A	0.22	10	7	2500	7	2500	• 4 layers • A curled a lot and was dragged after the 4th layer
	B	0.24						
	C	0.26						
	D	0.28						
Test 17 PolyOx N80	A	0.26	10	7	2500	7	2500	• Complete build • Ductile and strong parts
DTest 1 PolyOx N80	A	0.26	7	7	2500	7	2500	• 2 layers • B was dragged after the 2nd layer
	B		8					
	C	0.28	7					
	D		8					
DTest 2 PolyOx N80	A	0.28	5	5	2500	5	2500	• 2 layers • C was dragged after the 2nd layer • There's no repeatability
	B		6	6		6		
	C		7	7		7		
	D		8					

Figure 5.24: Processing map of PolyOx N80; plot power against beam offset; constant parameters: bed temperature 63.5°C, layer thickness 0.15mm, laser speed 2600mm/s, hatching distance 0.20mm

5.7   Summary

The main aspects that influenced the process window and subsequent consolidation quality were the thermo-physical properties of the powders. Semi-crystalline materials with high melting points resisted consolidation, while amorphous polymers needed to be processed at several degrees above their glass transition temperature. Materials with high levels of absorbed moisture exhibited cohesiveness and dehydration at elevated temperatures, leading to degradation upon the application of the laser beam. Furthermore, the particle morphology and size distribution that did not fit the recommended range for LS powders led to porosity or agglomeration. The information gathered through sintering of the materials is presented in Table 5.16, and was used to assess the sinter-ability of the powders and strengthen the material selection decisions on the formulation.

Table 5.16: Sinter-ability of the pharmaceutical excipients

	Spreading	Consolidation	Quality	Comments
Avicel 101	✓	✗		print failure, degradation
Foremost 316	—	✗		print failure, degradation
HPC SSL	✗			agglomeration
Eudragit 100-55	✓	✓	✓	optimal sintering, precision
PolyOx N80	✓	✓	—	successful sintering, shrinkage

The thermo-physical properties of Avicel 101, Foremost 316 and HPC limited their processability and prevented sintering. Eudragit L100-55 and PolyOx N80 were the only materials that formed multilayers. However, PolyOx N80 introduced difficulties due to the low packing efficiency of the larger particles, resulting in shrinkage and distortion of the finished parts. Since Eudragit L100-55 was the only excipient that achieved high part density and precision, it was selected as the matrix material for sintering a preliminary formulation for the initial investigation of LS of oral solid dosage forms. Further material decisions are discussed in the next chapter.

CHAPTER 6   LASER SINTERING OF PHARMACEUTICAL INGREDIENT BLENDS

6.1 Introduction

Every drug substance requires excipients with certain functionality based on the manufacturing process and the mode of drug delivery [88],[101], [209]. As discussed in Chapter 2, there are many factors that need to be taken into account when developing a new formulation, especially, in the case of this PhD where LS has been chosen as the preliminary manufacturing technology. Therefore, a deep understanding of the engineering principles involved was required, to design a formulation that would comply with the additive manufacturing process and challenges of sintering, and further with the design principles of a tablet. In that event, the next step of this study was to investigate the risks associated with processing, in terms of control, reliability and reproducibility of the pharmaceutical sintered parts, in order to design and fully develop a drug product manufactured by LS.

There are numerous choices when normally selecting excipients, however, the total number of excipients used in a formulation should be kept as low as possible [209]. According to the findings in Chapter 5, where the influence of the material characteristics on processing and also the influence of sintering on pharmaceutical materials were studied, a selection of two excipients was made to develop a preliminary composition for LS of oral solid dosage forms. These materials were Avicel 101 and Eudragit L100-55, and were chosen based on their pharmaceutical functionality and their LS processability. Avicel 101 is a pharmaceutical diluent and generally used as the main ingredient in tablet formulations, to provide the required density for manufacturing tablets of sufficient weight and size, and therefore is an important excipient. Although Avicel 101 was not able to be processed in the P100, it was selected as the filler material in the formulation, to provide sufficient density and facilitate the manufacturing process, since it demonstrated increased packing efficiency during spreading on the bed platform. On the other hand, Eudragit L100-55 exhibited enhanced processability and was chosen as a matrix material for sintering. The material acted as a matrix or binder, creating bridges between the particles of the two powders resulting in solid parts. Furthermore, Eudragit L100-55 is a pharmaceutical film coating agent, which is used for multiple purposes, such

as to enhance the flavour, the odour and the colour, to prevent drug degradation and improve tablet appearance, but mainly to control drug release. This varied the functionality of Eudragit L100-55 and in combination with its excellent sintering performance could potentially fill the criteria to produce functional oral solid dosage forms that may be designed for controlled release using LS technologies.

The approach developed in this chapter, was to explore the sinter-ability of a preliminary placebo blend consisting of a minimum of two components. A series of sintering tests were designed to investigate the consolidation quality of the two-component feedstock after exposure and the handling stability of the finished parts. The final density/or porosity of the sintered parts, which was determined by the degree of necking between the Avicel 101 and Eudragit L100-55 particles, was expected to strongly influence the performance of the developed tablets according to previous studies, and hence as reported, the expected release profile and functionality of a generic dosage form [20], [29], [36], [43], [44]. Therefore, the sintering performance of the blends was examined thoroughly to increase the level of scientific understanding of the many variables involved, developing a bridge between LS and pharmaceutics.

6.2   Laser Sintering of Avicel 101 – Eudragit L100-55 Blends

Three placebo blends were produced with material ratio of 50:50, 63:37, 37:63 (w/w), Avicel 101 to Eudragit L100-55. The use of varied compositions aimed to validate the influence of the mixture composition on the processing conditions, and hereafter, the impact on the physical and mechanical properties of the produced parts [20], [29], [42]. The two materials exhibited completely different sintering performance as described in the previous chapter, thus, the material ratio was expected to be the main determining factor of the sintering outcome. Sintering tests focused on the design of an optimal scanning strategy for each blend, intended to maximise the performance and result in fully dense or near-fully dense parts.

The two powders presented particles with average diameter of 50.29μm (Eudragit L100-55) and 70.22μm (Avicel 101) falling in the optimal LS region, and relatively similar bulk densities of 0.5gr/cm^3 (Eudragit L100-55) and 0.32gr/cm^3 (Avicel 101). The ideal spherical particles of Eudragit L100-55 that was found to glide on to each other with minimum friction, were easily blended with the Avicel 101 particles by simple

mechanical mixing. Specifically, the blended powders were prepared using a conventional rotary tumbler for 15min [42], [66], [72], [204], [210].

Sintering tests were conducted in the P100 using the same powder resources as in Chapter 5, having the same levels of use as in storage condition and time. Layer thickness was set at 100μm based on the small average size of the particles. Parts with a simple square geometry and size of 20 x 20 x 2mm were designed to be built flat in the x-y direction in the centre position of the build area. During the warm up phase a 2mm depth of powder was deposited onto the bed platform, while a further 2mm of powder layers were spread prior to exposure, which added 4mm of total powder height below the parts in order to provide insulation. In addition, 2mm of powder were deposited after the end of the scanning process for the cooling step. The average build time for each of the tests was approximately 2 h. A 30min window was allowed for the parts to cool down after every build was completed. Parts were then removed from the build platform and cleaned to separate the surrounding powder.

6.2.1   Processing of the 50:50 Av/Eu blend

Initial tests were performed in order to provide an indication of the sintering window of the two-component feedstock material. Laser power was found to be the most important parameter affecting the quality of the excipients in the previous chapter, related to deterioration effects. Therefore, a range of EDs were applied to the powder varying only the laser power, while the rest of the parameters were kept at default values, to gain some understanding of the effect of the input of the laser on the densification and degradation of the bi-system. The processing temperature targeted the Eudragit L100-55 phase, which presented a low glass transition compared to the high melting point of Avicel 101. Based on the preliminarily optimised Eudragit L100-55 sintering tests in section 5.5, the temperature was set at 120°C in order to soften the powder and join together the solid particles of Avicel 101 phase. The laser was set to scan using a single pattern alternating between the X and Y axis on consecutive layers. The laser power varied from 5W to 20W, to investigate the influence of low to high energy input. The scanning strategy resulted in three distinctive sintering effects, as illustrated in Figure 6.1. In Area 1 the powder was poorly sintered under low laser power of 5-8W. In Area 2 there was weak layer formation after small increase in the laser power at the range of 9-12W. And finally, in Area 3 sintering resulted in a clear colour change of the powder from white to yellow or brown

(also indicating degradation) between the laser powers of 13W and 20W, whilst fuming was observed.

Figure 6.1: Initial trials on the 50:50 Av/Eu blend at various laser powers. Area 1 resulted in poor consolidation; Area 2 resulted in weak layer formation; and Area 3 indicated degradation, whilst the powder fumed

The resulted degradation upon exposure in Area 3 was attributed to the degradation of Avicel 101. As explained in section 5.2, as soon as the energy input was increased when the laser scanned locally the powder, sintering resulted in caking of the Avicel 101 particles. Although degradation occurred, the scanned powder in Area 3 formed ductile layers with acceptable stiffness. This behaviour implied that the Eudragit L100-55 phase was spreading among the solid particles of Avicel 101 binding successfully the two phases together. This result was promising for the double-phase powder, demonstrating that the sintering effect can increase with increased ED and potentially produce structurally stable parts. Therefore, in order to maintain increased levels of energy input in an attempt to avoid degradation of the Avicel 101 phase, double scanning was selected in the next step to increase the heat transferred to the powder, and hence the degree of

consolidation and necking, whilst keeping the laser power low. A summary of the sintering effects under double scanning is listed below:

- The laser power was varied between 5-8W as the scanning speed was kept at the standard value of 2500mm/s, and same for the hatching distance which was set at 0.25mm. The amount of energy applied to the powder was insufficient to form strong layers in all cases. The build was cancelled after scanning of the first two layers, as the blade was caught on the newly formed layer of powder scanned at 5W, which demonstrated poor consolidation and resulted in increased stickiness.

- To improve consolidation and necking between the particles, and thus the sintering effect on the blend, the scanning speed was decreased to 2000mm/s to allow a longer dwell time as the laser scans the powder. However, powder exposed to 6-8W experienced degradation changing colour to yellow, while powder exposed to 5W resulted in weak layer formation.

- Based on the fact that a small increase in the ED resulting from an increase in power or decrease in speed, led to degradation of the Avicel 101 phase, it was decided to scan using a smaller hatching distance. This way the ED was possible to be maintained in safe levels, while the overlapping between the scan lines increased. The distance was set at 0.20mm while the power was set at 6W, and speed was tested at both 2000mm/s and 2500mm/s. The smaller distance applied resulted in the fabrication of complete parts as can be observed in Figure 6.2, which indicated that the degree of necking was increased improving the strength of the layers. However, there were still limitations as the ED applied at 2000mm/s was high enough that induced degradation and the part turned yellow, and also the ED applied at 2500mm/s resulted in relatively low strength.

- Considering the above effect, hatching distance was kept at 0.20mm, and the scanning speed at 2250mm/s to investigate the performance of the powder at powers of 5W to 8W. It was observed that parts scanned at 5W and 6W exhibited low stiffness, while parts scanned at 7W and 8W degraded. The ED applied using 8W was quite high that resulted in warped edges. Specifically, the blade was caught at the edges shifting slightly each layer on every run, which resulted in lack of precision, as shown in Figure 6.3.

Initial tests on the 50:50 Av/Eu blend resulted in the production of structurally stable parts. Using double layer scanning and smaller distance between the lines the heat transfer to the powder was increased, and hence the depth of fusion. Nonetheless, none of the exposure sets of parameters used resulted in optimal sintering performance. The observations revealed poor layer formation at low levels of applied energy [40]. Although, an increase in the ED gradually improved the stiffness of the parts, it resulted in degradation of the Avicel 101 phase. The selected scanning strategy during the first attempt to sinter the 50:50 Av/Eu blend is presented in Table 6.1, while the detailed laser parameters used in each test can be studied in Table 6.2.

Table 6.1: Process parameters investigated for initial sintering tests of the 50:50 Av-Eu blend

Process Parameters	Constant	Varied	
Layer thickness	0.10 mm		
Bed temperature	120°C ($T_g = 93$°C)		
Hatching power		5 - 20 W	
Scan speed		1500 - 2500 mm/s	
Contour power / speed	2500 mm/s	- (0-3) W lower than hatching power	
Hatching distance		0.20 - 0.25 mm	
Beam offset	0.15 mm		
Scan pattern		Single	Double

Table 6.2: Detailed scanning strategy for initial sintering tests of the 50:50 blend

Test/ blend	Temp (°C)	Sample	Layer Scan	Power (W)	Speed (mm/s)	Distance (mm)	C/PC P	C/PC S	Comments
Test 1 50:50 Av/Eu	120	A		5	2500	0.25	5	2500	• 1 layer • Powder was poorly sintered for A, B due to low power • C, D fumed and turned brown
		B		10			7		
		C		15			12		
		D		20			17		
Test 2 50:50 Av/Eu	120	A		5	2500	0.25	5	2500	• 1 layer • Poor consolidation • Formation of sticky membranes
		A1		6					
		A2		7					
		A3		8					
		B		9	2500	0.25	6	2500	• 1 layer • Layers were brittle and friable
		B1		10			7		
		B2		11			8		
		B3		12			9		
		C		13	2500	0.25	10	2500	• 1 layer • Stable layers • Layers turned yellow/brownish
		C1		14			11		
		C2		15			12		
		C3		16			13		
		D		17	2500	0.25	14	2500	• 1 layer • Ductile solid layers • Layers fumed and turned brown
		D1		18			15		
		D2		19			16		
		D3		20			17		
Test 3 50:50 Av/Eu	120	A		5	2500	0.25	5	2500	• 2 layers • A disintegrated • B was fragile • C, D were brittle
		B		6					
		C		7					
		D		8					
Test 4 50:50 Av/Eu	120	A		5	2000	0.25	5	2500	• 2 layers • A was brittle • B, C, D turned yellow
		B		6					
		C		7					
		D		8					
Test 5 50:50 Av/Eu	120	A		6	2500	0.20	5	2500	• Complete parts • A was weak • B was denser and stiffer but warped and fumed
		B			2000				
Test 6 50:50 Av/Eu	120	A		5	2250	0.20	5	2500	• 18 layers • A was brittle • D degraded and warped due to high ED
		B		6					
		C		7					
		D		8					

Figure 6.2: Hatching distance at 0.20mm resulted in multilayer formation for the 50:50 Av/Eu blend in Test 5. The yellow colour indicated degradation when scanned at 2000mm/s, while at 2500mm/s the edges were fragile

Figure 6.3: Sintering performance of the 50:50 Av/Eu blend in Test 6: Weak layer bonding under laser power of 5W (A); fragile edges and low strength at 6W (B); fragile edges and degradation at 7W (C); degradation and layer misplacement at 8W (D)

Towards the optimisation of the 50:50 Av/Eu blend it was decided to investigate various EDs at laser power of 6W and 7W, as at these values the sintering effect was relatively improved, showing minimum degradation and acceptable part stiffness. A wide range of scanning speeds between 2000mm/s and 2900mm/s in combination with varied hatching distance at the range of 0.18-0.22mm were explored, to identify the optimal combination of exposure parameters that increased the binding mechanism between the two phases, while at the same time prevented degradation of Avicel 101. The sets of laser parameters used are presented in Table 6.3 and Table 6.4 and in Figure 6.4. A 3D map of the total scanning strategy was produced in Figure 6.5, in which the optimal sintering region can be observed.

Table 6.3: Process parameters investigated for optimised sintering of the 50:50 Av/Eu blend

Process Parameters	Constant	Varied
Layer thickness	0.10 mm	
Bed temperature		120 - 125°C ($T_g = 93$°C)
Hatching power		6 - 7 W
Scan speed		2000 - 2900 mm/s
Contour power / speed	5 W	2000 - 2500 mm/s
Hatching distance		0.18 - 0.22 mm
Beam offset	0.15 mm	
Scan pattern	Double	

Table 6.4: Detailed scanning strategy for the optimisation of the 50:50 Av/Eu blend

Test/ blend	Temp (°C)	Sample	Hatching					Comments
			Power (W)	Speed (mm/s)	Distance (mm)	C/PC		
						P	S	
Test 7 50:50 Av/Eu	120	A	6	2100	0.20	5	2500	• 19 layers • A, B were dense but fumed • C had the best effect although it turned yellowish • D was brittle
		B		2200				
		C		2300				
		D		2400				
Test 8 50:50 Av/Eu	120	A	6	2300	0.21	5	2500	• Complete parts • A was dense • B was brittle • C was weak • D was stiff but turned yellow
		B		2350	0.20			
		C		2300	0.22			
		D		2350	0.18			
Test 9 50:50 Av/Eu	120	A	6	2300	0.21	5	2000	• 2 layers • Higher ED applied on the contour resulted in warping • Parts were dislodged and build was cancelled
		B						
		C						
		D						
Test 10 50:50 Av/Eu	120	A	7	2600	0.20	5	2500	• 19 layers • A, B were uniform but fumed • C, D showed relative low strength
		B		2700				
		C		2800				
		D		2900				
Test 11 50:50 Av/Eu	120	A	7	2300	0.21	5	2500	• 18 layers • High ED resulted in denser parts • A, B warped • D was relative weak
		B		2400				
		C		2500				
		D		2600				
Test 12 50:50 Av/Eu	120	A	7	2400	0.21	5	2500	• Complete parts • A was dense and stiff but too thick • B was uniform
		B		2500				
Test 13 50:50 Av/Eu	125	A	7	2500	0.21	5	2500	• Complete parts • There was no repeatability • Increased Temp increased stiffness
		B						
		C						
		D						
Test 14 50:50 Av/Eu	125	A	7	2500	0.21	5	2500	• Complete parts • 2 parts at a time minimised anisotropy • Parts were uniform
		B						
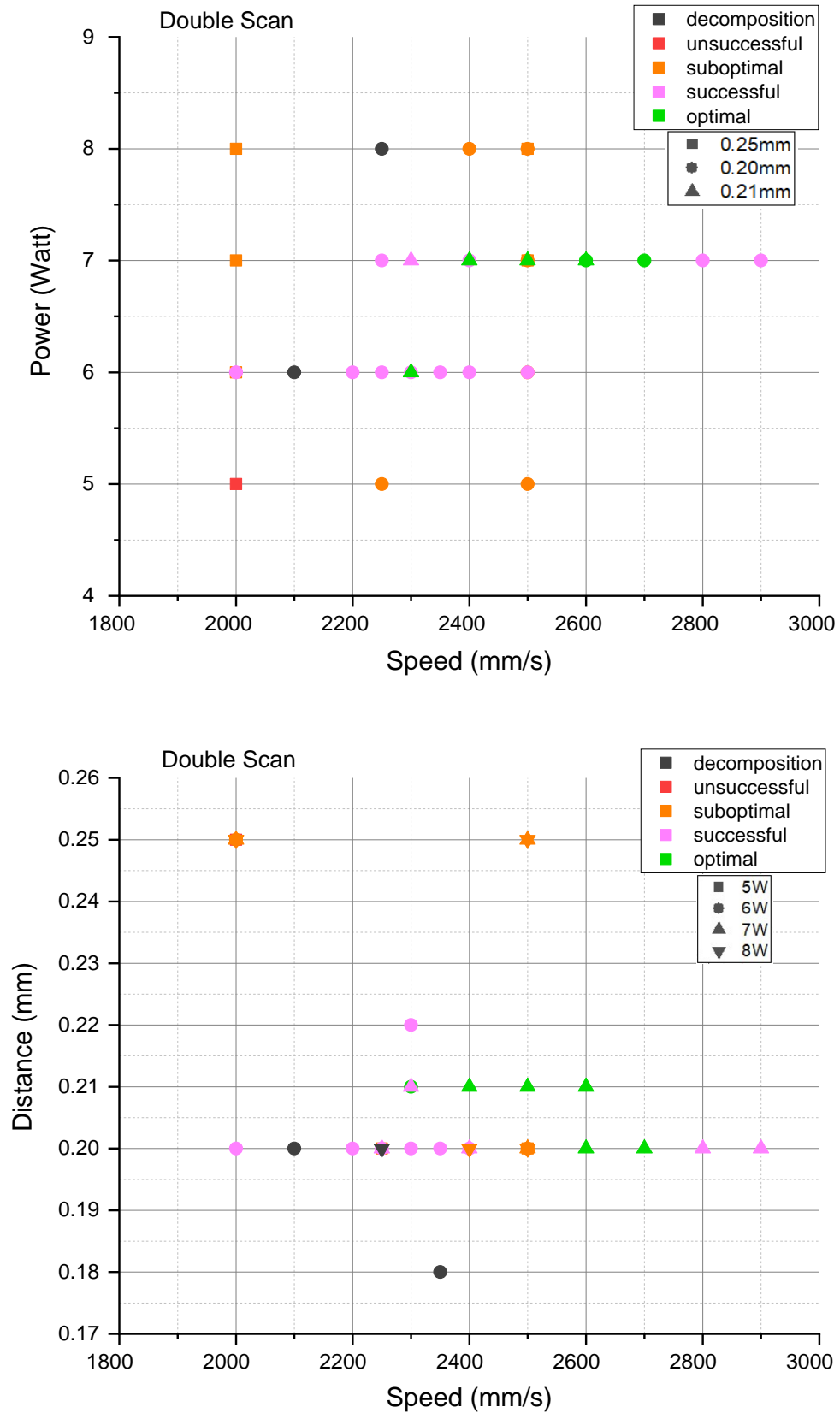
Figure 6.4: Processing map of the 50:50 Av/Eu blend under double scanning mode; plot power (top)/distance (bottom) against speed; constant parameters: layer thickness 0.10mm, beam offset 0.15mm
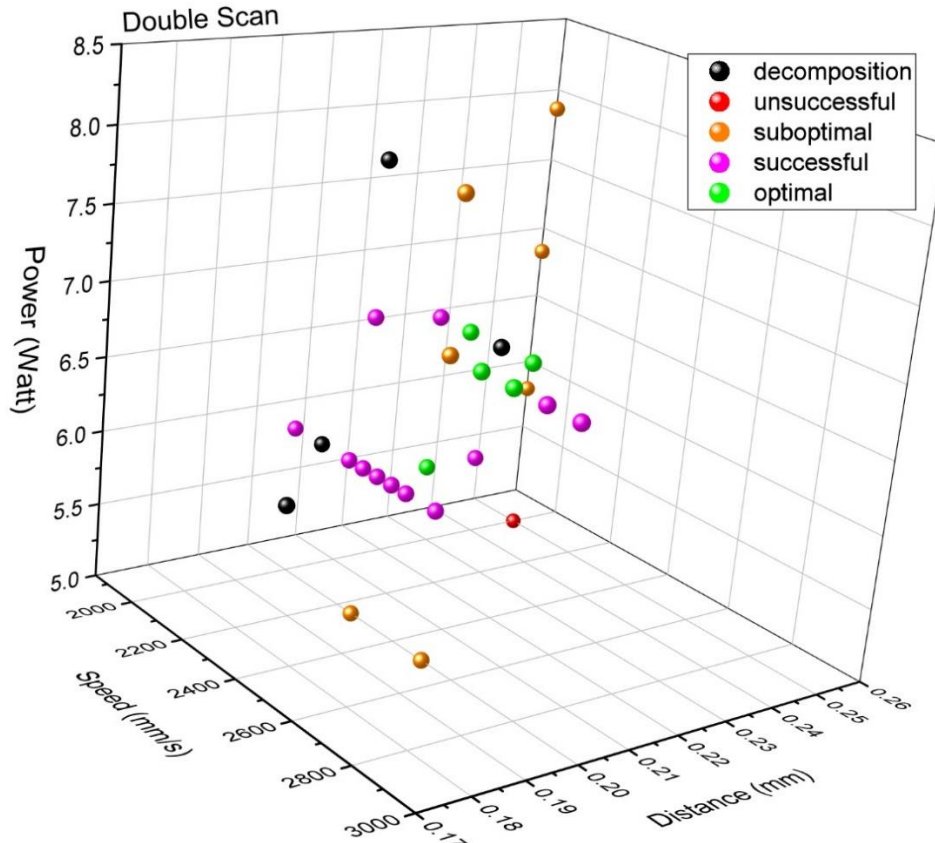
Figure 6.5: 3D Processing map of the 50:50 Av/Eu blend under double scanning mode. Plot distance against speed against power. Constant parameters: layer thickness 0.10mm, beam offset 0.15mm

The information given in the above graphs (Figure 6.4, Figure 6.5) revealed an optimum sintering area between 6W and 7W of laser power, at a scanning rate of 2300-2700mm/s, and 0.20-0.21mm distance between the lines. In this region the 50:50 Av/Eu blended powder formed uniform and stable parts. A brief discussion on every step taken towards the optimisation of the laser parameters during the final sintering tests of the 50:50 Av/Eu blend, is presented below:

- Power was set at 6W as a starting point to minimise degradation, while the distance was kept at 0.20mm. Scanning speed was varied between 2100mm/s and 2400mm/s. High ED resulting from 2100mm/s and 2200mm/s increased stiffness, which was desirable, but led to fuming. Increased speed at 2400mm/s resulted in fragility. The part formed at 2300mm/s showed high potential, presenting increased density and layer strength, however it changed colour to yellow.

- A narrow approach was applied setting the speed at 2300-2350mm/s at varied distances of 0.18-022mm in order to reduce degradation to minimum and increase the stiffness. The powder colour remained white in most cases, however the selected exposure parameters resulted in relative low ED which failed to improve the strength. In Figure 6.6 it can be observed that the finished parts presented low sphericity at the corners and friable edges.

- At this point, in order to improve precision, the ED at the contour was increased to improve the strength at the edges. Using the best set of the hatching parameters at 6W, 2300mm/s and 0.21mm, the contour speed was decreased to 2000mm/s. However, the layers warped at the edges and the build failed, as the blade dislodged the parts from the bed area.

- Based on the results so far, the laser power was increased to 7W and the distance was decreased to 0.20mm to improve the stiffness of the parts. The speed was increased to 2600-2900mm/s to allow sintering without degradation and explore a possible area at which the mechanical performance could be enhanced. Nevertheless, the scanning strategy followed resulted in fuming due to the excessive ED applied compared to the previous test.

- In the next step the distance was set at 0.21mm, while the speed was decreased to avoid compromise of the mechanical strength. The resulted parts scanned at 2400mm/s and 2500mm/s were dense with relative high precision and no evidence of degradation, as the powder maintained its white appearance (Figure 6.6). The two parts were repeated in a subsequent build to confirm the outcome. It was observed that the part scanned in the higher ED using 2400mm/s demonstrated decreased dimensional accuracy, as it was relative thick, and the part scanned at 2500mm/s had the best sintering performance.

- Using the optimum set of parameters at 7W, 2500mm/s and 0.21mm, four parts were attempted to be built at elevated temperature of 125°C, in order to improve adhesion of the layers, and further increase the density and the stiffness. The finished parts demonstrated indeed improved density and strength, however there was a noticeable reduction in precision. In the previous successful attempt, the build was set to scan only two parts instead of four. It was then assumed that there was temperature anisotropy in the chamber, which affected the final precision of

the parts. Therefore, the build was set to scan only two parts in the last attempt, which eventually, resulted in the best sintering performance observed so far.

In the last part of this investigation it was discovered that there was uneven temperature distribution in the chamber. It has been well documented in literature that thermal inconsistencies in the build chamber affected sintering according to the location of the parts on the bed platform, which led to inconsistencies in the mechanical properties of the parts [6], [71], [79], [194], [206], [211]. Based on these studies the powder bed surface is hotter in the middle and upper side of the build, while is cooler on the sides and bottom end, which is closer to the chamber door. Observations during processing of the 50:50 Av/Eu blend, revealed that the parts placed close to the upper side of the chamber experienced uniform sintering, whilst the parts placed close to the bottom experienced small shifting of the layers when the blade passed over to deposit fresh powder. It was then assumed that parts were subjected to heterogeneous cooling due to the uneven temperature distribution in the chamber resulting from convection from the environment, as is demonstrated in Figure 6.7. It was evident that the increased performance observed in the last sintering test of the 50:50 Av/Eu blend, resulted from the reduction of the inconsistencies on the powder surface temperature, as only two parts were selected to be scanned in the middle and upper position of the build area.

Considering that in the present investigation four parts were selected to be scanned in most tests that were placed in the middle position of the build platform and very close to each other, the difference in the surface temperature of each part and therefore sintering, should have been relatively small. Nonetheless, efforts on sintering the 50:50 Av/Eu blend, revealed a very narrow processing window due to the Avicel 101 phase, which has been proved already less able to adapt changes in the applied energy input, resulting in degradation. This behaviour prevented processing of the 50:50 Av/Eu blend under the optimum exposure parameters that could potentially lead to significantly improved density and mechanical performance of the finished parts. Considering that sintering was not optimal, it is most likely to be discovered that their mechanical behaviour had been diminished due to insufficient degree of consolidation and necking and the increased number of voids, similar to other reports [20], [21], [29], [42]–[44], [205]. Nevertheless, experiments conducted demonstrated that the mixed powder was processable by conventional LS, despite the difficulties introduced by the Avicel 101 phase and the

variations in the temperature. In practice parts were built with success with no other apparent difficulties in terms of powder flow and deposition, layer adhesion, shrinkage and curling, etc.

Subsequent builds were set in order to produce parts for quality analysis and mechanical testing, which follows in the next chapter. The best sintering performance was found to result when applying 0.0133 J/mm^3 of ED, which was calculated based on equation 2.1, under an optimised combination of the laser exposure resulting from 7W at a scanning rate of 2500mm/s and 0.21mm distance between the lines. This scanning strategy was concerned by positioning the parts in the upper centre of the building area to reduce the thermal gradients, as presented in Figure 6.8. Parts were produced successfully with improvements to the geometrical accuracy and density, as can be observed in Figure 6.9.
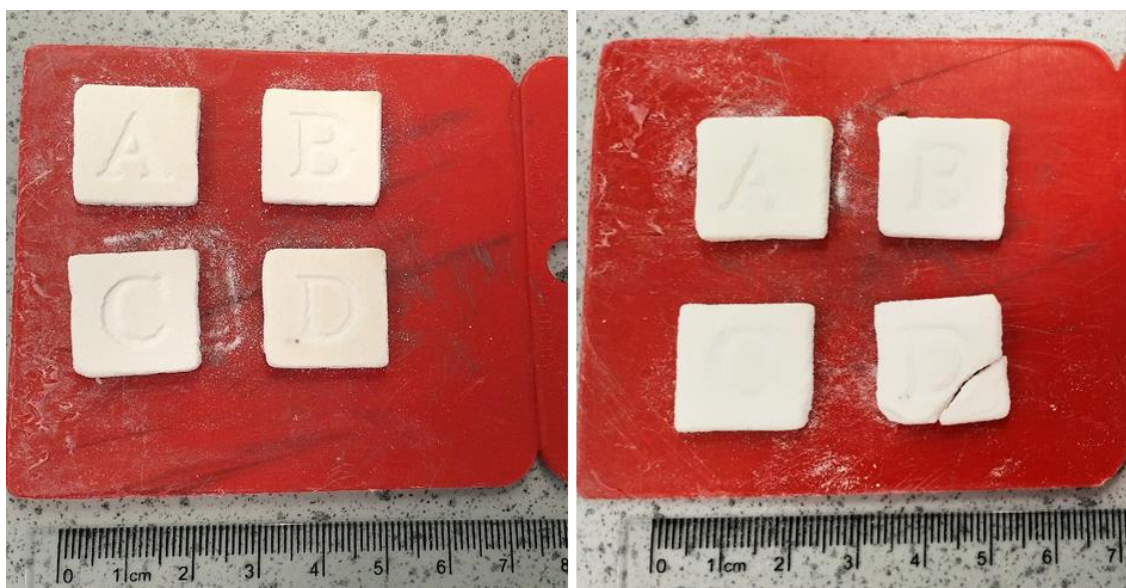
Figure 6.6: Reduction of degradation towards optimisation following a scanning strategy of relative low ED scanning at 6W, 2300-2350mm/s and 0.18-0.22mm (Test 8 left). Further improvement of degradation at 7W, 2400mm/s and 0.21mm resulted in decreased stiffness (Test 11 right)
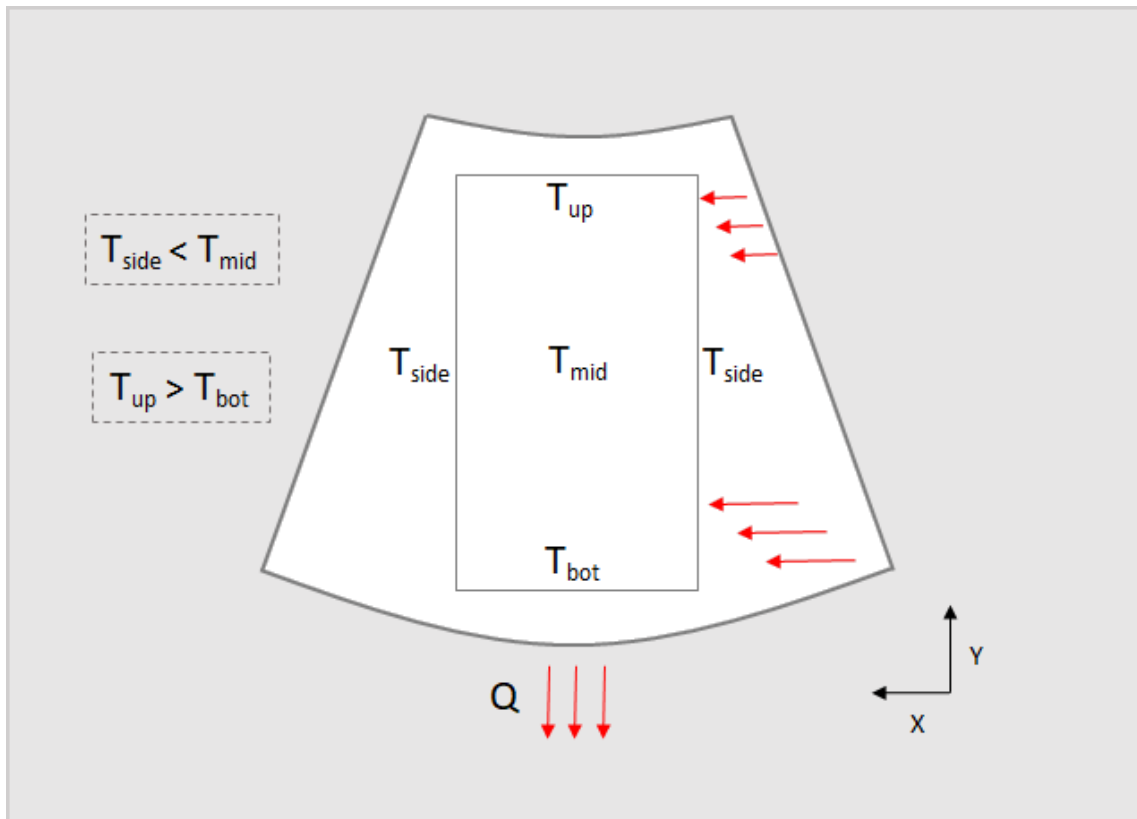
Figure 6.7: Schematic representation of the differences in the heat distribution in the P100 build chamber
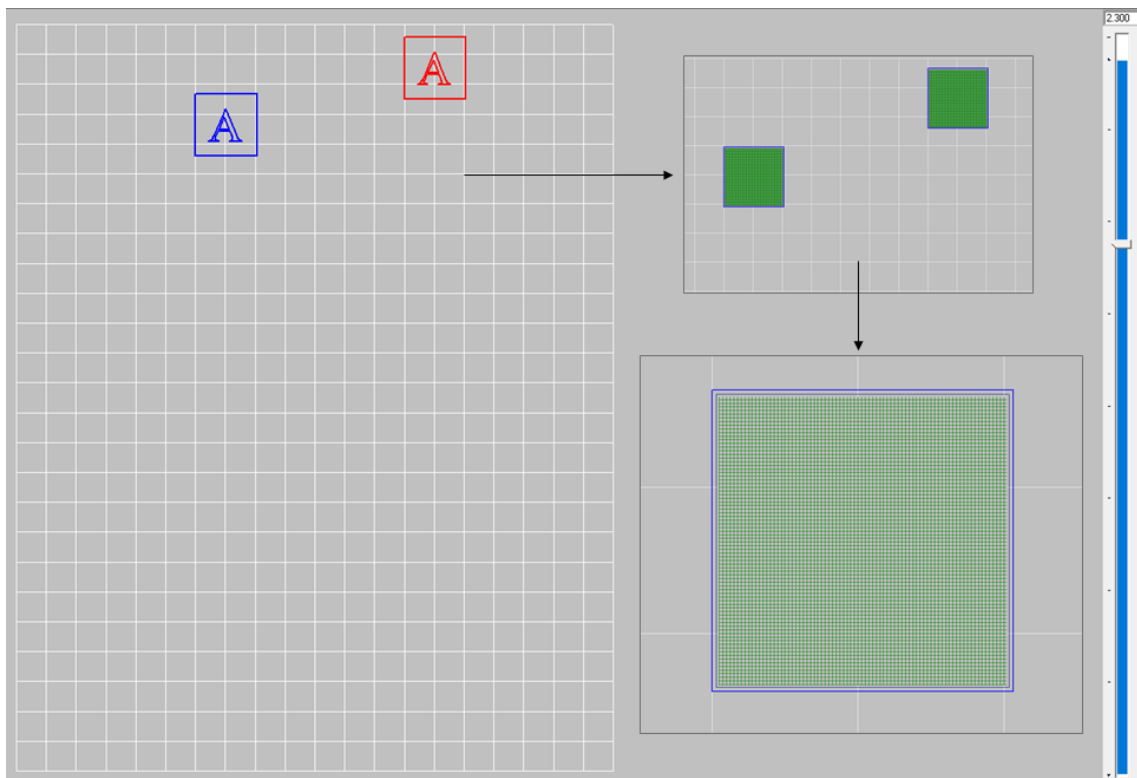
Figure 6.8: Build position and scanning pattern of the 50:50 Av/Eu parts; the green scan lines represent the x-y direction of the hatching and the blue line the contouring

Figure 6.9: Increased precision and clear features for the 50:50 Av/Eu parts produced at ED of 0.0133 J/mm^3; scanned at 125°C in the centre top area of the build platform

6.2.2 Processing of the 63:37 Av/Eu blend

Sintering tests for the 63:37 Av/Eu blended powder were designed according to the parameters used in the previous section. The Avicel 101 amount in this blend was high, therefore an optimal sintering would require high energy input in order to allow the Eudragit L100-55 phase to create an extended necking network and bind efficiently the particles together [20], [29], [41], [43], [205]. However, based on the results so far, a potential increase in the ED would induce degradation of the Avicel 101 phase. Considering the fast degradation of the material, the sintering window of the 63:37 Av/Eu blend was expected to be very narrow, therefore, the scanning strategy followed in this section was adapted to only a few small changes.

Specifically, the processing temperature was kept constant at 125°C. It has already been proven during this study that an increase in the bed temperature increases the mobility of the polymer chains, thus the degree of particle consolidation and the resulted density of the parts. Therefore, one would expect to apply a higher bed temperature than 125°C to improve the sintering effect on the 63:37 Av/Eu blend. However, above this temperature both the components in this blend experienced total dehydration based on the TGA results in Chapter 4. In order to avoid further degradation of the materials, it was decided to keep the temperature at a level that has already been tested safely, and thus it was set at 125°C. In addition, the laser power was kept constant at 7W, even though it was highly expected to induce partial degradation of the Avicel 101 phase. Considering the observations when sintering at 5W or 6W in section 6.2.1, a lower value of laser power would most likely result in poor consolidation. The available options for sintering the 63:37 Av/Eu blend included adjustments in the laser scan speed and hatching distance, in an attempt to identify a region that provided the minimum layer adhesion needed for the production of structurally stable parts. The approach taken towards an optimised scanning strategy for the 63:37 Av/Eu blend, is described in detail below:

- As a starting point two parts were scanned in double scan mode using 7W and 0.21mm, varying the speed at 2500mm/s and 1500mm/s, in order to explore the effect under opposite levels of ED applied on the system. Only one layer was formed in both cases. The layer formed at 2500mm/s was poorly sintered due to the low energy input and was impossible to manually handle. On the contrary, the layer formed at 1500mm/s resulted in severe degradation/fuming and warping of the edges, although it was observed to present increased ductility and strength.

Nonetheless, the build failed as the blade misplaced the layers from the build position.

- A narrow range of speed was applied as the initial trial proved that sintering of the blend was possible. Speed was set at 2250mm/s and 1750mm/s, which resulted in increased stability of the layers and warping with high degradation, respectively. To eliminate the degradation and to further increase the strength the speed was set at 2300mm/s and 2400mm/s. Three layers were obtained, however they exhibited increased fragility that it made impossible to handle.

- To improve consolidation of the particles and adhesion between the layers the distance was further decreased to 0.20mm, while the rest of the parameters were kept constant. Increased stability was indeed achieved and four layers were scanned. However, layers warped at 2300mm/s, while layers at 2400mm/s were still weak.

- A further decrease in distance was selected for scanning at 2400mm/s to improve the mechanical behaviour of the layers. The build failed. Scanning at 0.19mm apparently exceeded the critical point of the energy input allowed, since the layers resulted in increased warping. Although the efforts made, it was evident that the processing window of the 63:37 Av/Eu blend was extremely narrow.

- The available option left was to decrease the speed to 2350mm/s, whilst setting the distance back to 0.20mm. The resulted ED was 0.0149 J/mm^3, which allowed the build to be completed. The finished parts exhibited small curling and relative low stiffness.

- An optimised combination of hatching was used to increase stability of the finished parts and facilitate handling, cleaning and testing. The downskin was used to scan the first 4 layers at constant values for the laser power and distance, while decreasing the speed to 2300mm/s. The ED increased at 0.0152 J/mm^3 at the bottom layers and created a robust base for the parts. The rest of the layers were scanned on top of that base, using the hatching values aligned with the previous test. The resulted build was successful, and the parts exhibited increased strength and precision.

The application of the downskin allowed initial sintering of strong and dense layers, which formed a robust base for subsequent scanning of multilayers with use of lower

energy input. This way the stability was increased, while the warping was minimised and the finished parts demonstrated improved density, and hence stiffness. Specifically, the downskin increased the ED applied on the first four layers, which increased the temperature at the bottom. A subsequent raise of the temperature occurred for the newly sintered layer and was repeated at the next layer until the end of the process. Therefore, the heat transferred from the bottom to the top layers eventually improved the particle consolidation between the two phases, and led to improved adhesion and overall structural stability [7], [53], [66].

All the sintering details are presented in Table 6.5 and Table 6.6. Figure 6.10 illustrates the narrow sintering region applicable highlighting the limited available options to optimise the performance of the 63:37 Av/Eu blend. Sintering proved very challenging due to the increased amount of Avicel 101 in the composition. The low amount of Eudragit L100-55 was insufficient to bind the solid Avicel 101 particles and hold the test parts together. Nevertheless, parts were produced for mechanical testing applying the scanning strategy of the downskin used in the last attempt. The total ED was 0.015 J/mm^3, which resulted from the combination of the two different exposure sets of parameters used at the bottom and the top of the parts. Parts were produced successfully, however they appeared to have a light-yellow colour, which indicated the beginning of degradation, as shown in Figure 6.11. The presence of high surface roughness and unmolten powder on the surface of the parts is clear from the picture. The highly porous nature of the parts it was strongly expected to result in inferior mechanical performance [42], [155], [204].

Table 6.5: Process parameters investigated for sintering the 63:37 Av/Eu blend

Process Parameters	Constant	Varied
Layer thickness	0.10 mm	
Bed temperature	125°C (T_g = 93°C)	
Hatching power	7 W	
Scan speed		1500 - 2500 mm/s
Contour power / speed	5W / 2500 mm/s	
Hatching distance		0.19 - 0.21 mm
Beam offset	0.15 mm	
Scan pattern	Double	
Downskin (S / D)	2300 mm/s / 0.20mm	

Table 6.6: Detailed scanning strategy for sintering the 63:37 Av/Eu blend

Test/ blend	Temp (°C)	Sample	Power (W)	Speed (mm/s)	Distance (mm)	C/PC P	C/PC S	Comments
Test 1 63:37 Av/Eu	125	A	7	2500	0.21	5	2500	• 1 layer • A disintegrated • B was dense but fumed and turned dark brown
		B		1500				
Test 2 63:37 Av/Eu	125	A	7	2250	0.21	5	2500	• 1 layer • A was stable • B fumed and warped
		B		1750				
Test 3 63:37 Av/Eu	125	A	7	2300	0.21	5	2500	• 3 layers • Layers were weak and misplaced
		B		2400				
Test 4 63:37 Av/Eu	125	A	7	2300	0.20	5	2500	• 4 layers • A warped and failed • B was stable but weak
		B		2400				
Test 5 63:37 Av/Eu	125	A	7	2400	0.19	5	2500	• 3 layers • Parts warped and were dislodged
		B						
Test 6 63:37 Av/Eu	125	A	7	2350	0.20	5	2500	• Complete parts • Small warping • Decrease in the ED decreased strength
		B						
Test 7 63:37 Av/Eu	125	Hatching	7	2350	0.20	5	2500	• Complete parts • Build was successful • Parts were uniform
		Downskin	7	2300	0.20	5	2500	
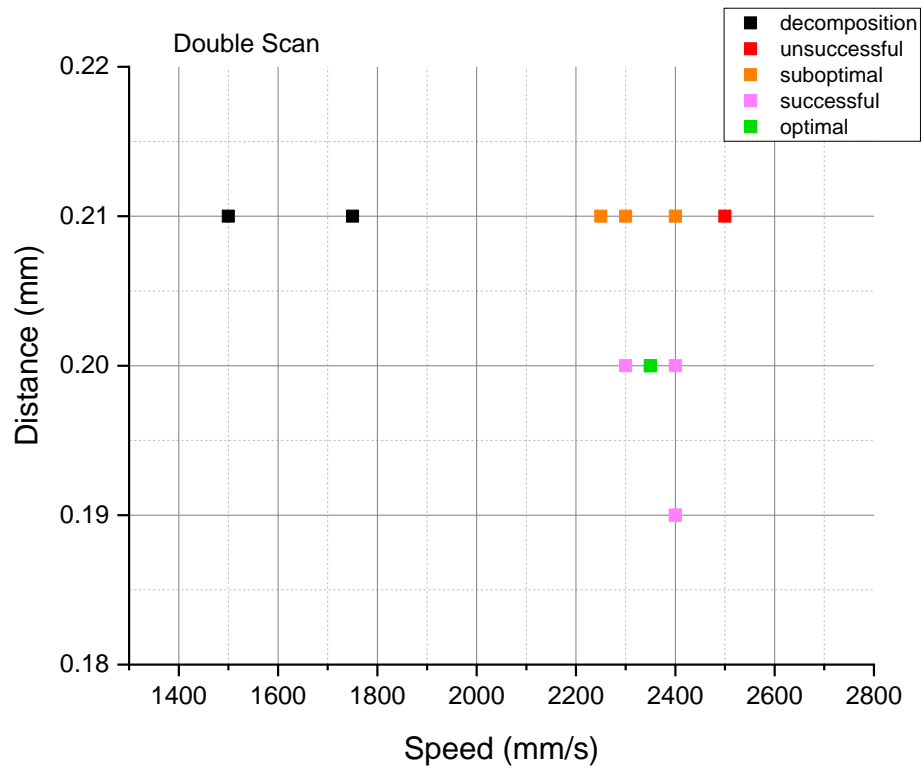
Figure 6.10: Processing map of the 63:37 Av/Eu blend under double scanning mode; plot distance against speed; constant parameters: bed temperature 125°C, layer thickness 0.10mm, laser power 7W, beam offset 0.15mm
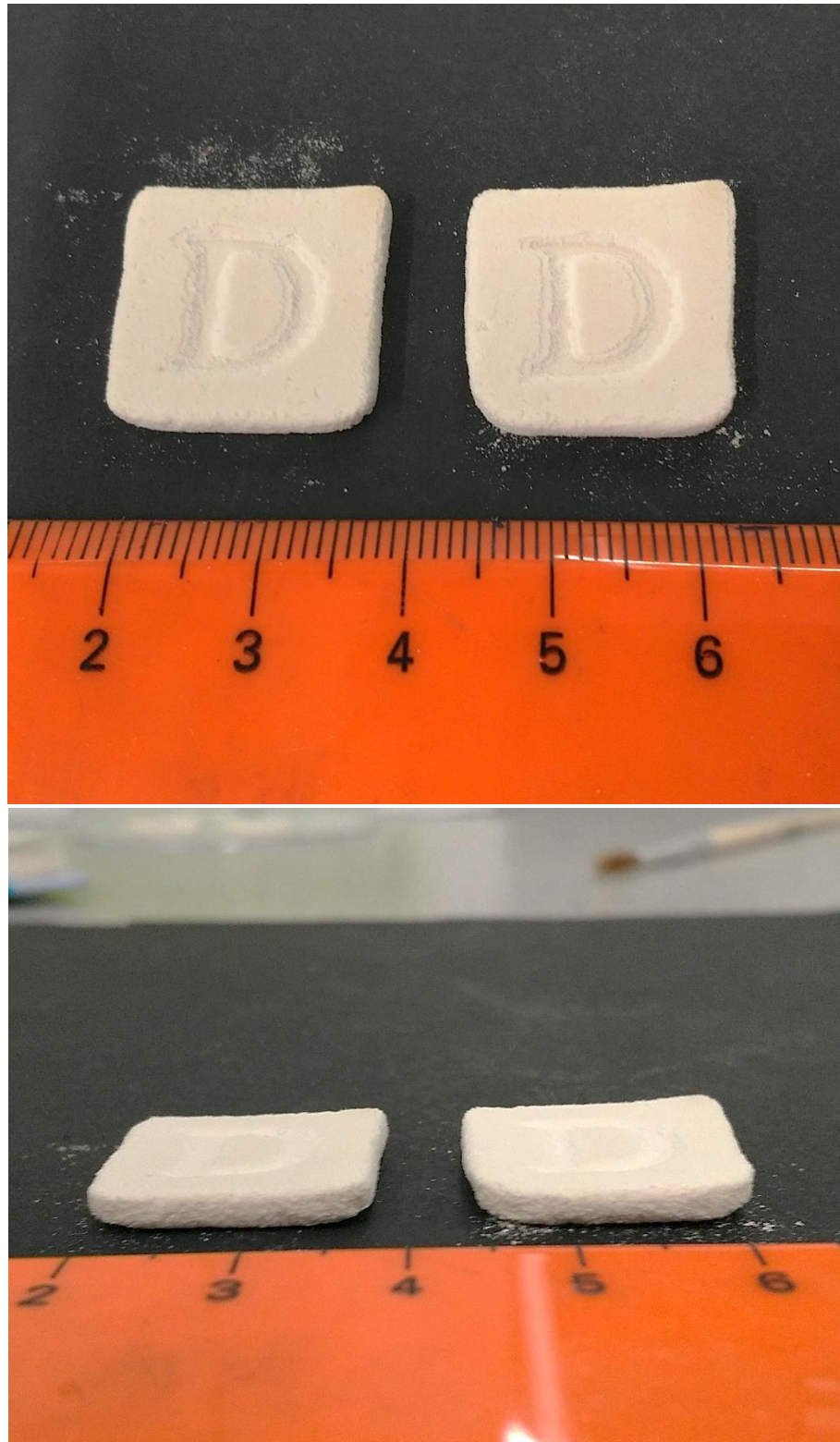
Figure 6.11: High roughness and loose powder at the surface of the 63:37 Av/Eu parts, scanned at ED of 0.015 J/mm^3; the powder appears yellowish due to degradation

6.2.3   Processing of the 37:63 Av/Eu blend

The Eudragit L100-55 dispersed phase was higher in this composition, and thus it was expected to result in dense uniform parts without apparent difficulties [20], [41], [42], [205]. The material exhibited high processability and suitability with LS in previous tests, therefore the exposure parameters used for processing the 37:63 Av/Eu blend were selected according to the preliminary sintering experiments in section 5.5. During those tests Eudragit L100-55 yielded fully-dense parts with increased stability and stiffness using double scanning mode at laser power and hatching distance of 6W and 0.25mm respectively, in a relative wide region of speeds between 2100mm/s and 2500mm/s. Based on these results, to begin with the scanning strategy followed in this section explored the sintering performance of the 37:63 Av/Eu blend under the same exposure conditions, in order to estimate the behaviour of the double-phase feedstock. Furthermore, the bed temperature was set at 120°C, a degree higher than the optimised processing conditions in section 5.5, to increase the degree of consolidation of the particles due to the presence of Avicel 101 in the mixture. A further increase in the temperature was not attempted at this point to avoid sticking of the Eudragit L100-55 on the recoating mechanism, as previously observed in Chapter 5. A summary of the observations while sintering the 37:63 Av/Eu blend, is listed below:

- Initial tests resulted in complete builds and stable parts. Despite the promising outcome, scanning at 2500mm/s resulted in relative fragility, indicating that the energy input was inadequate to provide parts with high layer adhesion and density. In contrast, scanning at 2100mm/s induced warping and degradation, as a light yellow colour was observed.

- Based on the observations in the previous sections, the necking between the particles needed to be improved. Therefore, the distance was decreased to 0.21mm and 0.23mm, to increase the overlapping between the scan lines and improve the bonding of the two phases. At the same time an average speed of 2400mm/s was used to prevent degradation and strike a balance between the two sintering effects. However, the finished parts did not present a significant change in properties compared to the previous test, as warping and low strength were observed respectively.

- Considering the fact that the optimal laser power for sintering the other two blends was at 7W, the power was raised at this value to boost the rate of energy delivered

to the powder. To avoid degradation, the speed and the distance were increased to 2500mm/s and 0.23-0.25mm, respectively. The increased energy input resulted in parts with increased ductility, which indicated that the Eudragit L100-55 phase bound the solid Avicel 101 particles together and improved density. Nonetheless, the part scanned at 0.25mm was relative weak, and the part scanned at 0.23mm exhibited warped edges.

- At this point the distance was set at 0.24mm to explore the possibility to scan parts with increased stiffness, while minimising the warping effect. The finished parts demonstrated improved density and strength, however the exposure resulted in dimensional growth and low precision.

- Towards the optimisation of the process, the temperature was decided to be increased, while the laser parameters were kept constant. The Eudragit L100-55 phase did not show any sticking behaviour so far, therefore the temperature was set at 125°C aligned with the process conditions in the previous sections (see 6.2.1 and 6.2.2), to further improve the bonding of the layers, which would further increase the density, and hence the precision. Indeed, the dimensional accuracy and the stiffness of the finished parts were remarkably improved, although the powder had an off white appearance.

- Considering the improved mechanical performance resulting from the higher temperature, the initiation of degradation was considered a drawback. In order to slightly reduce the heat transferred to the powder and at the same time maintain the enhanced properties of the parts, the hatching distance was increased to 0.25mm. The parts produced with the combination of increased bed temperature, laser power, and hatching distance, exhibited high density, strength, precision and a white appearance.

Sintering tests on the 37:63 Av/Eu blend were met with success. A suitable processing window was found applying adjustments mainly on the hatching distance, and can be observed in Figure 6.12. The best set of laser parameters used included a laser power of 7W, at a scanning rate of 2500mm/s, with 0.25mm distance between the lines. The latter two laser parameters were actually the default values of the P100. The bed temperature was set at 125°C, which increased the heat between the layers and facilitated the production of uniform parts with increased quality. The experimental sets of parameters are presented in Table 6.7 and Table 6.8.

Subsequent builds were designed using the optimised combination of exposure parameters described above, in order to obtain parts for mechanical testing. The ED applied on the blended powder was 0.0112 J/mm³, which was relative low in comparison with the other two blend compositions used. In spite this, the parts produced exhibited good handling stability and mechanical performance, revealing that the minimum level of the ED used was adequate enough to impart particle consolidation, and hence result in high layer adhesion. The sintered parts demonstrated an intact structure with high dimensional accuracy and enhanced features that can be seen in Figure 6.13.
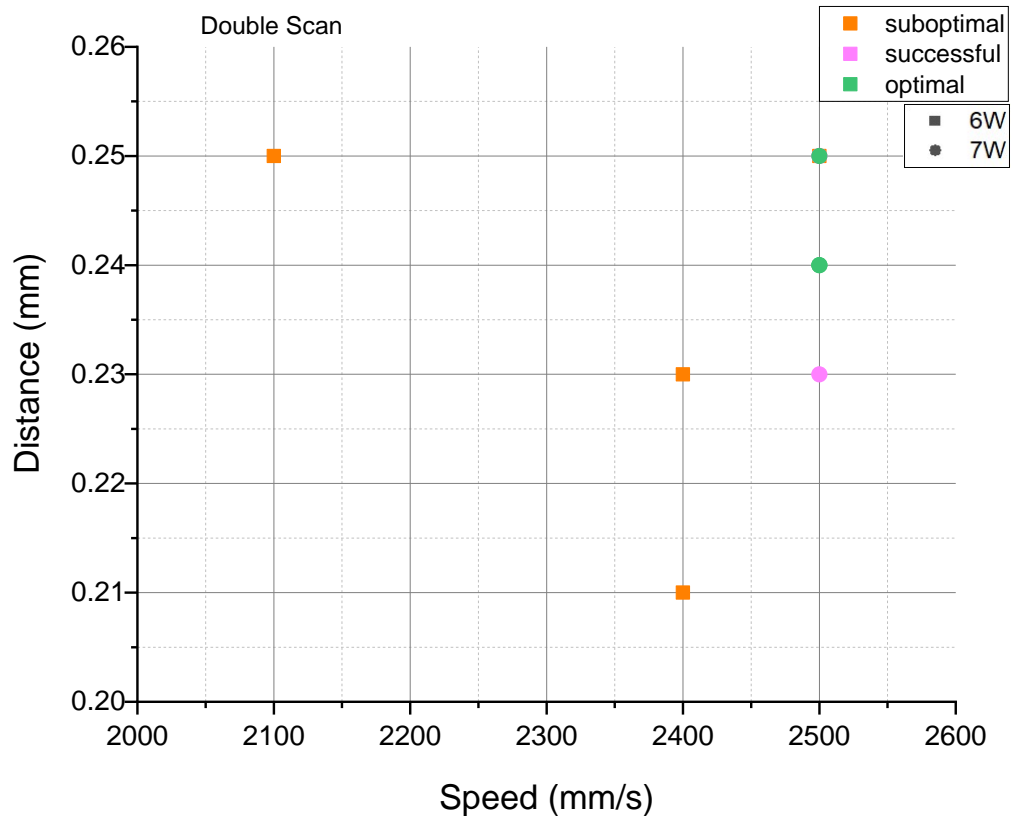
Figure 6.12: Processing map of the 37:63 Av/Eu blend under double scanning mode; plot distance against speed; constant parameters: layer thickness 0.10mm, beam offset 0.15mm

Table 6.7: Process parameters investigated for sintering the 37:63 Av/Eu blend

Process Parameters	Constant	Varied
Layer thickness	0.10 mm	
Bed temperature		120 - 125°C ($T_g = 93$°C)
Hatching power		6 - 7 W
Scan speed		2100 - 2500 mm/s
Contour power / speed	5W / 2500 mm/s	
Hatching spacing		0.21 - 0.25 mm
Beam offset	0.15 mm	
Scan pattern	Double	

Table 6.8: Detailed scanning strategy for sintering the 37:63 Av/Eu blend

Test/ blend	Temp (°C)	Sample	Hatching Power (W)	Speed (mm/s)	Distance (mm)	C/PC P	C/PC S	Comments
Test 1 37:63 Av/Eu	120	A	6	2500	0.25	5	2500	• Complete parts • A shifted and was friable • B warped due to high ED
		B		2100				
Test 2 37:63 Av/Eu	120	A	6	2400	0.23	5	2500	• Complete parts • A was stable but weak • B warped and was misplaced
		B			0.21			
Test 3 37:63 Av/Eu	120	A	7	2500	0.25	5	2000	• Complete parts • Increased ductility • A was relative weak • B warped and was misplaced
		B			0.23			
Test 4 37:63 Av/Eu	120	A	7	2500	0.24	5	2500	• Complete parts • Parts were uniform and dense but grew in thickness
		B						
Test 5 37:63 Av/Eu	125	A	7	2500	0.24	5	2500	• Complete parts • Observed degradation • Increased temperature improved density and dimensional accuracy
		B						
Test 6 37:63 Av/Eu	125	A	7	2500	0.25	5	2500	• Complete parts • Uniform and dense parts • Increased precision
		B						
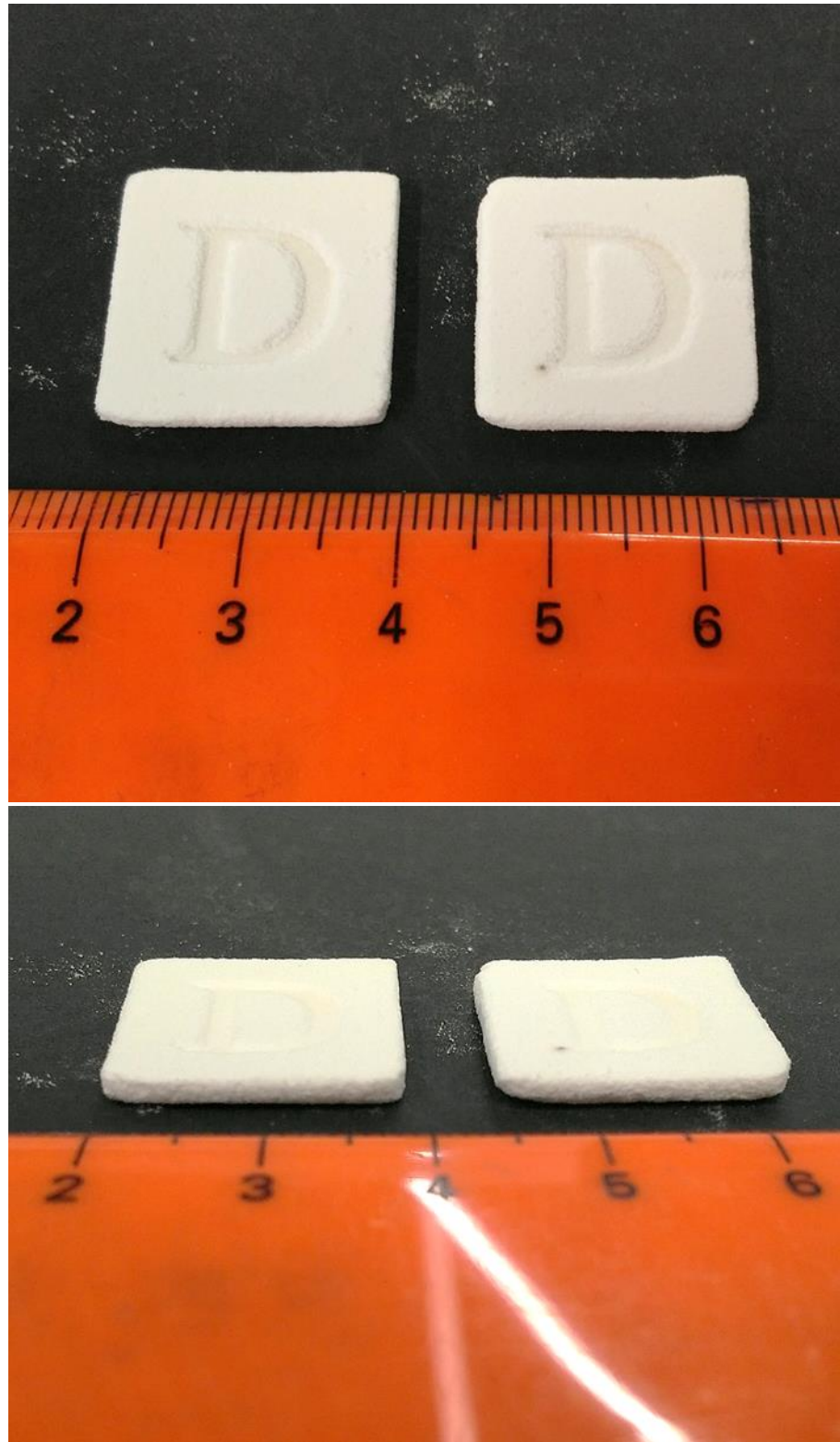
Figure 6.13: 37:63 Av/Eu parts scanned at ED of 0.0112 J/mm^3 exhibited high dimensional accuracy and enhanced features

6.3 Summary

Sintering of powder blends has been achieved in Chapter 6, showing the potential of LS to process pharmaceutical formulations resulting in solid tablets. Although, the processability of the blends presented limitations, it was demonstrated that the high-temperature Avicel 101 particles can be bound together without direct melting or sintering, using Eudragit L100-55 as a binder between the solid particles of Avicel 101, and sintering solid parts. Therefore, Eudragit L100-55 determined the processing window, however Avicel 101 determined the level of material degradation (turning yellow to brown) depending on the level of dehydration. Since the quality of Avicel 101 was strongly dependent on the energy input, the powder formulations were processed using relatively low ED to avoid degradation. Sintering tests revealed a linear relationship of the ED to the part density that was linked to the parts' handling stability, and further the part dimensions that were linked to part precision. Particularly, increased densification and thickness was achieved at higher energy levels, while increased dimensional accuracy was achieved at lower energy levels. A summary of the observations linked to the ED, is presented in Table 6.9 providing a comparison between the powder blends.

Table 6.9: Sinter-ability of the powder blends

Parts	Min ED (J/mm³)	Max ED (J/mm³)	Optimal ED (J/mm³)	Degradation	Stability	Precision
37:63 Av/Eu	0.0096	0.0122	0.0112	✓	✓	✓
50:50 Av/Eu	0.0119	0.0145	0.0133	—	✓	—
63:37 Av/Eu	0.0133	0.0222	0.015	✗	✗	✗

Since Avicel 101 presented low sinter-ability and high degradation rates, the ED used to sinter the powder formulations was very low, therefore, the sintered parts presented high porosity and relatively good stability. The resultant porosity within the microstructure of the parts was related to the final quality and pharmaceutical functionality of the printed tablets, which were both thoroughly investigated in the following chapter.

CHAPTER 7   QUALITY ANALYSIS OF LASER SINTERED PARTS

7.1   Introduction

Laser Sintering experiments in Chapter 6 revealed the strong connection between the laser parameters and the final properties of the built parts. Chapter 7 attempts to establish a correlation between the main LS influential processing factors in regard to the density and the mechanical properties of the final parts. An enhanced understanding of this interaction could contribute to the control of the microstructure for improved repeatability and part quality, and further, for the design of improved matrix-forming powder formulations and new process strategies to meet pharmaceutical design criteria of oral solid dosage forms.

The following sections analyse the quality of the sintered parts, which were compared to the ED used to sinter the parts in line with previous studies [5]–[18]. The part quality was assessed in terms of strength, precision and morphology. Firstly, routine pharmacopoeial tests evaluated the sintered tablet properties, such as tablet strength and friability, to ascertain the sustainability of the fabricated parts. In addition, disintegration characteristics revealed the corresponding tablet functionality, which was very important for the AM pharmaceutical research and development. Finally, the microstructure and the mechanical properties were investigated using imaging, dynamic and indentation scanning techniques that characterised the surface roughness and manufacturing-induced porosity of the parts and were related to the mechanical response, which were critical for the evaluation of the sintering quality linked to the process parameters and material composition.

7.2   Mass and Density

The first step in the analysis was the evaluation of the mass and density of the fabricated parts. Measurements of each feature were recorded, averaged and compared using the percentage difference of the deviation for each set of parts. The energy density ED, was used to relate the thickness and the sintered density of the parts with the process parameters and the material composition. As has been described in Chapter 2, the ED was

the ratio of the fill laser power used divided by the laser scan speed, and the hatching distance (line spacing) [86]. Therefore, the results of statistical analysis provided important information about the effectiveness of the scanning strategy compared to the material ratio and are presented in Table 7.1.

Table 7.1: Average dimensions and sintered density of the parts

Parts	Energy Density (J/mm³)	Length (mm)	Width (mm)	Height (mm)	Volume (mm³)	Mass (mg)	Sintered Density (mg/mm³)
37:63 Av/Eu	0.0112	19.96	19.73	2.28	897.88	343	0.382 ± 0.0030
50:50 Av/Eu	0.0133	19.80	19.47	2.51	967.62	381	0.394 ± 0.0015
63:37 Av/Eu	0.015	18.82	18.96	2.82	1006.25	418	0.415 ± 0.0141

Before the analysis of all the parts' features it is worth mentioning that the length on the top side of the parts exhibited a noticeable greater value than the middle and bottom measurements. The top right edge was responsible for the increased length of the parts at that side, as illustrated in Figure 7.1. With a closer look it can observed that the colour of the powder at the top right corner was darker than at the rest of the area, which indicated further degradation. This can be explained by the fact that the laser started to scan at the top right corner and there was an initial burst of energy, which was stabilised after a few milliseconds. This process was repeated each time the laser began to scan a new layer, which eventually resulted in a robust top right edge with increased precision, compared to the rest of the edges and the centre of the parts [132].

Another effect occurring with increased energy input was observed on the total height of the parts (see Table 7.1). It should be noted that the height of all parts measured was greater than intended, as the designed thickness of 20 layers should have resulted in a total of 2mm (20 x 0.10mm). It was observed that when the amount of Avicel 101 in the blends increased, the height of the parts was also increased, as shown in Figure 7.1. As it was described in Chapter 6, the higher amount of Avicel 101 in the composition required higher amounts of ED in order to form a sufficient network of necks among the particles and provide stability for the parts. Therefore, there was a link between the increased ED

and the increased thickness of the parts, which was aligned with other reports in literature [47], [51], [66]–[68], [82], [155]. In detail, the average thickness of the parts exposed to 0.015 J/mm^3 of ED (63:37 Av/Eu) was 12.4% higher than the parts exposed to 0.0133 J/mm^3 (50:50 Av/Eu) and 22.8% higher than the parts exposed to 0.0112 J/mm^3 (37:63 Av/Eu).

The same pattern was followed for the sintered density of the parts, which was also increased with increased ED, as illustrated in Figure 7.2. The average density of the parts exposed to 0.015 J/mm^3 was 3.1% greater than the parts exposed to 0.0133 J/mm^3 and 8.6% greater than the ones exposed to 0.0112 J/mm^3. Therefore, the increased ED sintered denser parts. It was then evident that the high energy input resulted in an increase in the sintering depth, which is well known to increase the part density [7], [30], [47], [66]–[68], [78], [82], [155], [206]. The parts exposed to 0.015 J/mm^3 were scanned using a 0.20mm spacing between the lines, the parts exposed to 0.0133 J/mm^3 were scanned using 0.21mm, and the ones exposed to 0.0112 J/mm^3 were scanned at 0.25mm. The rest of the parameters were kept constant (except for the scanning speed applied on the 63:37 Av/Eu powder that required a slower rate to improve stability). This fact indicated that at the same power and interaction time the sintering depth was increased while decreasing the hatching distance, which eventually resulted in growth of the thickness of the parts and increased density.

The inverse pattern was observed in the measurements of the parts' length and width, which revealed smaller average values than the designed ones at 20mm, as shown in Table 7.1. Specifically, the parts exposed to 0.0112 J/mm^3 exhibited 5.0% and 2.7% increase in average length and width than the parts exposed to 0.0133 J/mm^3, and 6.1% and 4.1% above the average length and width of the ones exposed to 0.015 J/mm^3. This reversed effect was primarily attributed to the inhomogeneous nature of the blended powder, since the degree of consolidation and necking was dependent on the material composition. It is evident in Figure 7.1 that the parts produced using 37:63 Av/Eu demonstrated increased precision, while the parts produced at 63:37 Av/Eu demonstrated increased roundness at the corners. It was discussed in section 6.2.2 that the increase of Avicel 101 powder in the composition increased the proportion of unmolten Avicel 101 particles in the structure, which was also related to the increased fragility of the 63:37 Av/Eu parts. Indeed, during handling and cleaning of the parts, the efforts to remove the loose powder eventually led to a decrease in length and width. Furthermore, the discontinuous

microstructure of the 63:37 Av/Eu parts due to the high unsintered phase, resulted in bigger variations in the deviation of the average values calculated for all the features, while the 50:50 Av/Eu parts exhibited the smallest variations, which was not expected and is going to be discussed in the following sections.

Figure 7.1: General views of the produced parts. Increased dimensional precision from the left 63:37 Av/Eu to the right 37:63 Av/Eu part, as the Eudragit L100-55 increased in the blend. Increased part thickness and degradation from the right to the left, as the ED was gradually increased from 0.0112 J/mm^3 to 0.015 J/mm^3. The robust top right corners are circled.
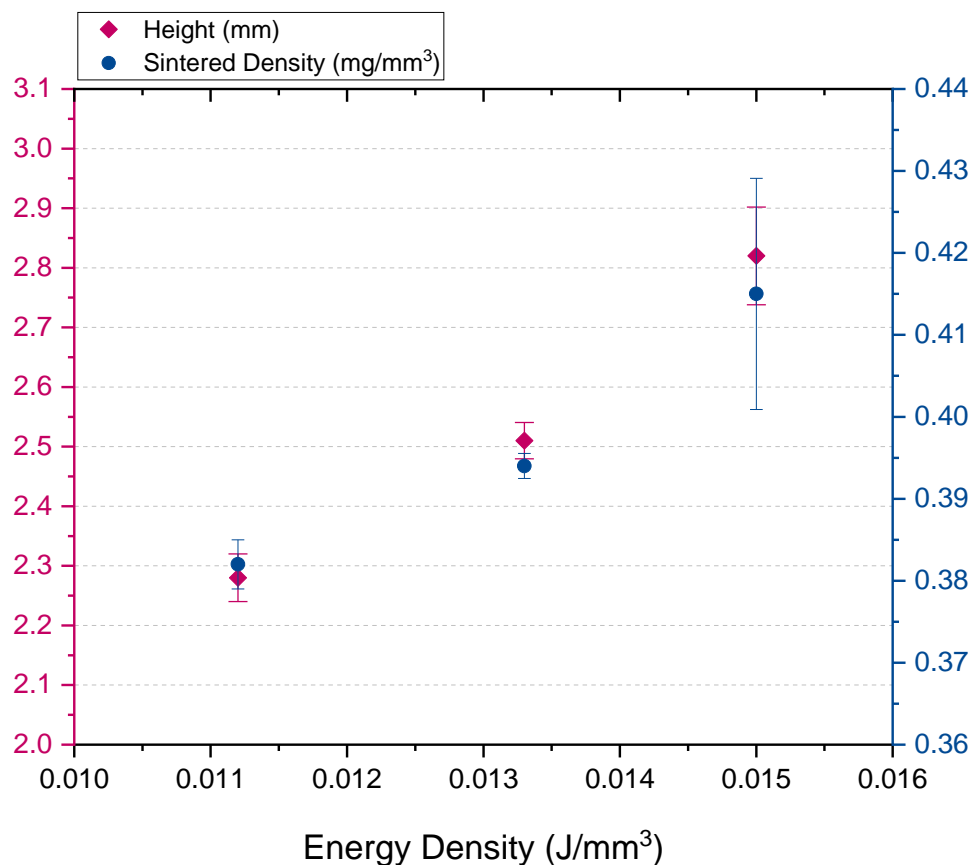
Figure 7.2: Average effect of the energy density upon the part height and the sintered density. The error bars indicate the standard deviation within each set of samples

7.3   Crushing Strength

Crushing strength was an important tablet quality characteristic to be investigated, as it was associated to the tablet integrity under conditions of packaging, shipping and handling before usage [213]–[217]. Crushing strength is widely used in commercial production for development and control procedures to prevent friability, which is linked to the disintegration and dissolution profiles of the tablets [108], [213]–[216]. Therefore, crushing tests were a very important step in this study for the understanding of the influence of LS layered manufacturing on the mechanical strength of the produced tablets and consequently the development of LS oral solid dosage forms of commercial significance. The parts of each blend were subjected to simple diametrical compression tests to investigate their failure, which is discussed in the following paragraphs. Aspirin, which is a commercial uncoated tablet, was additionally selected to be tested for comparison.

The force required to crush all the parts was very low compared to commercial materials, as can be observed in Table 7.2. The crushing strength presented a value of about 3N for all sets of parts, while Aspirin, presented an acceptable value just above 100N [107], [210], [217]–[219]. Similar values have been previously reported in literature for formulations based on Avicel 101 and Eudragit L100-55 [218], [220]–[222]. Therefore, the mechanical properties of the parts were independent of the mechanical properties of the materials. Clearly, the preliminary formulations developed in Chapter 6, presented an inferior mechanical strength and failed the crushing control.

Table 7.2: Average crushing strength of the parts

Parts	Energy Density (J/mm^3)	Crushing Strength (N)
37:63 Av/Eu	0.0112	3.0 ± 0.33
50:50 Av/Eu	0.0133	3.12 ± 0.22
63:37 Av/Eu	0.015	2.76 ± 0.40
Aspirin	-	103.67 ± 2.83

Moreover, small variations were observed between the different sets of parts, which indicated that variations in the concentration of the materials had little effect on the resulted mechanical strength. The main part failure mechanism occurring during the crushing test was delamination of the sintered layers, as illustrated in Figure 7.3, whilst Aspirin crushed in two halves due to cracking. The tendency for layer separation at such low forces revealed that the layers were weakly adhered [217]. It has been already previously discussed that the produced parts exhibited high fragility and low handling stability due to the presence of unmolten powder. Therefore, the poor cohesion of the layers was attributed to the low affinity between the Avicel 101 and Eudragit L100-55 particles. Apparently, the narrow distribution of necking due to the sub-optimal processing conditions, most likely increased the number of voids, and hence the overall porosity [3], [60], which increased the risk of delamination at the interface of the layers and compromised the quality of the parts. It was then evident that the mechanical strength

of the parts was controlled by the porosity of the structure [21], [29], [42], [44], [204], [213], [223].

The results in detail as shown in Table 7.2, revealed that the parts exposed to 0.015 J/mm^3 exhibited the lowest average crushing strength of 2.76N, showing the highest deviation, which was expected. A rise in the average crushing strength at 3N was recorded for the parts exposed to 0.0112 J/mm^3 and a further increase was recorded at 3.12N for the parts exposed to 0.0133 J/mm^3, showing the smallest deviation. The trend between the different set of parts is presented in Figure 7.4 as a function of the ED. This result did not agree with the results in section 7.2, in which the increase of the energy input was translated in increase in thickness and sintered density of the parts. Denser parts would be expected to demonstrate a linear increase in mechanical strength [7], [47], [55], [67], [68], [213], [215]. However, denser parts exhibited the lowest crushing strength. The parts exposed to 0.015 J/mm^3, were the parts that contained the highest concentration of Avicel 101. Therefore, despite the increased sintered density that the parts demonstrated, it was believed that the proportion of unmolten Avicel 101 particles trapped in the structure was quite high, which resulted in poor layer adhesion and low part strength, which was similar to other studies [20]. Furthermore, those parts exhibited a yellowish colour due to the small tolerance of Avicel 101 powder in degradation, which indicated that the ED used was excessive. The increased heat transferred from the laser may have damaged the Avicel 101 particles that perhaps caused a further drop in mechanical strength [34], [47], [51], [67], [68], [82], [207]. According to this, the 50:50 Av/Eu parts would be expected to demonstrate lower crushing strength than the 37:63 Av/Eu parts, as the volume of Avicel 101 particles was 50%. Instead of this, the parts exhibited a small increase of 4% in strength. In fact, the 50:50 Av/Eu parts were scanned using 0.21mm hatching distance in order to increase stability and improve handling, while the 37:63 Av/Eu parts were scanned using 0.25mm to minimise degradation. The notably smaller distance used on the 50:50 Av/Eu parts increased the overlapping and therefore the sintering depth, which improved the fusion of the particles, and thus, increased the part strength. Even though these parts appeared with an off-white colour indicating that the powder experienced light degradation, it was believed that the amount of the ED did not compromise the properties of the Avicel 101 particles.
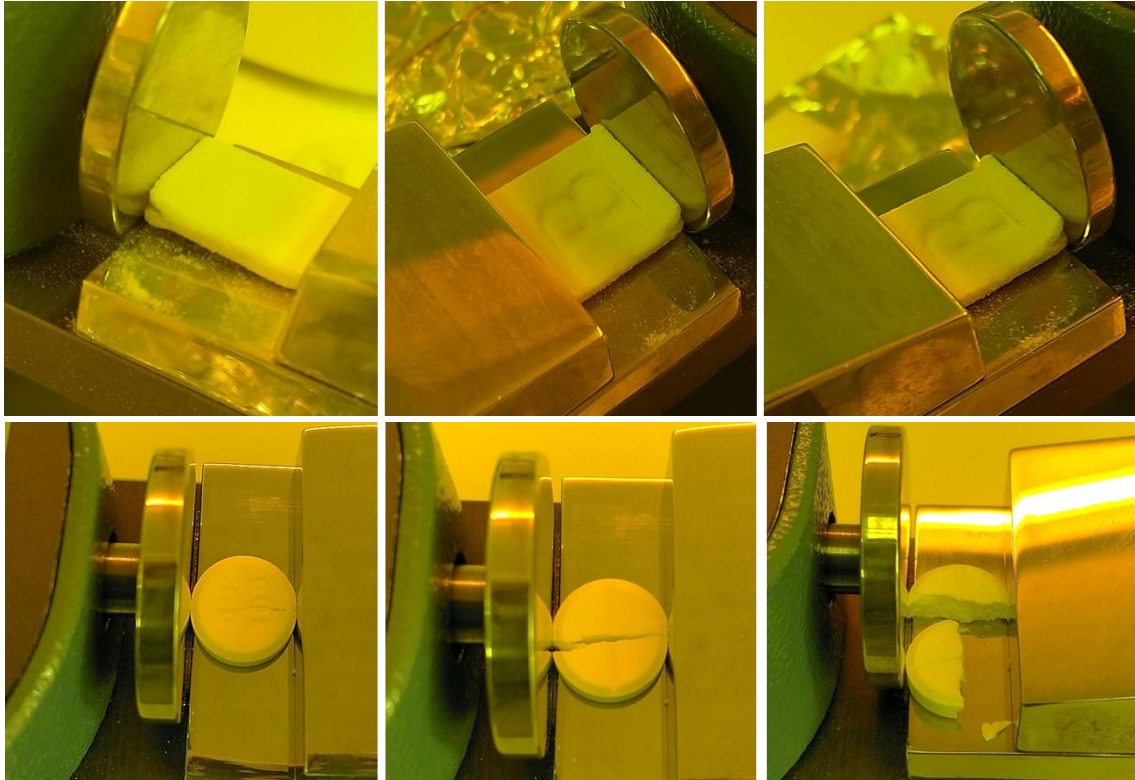
Figure 7.3: Failure of the sintered parts caused by delamination of the layers (top) during crushing tests. Failure of Aspirin caused by crack propagation (bottom)
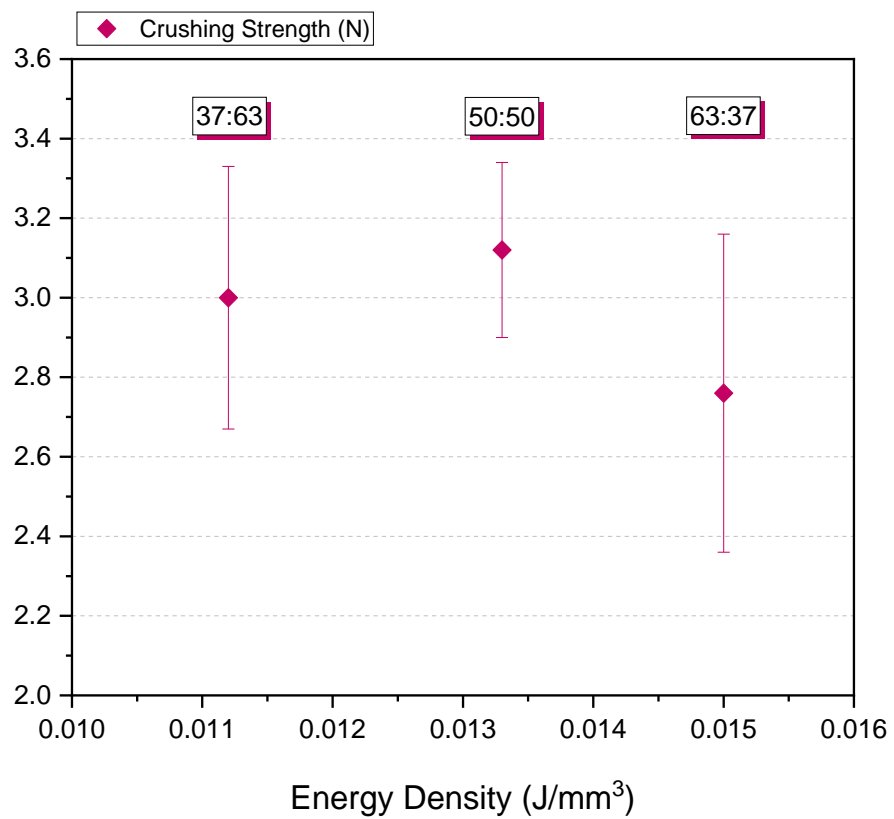
Figure 7.4: Average effect of the energy density and the material concentration upon the crushing strength. The error bars indicate the standard deviation within each set of samples

7.4 Friability

The observations made in the previous section were further supported by the results of the friability tests. As it was described in section 7.3 the sintered parts were very weak, since it was proved that the layer adhesion was very poor, and therefore presented increased fragility [3], [217]. Friability was another characteristic associated to the tablet integrity and is widely used to assess the risk of tablet failure during development and storage [213], [215]–[218]. During friability testing the sintered parts were subjected to abrasion and dropping during rotation inducing mechanical fracture, which was used to further estimate the failure mechanisms and their quality, as discussed in the following paragraphs.

All the parts presented significantly low friability. The percentage of mass loss was higher than >20%, which was unacceptable, as can be observed in Table 7.3. Friability values should not exceed the limit of 1%, which indicated that all sets of parts failed the friability test [3], [107], [108], [215], [217], [218], [221]. During the rotation cycle, the parts experienced cracking in the early cycles, which was followed by delamination of the surface layers, and finally led to complete fracture before the end of the test. The remaining pieces of the parts after testing are displayed in Figure 7.5. The mechanical strength was very low for the parts to survive the rotating forces, which revealed a correlation between the crushing strength and the friability. In fact, the weak layer adhesion observed during crushing tests was caused by increased porosity and fragility, and hence friability, which led to the complete failure of the friability control.

Table 7.3: Results of the friability tests

Parts	Energy Density (J/mm³)	Crack Initiation (cycle)	Fracture (cycle)	Initial Mass (gr)	Final Mass (gr)	Mass Loss (%)
37:63 Av/Eu	0.0112	5	56	3.44	2.52	26.74
50:50 Av/Eu	0.0133	10	64	3.84	2.91	24.22
63:37 Av/Eu	0.015	7	20	4.15	2.89	30.36

Particularly, friability testing showed that the parts exposed to 0.015 J/mm^3 experienced mass losses of 30.36% that was the lowest friability among the sets of parts, which according to the previous results it was highly expected. A smaller percentage of mass loss of 26.74% was recorded for the parts exposed to 0.0112 J/mm^3, and finally the highest friability was exhibited by the parts exposed to 0.0133 J/mm^3, with 24.22% of mass losses. These results were consistent to the crushing strength results, which revealed that the mechanical behaviour of the parts improved with increasing sintering depth, which most likely provided with a higher degree of sintering necks and improved structural stability [21], [40], [41], [44]. Furthermore, observations confirmed the weak performance of 63:37 Av/Eu parts despite the high ED used, attributed to the high concentration in Avicel 101 particles in the blend. Additionally, the improved performance of the 50:50 Av/Eu parts was verified, in which sintering was perhaps more effective improving the layer adhesion and the strength that resulted in higher friability. The percentage of mass loss as a function of the ED is presented in Figure 7.6, where is obvious that trend between the different set of parts correlated nicely with the trend in Figure 7.4.

Nevertheless, friability analysis revealed the poor sintering capacity of the Avicel 101/Eudragit L100-55 blended powders. As can be seen in Figure 7.5, big amounts of loose powder were recovered from the drum after the test cycle, which implied that the bonding between adjacent particles was very weak in all cases. It was discussed in Chapter 6 that the ED applied on the powders was kept to the lowest possible to prevent degradation of the Avicel 101 particles that provided with the minimum handling stability. It was evident at this point that the low energy input failed to induce sufficient bonding between the two materials, which compromised the mechanical performance and the structural integrity of the parts.
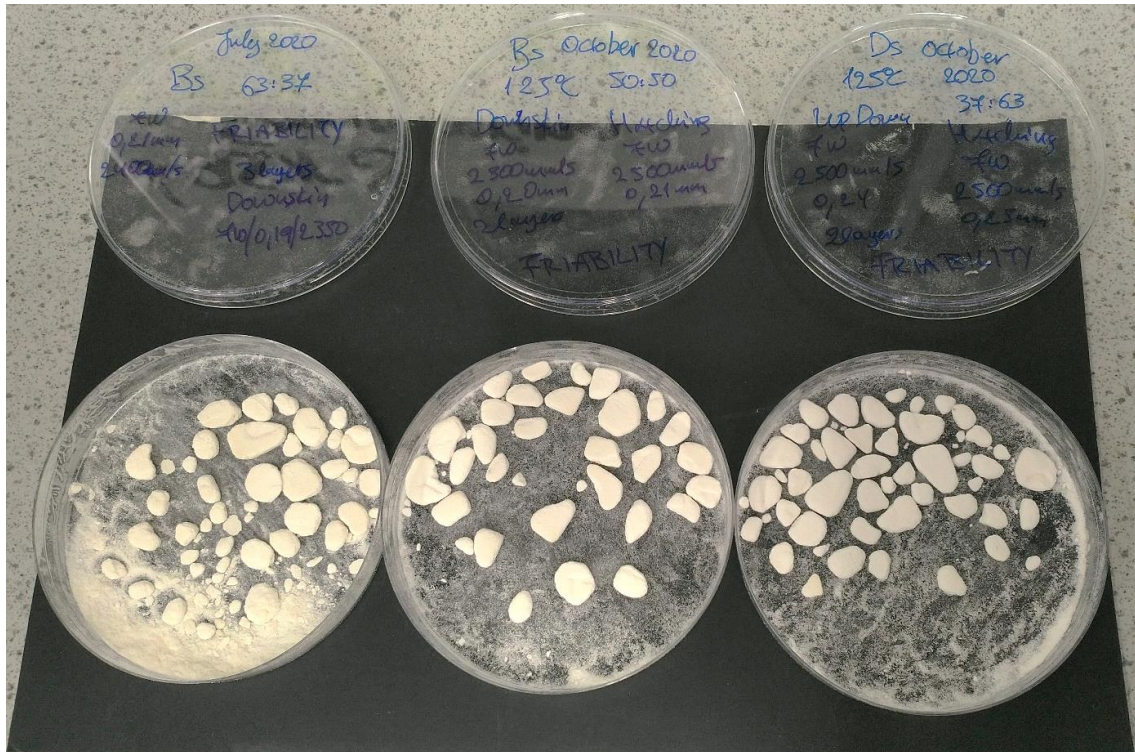
Figure 7.5: Fragmentation of the sintered parts caused by cracking and delamination of the layers during friability testing. From the left to the right parts of the 63:37, 50:50, 37:63 Av/Eu blends
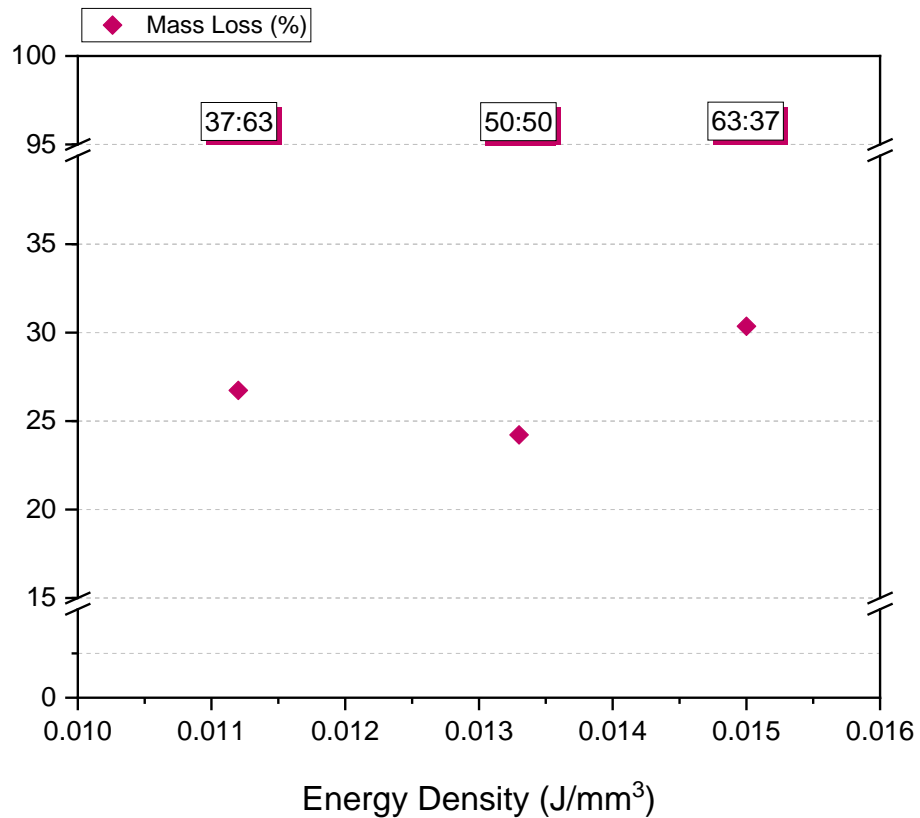
Figure 7.6: Average effect of the energy density and the material concentration upon the friability. The error bars indicate the standard deviation within each set of samples

7.5 Disintegration

The disintegration times revealed a high influence of the part porosity on the disintegration behaviour in accordance with other studies, which have reported that the internal structure of a tablet had a great impact on the disintegration process [20], [21], [25], [29], [43], [44], [210], [224], [225]. Specifically, the disintegration time of the sintered parts was surprisingly fast. As soon as the liquid medium penetrated into the parts, the materials started swelling fast, which led to a minimum disintegration time, as illustrated in Figure 7.7. It was suggested in the previous sections that the sintered parts exhibited very poor mechanical strength and increased fragility depending on their increased porosity, since the nature of the LS process is not based on compression. Therefore, it was assumed that the large distribution of voids in the structure increased the surface area that came into contact with the medium and enabled quick absorption, as proposed through other studies [20], [21], [36], [38], [44], [210].

During the experiments, water was used as a medium to mimic the saliva in contact with the sintered tablets, in action of administration. Disintegration times were tested under static and dynamic conditions (stirring rate of 0rpm, 1500rpm, and 2500rpm). The results did not give a significant variance in the disintegration performance between the different sets of parts. As demonstrated in Figure 7.7, disintegration occurred the second that the parts were immersed into water. While monitoring, it was observed that the parts were completely dispersed in a few seconds, forming a smooth dispersion. According to the European Pharmacopoeia monograph 'Oromucosal preparations (1807)', uncoated tablets disintegrated within 3 minutes resulting in a homogeneous dispersion, are defined as dispersible tablets. Therefore, the disintegration test demonstrated the ability of the sintered parts to rapidly disintegrate, which revealed their suitability for orodispersible applications [1], [20], [44]. In fact, Spritam® (Aprecia Pharmaceuticals), which was the first and only commercial AM oral solid dosage form, is a tablet for oral suspension. Spritam® rapidly disintegrates in the mouth with a sip of liquid in an average time of 11 seconds and was designed to treat epilepsy. However, there were several challenges introduced during the development of the product. Spritam® has been manufactured via the ZipDose® technology, which is a drop-of-powder (DoP) deposition process that uses a print head to deposit an aqueous binder to bind the particles together. In fact, the adhesion of the layers was solely dependent on the binder properties, since any polymerisation or consolidation mechanisms were not taking place [2], [3]. Therefore,

although Spritam® is a solid medicine, it exhibited increased porosity. The porous structure highly influenced the stability of the formulation and assisted in the fast disintegration properties, which established Spritam® as an orodispersible tablet.
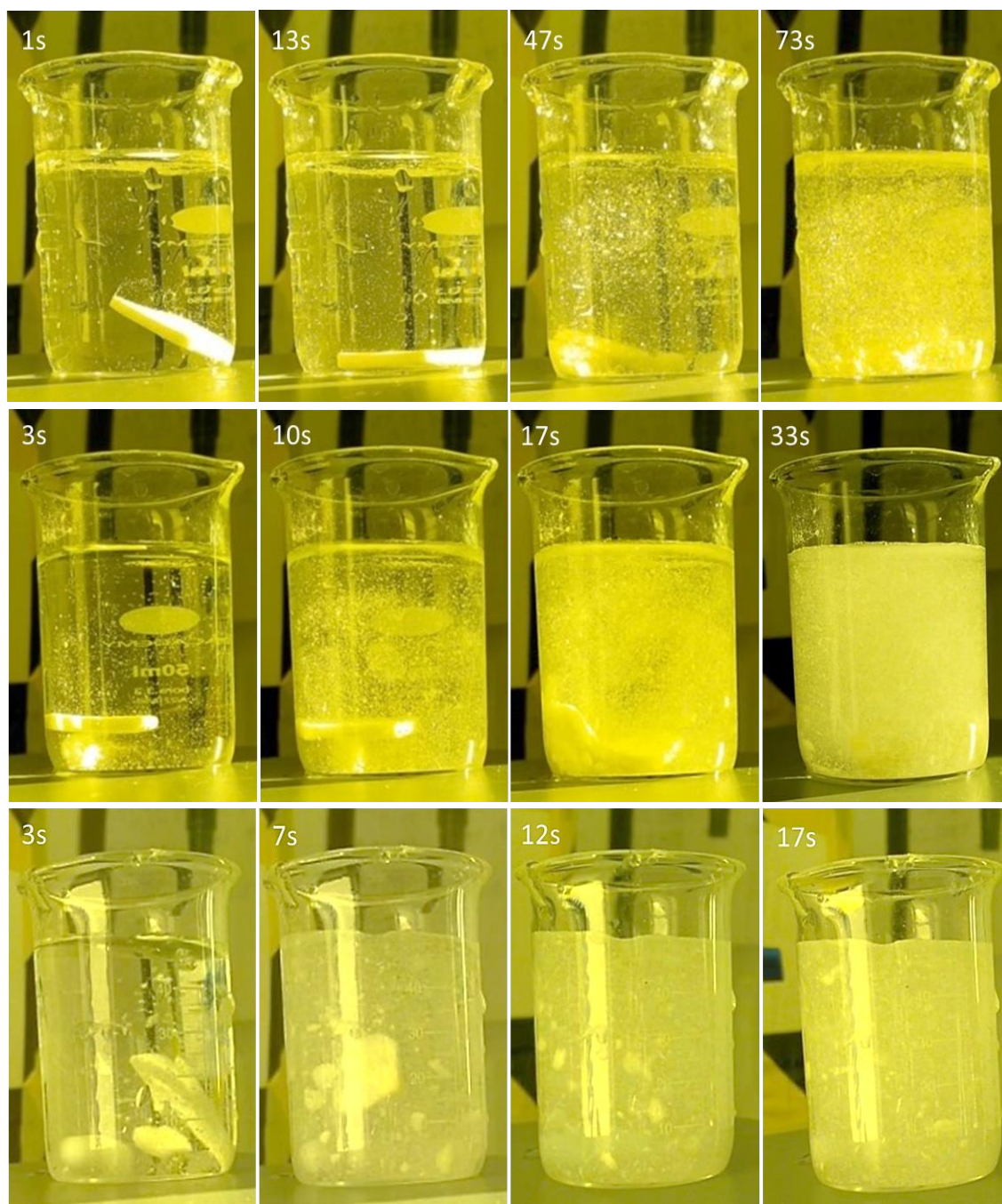
Figure 7.7: Disintegration times of the sintered tablets into water under zero stirring rate (top), low stirring rate of 1500rpm (middle) and high stirring rate of 2500rpm (bottom)

7.6   Dynamic Mechanical Analysis (DMA)

The highly porous nature of the sintered parts was found to affect the stability and the strength, as discussed in the previous sections. This fact, prevented the use of conventional mechanical testing for the investigation of the macroscopic mechanical properties of the sintered parts. For this reason, Dynamic Mechanical Analysis (DMA) in compression mode was employed, which applied a small sinusoidal force without deforming or breaking the parts during the handling process [66]. DMA is a sensitive tool that measured the viscoelastic properties of the parts related to primary relaxations, which were compared to Aspirin, to further estimate the stiffness and predict the overall mechanical performance of the sintered tablets [72], [134], [135]. The average values of the dynamic parameters for each of the blends are shown in Table 7.4, and were compared to the viscoelastic properties of Aspirin, as discussed in the following paragraphs.

Table 7.4: Average values of the dynamic mechanical properties of the parts

Parts	Energy Density (J/mm^3)	Storage Modulus (MPa)	Loss Modulus (MPa)	Tan δ
37:63 Av/Eu	0.0112	5.69 ± 0.53	0.46 ± 0.03	0.082 ± 0.003
50:50 Av/Eu	0.0133	6.24 ± 0.34	0.51 ± 0.03	0.102 ± 0.007
63:37 Av/Eu	0.015	5.45 ± 0.88	0.43 ± 0.05	0.080 ± 0.011
Aspirin	-	59.04 ± 1.44	14.38 ± 1.14	0.243 ± 0.015

The results from the dynamic scan showed very low E′ and E″ values, specifically an order of magnitude lower compared to Aspirin, which revealed the parts' minimum elastic and plastic recoveries. These values indicated that the parts had minimum ability to absorb and dissipate energy, which suggested reduced ductility and stiffness [66], [68], [72], [134], [135], [167]. This observation correlated well with the analysis so far, which demonstrated that the increased porosity in the structure negatively influenced the mechanical strength of the parts [42], [67], [68], [134], [204]. In fact, the low energy input used to manufacture the parts resulted in poor fusion and thereby insufficient particle necking, already discussed in section 7.4, which seemed to have enhanced fragility of the

174

sintered parts as further demonstrated through the DMA analysis [55], [63], [66], [67], [78], [82], [155], [204].

Figure 7.8 illustrates the DMA curves for the E′ and the tanδ as a function of temperature. During testing, the temperature was set to scan from room temperature up to 37°C, which is the body temperature, to investigate the changes in the parts' mechanical behaviour in action of tablet administration. In this temperature range both Avicel 101 and Eudragit L100-55 were kept in the glassy state without going through any phase transitions (see section 4.2). Therefore, any peaks related to changes in the dissipation of energy were not recorded. It is worth mentioning that the slope of the E′ initially was observed to increase, which was then followed a continuous linear behaviour, however this was an act of the sample temperature stabilisation process and not due to mechanical events. This slight change was aligned with the initial decrease observed in the slope of the tanδ.

Similarly to the analysis described for the crushing strength and friability in sections 7.3 and 7.4, the dynamic mechanical properties of the parts followed the same pattern. The trend in Figure 7.9 revealed that the parts exposed to 0.0133 J/mm^3 exhibited the highest elastic recovery, presenting an E′ of 6.24 MPa, and at the same time the highest plastic recovery, showing tanδ of 0.102 (see Table 7.4). The enhanced mechanical behaviour compared to the other parts, was attributed to the increased heat transferred to the powder that most likely improved densification and sintering, and therefore ductility. The parts exposed to 0.0112 J/mm^3 presented a small decrease in both the E′ and tanδ, with values of 5.69 MPa and 0.082 respectively. The reduced ductility was associated to the lower amount of ED used to sinter the specific parts that led to lower densification, and hence increased fragility, which agreed with previous studies [36], [43]. Finally, the parts exposed to the highest ED of 0.015 J/mm^3 displayed the lowest E′ and tanδ values of 5.45 MPa and 0.080, respectively, with the highest deviations. The limited elastic and plastic recoveries were explained by the increased amount of Avicel 101 particles in that blend that led to a limited sintering effect [20]. In fact, these parts exhibited decreased handling stability due to the increased structural porosity and therefore, experienced lower elastic and plastic deformations.

Nevertheless, the differences between the blends had little significance, since it was proved previously that the ED used to sinter the blended powders was insufficient to develop a uniform solid structure and produce strong parts in all cases. The resulted high porosity limited the elastic and plastic recoveries of the parts demonstrating minimum

energy dissipation, consequently increasing fragility, and hence, reducing the mechanical performance of the sintered parts.
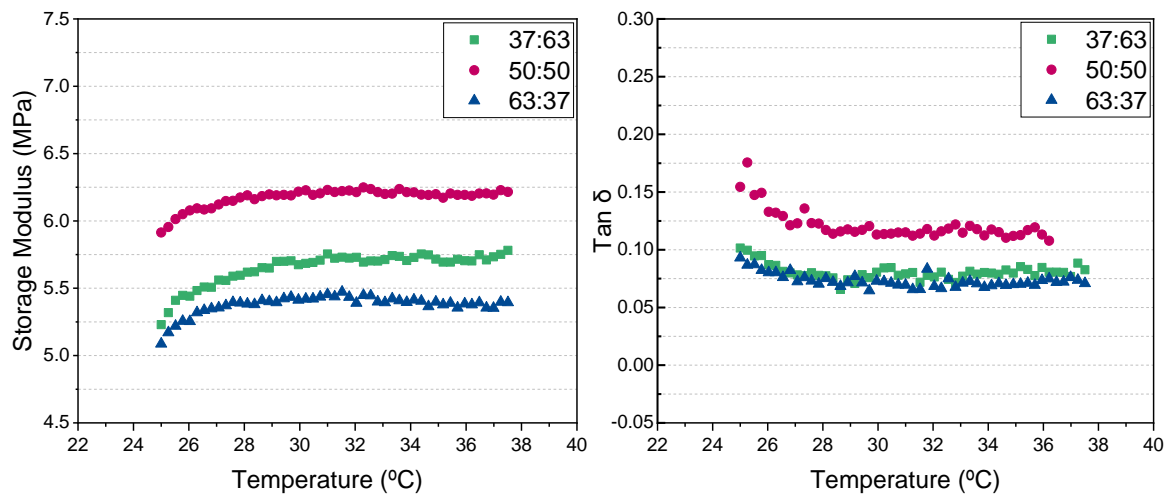
Figure 7.8: Characteristic DMA heat curves for all sets of parts for the storage modulus E', and the damping factor tanδ, as a function of temperature
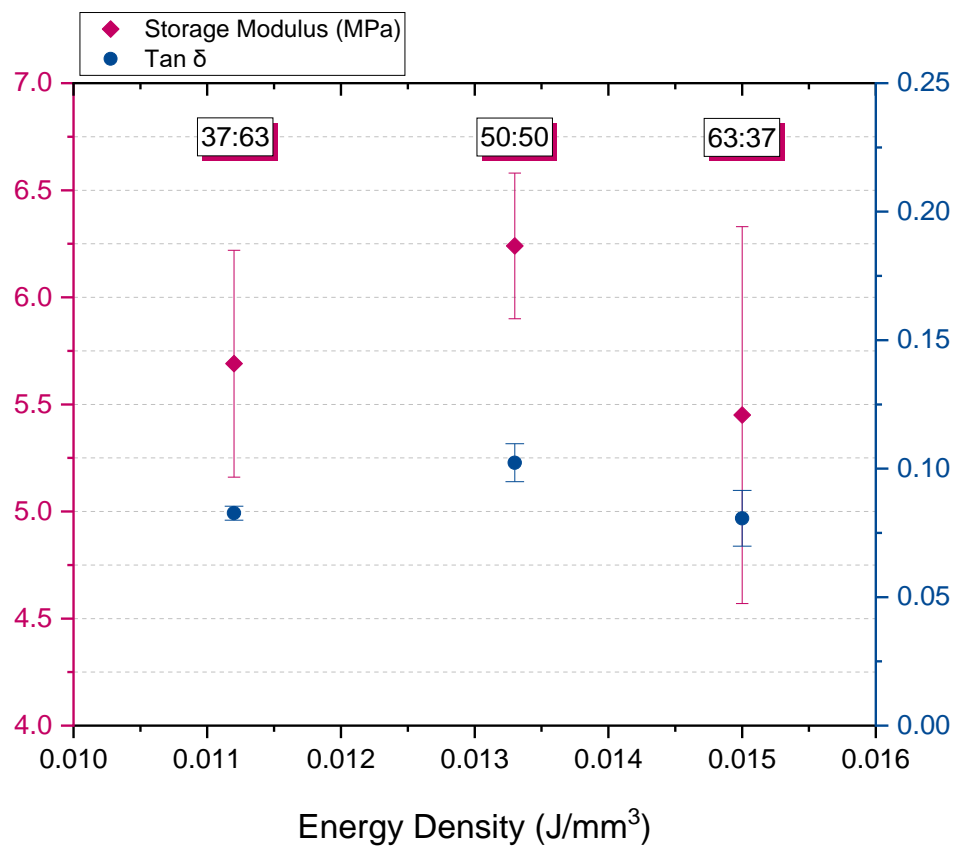
Figure 7.9: Average effect of the energy density and the material concentration upon the storage modulus E', and the damping factor tanδ. The error bars indicate the standard deviation within each set of samples

7.7   Nanoindentation

Nanoindentation was used to explore the variations in the characteristic microstructure of the sintered parts, which was determined by the energy input and the material concentration. The analysis was meant to gather information for the local mechanical properties at the top surface layer, to estimate the extent of particle necking and relative porosity that influenced the part strength. However, the high porosity of the parts introduced many difficulties in obtaining reliable results, considering that measurements in the micro scale were strongly depended on the surface properties of the samples [139]–[141], [144], [226]. In fact, prior to the measurements, the surface of the parts could not be brought into focus to identify a potential contact area with the indenter due to the increased part roughness [226], [227]. As it was expected testing led to large errors and failed to provide a proper evaluation of the local mechanical properties. It was considered that the indenter was slipping between the particles and the voids, which resulted in many inaccuracies in the determination of the contact area that was directly used to calculate the hardness H, and the reduced elastic modulus E_r, [138], [140], [141], [227].

More specifically, nanoindentation at high loads of 100mN, 250mN and 500mN prevented the indenter of maintaining good contact with the parts' surface. The tip hit the parts quickly and the porous surface collapsed, which resulted in penetration depths beyond the instrument's ability to measure [228]. At the lowest load of 10mN the depth could be controlled, however the measurements were not repeatable and the resulting penetration depth was significant. Furthermore, after indentation, pictures of the indents failed to be captured to analyse the profile of the residual contact area and study the local effects related to the mechanical deformation of the parts. Although the indents were not observed, the load - displacement curves were generated to distinguish any heterogeneities in the microstructure and roughly compare the resulting sintering effect between the different set of parts. The load - displacement (P-h) curves are presented for the lowest constant rate of 0.1 mN/s in Figure 7.10, which provided the time for the parts to respond to the applied load. The depth profiles at 0.5 mN/s and 1 mN/s were not considered, as the higher loading/unloading rates resulted in large vibrations and errors [140].
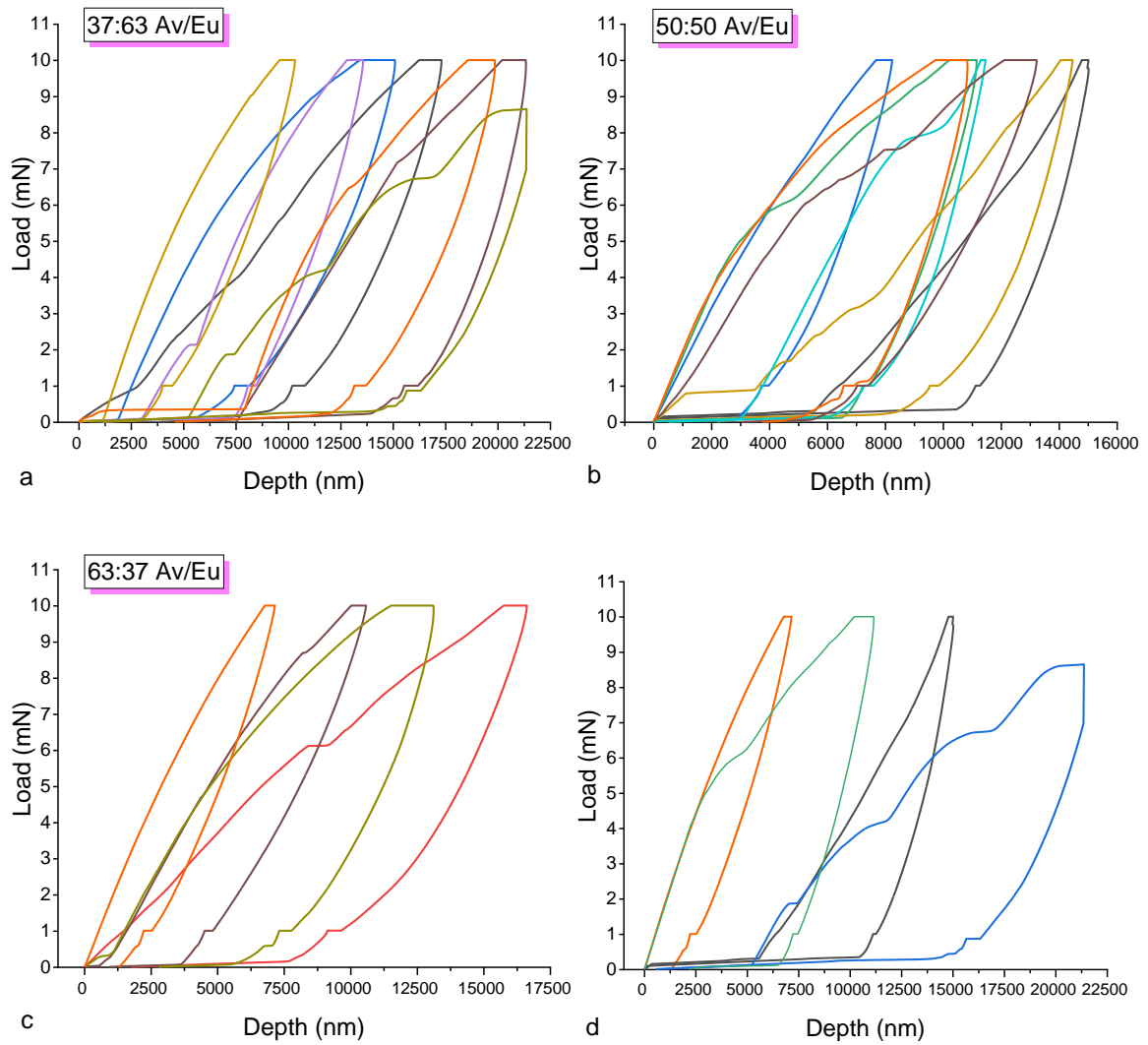
Figure 7.10: Load - displacement indentation curves obtained at 0.1mN/s for a) 37:63 Av/Eu parts, b) 50:50 Av/Eu parts, c) 63:37 Av/Eu parts. Figure d illustrates the most common types of profiles

The majority of the curves presented large discontinuities indicating bursts of displacement, which implied that the particles could flow on the part surface [138], [140], [141], [144], [226]. As mentioned earlier, it was considered that the presence of unsintered powder introduced vibrations due to the voids, which prohibited the tip to make good contact with the surface and impacted the indentations. In addition, the depth profiles presented large variations between the measurements, which further indicated that the part surface presented many inconsistencies due to poor consolidation. In Figure 7.10d, a few characteristic profiles were selected to demonstrate the variety of the observed surface effects. In particular, curves developed in both concave (black) and

convex shapes (red, green), whilst the loading portion appeared smooth (red, black) or with pop-in effects in the form of large steps (blue, green) [138], [140], [226]–[229]. Furthermore, curves presented both small hysteresis with low penetration depth, and therefore low plasticity (red), and wide hysteresis with increased penetration depth and high plasticity (green) [139], [141], [228]–[230]. It was also observed in some measurements the tip to initially hit a void, as the depth increased steeply at minimum force, which was followed by a smooth hysteresis (black), implying that the tip entered the densification zone and made proper contact with the surface [140], [228], [229].

It was obvious that the lack of defined contact points prior to the application of the indenter resulted in different surface effects, since the tip hit different elements/areas each time. As has been discussed in the previous sections, the parts presented both consolidated and non-consolidated areas formed by sintering necks and at the same time large voids, which introduced large inconsistencies in the structure. Therefore, the large variations in the measurements resulted from the unreliability of the area function, which made the results difficult to analyse. Nonetheless, despite the data variation in the indentation depth profiles, H and E_r values were obtained at similar contact depths and loads to compare the different sets of parts. As described in section 3.5.6, H was defined by the ratio of the maximum load to the residual contact area, and the E_r was measured through the slope of the unloading portion. Table 7.5 summarises the average experimental indentation values of H, E_r, creep relaxation, maximum depth, and plastic depth, with standard deviations.

Table 7.5: Average values of the mechanical properties determined by nanoindentation

Parts	ED (J/mm³)	Hardness (MPa)	Reduced Modulus (MPa)	Creep (nm)	Maximum Depth (nm)	Plastic Depth (nm)
37:63 Av/Eu	0.0112	7.24 ± 1.89	52.07 ± 7.03	1102 ± 342	16241 ± 4092	12844 ± 4226
50:50 Av/Eu	0.0133	8.14 ± 1.40	83.87 ± 12.44	642 ± 401	11253 ± 2837	8905 ± 2849
63:37 Av/Eu	0.015	10.21 ± 4.06	67.15 ± 21.17	843 ± 528	11863 ± 4002	8656 ± 3725
Aspirin	-	38.37 ± 12.25	3580.85 ± 1014.0	49 ± 19	1882 ± 633	1764 ± 635

To estimate the impact of the surface roughness of the parts on the indentation measurements, a few indents were performed on Aspirin (plots are not presented). Aspirin demonstrated high elasticity showing a steep slope of the unloading curve, since it exhibited a large extent of elastic recovery shown by the small difference between the maximum depth, h_{max} and the remaining plastic depth, h_p. The sintered parts exhibited much larger penetration depth at the same load, which in most cases resulted in errors, and therefore much lower values for H. Furthermore, the slope of the unloading curves was much lower, since the plastic depth was increased, which led to significantly low values for the E_r. These values did not agree with other indentation studies on Avicel and Eudragit solid structures, which reported values of two orders of magnitude higher [140], [141], [230]. As has been already observed in the previous sections, this difference was attributed to the high part porosity, which led to increased fragility and significant reduction of the mechanical performance of the parts.

The rank order of the mechanical response of the parts was the same for all the experimental parameters measured and was consistent with the profiles of the load - displacement curves: 50:50 Av/Eu parts > 63:37 Av/Eu parts > 37:63 Av/Eu parts. The trend for both H and E_r can be observed in Figure 7.11 in function of the ED to correlate the properties of the parts with the sintering effect. In contrast with the previous tests discussed in the sections above, the parts exposed to the highest ED of 0.015 J/mm^3 demonstrated relatively enhanced properties. However, these results failed to represent the actual mechanical behaviour of the 63:37 Av/Eu parts due to the large errors occurred during testing. As can be observed in Figure 7.10c a few curves were recorded, since most of the indents exceeded the limits of the measurement. The effects observed on indentation, which involved vibrations and displacement, became dominant during testing of this particular set of parts and led to many inaccuracies in the measurements. In fact, this demonstrated the impact of the increased number of voids and limited sintering effect that actually correlated well with the results of the previous tests. The few curves that were recovered exhibited relative small hysteresis and low average h_{max}, which matched the depth profiles of Avicel and Eudragit reported in literature [230], [231], and therefore it was considered that the indenter made contact with individual particles. However, the recorded values for the H and the E_r were very low compared to the other studies due to friction, which was already discussed above, and thus the results were considered unreliable.

For the rest of the parts the results were aligned with the analysis in the previous sections. As expected, the parts exposed to 0.0133 J/mm^3 demonstrated improved mechanical response presenting the highest average values for H and E$_r$. These parts had exhibited increased handling stability and stiffness, which was further confirmed by the indentation depth profiles. The load-displacement curves resulted in smaller average h$_{max}$ with smaller deviations, which indicated improved hardness and plastic behaviour compared to the ones recorded for the parts exposed to 0.0112 J/mm^3 [140], [141], [226], [230]. In addition, the slope of the curves appeared higher, reflecting an increase in the E$_r$ and the elastic response [140], [226], [228]. The smaller inconsistencies and errors for the 50:50 Av/Eu parts revealed a decrease in the surface roughness, and hence increased densification. The higher degree of necking would be expected to improve ductility and strength compared to the 37:63 Av/Eu parts at the same load, resulting in a smaller contact depth. This observation was further justified through the relaxation response of the two sets of parts. The holding period at the maximum load resulted in 71.65% higher h$_{max}$ for the latter parts, which indicated a significantly higher deformation [144]. The dwell time was originally applied to record the creep relaxation of the parts at constant load and monitor the deformation response of the surface. However, due to the increased porosity and the poor contact of the indenter with the parts' surface, the changes in depth were actually indicators of the tip movement through the voids and not because of creep relaxation events [229]. Therefore, the parts exposed to the lowest ED of 0.0112 J/mm^3 presented higher porosity than the parts exposed to 0.0133 J/mm^3, which reflected the lower sintering effect.

The variety of the depth profiles demonstrated the inhomogeneous nature of the sintered parts. Inaccuracies in the measurements reflected the difficulties arising from the high part surface roughness in determining the mechanics of the microstructure. Although, the results were influenced, the analysis was proved very valuable in predicting the physics of the microstructure and provide an insight of the sintering conditions needed to improve the handling stability and the strength of the parts.
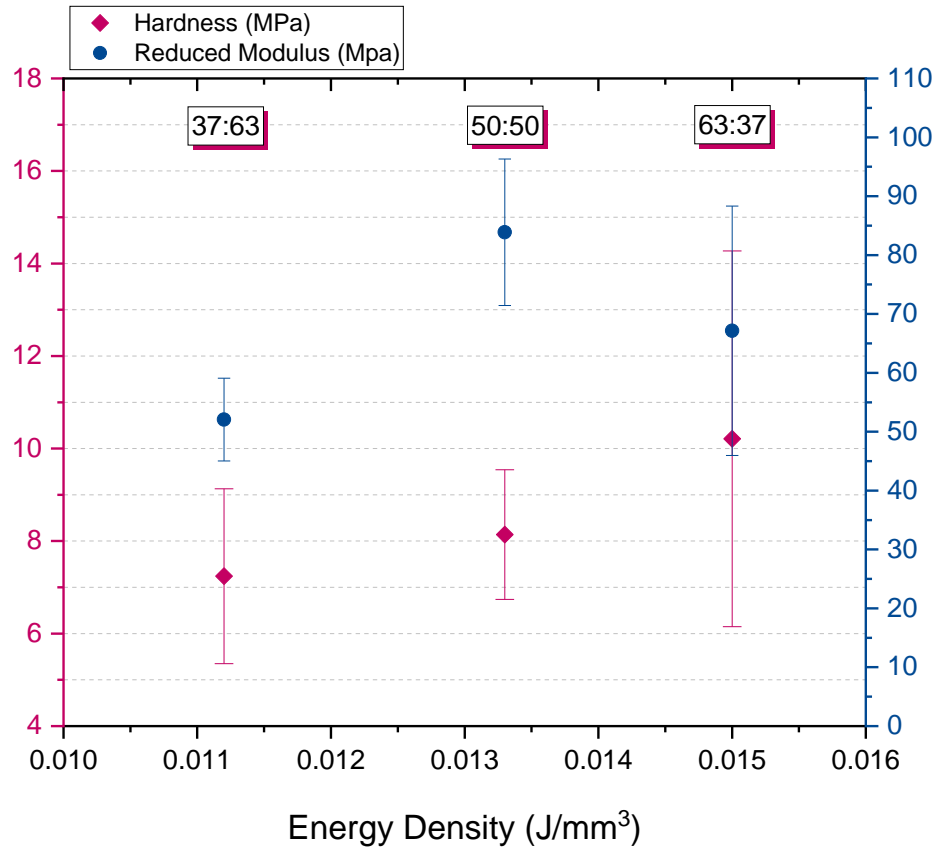
Figure 7.11: Average effect of the energy density and the material concentration upon the hardness H, and the reduced elastic modulus E_r. The error bars indicate the standard deviation within each set of samples

7.8 SEM

Scanning electron microscopy (SEM) was used to characterise the microstructure of each set of parts and the resulting porosity related to the energy input and the material concentration. Images were captured on the surface and the cross section of the parts to observe the degree of sintering and to confirm the limited inter-particle connectivity that influenced the mechanical performance of the parts. In particular, SEM analysis aimed to identify the differences arising by the varying amount of ED and material ratio and compare them to the mechanical properties investigated in the previous sections.

During scanning it was discovered that there were no differences in the microstructure at the top and cross-section surfaces of the parts and more importantly there was no evidence of layer formation. It was more than evident that there was incomplete densification and the particles were weakly adhered. As a result, the parts presented high porosity with a percolating void system, suggesting that the ED used to sinter the powders was

insufficient to provide increased particle coalescence. Furthermore, SEM analysis confirmed the presence of unmolten powder in the microstructure related to the sub-optimum processing conditions, which influenced the macroscopic behaviour of the parts resulting in poor stability and strength, as described in the previous sections.

The images displayed in Figure 7.12 - Figure 7.14 present the microstructure of the 37:63, 50:50 and 63:37 Av/Eu sintered parts, respectively, which revealed the heterogeneous nature of the blended powders with discontinuous dispersed phases being dependent on the material concentration. In the general view images in Figure 7.12a-b, Figure 7.13a-b and Figure 7.14a-c, the pores were clearly identified. It can be further observed that there was no substantial difference in the sintering effect between the different sets of parts. Further observations revealed that the parts containing higher amounts of Eudragit L100-55 presented lower open porosity. The ratio of the high volume in Eudragit L100-55 small spherical particles and the low volume in Avicel 101 large irregular particles resulted in more surface contact points, which reduced the pore size and number. Consequently, the pore distribution was a function of the average particle size of the blended powders [3], [36], [39], [42], [54], [66], [76], [205]. Figure 7.12a revealed that Eudragit L100-55 particles filled in the voids between the Avicel 101 particles more efficiently compared to Figure 7.14a, that presented large dark spots, which indicated higher open porosity related to the increased weight percentage of Avicel 101 [20], [36]. Therefore, the SEM images confirmed the extended porosity in the structure of the 63:37 Av/Eu sintered parts, which was linked to the decreased mechanical performance observed in the previous sections [39], [66]–[68], [204].

On closer inspection, the 37:63 Av/Eu parts consisted of a high population of unsintered Eudragit L100-55 small particles spread around the Avicel 101 particles. In addition, it was observed in Figure 7.12d-f that Eudragit L100-55 particles had experienced early stage neck growth, which led to the formation of bridges with Avicel 101 particles with a small average diameter [34], [71], [205]. It appeared more that the high volume of Eudragit L100-55 particles trapped the fewer Avicel 101 particles rather than forming a well interconnected particle network between the two materials (Figure 7.12c). This observation agreed with the previous observations that 0.0112 J/mm^3 of ED resulted in poor consolidation and sintering, which led to lower mechanical properties despite the increased volume in Eudragit L100-55 [29], [39], [40], [42], [43], [66], [67], [204]. In Figure 7.12f fracture of one of the bridges can be seen, which indicated the weak adhesion

between the two materials and further explained the poor strength of the 37:63 Av/Eu parts [31], [42], [68].

As the ED increased the sintering effect increased. It can be observed in Figure 7.13b-f, imaging the structure of the 50:50 Av/Eu parts that Eudragit L100-55 and Avicel 101 particles merged together developing interfaces. The higher ED of 0.0133 J/mm^3 resulted in an improved sintering effect, which reduced the pore size by forming wider and stronger bridges [40], [41], [66], [68], [71], [205]. It was revealed that the 50:50 Av/Eu parts presented better adhesion between the two materials, which in fact improved the macroscopic mechanical performance, as discussed in the previous sections [42], [67], [155], [204]. Further increase in the ED at 0.015 J/mm^3, induced better fusion of the Eudragit L100-55 particles, as shown in Figure 7.14d, f for the 63:37 Av/Eu parts. However, the structure of the parts presented limited coalescence between the particles due to the low volume in Eudragit L100-55. The ratio of Avicel 101 to Eudragit L100-55 was very high to provide enough contacts points for the development of a well interconnected network of interfaces and bridges that could potentially result in full coalescence and densification [36], [42], [204], [205]. Subsequently, the porosity was increased, which promoted fragility of the specific parts influencing the macroscopic mechanical response, observed during testing [42], [66], [68].

The image analysis directly supported the experimental findings of this chapter, which demonstrated that the mechanical properties of the sintered parts were dependent on the structural porosity. High energy levels induced material fusion and developed interfaces between the particles, however the presence of Avicel 101 prevented full densification of the structure. On the other hand, inadequate energy levels resulted in partial consolidation, which was the second reason that led to increased porosity. It was therefore evident that the poor response of the parts to mechanical testing was related to the interconnected pore distribution, which compromised the part integrity and the part strength.
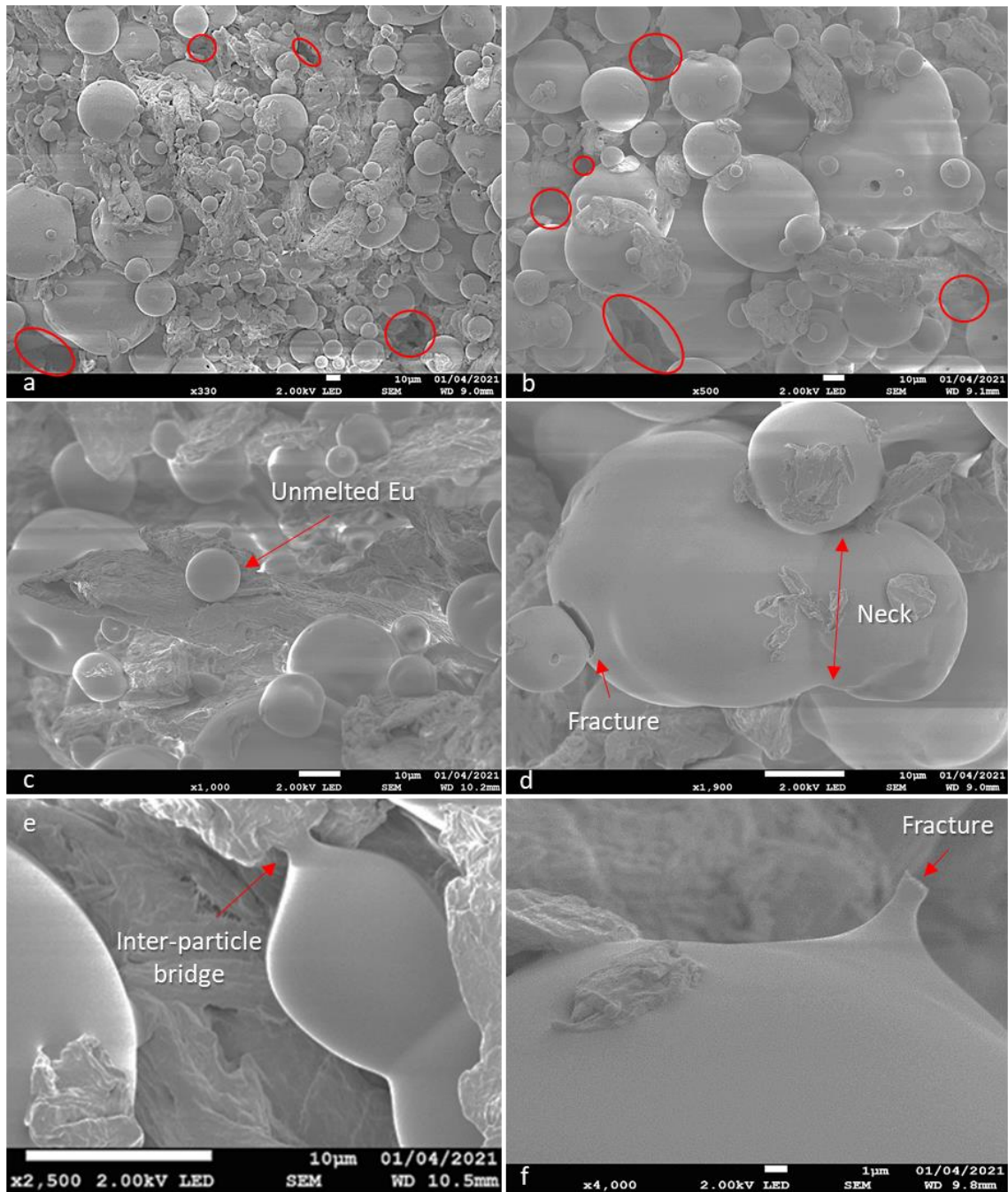
Figure 7.12: SEM micrographs of the sintered parts exposed to 0.0112 J/mm^3 using 37:63 Av/Eu of blended powder
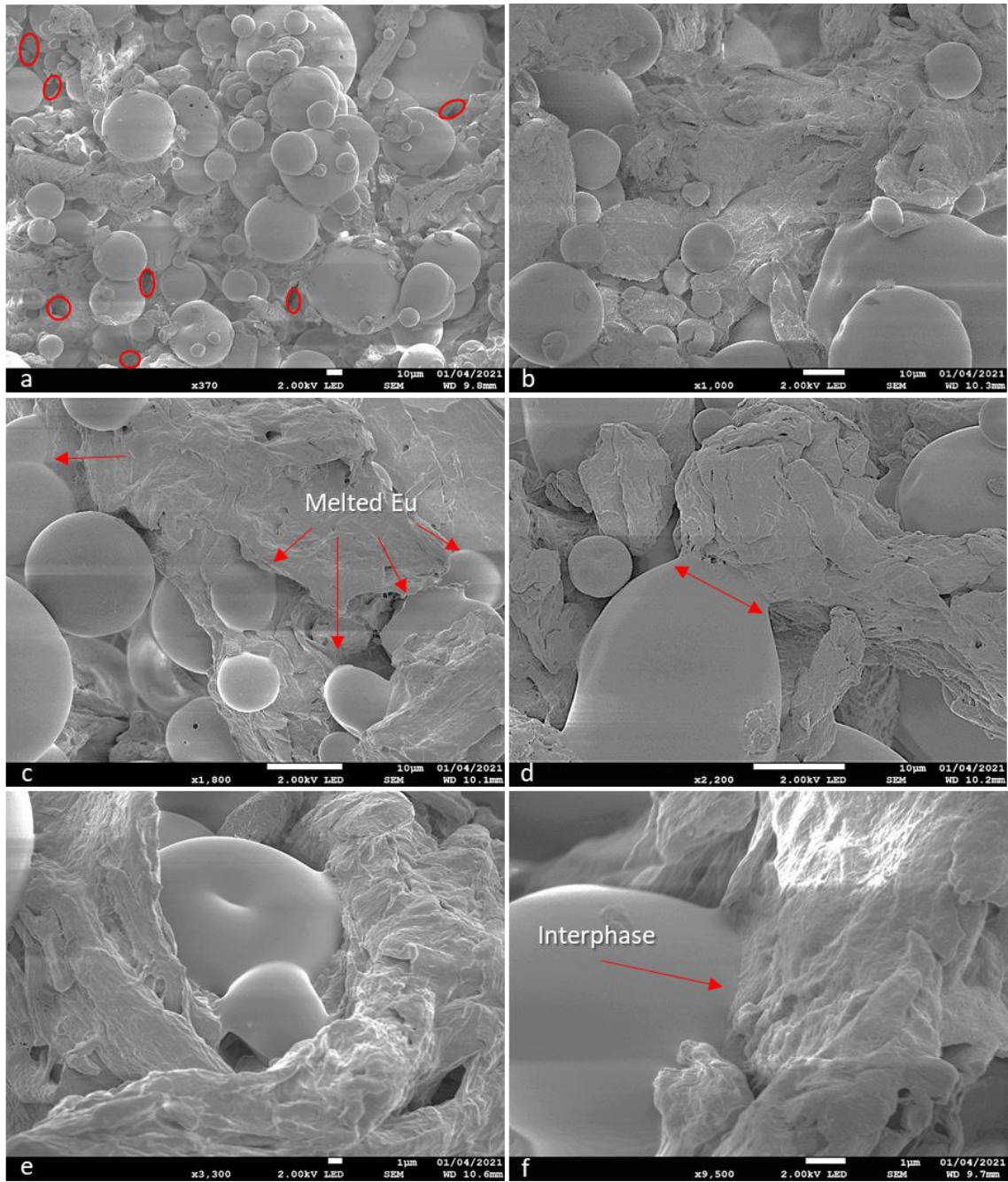
Figure 7.13: SEM micrographs of the sintered parts exposed to 0.0133 J/mm^3 using 50:50 Av/Eu of blended powder
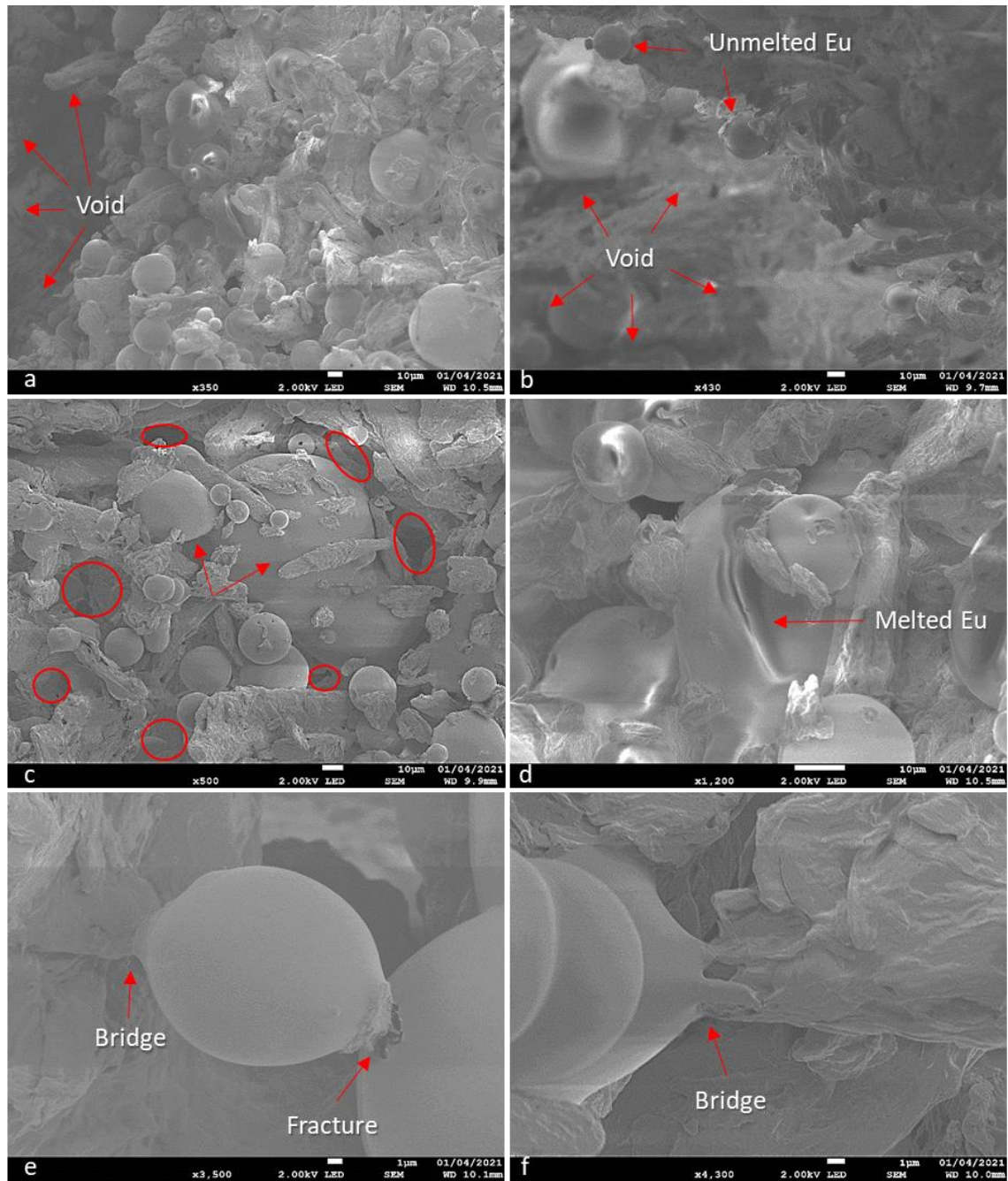
Figure 7.14: SEM micrographs of the sintered parts exposed to 0.015 J/mm^3 using 63:37 Av/Eu of blended powder

7.9 Summary

Chapter 7 demonstrated that the material properties and the processing conditions determined the final macroscopic behaviour of the produced LS tablets in terms of microstructural changes in the pore number and distribution. Thorough investigation of the mechanical properties of the sintered parts revealed the impact of the processing elements on their mechanical performance and enhanced the understanding of the design specifications for oral formulations. Particularly, crushing strength and friability measurements predicted the failure mechanisms of the LS tablets related to handling, packing and shipping. Disintegration measurements were critical and revealed the strong relationship between the part microstructure and the tablet functionality. Finally, DMA and nanoindentation analysis provided an insight of the internal porosity and surface roughness through measurements of the elastic modulus and hardness.

The analysis uncovered a distinct influence from the Avicel 101weight percentage within the powder formulation, due to its unfavourable thermal characteristics that resisted particle fusion and introduced structural limitations. The parts failed the crushing strength and friability control due to delamination of the layers that was caused by the presence of unmelted Avicel 101 particles. The presence of unmolten powder increased the number of voids in the structure and reduced layer adhesion. Therefore, all the parts presented high porosity that enhanced their fragility, and significantly reduced the tablet integrity. Specifically, the increased structural porosity restrained the elastic recoveries affecting the hardness, the elastic modulus and the damping factor, which presented significantly low values. Furthermore, the porosity allowed the fast penetration of water within the structure, which reduced the disintegration times, affecting the pharmaceutical functionality. All this information is gathered and presented in Table 7.6, outlining the challenges on processing pharmaceutical powder formulations using LS.

Table 7.6: Properties of the sintered tablets

Parts	Strength	Friability	Disintegration	tanδ	Elastic Modulus	Hardness
37:63 Av/Eu	✖	✖	✖	✖	✖	✖
50:50 Av/Eu	✖	✖	✖	✖	✖	✖
63:37 Av/Eu	✖	✖	✖	✖	✖	✖

Despite the small differences that were identified in the performance of the parts produced from the various blends and were related to the energy input applied to the powders, the sintered tablets did not exhibit significant differences in their overall mechanical response, as seen in Table 7.6. It was obvious that the unintentional manufactured structural porosity significantly reduced the tablet integrity and functionality, highlighting the need for alternative approaches on sintering pharmaceuticals instead of mixing ingredients together.

CHAPTER 8   FORMULATION OF COATED PARTICLES FOR LASER SINTERING

8.1   Introduction

Chapter 8 focuses on a new approach for LS powders for pharmaceutical tablets, in order to overcome the limitations found during processing and testing. It was described in Chapter 7 that Avicel 101 properties had a significant effect on sintering and consequently on the functionality and the mechanical response of the produced tablets. Therefore, it is worthwhile to introduce an alternative approach to safely process the powder mixture of Avicel 101/Eudragit L100-55 that could potentially improve the sintering and the formulation performance. Coating of the powder particles has been proven to enhance the final part properties in LS, however to the best of knowledge, it has not been widely employed [62], [74], [75], [205]. Therefore, a simple approach was developed based on chemical-precipitation and emulsion-solvent evaporation principles used in previous studies (see section 3.6), to coat Avicel 101 particles with Eudragit L100-55 instead of conventional powder mixing. The process exploited the pH-dependent solubility of Eudragit L100-55 to "entrap" the Avicel 101 particles aiming to minimise the negative effects of sintering on the Avicel 101 properties and produce a coated cellulose-based material with improved processability.

Precipitation and emulsion-evaporation methods are being used for the preparation of polymeric nano/micro particles, spheres or capsules for applications in electronics, medicine, environmental technology etc. [232], [233]. In fact, advances in the last decades in drug delivery involve the encapsulation of drugs in various polymer-based nano/micro particle systems [232]–[234]. Several techniques are been used for the preparation of nano/micro particles depending on the particular application such as, polymerisation, dispersion of preformed polymers or ionic gelation, which include popular methods like mini emulsion, micro emulsion, emulsion solvent-evaporation, precipitation, emulsion solvent diffusion, dialysis, etc. [232], [233], [235].

Polymer precipitation, also called solvent displacement method, is a process based on the interfacial deposition of a preformed polymer from an organic solution, following the displacement of the organic solvent in an aqueous medium [236]. Precipitation occurs in a four-step mechanism: supersaturation, nucleation, growth by condensation, and growth

by coagulation [233], [237]. More specifically, during the first step, polymer is dissolved in a water-miscible organic solvent. This organic phase is then added into a non-solvent aqueous solution, which causes diffusion of the solvent and a rapid decrease of polymer's solubility in a newly formed mixture of solvents. Following decline of its solubility, the polymer starts nucleating at the water-organic interface, and a colloidal suspension is formed [232], [233]. To remove the aqueous phase, centrifugation, filtration or freeze drying can be employed to separate the precipitate and obtain the polymer particles [233]. The most common organic solvents used in precipitation are methanol, ethanol, and acetone [233], [238]. The polymers that are commonly used in this method are film-forming materials that could be natural or synthetic, such as, starch, gelatin, polylactides (PLA), polycaprolactone (PCL), polyethylene glycol (PEG), polymethacrylates (Eudragit®), etc. [232], [233].

Emulsion-solvent evaporation involves the preparation of polymer solutions in volatile solvents for the formulation of emulsions [232]. The mechanism of the emulsion-solvent evaporation process involves two steps: emulsification and solvent removal. The process is quite simple, first a preformed polymer is dissolved in an organic solvent and then droplets of the organic phase are finely dispersed in an immiscible aqueous phase containing a surfactant that results in emulsification. Subsequently, the solvent is removed by slow evaporation and the polymer is deposited on the interface between the water and the solvent. Once this step is complete, polymer aggregates are obtained in the form of particles [232], [234], [235]. Emulsification can be achieved by direct emulsification of the organic phase in water (high-energy), or by inversed emulsification by adding water to the organic solution (low-energy) [234]. The most commonly used solvents are ethyl acetate, dichloromethane, acetone, methanol and ethanol. A wide variety of polymers are being used among which polylactides (PLA), polymethyl methacrylate (PMMA), polylactic-co-glycolic acid (PLGA), polyvinyl acetate (PVA), polymethacrylates (Eudragit®), etc. The versatility of the emulsion-solvent polymerisation process, its simplicity and the fast handling are offering an advantage for this method to be translated to new materials and structures [234], [235], [239].

In this study, two approaches based on precipitation and one approach based on emulsion-solvent evaporation were developed. To begin with, Eudragit L100-55 was chosen to be dissolved in methanol, which found to contribute to fast dissolution of the polymer during preliminary experiments. In the next step, Avicel 101 was added to the solution, while

diffusion or evaporation mechanisms forced Eudragit L100-55 to bind to the surface of the Avicel 101 particles. This system was aimed at forming a film coating around the particles in order to protect Avicel 101 from degradation during LS and potentially overcome the limitations applied when adjusting the laser parameters towards optimisation. In fact, the development of a powder with improved physical characteristics would allow the use of a scanning strategy of increased energy input that has been proved in the previous chapters to improve densification and handling stability of the parts and hence, the mechanical behaviour. In that event, the coating conditions were varied to prepare different batches in order to investigate the coating levels that could be achieved, and possibly reach the desirable characteristics that would tolerate high energy levels. The characteristics of the coating were examined using Fourier-transform Infrared Spectroscopy (FTIR), Thermogravimetric Analysis (TGA), Time-of-flight Secondary Ion Mass Spectrometry (ToF-SIMS) and Scanning Electron Microscopy (SEM), which revealed information related to the efficacy of the methods used and the level of the coating achieved, including material concentration levels, type and morphology of the coating.

8.2   Preparation of coated particles

The key to the coating of the Avicel 101 particles was the emulsification of the Eudragit L100-55/methanol/Avicel 101 system, as mentioned earlier. The efficacy of the process was mostly dependent on the concentration of Eudragit L100-55, and solvent (methanol) or non-solvent (water) in the mixture. Therefore, efforts were made to control and optimise the process using various amounts of all the components, which has already been described in detail in section 3.6.1. The methods that were developed, involved simple sample preparation in short time at a laboratory scale.

In the first approach that was used to coat the Avicel 101 particles, the varied Eudragit L100-55/methanol solutions were added to various Avicel 101/water suspensions under high speed homogenisation at 6000rpm, in order to increase the emulsification effect by increasing the interfacial area between the intermediate phases [151], [154], [180], [234]. It was found that the Eudragit L100-55 concentration had a significant impact on the process. The highest concentrations of 10wt%, 5wt% and 3.3wt% resulted in increase in the viscosity of the solution, therefore decreased the mobility of the Eudragit L100-55,

which resulted in very poor dispersion into the aqueous phase [148], [150], [154], [234], [240]. More specifically, once the solution was injected into the aqueous phase the polymer crushed out due to fast diffusion, as can be observed in Figure 8.1 [153], [154], [232]. Furthermore, during the homogenisation process the polymer was deposited on the mixer resulting in serious material losses. By the completion of the centrifugation and drying of the intermediate phases only a few particles were recovered. It can be seen in Figure 8.2 that Eudragit L100-55 formed small bulks of mass, whilst trapped most of the Avicel 101 particles, and for this reason the remaining particles were very few. On the other hand, Figure 8.2b demonstrates the ability of Eudragit L100-55 to form a continuous film around the Avicel 101 particles, since it was proved to be able to form a stable emulsion, which was very promising. The rest of the batches produced (see Table 3.3), contained lower concentrations of 2.5wt% and 2wt% in Eudragit L100-55, which reduced the viscosity of the solution [153], [154]. At the same time, the suspension phase contained lower amounts of water, to prevent faster diffusion, which in fact resulted in a homogeneous dispersion [153], [154]. After all the steps were completed, larger samples of single particles were collected.
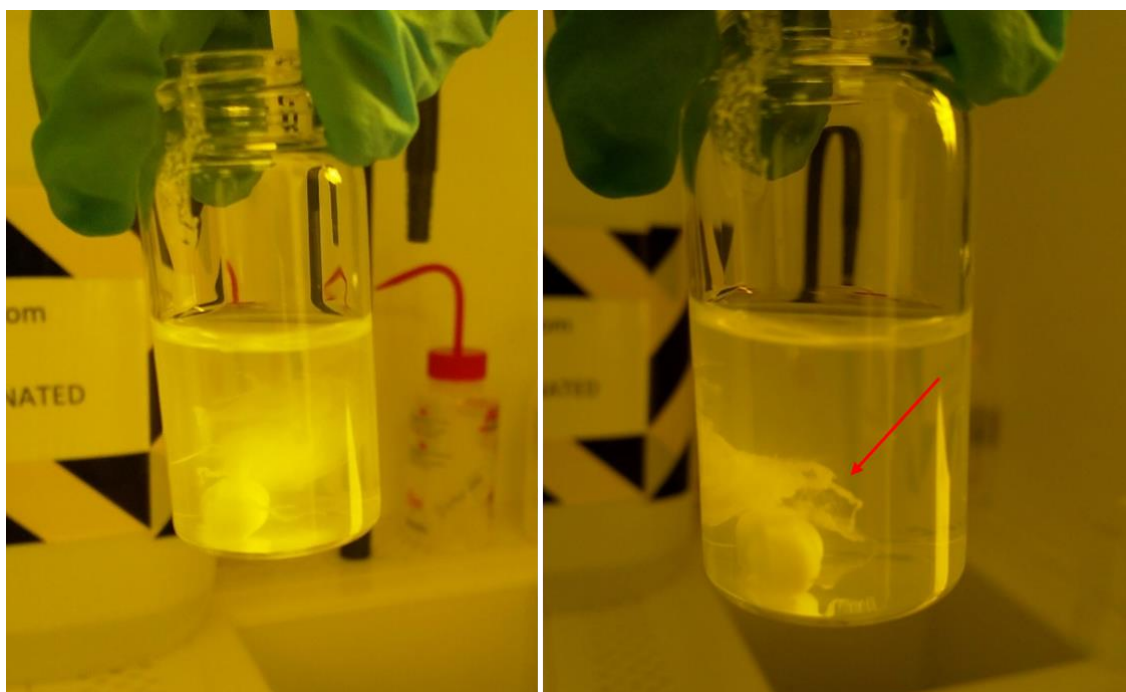
Figure 8.1: High viscosity solutions led to poor dispersion of the organic phase into the aqueous phase

The second approach that was used involved the dispersion of Avicel 101 into the organic solution containing the Eudragit L100-55, followed by injection of the mixture into water. This system aimed to increase the film formation on individual Avicel 101 particles, since Eudragit L100-55 started to precipitate out being already in contact with Avicel 101, as the two materials were added together in the aqueous phase. In addition to this, the concentration in water was decreased to resist faster diffusion and the speed was reduced to 600rpm to further prevent deposition of Eudragit L100-55 on the rotor. Similarly to previous efforts, the higher concentrations of the organic phase forced Eudragit L100-55 to crash out, since the viscosity of the solution was very high in the aqueous phase, as illustrated in Table 3.4. This resulted due to the presence of small amounts of water in the mixture, showing that the solvent-non solvent interaction strongly affected the emulsification mechanism [153], [154], [232]. For this reason, a few batches were produced with increasing water amounts, while using lower concentrations in Eudragit L100-55, to investigate the critical concentration of the organic phase in the aqueous phase, which presented higher dispersion rates [234], [240]. It was observed that the increase in water gradually improved dispersability of the organic phase and reduced the material losses [153], [154]. This led to the reinforced precipitation of single particles, as it was observed after centrifugation and drying. Therefore, it was discovered that the efficacy of the process was increased when mixing 2wt% of Eudragit L100-55 in 30ml, 40ml or 50ml of water, which resulted in 6.7wt%, 5wt% and 4wt% concentration of the aqueous phase.

In the last approach that was developed, Avicel 101 coated particles were prepared by a simplified emulsion-solvent evaporation method, as has previously been described. Briefly, Eudragit L100-55 was dissolved in methanol preparing batches of the organic phase at 2wt% concentration. Then, varied amounts of Avicel 101 were separately dissolved in methanol, to prepare various batches of the suspension phase (see

Table 3.5). This system allowed the formation of a uniform emulsion at 600rpm, since Eudragit L100-55 remained dissolved in the mixture [150]. The mixture was left to evaporate the solvent at ambient temperature without the use of any equipment. The process involved minimum material losses. Therefore, after evaporation of the methanol, large samples of single particles were recovered. The coating levels achieved were examined thoroughly in the next sections, to reveal the critical core-coat ratio that reached the maximum of the process.
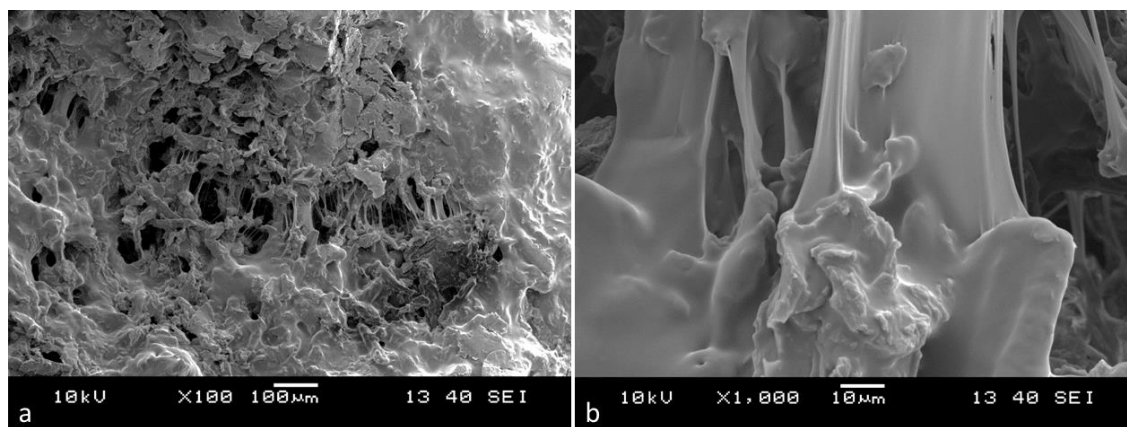
Figure 8.2: SEM micrographs of the recovered samples after precipitation of the organic phase into the aqueous phase. a) Eudragit L100-55/Avicel 101 bulks of mass, b) film coating on Avicel 101 particles

8.3 Fourier Transform Infrared Spectroscopy (FTIR)

In order to identify the presence of the Eudragit L100-55 in the recovered particles and to investigate any possible interactions with the Avicel 101, a spectroscopic analysis was performed. The analysis aimed to quantify the characteristic absorption bands of the samples and depict any changes in the shape and the volume of the peaks, any shifts in the position or even the emergence of any new peaks. Initially, pure Avicel 101 and Eudragit L100-55 samples were scanned to record the absorption band positions of the functional groups of each material as a reference. The representative FTIR spectrum of Avicel 101 and Eudragit L100-55 is presented in Figure 8.3 and Figure 8.4, respectively. The absorption bands identified from the analysis and the respective chemical bonds, are displayed in Table 8.1 for Avicel 101 and Table 8.2 for Eudragit L100-55. It can be observed in Figure 8.3 that the typical characteristic peaks of Avicel 101 appeared at 3330cm^{-1} corresponding to stretching of the O-H groups, and at 1056cm^{-1}, 1034cm^{-1} showing a sharp double peak, which was related to C-O-C and C-OH stretching,

respectively [160], [166], [167], [241], [242]. Eudragit L100-55 presented a characteristic sharp double peak at 1725cm^{-1}, 1701cm^{-1} attributed to stretching of the C=O (esteric) groups, and an additional sharp characteristic double peak at 1177cm^{-1}, 1159cm^{-1} representing C-O stretching, as shown in Figure 8.4 [149], [150], [171], [175], [221], [243], [244].
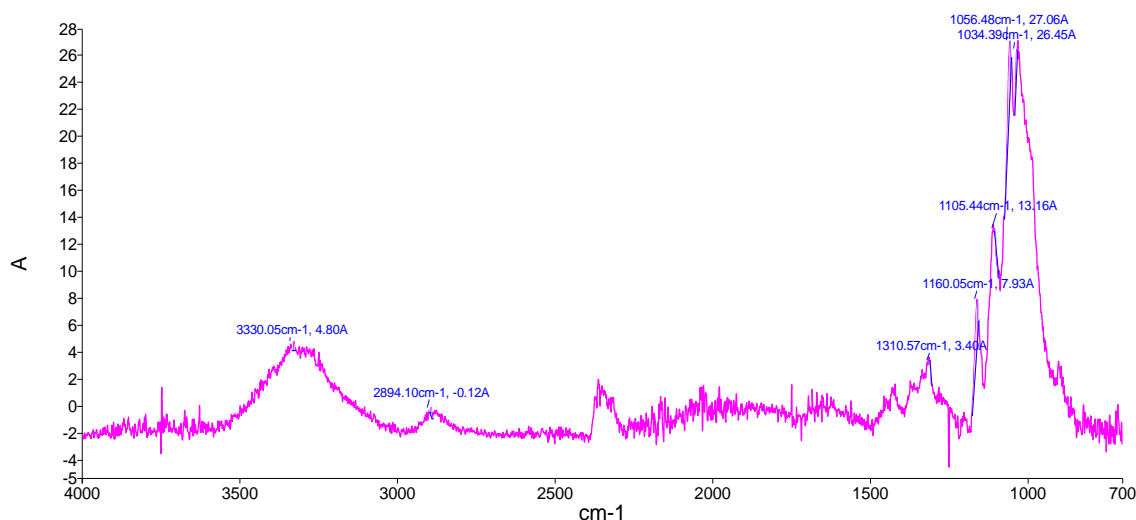
Figure 8.3: Characteristic FTIR spectrum of Avicel 101

Table 8.1: Infrared spectral interpretation table for Avicel 101

Peak No.	Peak (cm^{-1})	Absorption region (cm^{-1})	Functional Group	Vibration type	Compound Class	Comments
1	3330.05	3550-3584	O-H stretching		phenol	Wide peak due to the presence of hydrogen bonds
2	2894.1	3000-2840	C-H stretching	CH$_2$ symmetric	alkane	
3	1310.57	1390-1310	O-H bending		phenol	weak vibration
4	1160.05	1210-1100	C-O stretching			double peak
5	1105.44					
6	1056.48	1310-1020	C-O-C stretching		aromatic ether	double peak
7	1034.39	1200-1020	C-OH stretching		primary alcohol	
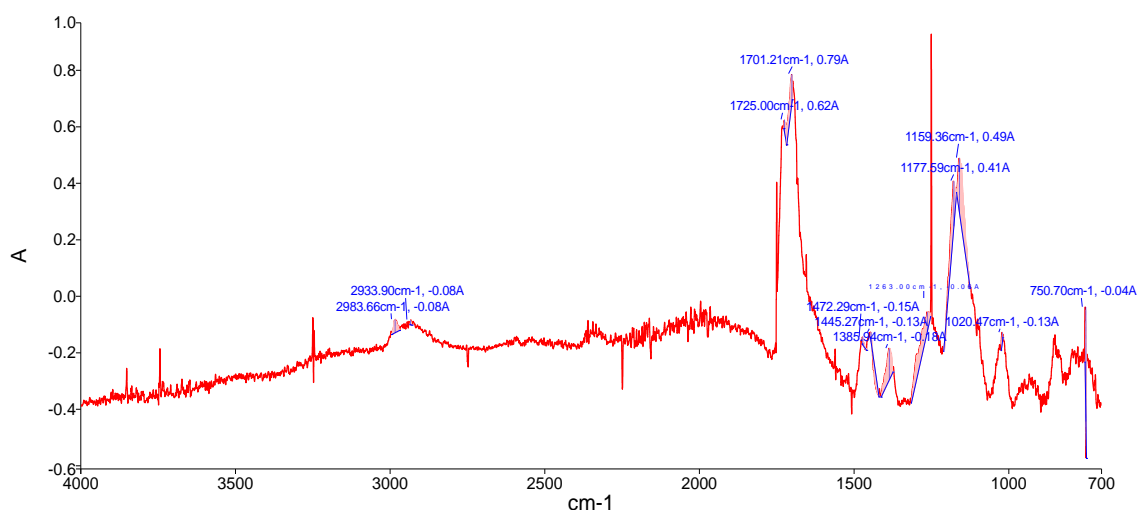
Figure 8.4: Characteristic FTIR spectrum of Eudragit L100-55

Table 8.2: Infrared spectral interpretation table for Eudragit L100-55

Peak No.	Peak (cm⁻¹)	Absorption region (cm⁻¹)	Functional Group	Vibration type	Compound Class	Comments
1	2983.66	3000-2840	C-H stretching	CH_3 asymmetric	alkane	double peak
2	2933.9			CH_2 asymmetric		
3	1725	1750-1735	C=0 stretching		saturated ester	double peak
4	1701.21					
5	1472.29	1465	C-H bending	$C\text{-}CH_3$ asymmetric	alkane	double peak
6	1445.27	1450		$C\text{-}CH_2$ scissors		
7	1385.94	1385-1380	C-H bending	CH_3 symmetric	alkane	
8	1263	~1240	C-C-O stretching		saturated ester	
9	1177.59	1210-1163	C-O stretching			one broad peak
10	1159.36	1205-1124				
11	1020.47	1100-1020	$CH_3\text{-}CO\text{-}$	rocking		
12	750.7	730-720	C-H bending	$C\text{-}CH_2$ rocking	alkane	

Figure 8.5 presents the FTIR spectra obtained from the samples prepared using the first method described in the previous section, compared to Avicel 101 and Eudragit L100-55. The spectra of the samples with the highest concentrations of 10wt%, 5wt% and 3.3wt% in Eudragit L100-55, were similar showing typical features of the Avicel 101. Four main characteristic bands were identified at 3330, 2894, 1310 and 1056, 1034 cm^{-1}, related to stretching of the O-H, C-H, bending of the O-H, and stretching of the C-O-C, C-OH functional groups of Avicel 101. Absorption bands related to Eudragit L100-55 were not identified, since the material crushed out and was completely removed before centrifugation and drying. On the contrary, for the samples containing lower concentrations of 2.5wt% and 2wt% those peaks were decreased. In fact, the samples presented absorption in the regions of 1725-1701, 1472-1445, and 1177-1159 cm^{-1}, showing small peaks corresponding to C=O stretching, C-H bending and C-O stretching related to Eudragit L100-55 chemical bonds, which indicated the presence of Eudragit L100-55. As described in the previous section, decreasing the viscosity of the organic phase improved the dispersion in the aqueous phase, which in fact increased effectiveness of the process.

Figure 8.5: FTIR spectra of the samples prepared using 10, 5, 3.3, 2.5 and 2wt% of Eudragit L100-55 in methanol solutions, precipitated into water containing 1, 2, 3.3, 2.5 and 2wt% of Avicel 101 suspensions

The samples prepared using the second method, presented several characteristic bands corresponding to the functional groups of both Avicel 101 and Eudragit L100-55, as illustrated in Figure 8.6 and Figure 8.7. The spectra of the samples revealed a double peak at 2983, 2894 cm^{-1} corresponding to stretching of C-H functional groups of Eudragit L100-55 and Avicel 101, respectively. Furthermore, a strong peak at 1159cm^{-1} was present related to stretching of C-O groups of Eudragit L100-55, which overlapped with C-O stretching of Avicel 101 groups at 1160cm^{-1}. Additional double peaks in the regions of 1725-1701 and 1472-1445 cm^{-1} that were characteristic of Eudragit L100-55 were observed. In Figure 8.6, the samples prepared using constant concentration of the aqueous phase at 20wt%, did not present any differences in the intensity of the peaks, although the concentration was varied in the organic phase. More specifically, the absorption bands attributed to the Avicel 101 groups were strong, while the absorption bands attributed to the Eudragit L100-55 were weak, indicating the small concentration in Eudragit L100-55 present in the samples. Only exception, was the sample prepared using 5wt% of Eudragit L100-55 in the organic phase, which presented stronger intensity in the absorption regions related to Eudragit L100-55 and smaller intensity in the regions related to Avicel 101, compared to the other samples that contained lower concentrations in the organic phase at 3.3wt%, 2.5wt% and 2wt%. It was indicated in the previous section that this sample presented increased viscosity and was expected to exhibit reversed effect in the absorption intensity. It should be noted that particles from the samples prepared using the highest concentration at 10wt% were not recovered due to the significant high viscosity of the organic phase. Therefore, it was believed that the sample at 5wt% contained traces of Eudragit L100-55 bulks of mass, which was not completely removed before centrifugation and drying, and for this reason it presented stronger characteristic bands related to Eudragit L100-55. In Figure 8.7 it can be observed that the increased amount in water for the samples prepared at 2wt% concentration in Eudragit L100-55, enhanced the characteristic features of the double peaks at 2983, 2933 cm^{-1}, 1472, 1445 cm^{-1} and 1177, 1159 cm^{-1} corresponding to the C-H stretching, bending and C-O stretching of the Eudragit L100-55 chemical bonds respectively. Further analysis revealed that the intensity of the peaks was increased gradually with increasing amounts in water from 10ml to 40ml of the aqueous phase, while the intensity of the Avicel 101 characteristic bands was decreased. This observation correlated well with the observations in the previous section, which described the improvement of the organic phase's dispersability in the aqueous phase, whilst increasing the water content. An exception was discovered

for the sample prepared with the highest amount of 50ml in water, which presented stronger intensity of the Avicel 101 characteristic peaks, compared to the samples prepared with 30ml and 40ml. This behaviour indicated a reduction of the Eudragit L100-55 concentration, although the sample contained 2wt% in the organic phase, which was constant for all the samples, and had exhibited increased dispersability. It is more than likely that the amount of water exceeded the critical concentration of the organic phase in the aqueous phase, resulting in reduced Eudragit L100-55 concentration in the samples.
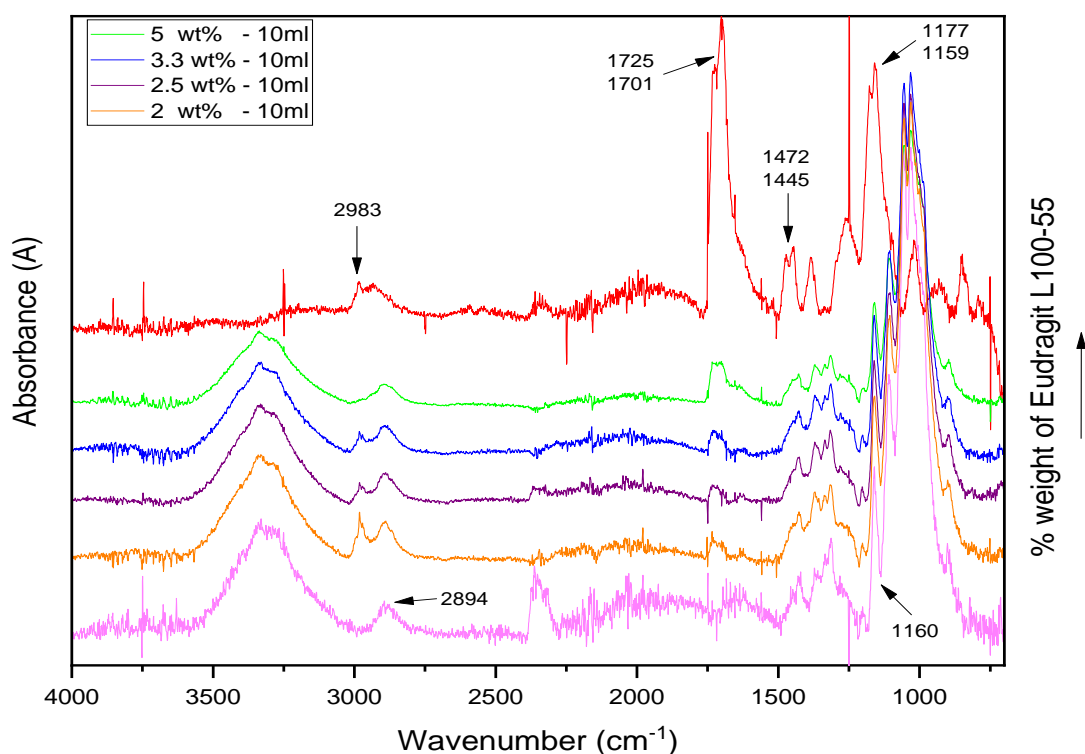
Figure 8.6: FTIR spectra of the samples prepared using 5, 3.3, 2.5 and 2wt% of Eudragit L100-55 in methanol containing Avicel 101 suspensions, precipitated into 10ml of water
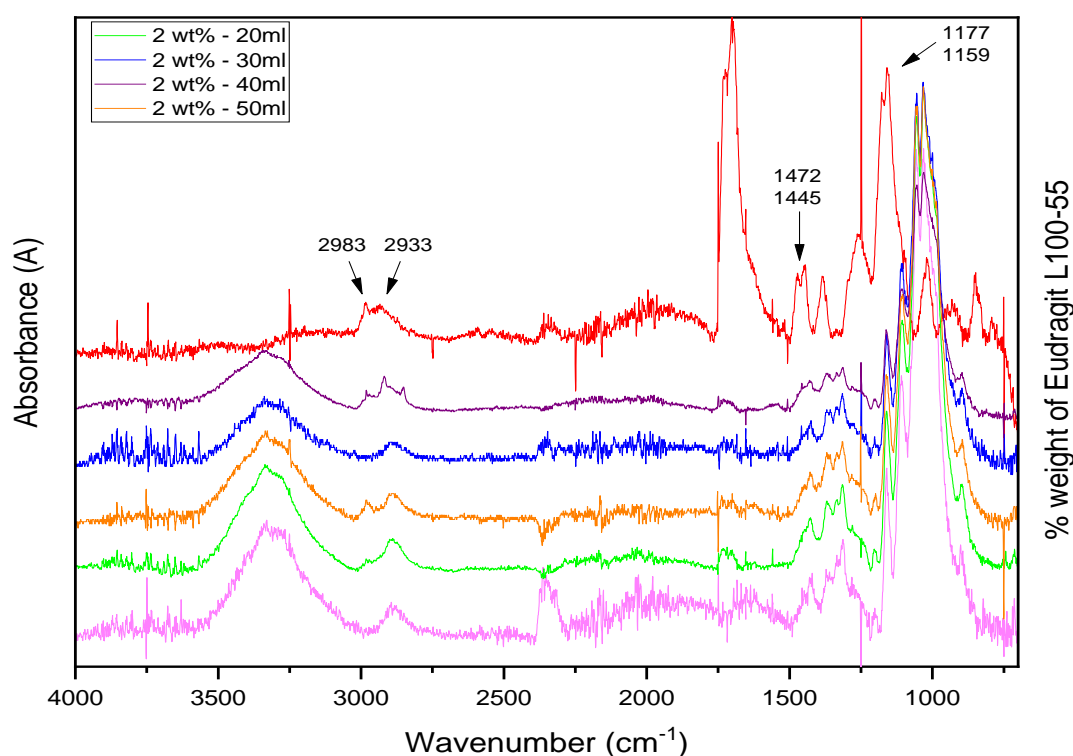
Figure 8.7: FTIR spectra of the samples prepared using 2wt% of Eudragit L100-55 in methanol containing Avicel 101 suspensions, precipitated into 20, 30, 40 and 50ml of water

The third method that was used minimised the material losses during the evaporation step as discussed in the previous section. It can be seen at a glance in Figure 8.8 that the important absorption regions of Eudragit L100-55 presented clear strong peaks, which confirmed the increased amount of the material in the samples, compared to the previous methods used. The intensity of the characteristic bands corresponding to either the Avicel 101 or the Eudragit L100-55 presented differences between the samples that were directly related to the material concentration used during the preparation process. In more detail, in case of the sample containing 2wt% of Eudragit L100-55 in the organic and 2wt% of Avicel 101 in the suspension phase (4:1 core-coat), the absorption bands of O-H and C-O stretching at 3330 and 1160 cm^{-1} exhibited increased intensity, while the double peak of C=O stretching at 1725-1701 cm^{-1} was considerably reduced, which indicated reduced amount of Eudragit L100-55 compared to other samples. In case of the sample containing 2wt% of Eudragit L100-55 and 1wt% of Avicel 101 (2:1 core-coat), the corresponding peaks to O-H and C-O stretching were less intense and the C=O absorption peak got stronger. In addition, the double peak at 1472, 1445cm^{-1} corresponding to the absorption

of the C-CH$_2$, C-CH$_3$ Eudragit L100-55 functional groups, appeared to be stronger. Finally, the sample containing 2wt% of Eudragit L100-55 and 0.5wt% of Avicel 101 (1:1 core-coat) presented reduced intensity peaks at the absorption regions of the Avicel 101 functional groups and significant intensity increase in the absorption bands of the esteric C=O bonds and C-CH$_x$ bonds, indicating the strong presence of Eudragit L100-55 in the sample. The results showed that the Eudragit L100-55 concentration was increased as the concentration of Avicel 101 decreased in the formulation, which was highly expected due to the simplicity of the method.

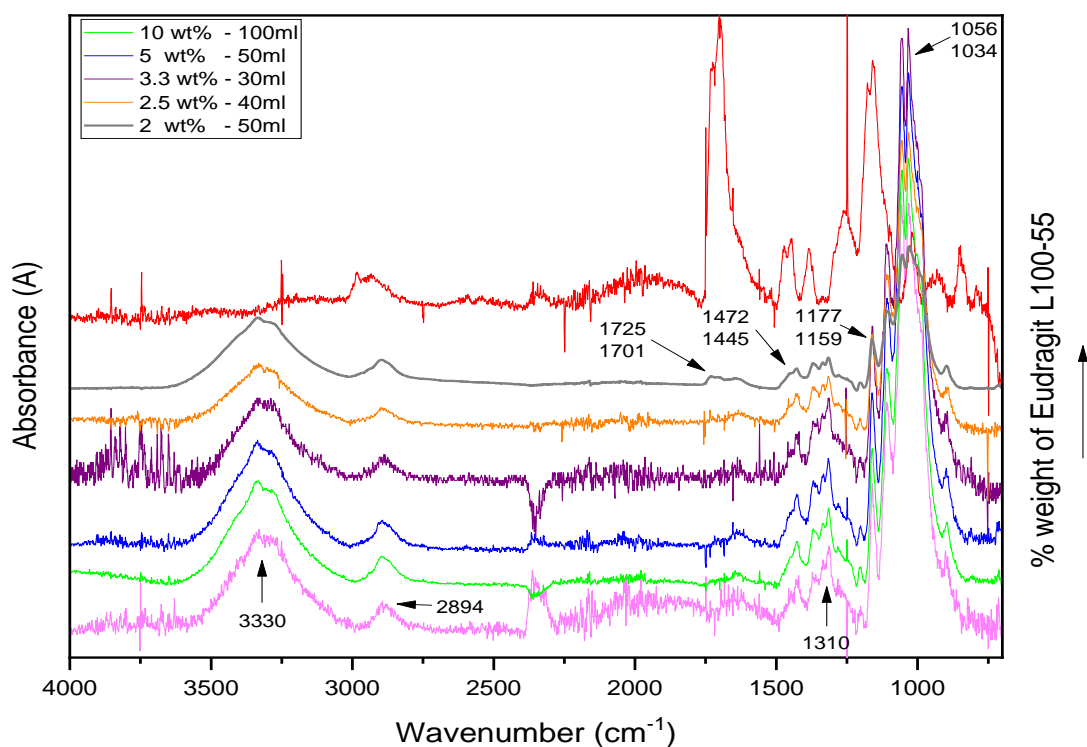**Figure 8.8:** FTIR spectra of the samples prepared using 2wt% of Eudragit L100-55 in methanol solutions, precipitated into methanol containing 2, 1 and 0.5wt% of Avicel 101 suspensions

8.4 Thermogravimetric Analysis (TGA)

TGA analysis was performed to examine the physical transitions of the samples through monitoring the changes in mass. Initially, Avicel 101 and Eudragit L100-55 were tested to record the decomposition temperatures of the pure components and use them for the analysis. Specifically, the weight loss percentage of the samples over the specified temperature ranges for Avicel 101 and Eudragit L100-55 was used to quantify the

concentration of each component in the samples. The thermograms in Figure 8.9 present the evolution of mass loss of the initial materials. It was previously described in section 4.2 that Avicel 101 exhibited an early 5% of mass loss up to 250°C related to water evaporation [162], [165], [166], [241]. The main decomposition of the material, which involved the reduction of ~90% of the total mass initiated at approximately 270°C and was completed at about 370°C, showing a midpoint (50% mass losses) at around 347°C [162], [165]–[167], [241]. Eudragit L100-55 presented an initial 5% of mass loss during the dehydration process up to 200°C. The main decomposition of the material occurred in a wider temperature range, which involved a slow decomposition of 5% of mass loss up to 270°C, presenting a midpoint at ~386°C, which was then followed by the total reduction of mass at about 440°C [172], [175].
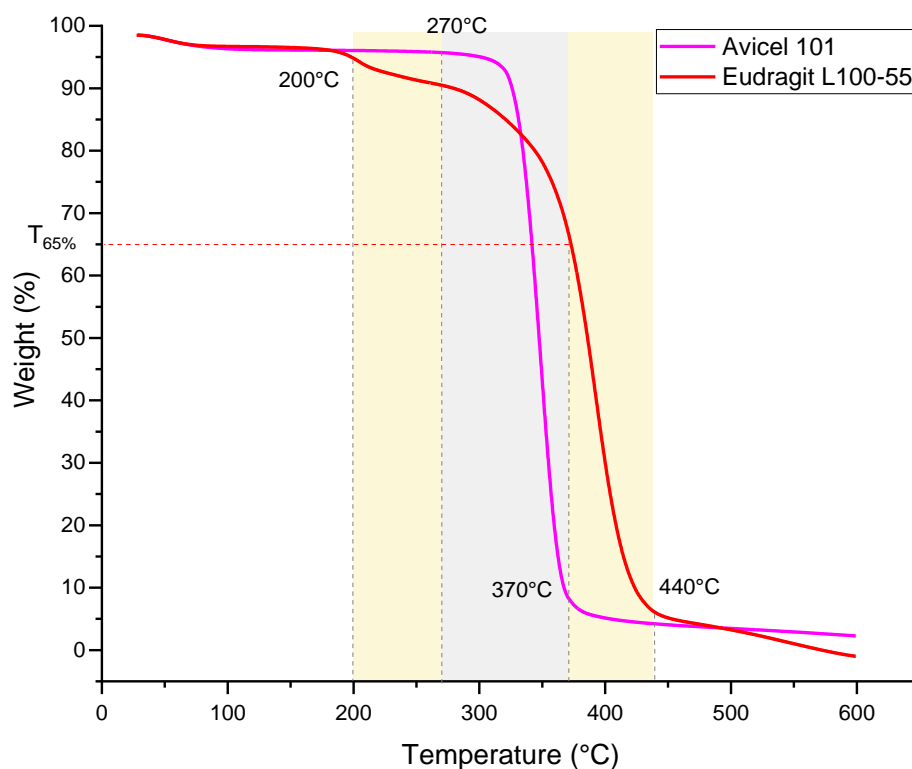
Figure 8.9: TGA thermograms as a function of temperature for Avicel 101 and Eudragit L100-55

The samples prepared using the first method followed similar degradation patterns with Avicel 101, as illustrated in Figure 8.10. The samples containing high concentrations of Eudragit L100-55 in the organic phase of 10wt%, 5wt% and 3.3wt%, reduced 95% of the

mass at the exact same temperature range as Avicel 101. The decomposition pattern implied the absence of Eudragit L100-55 from the particles recovered, which was highly expected based on the increased viscosity of the organic phase and the FTIR results in the previous section. On the other hand, as it was pointed out earlier through the FTIR analysis, the samples prepared at lower concentrations of 2.5wt% and 2wt% that showed decreased viscosity, exhibited slower decomposition rates, which occurred in two steps. The first one was attributed to the degradation of the Avicel 101 up to ~370°C and the second one to the degradation of the Eudragit L100-55 up to ~440°C. However, the curves appeared to have been shifted slightly to the right presenting a higher midpoint, which indicated the simultaneous degradation of the materials up to ~370°C. For this reason, the decomposition end point of Avicel 101 was considered as the $T_{65\%}$ in the numerical analysis, as highlighted in Figure 8.9, in order to calculate the total Eudragit L100-55 mass in the samples. From the analysis it was found that the samples with the lowest concentrations contained 19.38% and 20.73% of Eudragit L100-55. Table 8.3 summarises the percentage of mass losses for all samples.
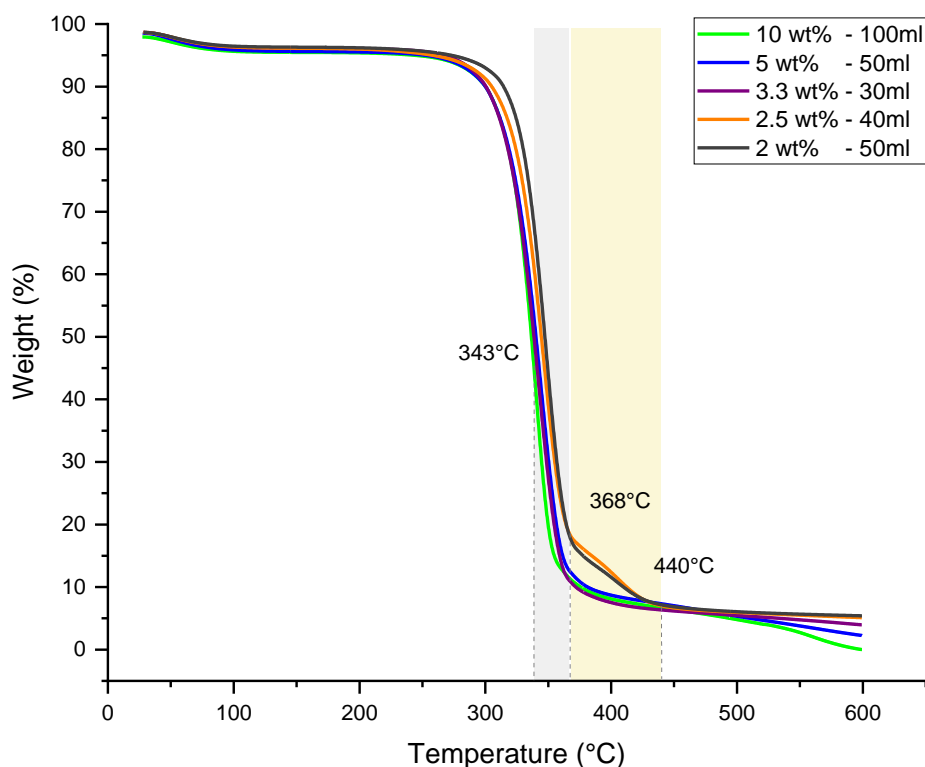
Figure 8.10: TGA thermograms as a function of temperature for the samples prepared using 10, 5, 3.3, 2.5 and 2wt% of Eudragit L100-55 in methanol solutions, precipitated into water containing 1, 2, 3.3, 2.5 and 2wt% of Avicel 101 suspensions

Table 8.3: Percentage weight loss of the samples during decomposition

Sample		Method	% Avicel 101	% Eudragit L100-55
10wt% - 100ml	Method 1	Precipitate Eudragit into Avicel, centrifuge, evaporate	87.64	-
5wt% - 50ml			88.12	-
3.3wt% - 30ml			89.18	-
2.5wt% - 40ml			76.70	19.38
2wt% - 50ml			74.40	20.73
10wt% - 10ml	Method 2	Precipitate Eudragit and Avicel into water, centrifuge, evaporate	no sample	no sample
5wt% - 10ml			73.97	22.43
3.3wt% - 10ml			79.60	11.09
2.5wt% - 10ml			81.33	10.31
2wt% - 10ml			83.80	9.00
2wt% - 20ml	Method 2 – anti-solvent	Precipitate Eudragit and Avicel into water, change the amount of anti-solvent, centrifuge, evaporate	81.26	9.02
2wt% - 30ml			75.86	18.68
2wt% - 40ml			75.66	19.58
2wt% - 50ml			80.21	11.17
2wt% - 2wt%	Method 3	Precipitate Eudragit into Avicel, evaporate methanol in petri dish	78.77	18.61
2wt% - 1wt%			59.65	37.46
2wt% - 0.5wt%			46.00	47.85

TGA curves of the samples prepared using the second method revealed similar decomposition patterns to Avicel 101, as demonstrated in Figure 8.11a and b. The midpoint of the curves was shifted to the right, indicating the presence of Eudragit L100-55 in all the samples. More specifically, the samples prepared using a constant concentration of the aqueous phase at 20wt%, showed weight losses attributed to the presence of Eudragit L100-55 between 9% and 11%, since the temperature differences were very small, as can be observed in Figure 8.11a. A more notable difference was exhibited by the sample prepared using the highest concentration of Eudragit L100-55 at 5wt% in the organic phase, which presented a second decomposition between 370-440°C. This behaviour was associated to the increased amount of Eudragit L100-55 in the sample, which was measured at 22.43%, and correlated well with the FTIR results. When the concentration of the organic phase was kept constant at 2wt%, the decomposition rate

was found to decrease while the concentration of water in the aqueous phase was increased. Figure 8.11b demonstrates the evolution of mass reduction towards higher temperatures, as the water amount was increased from 10ml to 40ml. The weight loss recorded at the decomposition temperature ranges matching the degradation of Eudragit L100-55, was gradually increased from 9% to 20%. Once the critical concentration was achieved at 50ml of water concentration, the percentage of Eudragit L100-55 was decreased at 11%.
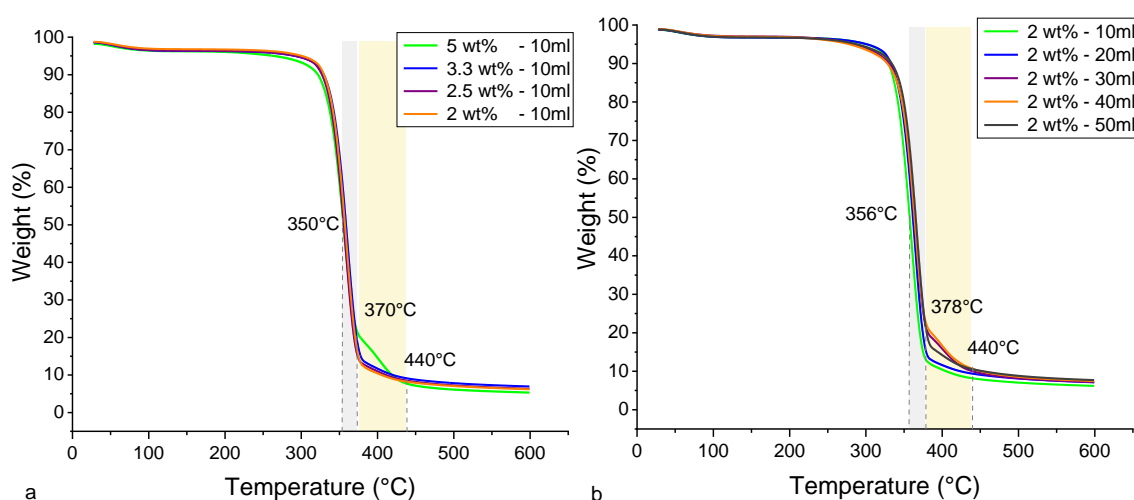
Figure 8.11: TGA thermograms as a function of temperature for a) samples prepared using 5, 3.3, 2.5 and 2wt% of Eudragit L100-55 in methanol containing Avicel 101 suspensions, precipitated into 10ml of water and b) samples prepared using 2wt% of Eudragit L100-55 in methanol containing Avicel 101 suspensions, precipitated into 20, 30, 40 and 50 of water

The TGA results of the samples prepared using the third method were also aligned with the observations made from the FTIR analysis. The curves in Figure 8.12 revealed a wide decomposition temperature range with typical degradation characteristics of both Avicel 101 and Eudragit L100-55 for all the samples. The decomposition occurred in two broad steps, one in the region of 270-370°C related to the destruction of the Avicel 101 backbone, and one in the region of 370-440°C corresponding to the degradation of Eudragit L100-55. It can be clearly observed that the midpoint temperature shifted to the right as the concentration in Avicel 101 decreased in the mixture. Samples prepared using 2wt% of Avicel 101 (4:1 core-coat) exhibited high decomposition rate with a midpoint at 344°C. Samples prepared using 0.5wt% of Avicel 101 (4:1 core-coat) exhibited an extended decomposition with a midpoint at 370°C, suggesting the strong presence of

Eudragit L100-55, which decomposed at higher temperatures. Additionally, the weight loss calculations revealed an increase in Eudragit L100-55 concentration from 18.61% to 47.85% as the amount of Avicel 101 was gradually decreased.
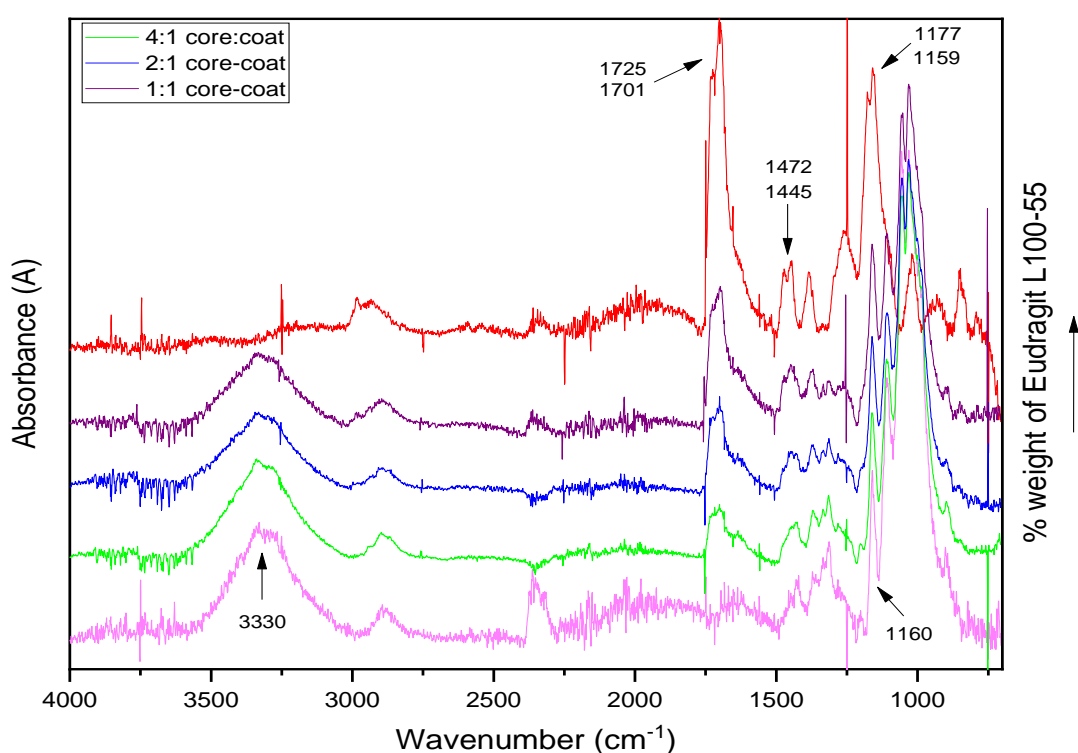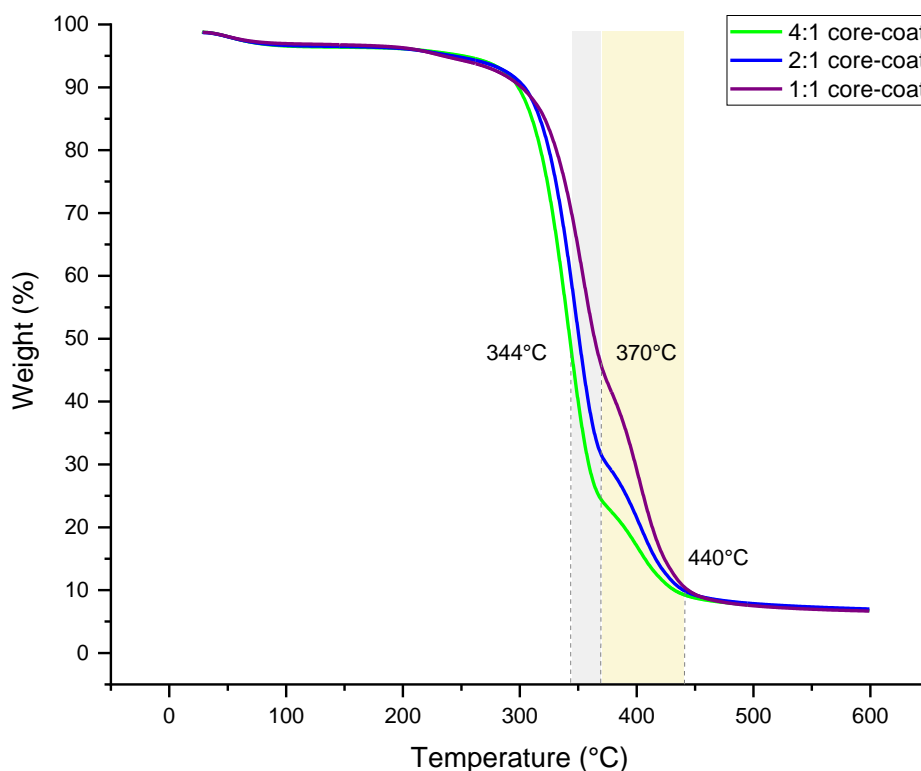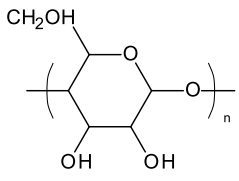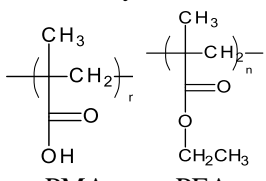

Figure 8.12: TGA thermograms as a function of temperature for the samples prepared using 2wt% of Eudragit L100-55 in methanol solutions, precipitated into methanol containing 2, 1 and 0.5wt% of Avicel 101 suspensions

8.5 Time-of-Flight Secondary Ion Mass Spectrometry (ToF-SIMS)

ToF-SIMS was used for the molecular chemical identification of the recovered particles to review the distribution of the different components over the surface of the particles and estimate the efficacy of the coating. Firstly, the chemical composition of Avicel 101 and Eudragit L100-55 was examined in order to generate reference spectra of the characteristic ions of each material. The characteristic peaks and the corresponding chemical compositions that were identified using both positive and negative polarities, are listed in Table 8.4. In the negative ion ToF-SIMS spectrum of Eudragit L100-55 a unique signal was detected at m/z 85, which was specific for the methacrylic acid repeat unit [119]. Therefore, the negative mode was used for the analysis and imaging of the

distribution of Eudragit L100-55 on all samples. Furthermore, a significant signal for Avicel 101 was found at m/z 59, which was useful for imaging [119]. The characteristic negative signals identified for the two materials are illustrated in Figure 8.13. Once the peaks in the spectrum of each material were evaluated, images of specific ions were generated to analyse the surface of the pure components. The signals at m/z 59⁻, 71⁻, 101⁻ and 113⁻ were used to map the Avicel 101 particles, which is demonstrated in Figure 8.14, and the signals at m/z 85⁻, 97⁻, and 265⁻ were used to map the Eudragit L100-55 particles, as demonstrated in Figure 8.15. These signals were further used to generate total images of the specific ions in the recovered particles, which were compared to the reference images. The intensity of the specific peaks corresponding to Eudragit L100-55 showed the location of the material that provided important information about the coating.

Table 8.4: Characteristic ToF-SIMS peaks for Avicel 101 and Eudragit L100-55

Material	Characteristic Peak	Chemical Composition	Ion Description
Avicel 101 (microcrystalline cellulose) $C_6H_{10}O_5$	57^+	$C_4H_9^+$	cellulose fragment
	115^+	$C_8H_3O^+$	cellulose fragment
	127^+	$C_6H_7O_3^+$	cellulose fragment
	135^+	$C_6H_{15}O_3^+$	cellulose fragment
	267^+	$C_{16}H_{27}O_3^+$	cellulose fragment
	59^-	$C_2H_3O_2^-$	cellulose fragment
	71^-	$C_3H_3O_2^-$	cellulose fragment
	87^-	$C_3H_3O_3^-$	cellulose fragment
	101^-	$C_4H_5O_3^-$	cellulose fragment
	113^-	$C_5H_5O_3^-$	cellulose fragment
	127^-	$C_6H_7O_3^-$	cellulose fragment
Eudragit L100-55 (polymethacrylic acid ethyl acrylate) PMA $C_4H_5O_2$ PEA $C_5H_8O_2$	23^+	Na^+	sodium
	77^+	$C_3H_9O_2^+$	Eudragit fragment
	100^+	$C_5H_8O_2^+$	repeat unit of PEA
	102^+	$C_5H_{10}O_2^+$	Eudragit fragment
	121^+	$C_7H_5O_2^+$	Eudragit fragment
	85^-	$C_4H_5O_2^-$	repeat unit of methacrylic acid
	97^-	SO_4H^-	unexpected
	99^-	$C_5H_7O_2^-$	repeat unit of PEA
	265^-	$C_{12}H_{25}O_6^-$	Eudragit fragment
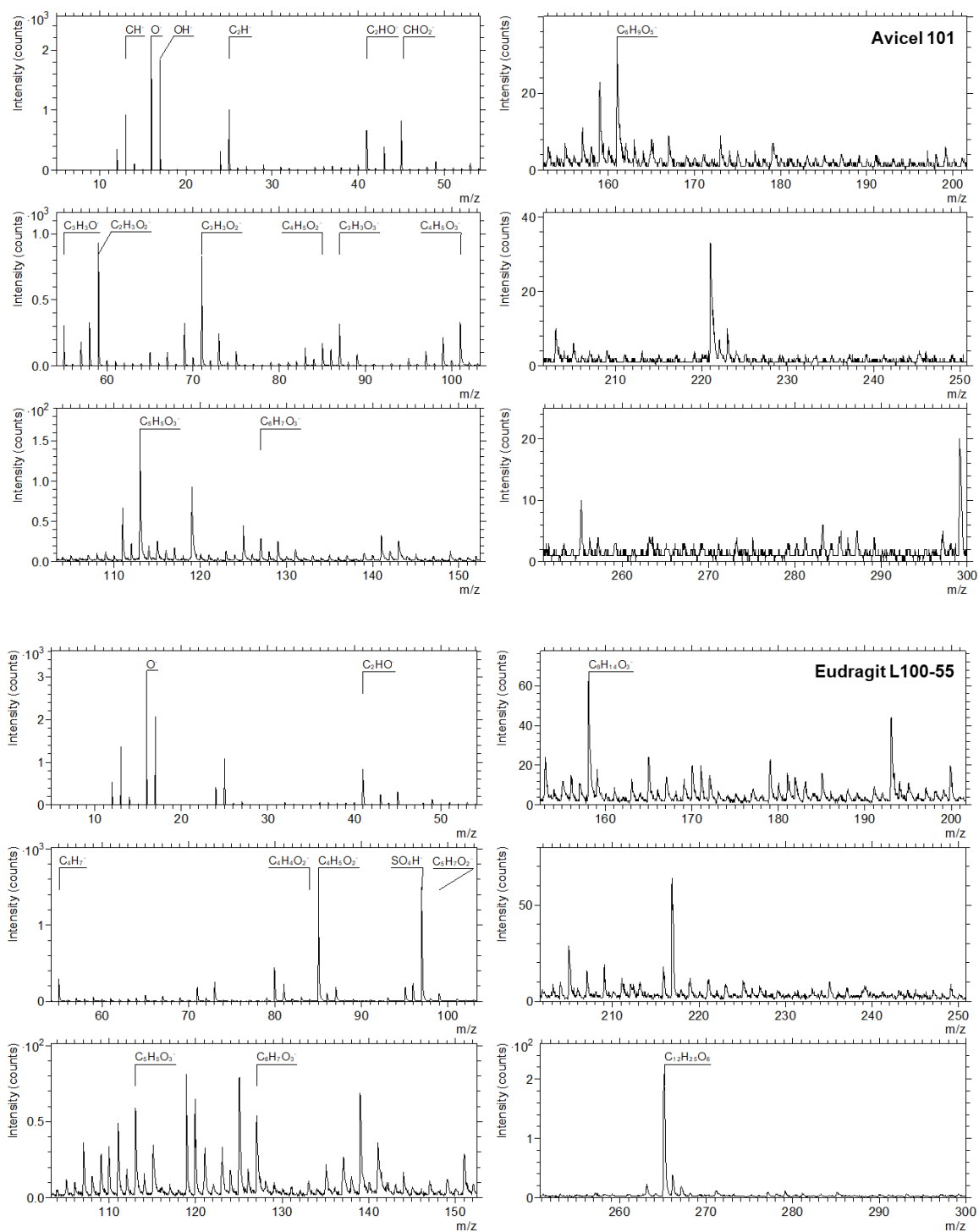
Figure 8.13: ToF-SIMS negative spectra for Avicel 101 and Eudragit L100-55. The characteristic peaks are labelled
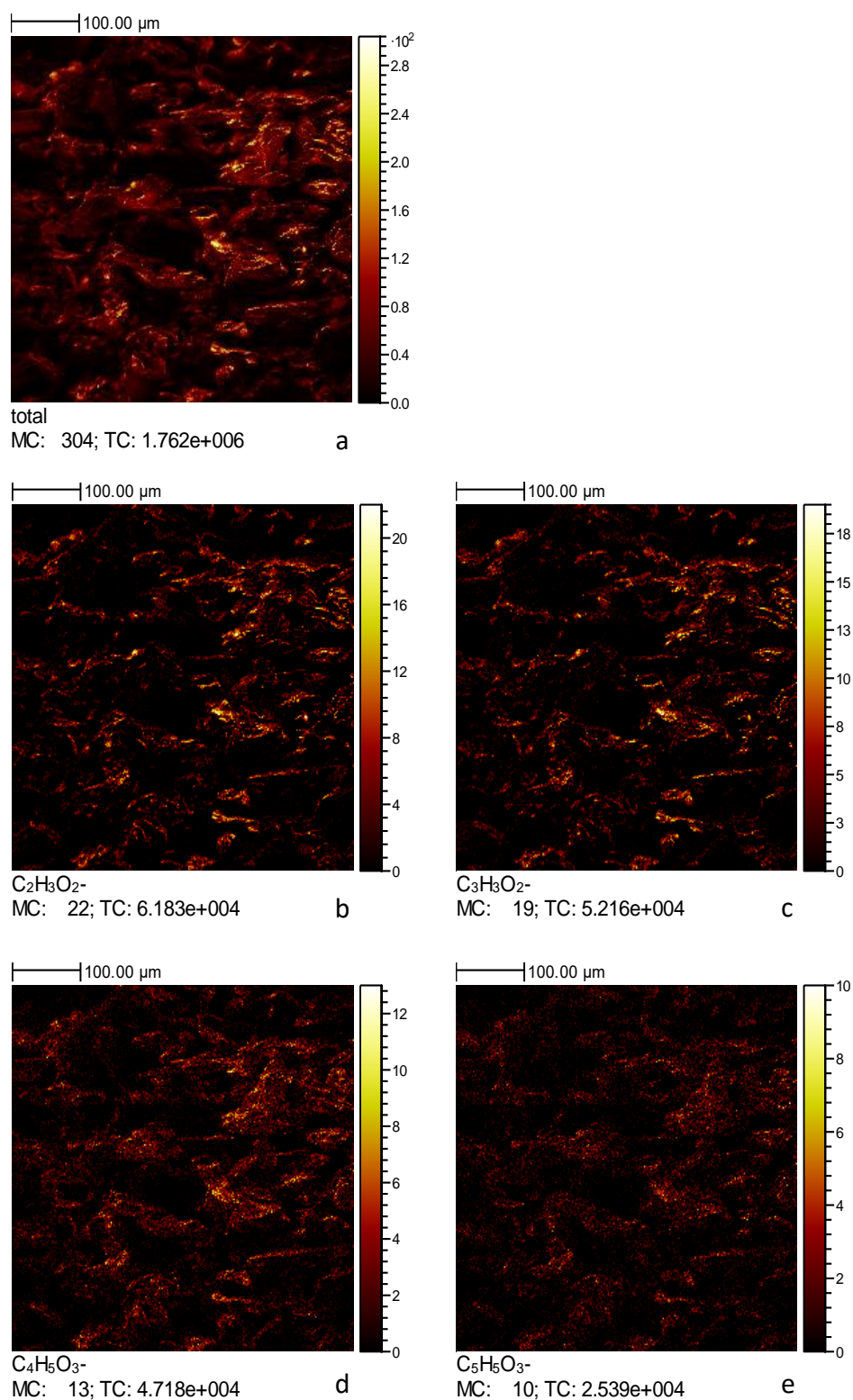
Figure 8.14: ToF-SIMS ion images of Avicel 101 particles (500 x 500 μm^2) representing the negative ions a) total, b) $C_2H_3O_2$-, c) $C_3H_3O_2$-, d) $C_4H_5O_3$- and e) $C_5H_5O_3$-
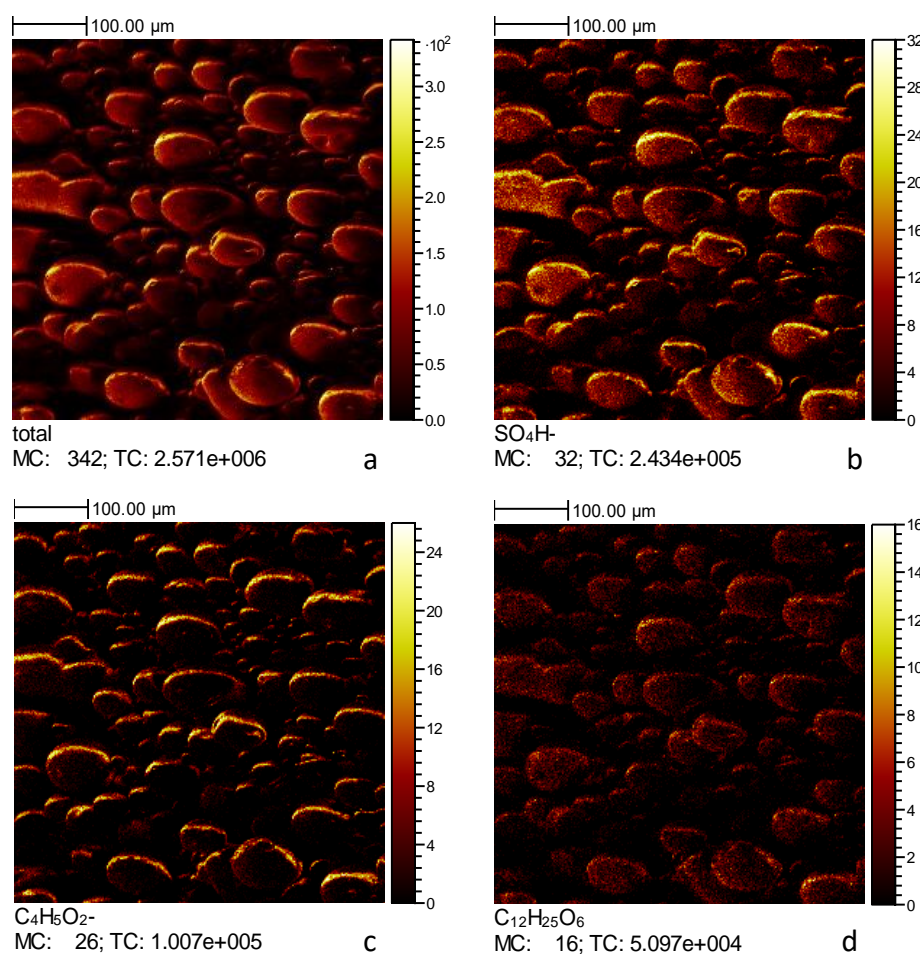
Figure 8.15: ToF-SIMS ion images of Eudragit L100-55 particles (500 x 500 μm^2) representing the negative ions a) total, b) SO4H-, c) C4H5O2- and d) C12H25O6-

The ToF-SIMS analysis of the samples prepared using the first method agreed with the previous observations made through FTIR and TGA analysis (see sections 8.3 and 8.4). The recovered particles from the batches containing high amounts of Eudragit L100-55 (10wt%, 5wt%, 3.3wt%) were dominated by the signals corresponding to Avicel 101, while the batches containing lower amounts (2.5wt%, 2wt%) presented strong signals corresponding to Eudragit L100-55. ToF-SIMS analysis further confirmed that the batches with increased viscosity inhibited the precipitation of Eudragit L100-55 on the surface of the Avicel 101 particles. In Figure 8.16, it is obvious from the extracted spectrum of the sample prepared using 5wt% of Eudragit L100-55 that the intensity of the characteristic ions related to Avicel 101 was very high compared to Eudragit L100-55. The overlap total image revealed that the sample contained mainly Avicel 101

particles (red) with small deposits of Eudragit L100-55 (green) on the surface. Further from the FTIR and the TGA analysis, ToF-SIMS detected small amounts of Eudragit L100-55 on the sample. In the FTIR spectrum and the TGA thermogram it was very difficult to distinguish the presence of the polymer. Apparently, there was an overlap with the characteristic FTIR peaks of Avicel 101, which made it impossible to identify any peaks related to Eudragit L100-55, since the concentration of the material in the sample was very small. Similarly, the percentage weight loss was most likely very small to cause any changes in the decomposition pattern, and hence it was impossible to be measured. Nevertheless, the surface analysis revealed that the concentration in Eudragit L100-55 was very low to create a film coating.

Figure 8.16: ToF-SIMS ion images of the sample prepared using 5wt% of Eudragit L100-55 in methanol solutions, precipitated into water containing 2wt% of Avicel 101 suspensions. The images represent the negative ions for a) total, b) surface overlay of Avicel 101 (red) and Eudragit L100-55 (green), c) total of Avicel 101 and d) total of Eudragit L100-55

On the contrary, Figure 8.17 revealed a broad distribution of Eudragit L100-55 (green) on the surface of the Avicel 101 particles (red) for the sample prepared at 2wt% concentration. The signal of the Eudragit L100-55 was increased, while the signal of Avicel 101 became weaker. The spectrum indicated that the chemical composition on the surface of the particles was mainly consisted of Eudragit L100-55. Although it seemed that Eudragit L00-55 formed a coating film on the surface of the particles, it was observed that the distribution was not homogeneous. Regions which presented strong Avicel 101 signals were clearly identified, and this indicated that the coating was not uniform.

Figure 8.17: ToF-SIMS surface images of the sample prepared using 2wt% of Eudragit L100-55 in methanol solutions, precipitated into water containing 2wt% of Avicel 101 suspensions. The images represent the negative ions for a) total, b) surface overlay of Avicel 101 (red) and Eudragit L100-55 (green), c) total of Avicel 101 and d) total of Eudragit L100-55

The extracted spectra of the samples prepared using the second method revealed a completely different distribution compared to the first method. In Figure 8.18, it can be observed that the surface of the particles was mainly composed of Eudragit L100-55 (green). The samples exhibited strong signals related to Eudragit L100-55 that almost covered the signals related to Avicel 101 (red). In particular, the sample containing the highest concentration in Eudragit L100-55 of 5wt%, presented a nearly continuous dispersion of the polymer on the surface of the particles. The sample containing 3.3wt% of Eudragit L100-55 presented small regions of Avicel 101 signals, while the sample with the smallest concentration of 2wt% demonstrated stronger intensity of the characteristic signals related to Avicel 101, compared to the rest of the samples. The ToF-SIMS analysis revealed an increase in the effectiveness of the coating process with an increase in the concentration of Eudragit L100-55 in the organic phase, which in fact opposed to the analysis described in the previous sections. Based on the low amount of 10ml in water that was used in the method, it was believed that the increased viscosity of the emulsion prepared, resulted in the formation of Eudragit L100-55 bulks of mass, instead of a film coating.
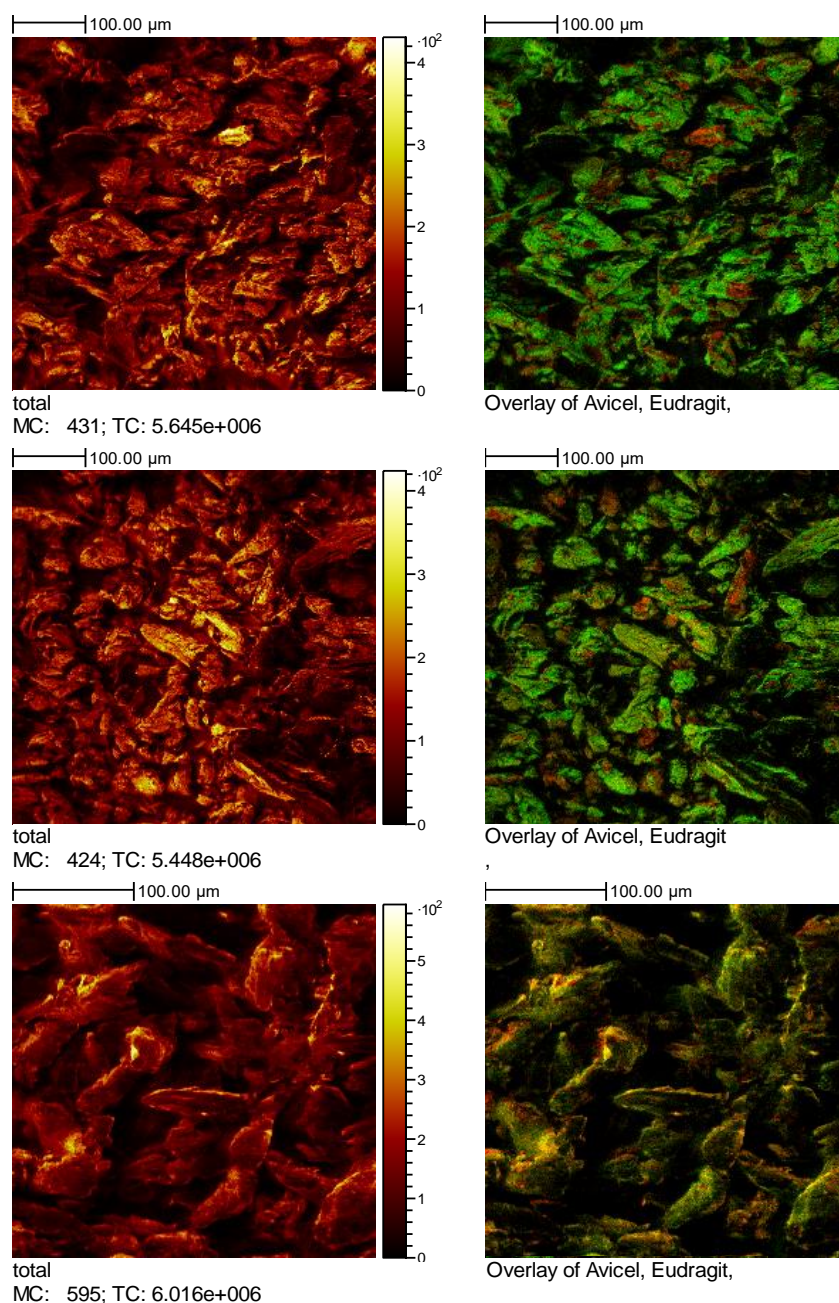
Figure 8.18: ToF-SIMS surface images of the samples prepared using 5, 3.3 and 2wt% of Eudragit L100-55 (from top to bottom) in methanol containing Avicel 101 suspensions, precipitated into 10ml of water. The images represent the total negative ions on the left, and the surface overlay of Avicel 101 (red) and Eudragit L100-55 (green) on the right

Further analysis of the depth profiles of the samples, showed a gradual decrease in the intensity of the Eudragit L100-55 signal and a gradual increase in the Avicel 101 signal, as presented in Figure 8.19, which demonstrated the application of a film coating over the particles. Clearly, when mixing the two materials together in the organic phase improved the precipitation mechanism, resulting in direct coating of Avicel 101 particles with Eudragit L100-55. Furthermore, it was observed that the higher concentrations in Eudragit L100-55 improved the distribution of the coating on the surface of the particles. However, the extracted spectra of the samples prepared at 2wt% of Eudragit L100-55, which was the lowest, in increasing amounts of water of 30ml (Figure 8.20) and 40ml, presented similar distributions demonstrating strong characteristic signals related to Eudragit L100-55.
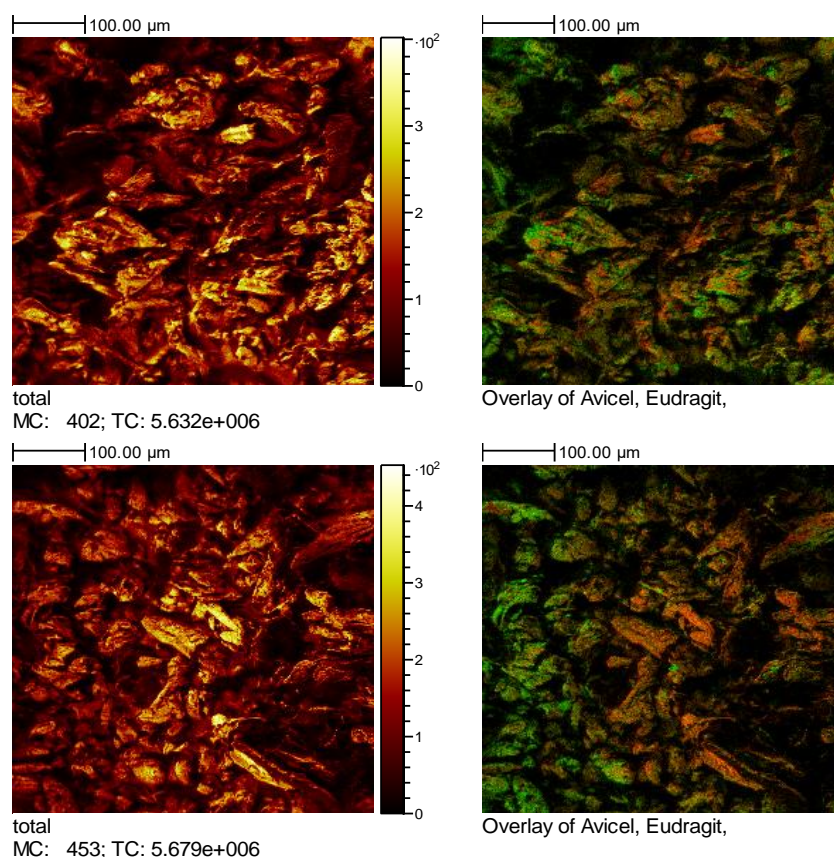
Figure 8.19: ToF-SIMS depth profile images at 30 scans (-) of the samples prepared using 5wt% (top) and 3.3wt% (bottom) of Eudragit L100-55 in methanol containing Avicel 101 suspensions, precipitated into 10ml of water. The images represent the total negative ions on the left, and the surface overlay of Avicel 101 (red) and Eudragit L100-55 (green) on the right

The samples prepared using 20ml and 50ml (Figure 8.20) of water presented extended regions with strong characteristic signals corresponding to Avicel 101 and poor dispersion of the coating. In fact, this result correlated well with the previous sections, which described the increase in the concentration of Eudragit L100-55 in the samples, whilst increasing the amount of the water in the aqueous phase. Nonetheless, ToF-SIMS analysis of the samples prepared by mixing the two polymers together, revealed the efficiency and the versatility of the method, when using both high and low viscosity samples. This method could be optimised by adjusting the aqueous phase, which would potentially result in a continuous film coating on the surface of the particles.

Figure 8.20: ToF-SIMS surface images of the samples prepared using 2wt% of Eudragit L100-55 in methanol containing Avicel 101 suspensions, precipitated into 30ml (top) and 50ml (bottom) of water. The images represent the negative total ions on the left, and the surface overlay of Avicel 101 (red) and Eudragit L100-55 (green) on the right

For the third method that was used, ToF-SIMS analysis aligned with the previous results, which demonstrated an increase in the Eudragit L100-55 concentration in the recovered particles, occurring after decreasing the Avicel 101 concentration in the suspension phase during process preparation. In more detail, the total ion images of the sample containing 2wt% of both Avicel 101 and Eudragit L100-55 (4:1 core-coat), presented dominate signals corresponding to Avicel 101 (red) rather than Eudragit L100-55 (green), which indicated that the sample was mainly consisted of the filler material. Although the sample contained relative high amounts of Eudragit L100-55, as discovered via FTIR and TGA analysis, ToF-SIMS revealed a rather poor distribution of the coating, as illustrated in Figure 8.21. The spectrum extracted from the sample prepared at 2wt% of Eudragit L100-55 and 1wt% of Avicel 101 (2:1 core-coat), presented an increase in the intensity of Eudragit L100-55 characteristic signals, which resulted from the decrease of Avicel 101 concentration. Surprisingly, the overlap ion image, revealed a very poor distribution of Eudragit L100-55 throughout the sample. It seemed that the material formed clusters instead of a coating film. In addition, the sample with the lowest concentration in Avicel 101 of 0.5wt% (1:1 core-coat) presented strong signals related to Eudragit L100-55, which was expected. However, the coating appeared in small deposits on the surface of the particles, since the characteristic signals of the underlying filler material were easily identified. The surface analysis revealed a larger population in clusters, which indicated a strong tendency towards Eudragit L100-55 core formation during the process rather than film formation. Even though the samples exhibited high concentration in Eudragit L100-55, the static evaporation of the organic phase limited the homogenisation of the materials in the mixture, which inhibited the formation of a continuous film.
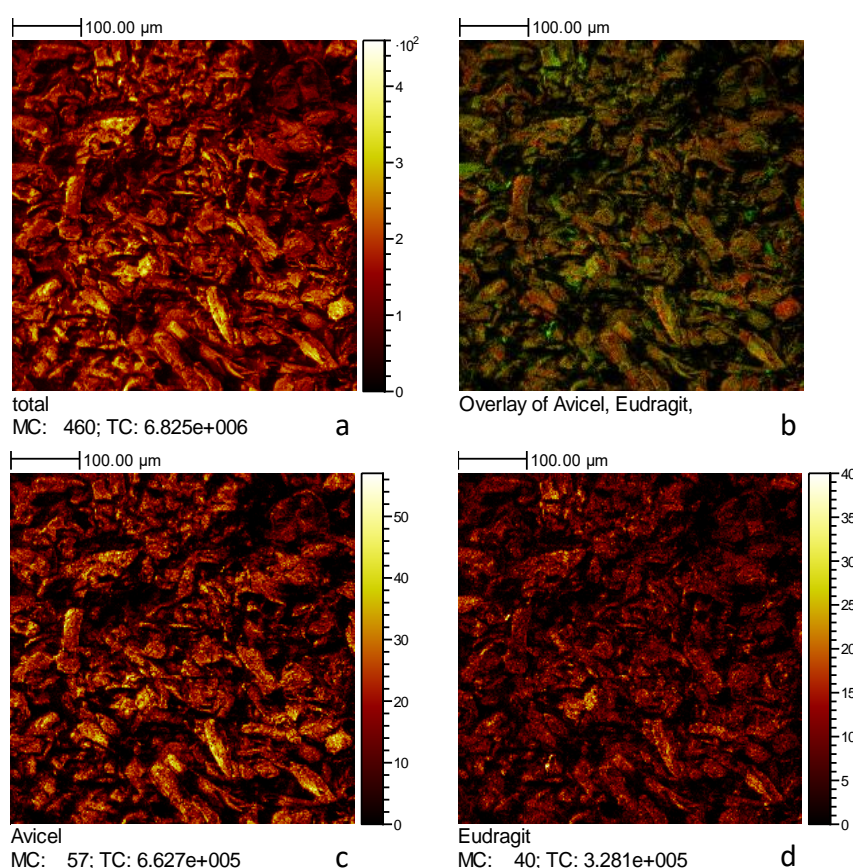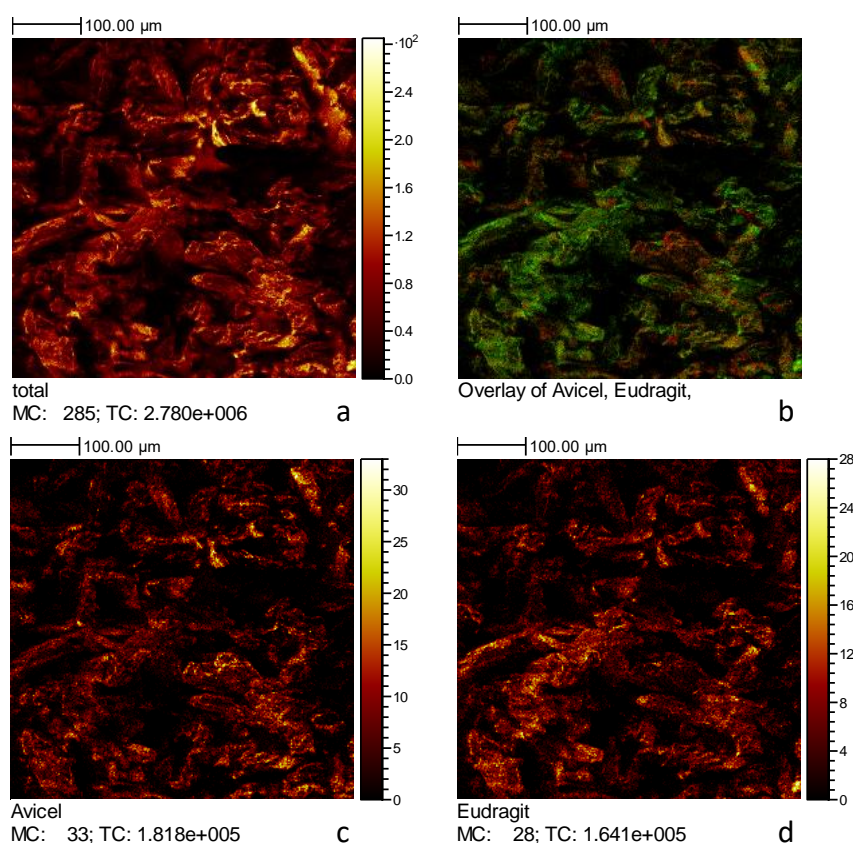
Figure 8.21: ToF-SIMS surface images of the samples prepared using 2wt% of Eudragit L100-55 in methanol solutions, precipitated into methanol containing 2, 1 and 0.5wt% (from top to bottom) of Avicel 101 suspensions. The images represent the total negative ions on the left, and the surface overlay of Avicel 101 (red) and Eudragit L100-55 (green) on the right

8.6   Scanning Electron Microscopy (SEM)

The type and the quality of the coating were examined through Scanning Electron Microscopy (SEM). Images of high magnification were captured on the surface of the recovered particles to identify the regions that were coated. To the best of the analysis, the surface texture of the coated particles was compared to the surface texture of Avicel 101 and Eudragit L100-55 and their individual characteristics. In Figure 8.22, it can be observed that Avicel 101 presented irregular shape particles with a rough external morphology, which could be easily distinguished from Eudragit L100-55 particles that looked like ideal globes with a more polished surface.
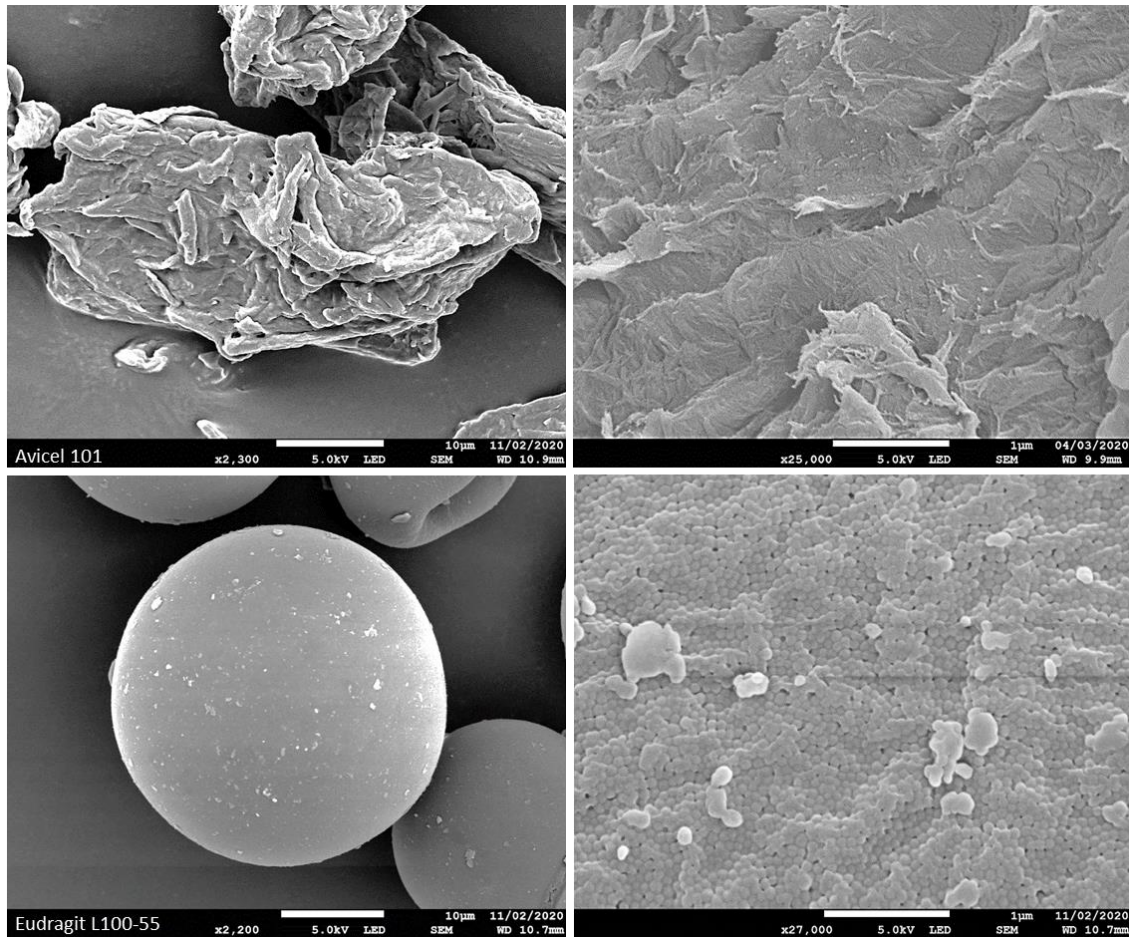
Figure 8.22: SEM micrographs of the surface morphology of the Avicel 101 (top) and Eudragit L100-55 (bottom) particles

The surface analysis of the samples prepared using the first method, revealed a gradual increase in the distribution of the coating by decreasing the concentration in Eudragit L100-55. The SEM analysis correlated well with all the previous observations made through FTIR, TGA and ToF-SIMS analysis, which demonstrated a relation between the coating efficiency and the viscosity of the organic phase. The micrographs in Figure 8.23 demonstrate the limited coating effect that occurred at higher viscosity, compared to lower viscosity, which resulted in improved coating dispersion. In particular, the micrographs obtained from the sample containing 5wt% of Eudragit L100-55, presented a typical Avicel 101 surface texture. The higher magnification image revealed regions at which Eudragit L100-55 was deposited in small amounts, which in fact explained the weak signals of the polymer detected on the surface of the particles via ToF-SIMS. On the contrary, the sample prepared at 2wt% concentration, presented a thin layer of coating. However, the higher magnification image revealed discontinuities in the deposition of the coating. Specifically, on the left side of the micrograph a rough fibrous texture similar to Avicel 101 can be observed, while the right side was covered by a thin layer with a smooth texture similar to Eudragit L100-55. In fact the SEM findings, agreed with the ToF-SIMS images that revealed a non-homogeneous coating distribution with regions displaying signals related to both Eudragit L100-55 and Avicel 101.

Figure 8.23: SEM micrographs of the samples prepared using 5wt% (top) and 2wt% (bottom) of Eudragit L100-55 in methanol solutions, precipitated into water containing 2wt% of Avicel 101 suspensions. Arrows indicate regions of coating

On the contrary, a reversed relationship was found for the samples prepared using the second method, which in fact agreed with the ToF-SIMS results in the previous section. SEM analysis revealed a gradual decrease in the coating distribution with the gradual decrease of Eudragit L100-55 in the organic phase, while an increase in the coating distribution was observed by increasing the water amount in the aqueous phase. In particular, in Figure 8.24 it can be observed that enhanced coating effect resulted using the highest concentration in Eudragit L100-55 of 5wt%, compared to the limited coating effect resulted at the lowest concentration of 2wt%. The micrographs revealed that the sample containing higher amount in Eudragit L100-55 presented a smooth surface texture, while the sample containing lower amount, presented a rough surface texture similar to Avicel 101. It was obvious that the increased concentration in Eudragit L100-55 resulted in the formation of a thick layer of coating, which nearly-fully covered the Avicel 101 particles. Whereas by reducing the concentration, the polymer was deposited

in small amounts leaving regions on the surface of the particles that were clearly uncovered [153]. Although, it seemed that high concentrations in Eudragit L100-55 were required to provide with a continuous film, Figure 8.25 demonstrates the ability to increase efficiency of the process by increasing the amount of water in the aqueous phase. The sample prepared using 30ml of water at the lowest concentration of 2wt%, presented an improved coating distribution on the surface of the particles compared to the sample described above prepared in 10ml, showing small discontinuities that matched the distribution observed in the ToF-SIMS images. Further increase of the water content at 50ml, prevented the deposition of Eudragit L100-55 as a film coating, since only small regions of the coating were identified. This observation confirmed the analysis in the previous sections, which suggested that the amount of the polymer and the non-solvent used, should not exceed the critical concentration.
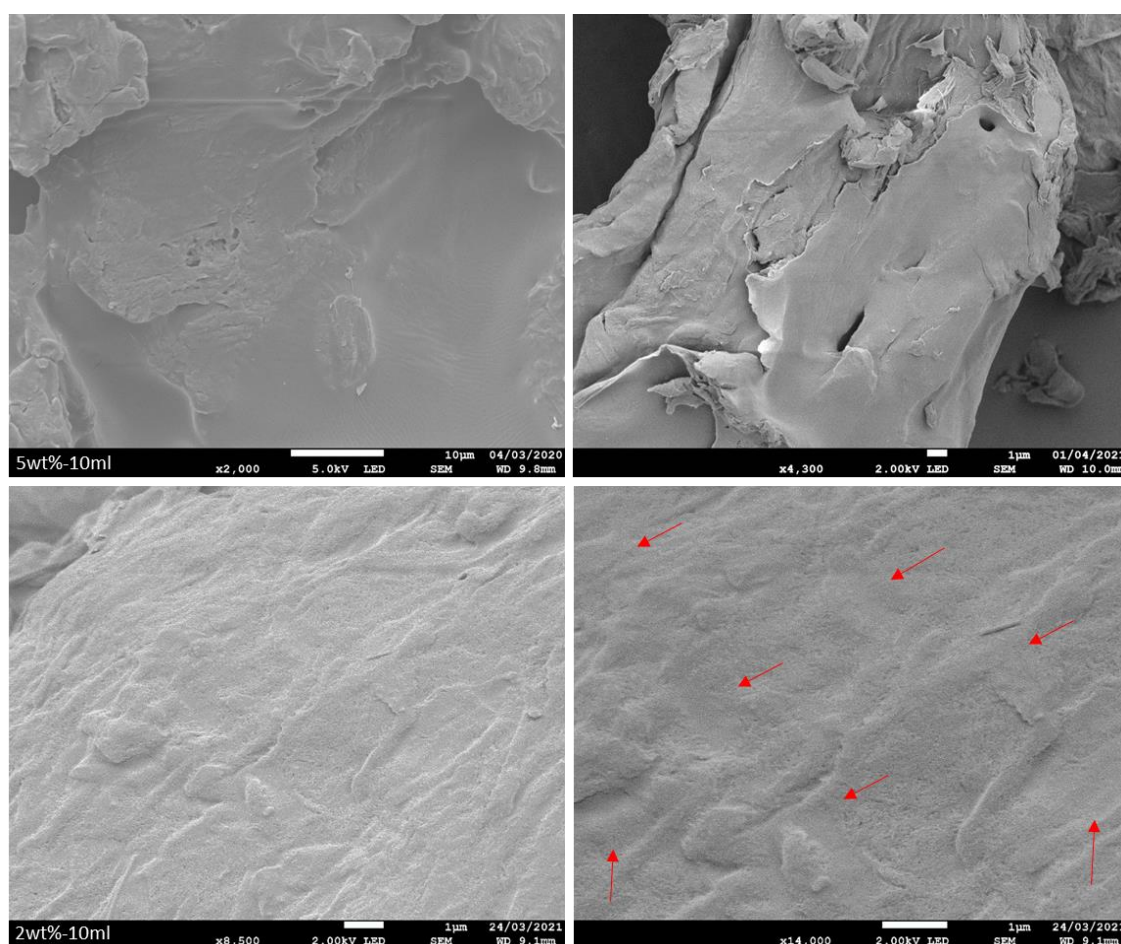
Figure 8.24: SEM micrographs of the samples prepared using 5wt% (top) and 2wt% (bottom) of Eudragit L100-55 in methanol containing Avicel 101 suspensions, precipitated into 10ml of water. Arrows indicate regions of coating
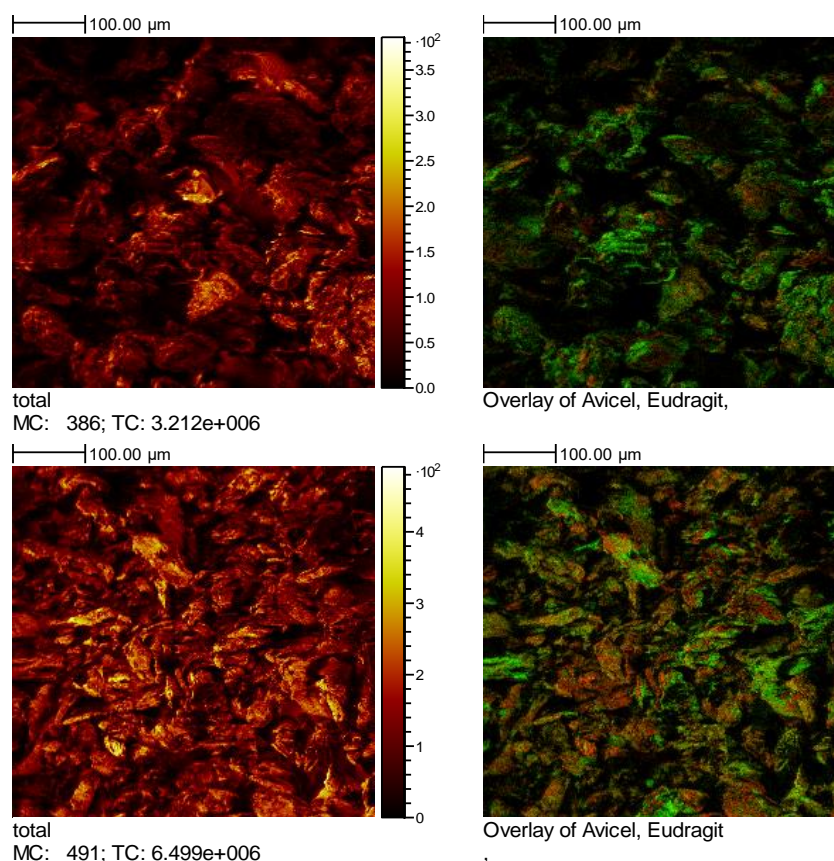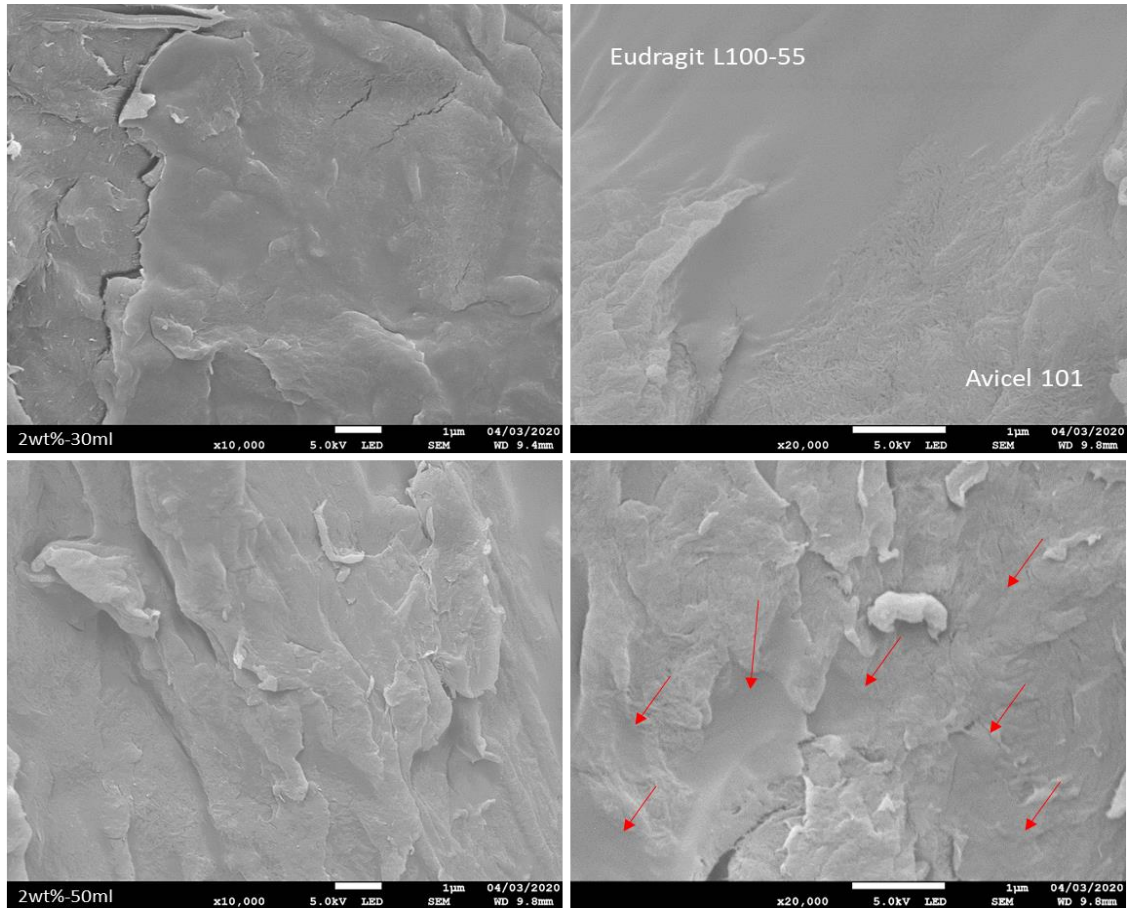
Figure 8.25: SEM micrographs of the samples prepared using 2wt% of Eudragit L100-55 in methanol containing Avicel 101 suspensions, precipitated into 30ml (top) and 50ml (bottom) of water. Arrows indicate regions of coating

SEM analysis of the samples prepared using the third method revealed an increase in the coating efficiency by decreasing the amount of Eudragit L100-55 in the core-coat ratio from 1:1 to 4:1, which agreed with past observations in previous studies [150], [154]. The analysis showed that Eudragit L100-55 aggregated during the evaporation step, which explained the reduced effectiveness when higher amounts of the polymer were used in the mixture [149], [150]. Figure 8.26 presents micrographs captured for the sample containing 2wt% of both materials in the ratio of 4:1, demonstrating the deposition of a thin film coating on the surface of the particles with small discontinuities. More specifically, despite the fact that the material aggregated, high magnification images revealed Eudragit L100-55 particles in a semi-diffused state forming a thin film on the surface of Avicel 101 particles. In fact, this observation proved that the absence of stirring during evaporation inhibited the complete formation of a coating film.
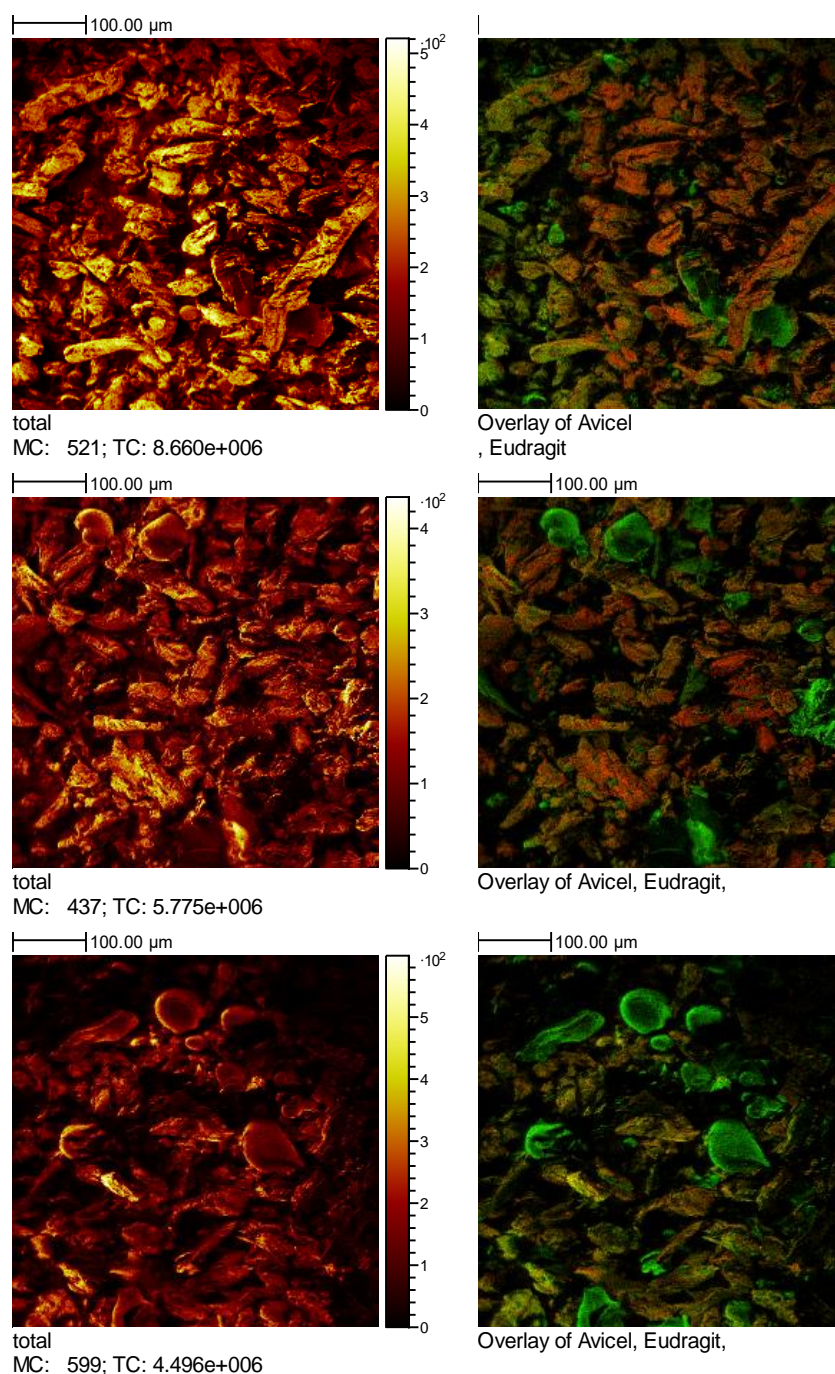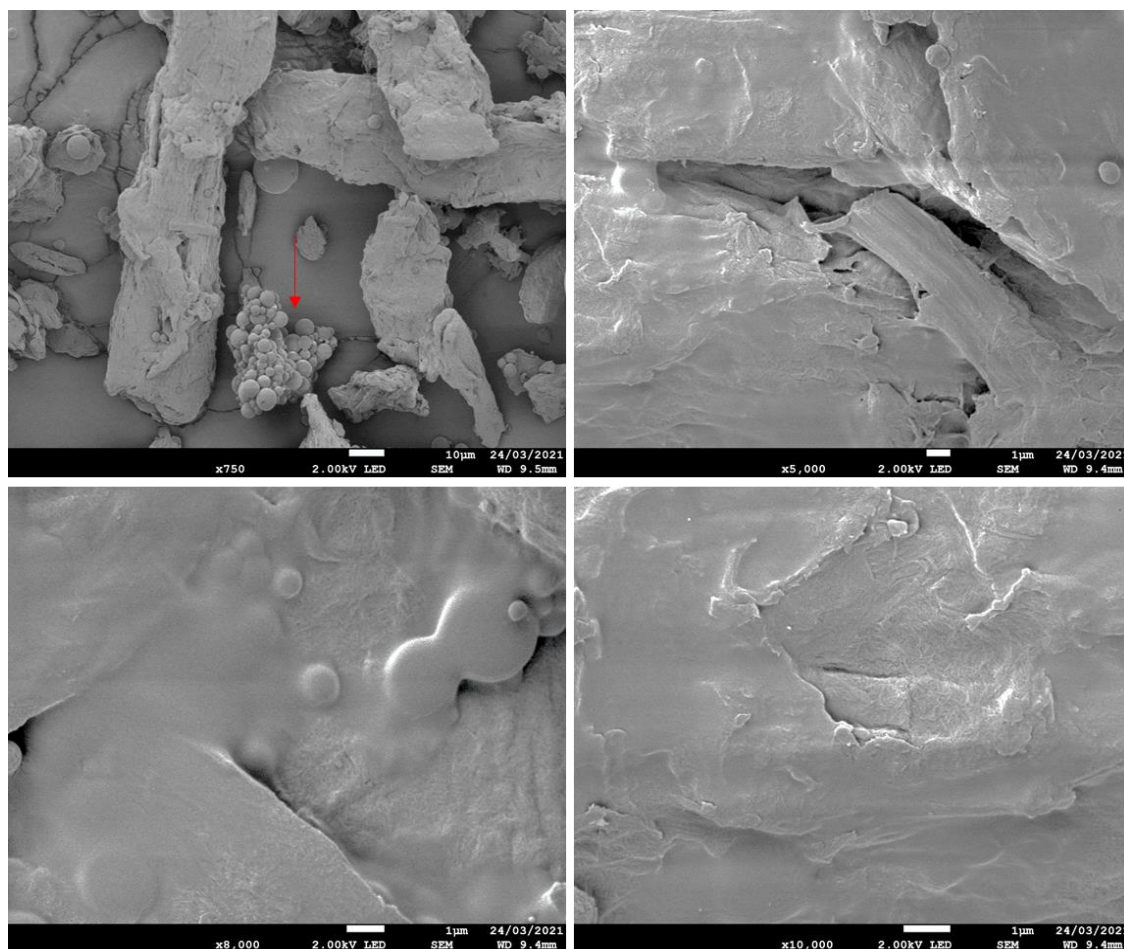
Figure 8.26: SEM micrographs of the samples prepared using 2wt% of Eudragit L100-55 in methanol solutions, precipitated into methanol containing 2wt% of Avicel 101 suspensions. The arrow shows the presence of aggregates

Additionally, the micrographs in Figure 8.27 of the sample containing 2wt% of Eudragit L100-55 and 1wt% of Avicel 101 in the ratio 2:1, revealed the presence of large Eudragit L100-55 clusters dispersed among the Avicel 101 particles, which explained the strong Eudragit L100-55 signals found in certain regions via ToF-SIMS. In higher magnification images, random coated regions were discovered, however most of the surface of the particles was uncovered. It seemed that the formation of bigger structures limited the amount of material that was deposited on the surface of the particles, which further indicated the need for stirring during evaporation. Moreover, the micrographs of the sample containing the lowest concentration in Avicel 101 of 0.5wt% in the ratio of 1:1, in Figure 8.28, revealed a large population in compacted Eudragit L100-55 structures in the form of clusters and large angular planes, explaining the increased signals related to Eudragit L100-55 in the ToF-SIMS images. The high magnification images showed a few regions with a smooth surface texture corresponding to the coating, whilst most of the

surface of the particles was uncoated. Therefore, the SEM results discovered an inverse relation between the coating material concentration and the coating efficiency. The image observations indicated the tendency of Eudragit L100-55 towards core formation rather than film formation, which was improved by reducing the amount of the polymer in the mixture.
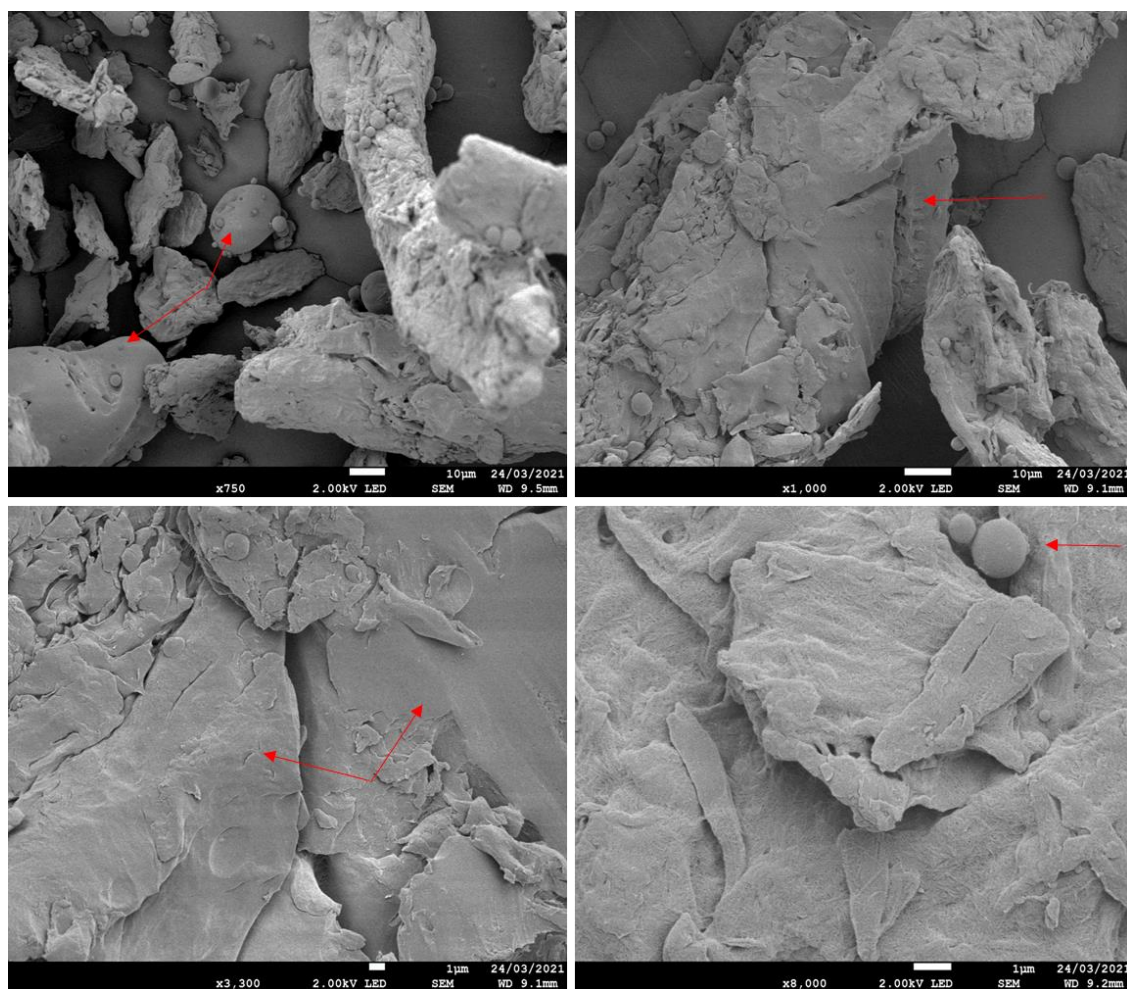
Figure 8.27: SEM micrographs of the samples prepared using 2wt% of Eudragit L100-55 in methanol solutions, precipitated into methanol containing 1wt% of Avicel 101 suspensions. Arrows show the presence of clusters and film coating

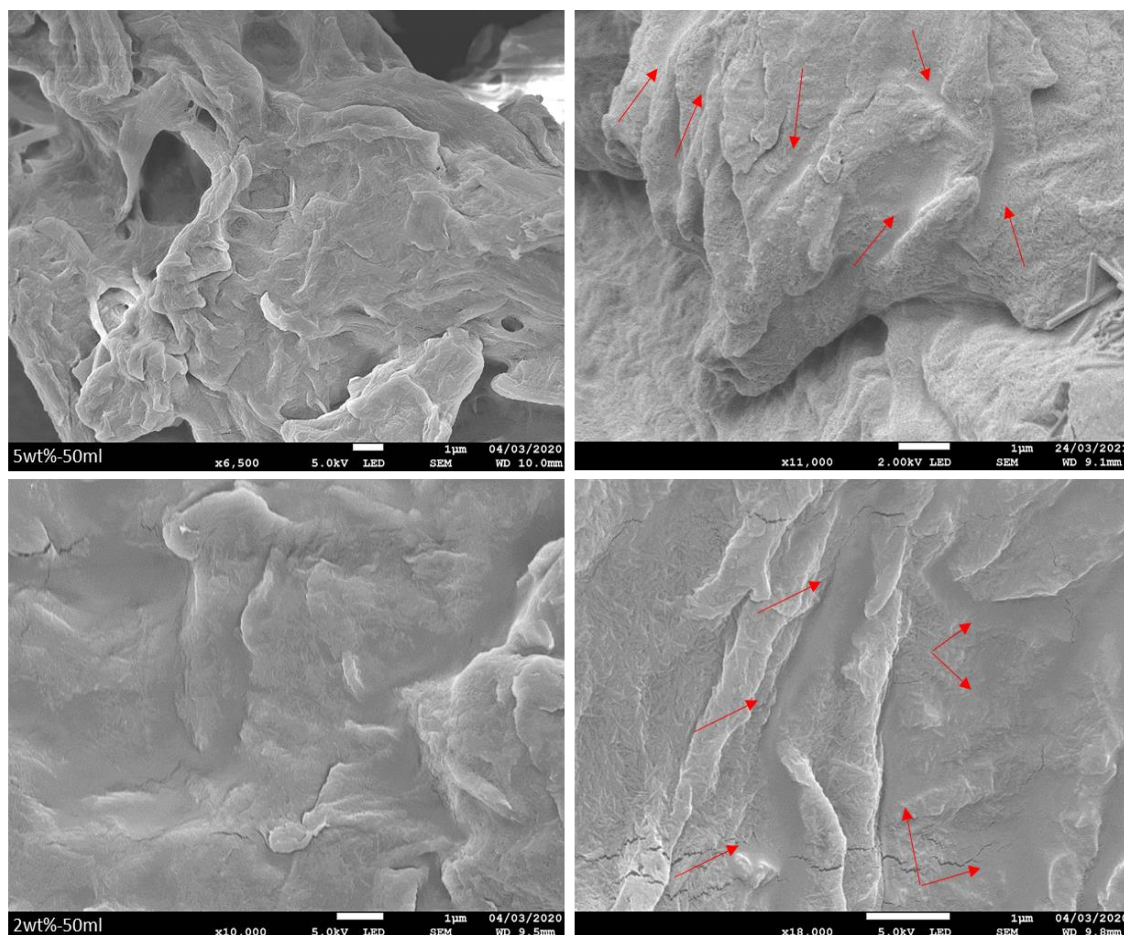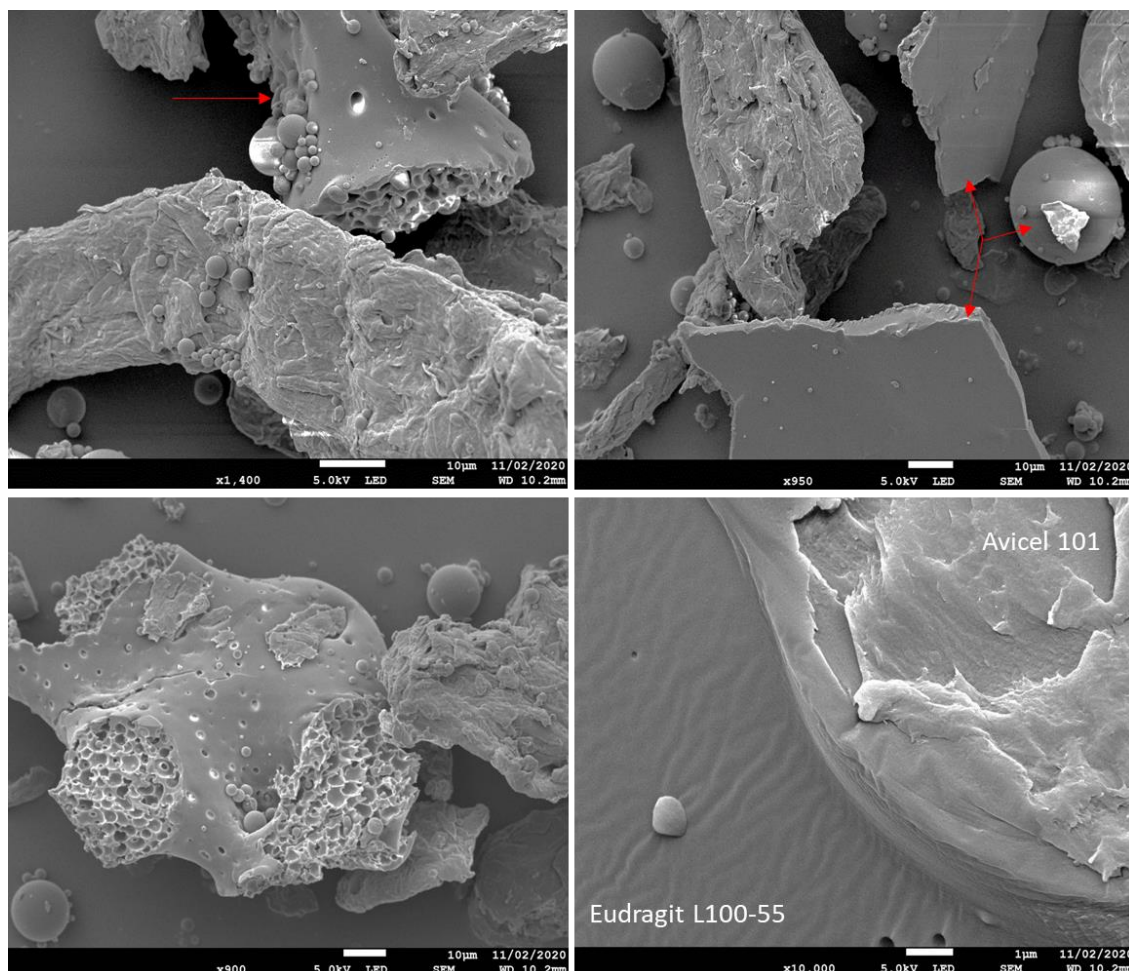**Figure 8.28:** SEM micrographs of the samples prepared using 2wt% of Eudragit L100-55 in methanol solutions, precipitated into methanol containing 0.5wt% of Avicel 101 suspensions. Arrows show the presence of clusters

8.7   Summary

Chapter 8 introduced a coating approach using three simple and reproducible methods based on precipitation and emulsion-solvent evaporation principles, to produce a core/shell particle. The results revealed that it was possible to produce a homogeneous Eudragit L100-55 film on the surface of the Avicel 101 particles. The materials, the preparative variables, the process conditions and the formation mechanisms were reviewed via analytical testing, revealing the advantages and the limitations involved in the application.

The methods used for the characterisation of the recovered particles allowed the full examination of the achieved coating and its quality. Firstly, FTIR analysed the molecular structure and composition of the samples, which revealed no chemical interaction

between Eudragit L100-55 and Avicel. There were a few peaks that overlapped in the spectra, however new bands corresponding to new chemical bonds were not detected. TGA monitored the physical changes in the samples, which occurred over specific temperature ranges. The unique sequence of the physicochemical reactions determined the percentage weight loss of each of the components, which was directly linked to the percentage of the final concentration of Eudragit L100-55. Despite the usefulness of the above techniques, they presented limitations due to peak overlapping, which introduced mistakes in the analysis. ToF-SIMS allowed imaging of the samples with high spatial resolution that was proved very valuable for the analysis of the distribution of the coating. Large areas of the samples were characterised by imaging specific species, which provided with the localised molecular identification of each of the components. The final evaluation of the coating was achieved through the application of SEM. Images of the surface of the recovered particles gathered the missing information regarding the morphology and distribution of the coating. The observations provided with answers about the impact of the multiple factors involved during the process on the coating mechanisms, which fully completed the analysis and the understanding.

Through the analysis it was discovered that the most influential factor was the initial and final concentration of the materials in the prepared mixtures. Besides the concentration of Eudragit L100-55, there were other parameters which affected the efficacy of the process, such as the dispersion mechanism of Avicel 101, the homogenisation speed and the ratio of methanol to water, and are compared in Table 8.5. The acquired knowledge of the various factors affecting the coating mechanism was very useful for the design of a method that could reach high coating distributions, since Eudragit L100-55 proved to be an effective film-forming material and at the same time a suitable LS powder.

Table 8.5: Process variables compared to coating efficiency

Method	Viscosity	Speed	Dispersion	Coating Distribution	Min % Eud L100-55	Max % Eud L100-55
1	↑	↑	↓	↓	0	20
2	↑	—	↑	↑	0	22
3	↓	↓	—	—	18	48

CHAPTER 9   DISCUSSION

9.1   Introduction

Chapters 4 to 8 explored the processability of pharmaceutical materials with Laser Sintering to produce oral solid dosage forms. The materials were selected based on their low cost and pharmaceutical functionality, such as increase of the bulk volume, improvement in elasticity and plasticity, enhancement in flow, prevention of degradation, control drug release, etc. (see section 2.6). Within this PhD a comprehensive knowledge base with the performance capabilities and limitations of the materials used was established that could expand the currently limited LS material portfolio in pharmaceutics and allow further adoption of AM technologies.

Chapter 9 provides a summary discussion on the results presented in the previous chapters and their significance within the overall aims of the PhD.

9.2   Material Characterisation

The most influential material characteristics on the LS process were the complex interactions between polymer materials and the process. Quantitative information was acquired through analytical testing to analyse the effects of the thermal and physical properties on the materials by LS. Therefore, general knowledge was established that was used to continue the development of the formulation. It was successfully demonstrated that the crystallinity level of the polymers that allowed complete melt transitions in the processing window, was desirable to achieve full consolidation. In parallel, it was shown that high particulate flow efficiency was necessary to reach full density. Finally, it was also discovered that the particle morphology strongly influenced the packing efficiency. A basic comparison based on this information was made between the different materials used, to strengthen material selection decisions.

It was discovered that Avicel 101 and 102 failed the thermal criteria for LS. Although the material appeared to be semi-crystalline, which is favourable, the required powder bed temperature for inducing melting of Avicel particles would need to exceed the maximum bed temperature of the P100 by ~65°C. Furthermore, the material showed decomposition at 270°C just above its melting point, which suggested potential material degradation

upon exposure. It was found that the physical characteristics of the powders were similar to commercially available LS materials. Specifically, an acceptable average particle size of 70.2μm and 128.2μm was measured for Avicel 101 and 102, respectively, able to pack into effective formations and result in enhanced flowability. Although, Avicel demonstrated desirable physical properties, the thermal properties were not compatible with the LS process, likely leading to failure of sintering.

Corresponding results were obtained for Foremost 316, which was found to have a semi-crystalline structure. Foremost 316 exhibited relatively stable flow with the particle size and shape falling into the acceptable diameter range. Measurements revealed an average diameter of 118μm, and presented relative low irregularities, characteristics that were similar to commercial powders and would perhaps lead to a good sintering performance. However, the material demonstrated a high melting point at 219.30°C, which would obstruct the consolidation of particles within the P100, similarly described for Avicel.

In contrast to Avicel and Foremost 316 powders, PolyOx N80 presented a very distinct melting point around 67°C, which required an ability to control the bed temperature in the P100 to achieve full consolidation of the particles and form layers. However, the size distribution of the powder revealed a large population of bigger particles above 200μm that would most likely inhibit the deposition of homogeneous layers on the powder bed. Large particles would be expected to increase porosity and roughness, thereby reducing the mechanical performance of the parts. Sieving of the PolyOx N80 powder to remove the larger particles, could increase the packing efficiency, and hence, the density and the mechanical performance of the parts.

Different material properties were discovered for the Eudragit family of powders that were found to possess amorphous characteristics. The L100-55 grade presented a single glass transition at 93.21°C and the FS100 grade at 55.56°C, falling into the operating temperature range of the P100. Eudragit powders would be expected to soften gradually above their T_g, and lead to partial consolidation due to their amorphous nature. However, this would lower the flow and the sintering rate, compared to semi-crystalline materials that fully melt above their T_m. The amorphous nature of Eudragit could result in higher porosity and subsequently low strength. However, L100-55 grade possessed "ideal" spherical particles and size diameter for LS, revealing an ideal flowability. These characteristics could improve the performance of the powder in the P100, despite the lower degree of consolidation, as the spherical particles would be expected to pack in

tighter structures and improve the final density. On the contrary, FS100 particles were found to be high irregular with sharp edges, which resisted free flow, due to increased inter-particulate mechanical locking. This would likely result in poor sintering performance.

In the case of HPC, a semi-crystalline nature could not be detected. HPC behaved as amorphous, exhibiting a single transition at about 90°C, corresponding to the T_g. As a result of the increased amorphous content of the polymer detected, HPCs molecular mobility and plasticity were influenced. It was successfully demonstrated that the plastic behaviour of HPC was linked to increased moisture content, which enhanced the cohesive characteristics affecting the flow. Moreover, the average particle size was found to reduce in size from the SL grade to the SSL SFP, enhancing the cohesion forces in the latter. Nevertheless, all HPC grades consisted of fine particles leading to increased agglomeration, and likely limit their ability to spread the powders evenly on the P100 platform.

Finally, AQOAT powders were determined to be amorphous in nature, presenting a T_g at 85°C. This temperature can be suited to the P100, however the material exhibited very poor flowability that would likely inhibit the spreading on the powder bed. It was discovered that the powders consisted of cylindrical shaped particles and sharp fibrils in a broad range of diameters, which influenced the packing efficiency. Additionally to this, the average particle sizes of the three grades were above 200μm that similarly to the case of PolyOx N80 would lead to inconsistencies during the deposition of the layers, and decrease the final precision of the parts.

All the materials presented incompatibilities with LS, however some of the excipients presented a set of properties that with the right combination of processing parameters could achieve sintering. Therefore, Avicel 101 was found to be a semi-crystalline polymer with high T_m and was chosen for its particle size and relatively good flowability, to study the effect of the bed temperature and thermal transitions during processing in lower temperatures. Foremost 316, another semi-crystalline material with high T_m, showed acceptable particle size and flowability, and was chosen to study the effect of the bed temperature on the dehydration of the polymer chain, since it was found to absorb moisture. HPC SSL even a semi-crystalline polymer, it presented amorphous thermal characteristics with a T_g low enough to allow sintering, and an ideal particle size distribution. However it was very cohesive, consequently it was chosen to examine the

influence of the cohesive forces on the packing efficiency and spreading of the powder. Eudragit L100-55 although an amorphous polymer, presented an ideal particle morphology for LS and was selected to study the thermal transitions and packing efficiency of an amorphous material. Finally, PolyOx N80 was chosen for its favourable melting characteristics. Even though it presented large and irregular particles it was selected to study the effect of the particle morphology on the porosity between the layers and the final density.

9.3   Processing

To understand the P100 process boundaries for polymer LS of the selected materials, a series of experiments were carried out to identify each materials process window and subsequent consolidation quality. Therefore, the process parameters needed to be identified for each material according to each powder's properties. The most important parameters found to control sintering were the bed temperature, the laser power and the laser scan speed. These parameters defined the energy input and was directly related to the quality of sintering. In addition, hatching distance, beam offset and contouring were found to be valuable in the optimisation of the process. Meanwhile, the melting temperature of the materials, the moisture content, and the shape and size distribution of the particles, consequently determined the amount of energy needed. It was demonstrated that an increased melting point required increased energy input. However, an excess in the energy input was found to lead to polymer degradation. Furthermore, particle morphology was proved to influence the packing density and thermal conductivity of the powder bed, correlating with the conclusions on material morphology and packing efficiency. Generally, a minimum amount of energy was needed to initiate sintering, nonetheless, in most cases, a raise in the energy density was required to increase the density and the stiffness of parts. The advantage of double scanning was demonstrated, resulting in high heat transfer and greater definition. Finally, high moisture absorption was discovered to increased cohesion that strongly affected the spreading of the powders, and could potentially be improved with the use of additives/flow enhancers.

Avicel 101 revealed strong material degradation when the powder was exposed to the laser energy. A range of scanning strategies was explored in order to transfer adequate heat to the powder and induce particle fusion as there was a large temperature difference

between the melting point and the surface bed temperature. Unfortunately, the powder showed no evidence of fusion, and showed fuming and a change of colour from white to brown during processing, which indicated degradation of the polymer structure. This behaviour was related to the dehydration of the liquid inter-particle bridges occurring during preheating, which resulted in caking of the particles as the laser scanned the powder. This limited the options to explore sintering of Avicel 101 with the P100.

Foremost 316 failed to spread on the P100 platform due to increased moisture content that increased the cohesive behaviour of the powder. Two percent of glyceryl dibehenate was found to improve the flow which was successful, however, sintering of Foremost 316 induced degradation. Similarly to Avicel 101, the absorbed water content vaporised during the preheating step, and led to the crystallisation of the liquid bridges upon laser exposure. Unfortunately, the processing temperature was very low to melt the crystals and form layers, which made Foremost 316 unsuitable for the P100.

Similarly to Foremost 316, HPC SSL was very cohesive. The high moisture content of the powder increased the plasticity of the amorphous phase of HPC SSL, resulting in the compaction of the powder in the powder well. Although it was attempted to improve the flow by adding 1% of MgSt, yet the powder agglomerated and formed lumps over the P100 bed area. The extreme cohesiveness of HPC SSL was due to the strong inter-particle charges dominating the bulk properties of the powder. These particle interactions were connected to capillary forces generated from the water content on the surface of the particles, and van der Waals forces developed within the large surface area of the fine HPC SSL particles. Subsequently, HPC SSL is unsuitable for processing in a powder bed system.

On the contrary, spreading and sintering of Eudragit L100-55 was very successful. Solid parts demonstrating high quality and precision were produced 25°C above the glass transition of Eudragit L100-55. Successful sintering of Eudragit L100-55 proved that amorphous polymers can be processed using LS as soon as the powder meets the rest of the LS material requirements.

Laser sintering of PolyOx N80 was challenging since the presence of large particles increased the structural porosity due to their poor packing efficiency. The exposure parameters required a careful control to increase the energy input and therefore the sintering necks, to sinter solid layers without degradation. Despite this, the material

exhibited high shrinkage upon complete densification of the layers, as the pores shrank, resulting in high distortion and low precision of the printed parts. This negative effect of shrinkage limited the ability to sinter PolyOx N80 successfully and produce solid parts with high dimensional accuracy.

Since Eudragit L100-55 was the only excipient that could be processed in multilayers achieving high density and precision, the decision on materials was based on their pharmaceutical functionality. Eudragit L100-55 is a pharmaceutical film coating agent mainly used to control drug release, and Avicel 101 is a pharmaceutical diluent/filler used as a main ingredient in oral formulations, providing the required density to produce tablets of sufficient weight and size. Therefore, the two excipients were selected to develop a preliminary formulation for the initial investigation of LS for oral solid dosage forms.

9.4   Sintering of Tablets

In order to meet the design criteria of oral solid dosage forms, Avicel 101 and Eudragit L100-55 were mixed in various blends. Although Avicel 101 was not ideal for LS, it was demonstrated that its high-temperature particles can be bound together without direct melting or sintering, using Eudragit L100-55 as a binding powder to create necks. Eudragit L100-55 is suited for LS, consequently, fusing its particles was the key to the formation of multilayers and structurally stable parts.

The main disadvantage during processing of pharmaceutical blends was the weak interlayer adhesion, which affected the mechanical performance of the parts, as the double-phase powder system resulted in partial sintering, thereby increasing the internal porosity. The weight percentage of the Eudragit L100-55 phase in the mixture determined the degree of sintering and necking between the particles, therefore, the number of voids and the adhesion between the layers, and further the density and the stiffness of the final parts. On the other hand, the weight percentage of Avicel 101 determined the sintering window and the degree of material degradation, correlated to the final quality of the parts.

More specifically, high concentrations in Avicel 101 required increased amounts in energy input, to boost the energy transferred to the Eudragit L100-55 phase and increase the necking between the solid Avicel 101 particles. In the 63:37 Av/Eu blend the required ED was 0.015 J/mm^3, which resulted in degradation and limited the processing window. Unfortunately, the finished parts contained unmolten powder, resulting in high surface

roughness, and affecting the stability and the handling of parts. Increasing the amount of Eudragit L100-55, as in the 50:50 Av/Eu blend, improved the sintering ability of the powder, allowing the production of solid parts with no apparent difficulties. The required ED was decreased at 0.0133 J/mm^3, which was the maximum possible to avoid degradation of the Avicel 101 phase. Although the energy input was lower, improvements were made in concern of the handling stability, the part density and precision. Further increasing the Eudragit L100-55 amount in the powder composition resulted in high definition and enhanced part features. Experiments on the 37:63 Av/Eu blend revealed a wider processing window, allowing the control optimisation of the process parameters. The ED that was required was at the lowest of 0.0112 J/mm^3, which eliminated degradation and yielded parts with good stability and improved density.

The quality of the Avicel 101 powder was strongly dependent on the energy input applied during exposure. The most influential parameters were found to be the laser power and the scanning speed, as for high laser power and/or low speed, an immediate degradation of Avicel 101 was observed, while the ductility of the layers was increased. Therefore, sintering tests were designed to maximise the heat transferred to the powder and keep the laser power to the lowest possible and the scanning speed to the highest possible to prevent degradation. It was revealed that scanning each of the layers twice, while using a smaller distance between adjacent lines, increased the scanning overlapping and hence, the heat and the depth of fusion. In addition, it was found that minimising the thermal inconsistencies within the build chamber ensured a uniform sintering and further improved the quality of the parts. This was achieved by increasing the bed temperature, keeping a balance between the scanned and the surrounding powder, thereby increasing the part density, and by positioning the parts in the upper centre of the building area, providing greater definition.

9.5   Mechanical Testing

To evaluate the final quality of the sintered parts and predict their performance during packaging, shipping and dispensing, a series of mechanical tests were carried out. The analysis focused on the influence of the materials used in the formulation on the properties of the parts, and gained an insight of the design requirements of tablets for LS. This approach did not focus on the individual excipients in the blends, but rather to understand

the balance needed between the bulk characteristics of the feedstock and the sintering process, in order to design an optimum powder that could exploit full potential of LS and achieve industrial pharmaceutical functionality.

The quality of the parts was assessed in respect to their precision, microstructure and mechanical response, as a function of the ED. The results confirmed the strong relationship between the energy input and the depth of sintering that controlled the degree of particle fusion, which was linked to the final properties of the parts. In general, through image analysis and mass/density measurements, it was found that higher ED increased particle coalescence resulting in increased densification and also thickness of the parts. It was evident that the higher ED contributed in the reduction of the pore size and number, improving the surface roughness and internal structural porosity, which reflected on the improvement on the local and macroscopic mechanical properties of the parts. More specifically, the average strength, stiffness and ductility of the parts were found to increase with increasing ED, as further discovered through compression and indentation measurements.

Despite the differences identified, related to the amount of the energy input applied to the three powder blends, the final parts did not exhibit significant differences in their overall mechanical response. It was discovered via image analysis that the microstructure of the parts was heterogeneous containing a large volume of dispersed unsintered particles. It was evident that variations in the Eudragit L100-55 concentration determined the number of inter-particle bridges, while Avicel 101 was responsible for the formation of voids, preventing complete part densification despite optimisation of the sintering conditions. Therefore, the induced and unintentional increased structural porosity, enhanced fragility of the parts, as was found via dynamic and surface mechanical analysis, significantly reducing the tablet integrity in respect to strength and friability.

Problems in the production of tablets with high structural integrity using LS technologies were demonstrated, reflecting the challenges in the design of drug formulations. There are many considerations to be made towards safe processing of pharmaceutical materials, while achieving reliable adhesion between the particles, to obtain high strength and functionality of the resultant tablets. Eudragit L100-55 proved to be a suitable material for processing in LS, showing acceptable fusion and ability to bind the particles together. However, the required amount in Eudragit L100-55 to achieve better sintering was higher than the amount traditionally used for tableting, since Eudragit L100-55 is used more as

a coating agent rather than a filler/binder in pharmaceutics, which is adding more design limitations.

9.6 Coating of Particles

To overcome the many challenges of sintering pharmaceutical formulations, a novel approach for developing new and improved powders for LS without the use of additives, was demonstrated. To accomplish that, three simple and reproducible methods based on precipitation and emulsion-solvent evaporation principles were used, to apply a film around Avicel 101 particles. This concept, exploited the properties of Eudragit L100-55, which is widely used as a film coating material in pharmaceutics, in an attempt to coat Avicel 101 and prevent its degradation during LS improving its processability. Initial results showed promise for further investigation, showing that it was possible to produce a homogeneous film coating on the surface of the Avicel 101 particles.

The methods that were developed involved, the dispersion of Eudragit L100-55 and Avicel 101 in organic and aqueous liquids, and solidification based on diffusion mechanisms. The most important factor that influenced the efficacy of the methods was the concentration of the materials in the prepared mixtures. Specifically, variations in the Eudragit L100-55 concentration revealed that the amount of the material needed to be high enough to achieve complete cover of the Avicel 101 particles, however it was discovered that excessive amounts of material could have the opposite result.

In the initial method, the organic phase was prepared by dissolving Eudragit L100-55 in methanol, while the aqueous phase was prepared by dispersing Avicel 101 in water. The diffusion mechanism initiated the nucleation of the material over the surface of the dispersed Avicel 101 particles. It was discovered that the initial viscosity of the organic phase was related to the uniform dispersion in the aqueous phase and the stability of the emulsion. As viscosity of the solutions increased with the concentration of Eudragit L100-55, the dispersion was reduced, and the material precipitated in large bulks of mass. Therefore, the high viscosity batches resulted in small samples with low coating distribution due to the increased material losses, while the low viscosity batches exhibited improved dispersion and larger samples of coated particles. Surface analysis and TGA revealed that these samples presented higher coating distribution around Avicel 101 particles and consisted of approximately 20% in Eudragit L100-55.

In the second method, Avicel 101 was dispersed in the organic solution containing Eudragit L100-55. Mixing the two materials together in the organic phase increased the contact area between Eudragit L100-55 and Avicel 101, facilitating its deposition on the surface of the dispersed Avicel 101 particles over diffusion. The results showed that batches with high concentration in Eudragit L100-55 exhibited high distribution of the coating, however, the final concentration in Eudragit L100-55 was not higher compared to the first method, since the material losses observed during the diffusion step were similar. The difference was that the organic phase in this method was injected in 10ml of water using a slow stirring rate, which were both lower than the ones used in the first method, thereby, the viscosity of the emulsion was increased resulting in poor dispersion, and high material losses. However, ToF-SIMS and SEM analysis revealed higher coating distribution, proving the improved effectiveness of this process compared to the previous method. Furthermore, the results revealed that the samples with the highest viscosity nearly formed a continuous coating film around the Avicel 101 particles, while the distribution was decreasing at lower viscosities. This could be considered as the reversed effect to the one observed in the first method. Considering, the relationship between the viscosity and the dispersion rate that found to control the emulsification mechanism, and thus the materials losses, the effect was actually the same. In fact, the results in the second method demonstrated that there is a critical concentration in Eudragit L100-55 that needs to be overcome in order to achieve adequate amounts of film coating. It was found that increasing the water concentration the viscosity was reduced, improving the dispersion in the aqueous phase, and triggering spontaneous emulsification. This behaviour increased the Eudragit L100-55 concentration in the samples by 116%, however, the film distribution yet presented small discontinuities, which indicated that the initial concentration in Eudragit L100-55 was lower than needed.

In the third method, Eudragit L100-55 was dissolved in methanol and was injected into a second organic phase consisting of Avicel 101 and methanol. The two phases formed a stable emulsion without additional care or control that was left to evaporate. The usefulness of this simple method was the reduction of the material losses up to the minimum, presenting final concentrations in Eudragit L100-55 up to 48%, compared to the maximum of 20% of the other methods. Although, the concentration in Eudragit L100-55 was increased and would be expected to fully cover the Avicel 101 particles, SEM and ToF-SIMS analysis revealed the formation of aggregates instead of a film

coating, resulting from the zero stirring conditions applied during the evaporation step and proving that is necessary to introduce large amounts of energy to the system to avoid coalescence of the polymer and increase effectiveness of the coating deposition.

CHAPTER 10   CONCLUDING REMARKS

This PhD explored the use of LS to produce oral solid dosage forms that may be subsequently designed for tailored release properties. LS was chosen because is a process applicable to powder-based biocompatible material systems, is a single-step and solvent-free process that does not require prior production of filaments or support structures and additional post processing steps, and offers industrial scale opportunities, compared to other AM processes. Although prior work has been published on AM applications in pharmaceuticals, research involving LS has gained interest recently.

Prior work has explored several pharmaceutical powders, mainly with a focus on fast-dissolving tablets. This begins from the complex physical mechanisms that occur during LS and generate stringent material requirements, thereby most of the materials researched, presented limited sinter-ability and failed to produce solid tablets with high structural integrity. Researchers have incorporated additives to their formulations to improve sintering, however the use of additives is not desired as it can compromise the final tablet functionality and result in further need for regulatory testing.

This PhD, developed preliminary placebo formulations to investigate the factors that influenced processing and the final part properties, and suggested new ways to formulate a powders' properties.

The first objective was the characterisation and processing of several pharmaceutical excipients prior to the design of the formulations, which developed a comprehensive understanding of the link between the material properties and processing parameters and the effect of this on the quality of sintering. It was found that the LS powder must present a very specific combination of thermal and physical properties to ensure uniform sintering, which explained why it is difficult to expand the LS material portfolio.

The second objective involved processing and testing of physically blended powders that further investigated those critical factors that determined the mechanical performance of the final parts, and contributed to the understanding of the design criteria necessary to develop LS oral solid dosage forms.

The third and final objective was the development of new ways to enhance processing of the powder formulations, for future improvements in the parts' final quality and reproducibility.

Overall, this work provided a systematic way to analyse and select potential pharmaceutical excipients, with a focus on the material and processing aspects that need to be controlled in order to enable the production of oral solid dosage forms with improved functionality using LS technologies. It is hoped that the basis of powder development and formulation presented in this thesis can form the foundation for future design and production of tailored release formulations, not currently possible by LS.

For the scope of this PhD, common pharmaceutical excipients were selected and thoroughly characterised. From the analysis it was revealed that all the excipients that were tested presented important incompatibilities reducing their suitability for LS. Since all the materials presented incompatibilities, the ones that showed both unfavourable thermal and physical characteristics were excluded. The remaining materials were processed in the P100 to study the effect of the material aspects on processing, and the effect of process conditions on materials properties, which was proved valuable to gain a greater understanding of the rules required during sintering in searching for new materials.

Through the experiments it was shown that LS is a versatile tool that can adjust a number of build parameters to increase the sintering performance of materials and achieve optimised results, and showed potential for processing pharmaceutical grade materials. However, some limiting factors need to be taken into consideration for the safe processing of pharmaceuticals. The key observations in line with the literature related to the sintering performance of the powders are summarised below:

- The thermal characteristics of the materials were of great importance for sintering; high melting points introduced difficulties in consolidation and solidification of the powders; amorphous polymers can be processed at several degrees above their glass transition temperature.
- Natural polymers experienced dehydration at elevated temperatures that caused severe degradation upon the application of the laser beam.
- Particles with rough morphology can be spread efficiently on the powder bed and successfully processed, if their size distribution fits the recommended range for

LS powders; larger particles resulted in high porosity and shrinkage; fine particles formed lumps due to high cohesion forces hindering the deposition of layers on the bed platform.

- High moisture content stored in the molecular chain of the polymers led to cohesiveness that inhibited the free flow and spreading of the powders.

Towards the production of oral solid dosage forms using LS, two excipients were selected to develop placebo formulations. Although Avicel 101 showed poor sinter-ability, processing of the material using Eudragit L100-55 as a binder showed potential by direct sintering of Eudragit L100-55, which bound together the solid particles of Avicel 101. However, the sintered parts demonstrated high pore interconnectivity resulting in high fragility, which significantly reduced the tablet integrity and affected the pharmaceutical functionality, since the printed tablets exhibited fast disintegration properties. The following trends were observed upon processing and testing of the placebo formulations:

- The weight composition of the two materials in the mixture determined the quality of the parts; high concentration in Eudragit L100-55 increased the degree of consolidation and the number of inter-particle bridges; high concentration in Avicel 101 increased the porosity and reduced the quality of the parts.
- The parts failed the crushing strength and friability control due to delamination of the layers that was caused by the presence of unmelted Avicel 101 particles, which reduced the layer adhesion.
- The presence of unmolten powder increased the number of voids in the structure; high porosity allowed the fast penetration of water, reducing the disintegration times; high porosity restrained the elastic recoveries affecting the hardness, the elastic modulus and the damping factor, which presented significantly low values.

The demand to enable more materials for processing using LS, led this PhD to alternative routes in order to improve processing of current pharmaceutical powders. Aiming at developing suitable conditions to process Avicel 101, the material was coated with Eudragit L100-55 instead of blending the two powders. This approach was taken to minimise the effects of sintering on Avicel 101 by creating a film coating and potentially protect the material from degradation. Three methods were developed based on precipitation and emulsion-solvent evaporation principles that were simple and easy to

reproduce and were proved suitable to create a film on the surface of Avicel 101 particles. The characteristics of the film were examined with several analytical techniques revealing important information related to the efficacy of the methods and the various parameters involved. The key points during the development of the methods are listed below:

- A critical concentration of the film forming polymer needed to provide with a homogeneous coating; high concentrations led to the formation of a continuous film; low concentrations presented discontinuities.

- The viscosity of the organic phase strongly influenced the dispersion of the polymer in the aqueous phase; high viscosity solutions resulted in the precipitation of large bulks of material; low viscosity solutions were dispersed efficiently delivering individual coated particles.

- The dispersion rate during the emulsification step had an impact on the coating distribution; high rates increased the contact points between the two phases and improved the distribution of the film; low rates led to poor dispersion and therefore emulsification, resulting in low film distribution.

This PhD established an understanding of the performance capabilities and limitations of common pharmaceutical excipient materials in LS. The PhD went on to manifest a surface treatment approach to improve processability and enable the use of new materials in LS that could expand the range of applications in many industries. This coating method could have wide implications for LS materials providing a new route for materials development for LS, something that has been lacking for many years. This could impact not just pharmaceutical applications but have broader applicability, due to the ability of introducing novel coated elements for material property modification, such as, for impact modification, powder stickiness or disintegration.

CHAPTER 11   FUTURE RECOMMENDATIONS

Additive Manufacturing has offered great potential to the pharmaceutical industry that is expected to change the future manufacturing of drug delivery systems. The freedom of design revolutionised the microarchitecture of drug dosage forms, which opened the way to the manufacturing of small volume units and novel drug devices with controlled local composition. This further allowed the development of personalised medicines, however research needs to be carried out until the development of multi-component dosage forms that will demonstrate complex release profiles towards the needs of everyone.

In this PhD it was demonstrated that is feasible to manufacture tablets using LS technologies, however the tablets exhibited limited functionality showing fast disintegration properties. The analysis revealed that there are various physical mechanisms related to material properties that influenced processing in the LS system and need to be taken under consideration for further research. Therefore it was noted that the material characteristics are of great importance and that is necessary for the thermal and physical properties to be tuned for successful sintering. Consequently, future work needs to focus on exploring a larger range of pharmaceutical excipients (ideally those that have semi-crystalline properties) and ways to improve their processability in order to expand the application of LS in pharmaceutics. With a careful selection of materials and potentially the incorporation of additives, particle coalescence could be promoted and raise the probability of producing denser and stronger parts. Further work could involve chemical and mechanical treatment of materials that could improve the powder characteristics and enable the use of current commercial materials that do not meet the criteria of LS powders. Modifications in the polymer chemical structure could potentially decrease the melting temperature of the materials, and further could prevent the moisture absorption. In addition, spheroidization techniques could change the geometry of the particles to a more spherical shape that would most likely demonstrate improved packing efficiency.

The powder mixture that was used in this PhD, represented a simple pharmaceutical formulation, however it contributed to the understanding of the various factors involved during processing of a double-phase powder system, which could be very valuable to guide the future formulation design of laser sintered oral solid dosage forms. The analysis

of the energy density effects on the final properties established important correlations between the processing conditions, the material properties and the mechanical behaviour of the final parts that could be used in future research focused on the careful control of the LS process conditions according to the properties of the powder mixture. Along with future research in materials development this could provide with improvements in the interfacial adhesion, the structural density and the mechanical strength of the LS tablets. An optimised sintering behaviour and mechanical response would overcome manufacturing limitations and encourage the production of LS tablets with enhanced quality and functionality.

Furthermore, future efforts should focus on the incorporation of alternative excipients in the mixture that could demonstrate a more optimal sintering profile and increase the distribution of the contact points and the number of the inter-particle bridges. Additionally, a drug substance could act as a liquid binder above its melting point, which makes it necessary to develop real pharmaceutical formulations using drugs in the mixture and conduct further research. Alternatively, coating approaches could be considered to reduce the sensitivity of natural diluents (such as cellulose and lactose) to the laser power. Suitable materials for sintering can apply a coating layer on sensitive particles to protect them from degradation. Following the suggested elements, the microstructure of the parts can be partially predetermined and allow the control of the mechanical strength and the disintegration properties of the sintered tablets.

To achieve high coating distributions, future work should focus on the design optimisation of a coating method. Eudragit L100-55 proved to be an effective film-forming material and at the same time a suitable LS powder. With the proper adjustments in the concentration of materials and solvents, and the emulsification conditions, the process can be optimised to achieve a thick continuous layer of coating. Avicel 101 particles coated with Eudragit L100-55 would be a promising alternative to conventional material blends, which can enhance the processability of the powders without the incorporation of additives. The production of high-quality parts could lead to the future exploitation of the greater design freedom of LS and enable the development of oral solid dosage forms with complex geometries and various release profiles. The pharmaceutical industry will benefit by the production of oral solid dosage forms with increased functionality, as it will open the way for innovative opportunities in modern pharmaceutics.

References

[1] A. Awad, F. Fina, A. Goyanes, S. Gaisford, and A. W. Basit, "3D printing: Principles and pharmaceutical applications of selective laser sintering," *Int. J. Pharm.*, vol. 586, no. June, p. 119594, 2020, doi: 10.1016/j.ijpharm.2020.119594.

[2] J. Goole and K. Amighi, "3D printing in pharmaceutics: A new tool for designing customized drug delivery systems," *Int. J. Pharm.*, vol. 499, no. 1–2, pp. 376–394, 2016, doi: 10.1016/j.ijpharm.2015.12.071.

[3] S. Infanger, A. Haemmerli, S. Iliev, A. Baier, E. Stoyanov, and J. Quodbach, "Powder bed 3D-printing of highly loaded drug delivery devices with hydroxypropyl cellulose as solid binder," *Int. J. Pharm.*, vol. 555, no. August 2018, pp. 198–206, 2019, doi: 10.1016/j.ijpharm.2018.11.048.

[4] "ISO/ASTM 52950:2021, Additive Manufacturing - General principles - Overview of data processing." © CEN - European Committee for Standardisation, Brussels, 2021.

[5] N. Hopkinson and P. Dickens, "Analysis of Rapid Manufacturing — Using Layer Manufacturing Processes for Production," *Mech. Eng. Sci.*, vol. 217, pp. 31–39, 2003.

[6] R. D. Goodridge, C. J. Tuck, and R. J. M. Hague, "Laser sintering of polyamides and other polymers," *Prog. Mater. Sci.*, vol. 57, no. 2, pp. 229–267, 2012, doi: 10.1016/j.pmatsci.2011.04.001.

[7] I. Gibson, *Additive Manufacturing Technologies*, 2nd editio. New York: Springer, 2015.

[8] C. L. Ventola, "Medical Applications for 3D Printing: Current and Projected Uses.," *P T*, vol. 39, no. 10, pp. 704–711, 2014, doi: 10.1016/j.infsof.2008.09.005.

[9] T. D. Ngo, A. Kashani, G. Imbalzano, K. T. Q. Nguyen, and D. Hui, "Additive manufacturing (3D printing): A review of materials, methods, applications and challenges," *Compos. Part B Eng.*, vol. 143, no. December 2017, pp. 172–196, 2018, doi: 10.1016/j.compositesb.2018.02.012.

[10] K. V. Wong and A. Hernandez, "A Review of Additive Manufacturing," *ISRN Mech. Eng.*, vol. 2012, pp. 1–10, 2012, doi: 10.5402/2012/208760.

[11] B. C. Gross, J. L. Erkal, S. Y. Lockwood, C. Chen, and D. M. Spence, "Evaluation of 3D printing and its potential impact on biotechnology and the chemical sciences," *Anal. Chem.*, vol. 86, no. 7, pp. 3240–3253, 2014, doi: 10.1021/ac403397r.

[12] "ISO/ASTM DIS 52900:2018(E), Additive manufacturing - General principles - Terminology." ISO/ASTM International, Geneva, 2018.

[13] O. R. Ghita, E. James, R. Trimble, and K. E. Evans, "Physico-chemical behaviour of Poly (Ether Ketone) (PEK) in High Temperature Laser Sintering (HT-LS)," *J. Mater. Process. Technol.*, vol. 214, no. 4, pp. 969–978, 2014, doi: 10.1016/j.jmatprotec.2013.11.007.

[14] R. J. Hague, "Implications on design of rapid manufacturing," *Proc. Instn Mech. Engrs Part C J. Mech. Eng. Sci.*, vol. 217, pp. 25–30, 2003.

[15] S. A. M. Tofail, E. P. Koumoulos, A. Bandyopadhyay, S. Bose, L. O'Donoghue, and C. Charitidis, "Additive manufacturing: scientific and technological challenges, market uptake and opportunities," *Mater. Today*, vol. 21, no. 1, pp. 22–37, 2018, doi: 10.1016/j.mattod.2017.07.001.

[16] R. I. Campbell, R. J. Hague, B. Sener, and P. W. Wormald, "The Potential for the Bespoke Industrial Designer," *Des. J.*, vol. 6, no. 3, pp. 24–34, 2003, doi: 10.2752/146069203789355273.

[17] N. Guo and M. C. Leu, "Additive manufacturing: Technology, applications and research needs," *Front. Mech. Eng.*, vol. 8, no. 3, pp. 215–243, 2013, doi: 10.1007/s11465-013-0248-8.

[18] A. Goyanes, P. Robles Martinez, A. Buanz, A. W. Basit, and S. Gaisford, "Effect of geometry on drug release from 3D printed tablets," *Int. J. Pharm.*, vol. 494, no. 2, pp. 657–663, 2015, doi: 10.1016/j.ijpharm.2015.04.069.

[19] S. A. Khaled, J. C. Burley, M. R. Alexander, and C. J. Roberts, "Desktop 3D printing of controlled release pharmaceutical bilayer tablets," *Int. J. Pharm.*, vol. 461, no. 1–2, pp. 105–111, 2014, doi: 10.1016/j.ijpharm.2013.11.021.

[20] N. Allahham *et al.*, "Selective laser sintering 3D printing of orally disintegrating printlets containing ondansetron," *Pharmaceutics*, vol. 12, no. 2, pp. 1–13, 2020, doi: 10.3390/pharmaceutics12020110.

[21] F. Fina *et al.*, "3D printing of drug-loaded gyroid lattices using selective laser sintering," *Int. J. Pharm.*, vol. 547, no. 1–2, pp. 44–52, 2018, doi: 10.1016/j.ijpharm.2018.05.044.

[22] S. A. Khaled, J. C. Burley, M. R. Alexander, J. Yang, and C. J. Roberts, "3D printing of tablets containing multiple drugs with defined release profiles," *Int. J. Pharm.*, vol. 494, no. 2, pp. 643–650, 2015, doi: 10.1016/j.ijpharm.2015.07.067.

[23] A. Goyanes, A. B. M. Buanz, A. W. Basit, and S. Gaisford, "Fused-filament 3D printing (3DP) for fabrication of tablets," *Int. J. Pharm.*, vol. 476, no. 1, pp. 88–92, 2014, doi: 10.1016/j.ijpharm.2014.09.044.

[24] K. F. Leong, F. E. Wiria, C. K. Chua, and S. H. Li, "Characterization of a poly-epsilon-caprolactone polymeric drug delivery device built by selective laser sintering," *Biomed. Mater. Eng.*, vol. 17, no. 3, pp. 147–157, 2007.

[25] F. Fina, A. Goyanes, S. Gaisford, and A. W. Basit, "Selective laser sintering (SLS) 3D printing of medicines," *Int. J. Pharm.*, vol. 529, no. 1–2, pp. 285–293, 2017, doi: 10.1016/j.ijpharm.2017.06.082.

[26] S. Singh, S. Ramakrishna, and R. Singh, "Material issues in additive manufacturing: A review," *J. Manuf. Process.*, vol. 25, pp. 185–200, 2017, doi: 10.1016/j.jmapro.2016.11.006.

[27] I. S. Kinstlinger *et al.*, "Open-Source Selective Laser Sintering (OpenSLS) of nylon and biocompatible polycaprolactone," *PLoS One*, vol. 11, no. 2, pp. 1–25, 2016, doi: 10.1371/journal.pone.0147399.

[28] B. M. Wu, S. W. Borland, R. A. Giordano, L. G. Cima, E. M. Sachs, and M. J. Cima, "Solid free-form fabrication of drug delivery devices," *J. Control. Release*, vol. 40, no. 1–2, pp. 77–87, 1996, doi: 10.1016/0168-3659(95)00173-5.

[29] S. F. Barakh Ali *et al.*, "Understanding the effects of formulation and process variables on the printlets quality manufactured by selective laser sintering 3D printing," *Int. J. Pharm.*, vol. 570, no. August, p. 118651, 2019, doi: 10.1016/j.ijpharm.2019.118651.

[30] S. F. S. Shirazi *et al.*, "A review on powder-based additive manufacturing for tissue engineering: selective laser sintering and inkjet 3D printing," *Sci. Technol. Adv. Mater.*, vol. 16, no. 3, p. 033502, 2015, doi: 10.1088/1468-6996/16/3/033502.

[31] B. Partee, S. J. Hollister, and S. Das, "Selective Laser Sintering Process Optimization for Layered Manufacturing of CAPA[sup ®] 6501 Polycaprolactone Bone Tissue Engineering Scaffolds," *J. Manuf. Sci. Eng.*, vol. 128, no. May, p. 531, 2006, doi: 10.1115/1.2162589.

[32] C. M. Cheah, C. K. Chua, C. W. Lee, C. Feng, and K. Totong, "Rapid prototyping and tooling techniques: A review of applications for rapid investment casting," *Int. J. Adv. Manuf. Technol.*, vol. 25, no. 3–4, pp. 308–320, 2005, doi: 10.1007/s00170-003-1840-6.

[33] "ISO/ASTM 52911-2:2019 Additive manufacturing — Design, Part2: Laser-based powder bed fusion of polymers." © CEN - European Committee for Standardisation, Brussels, 2019.

[34] G. M. Vasquez, C. E. Majewski, B. Haworth, and N. Hopkinson, "A targeted material selection process for polymers in laser sintering," *Addit. Manuf.*, vol. 1, pp. 127–138, 2014, doi: 10.1016/j.addma.2014.09.003.

[35] J. Y. Lee, J. An, and C. K. Chua, "Fundamentals and applications of 3D printing for novel materials," *Appl. Mater. Today*, vol. 7, pp. 120–133, 2017, doi: 10.1016/j.apmt.2017.02.004.

[36] G. V. Salmoria, P. Klauss, and L. A. Kanis, "Laser Printing of PCL/Progesterone Tablets for Drug Delivery Applications in Hormone Cancer Therapy," *Lasers Manuf. Mater. Process.*, vol. 4, no. 3, pp. 108–120, 2017, doi: 10.1007/s40516-017-0040-4.

[37] P. H. Warnke *et al.*, "Ceramic scaffolds produced by computer-assisted 3D printing and sintering: Characterization and biocompatibility investigations," *J. Biomed. Mater. Res. - Part B Appl. Biomater.*, vol. 93, no. 1, pp. 212–217, 2010, doi: 10.1002/jbm.b.31577.

[38] K. C. R. Kolan, M. C. Leu, G. E. Hilmas, and M. Velez, "Effect of material, process parameters, and simulated body fluids on mechanical properties of 13-93 bioactive glass porous constructs made by selective laser sintering," *J. Mech. Behav. Biomed. Mater.*, vol. 13, pp. 14–24, 2012, doi: 10.1016/j.jmbbm.2012.04.001.

[39] G. V. Salmoria, P. Klauss, R. A. Paggi, L. A. Kanis, and A. Lago, "Structure and mechanical properties of cellulose based scaffolds fabricated by selective laser sintering," *Polym. Test.*, vol. 28, no. 6, pp. 648–652, 2009, doi: 10.1016/j.polymertesting.2009.05.008.

[40] G. V. Salmoria, P. Klauss, K. M. Zepon, and L. A. Kanis, "The effects of laser energy density and particle size in the selective laser sintering of polycaprolactone/progesterone specimens: Morphology and drug release," *Int. J. Adv. Manuf. Technol.*, vol. 66, no. 5–8, pp. 1113–1118, 2013, doi: 10.1007/s00170-012-4393-8.

[41] G. V. Salmoria, M. R. Cardenuto, C. R. M. Roesler, K. M. Zepon, and L. A. Kanis, "PCL/Ibuprofen Implants Fabricated by Selective Laser Sintering for Orbital Repair," *Procedia CIRP*, vol. 49, pp. 188–192, 2016, doi: 10.1016/j.procir.2015.11.013.

[42] G. V. Salmoria, J. L. Leite, R. A. Paggi, A. Lago, and A. T. N. Pires, "Selective laser sintering of PA12/HDPE blends: Effect of components on elastic/plastic behavior," *Polym. Test.*, vol. 27, no. 6, pp. 654–659, 2008, doi: 10.1016/j.polymertesting.2008.04.007.

[43] G. Salmoria, F. Vieira, G. Ghizoni, M. Marques, and L. Kanis, "3D printing of PCL/Fluorouracil tablets by selective laser sintering: Properties of implantable drug delivery for cartilage cancer treatment," *Rheumatol. Orthop. Med.*, vol. 2, no. 3, pp. 1–7, 2017, doi: 10.15761/rom.1000121.

[44] F. Fina, C. M. Madla, A. Goyanes, J. Zhang, S. Gaisford, and A. W. Basit, "Fabricating 3D printed orally disintegrating printlets using selective laser sintering," *Int. J. Pharm.*, vol. 541, no. 1–2, pp. 101–107, 2018, doi: 10.1016/j.ijpharm.2018.02.015.

[45] R. Goodridge and S. Ziegelmeier, "Powder bed fusion of polymers," in *Laser Additive Manufacturing: Materials, Design, Technologies, and Applications*, M. Brandt, Ed. Woodhead Publishing Series in Electronic and Optical Materials, 2017, pp. 181–204.

[46] D. Drummer, D. Rietzel, and F. Kühnlein, "Development of a characterization approach for the sintering behavior of new thermoplastics for selective laser sintering," *Phys. Procedia*, vol. 5, no. PART 2, pp. 533–542, 2010, doi: 10.1016/j.phpro.2010.08.081.

[47] A. Wegner and T. Ünlü, "Powder life cycle analyses for a new polypropylene laser sintering material," *Solid Free. Fabr. 2016 Proc. 27th Annu. Int. Solid Free. Fabr. Symp. - An Addit. Manuf. Conf. SFF 2016*, pp. 834–846, 2016.

[48] A. Wegner, "New polymer materials for the laser sintering process: Polypropylene and others," *Phys. Procedia*, vol. 83, pp. 1003–1012, 2016, doi: 10.1016/j.phpro.2016.08.105.

[49] D. L. Bourell, T. J. Watt, D. K. Leigh, and B. Fulcher, "Performance limitations in polymer laser sintering," *Phys. Procedia*, vol. 56, no. C, pp. 147–156, 2014, doi: 10.1016/j.phpro.2014.08.157.

[50] S. Ruesenberg and H. J. Schmid, "Advanced characterization method of nylon 12 materials for application in laser sinter processing," *AIP Conf. Proc.*, vol. 1593, no. February 2015, pp. 713–718, 2014, doi: 10.1063/1.4873877.

[51] A. Franco, M. Lanzetta, and L. Romoli, "Experimental analysis of selective laser sintering of polyamide powders: An energy perspective," *J. Clean. Prod.*, vol. 18, no. 16–17, pp. 1722–1730, 2010, doi: 10.1016/j.jclepro.2010.07.018.

[52] I. Gibson and D. Shi, "Material properties and fabrication parameters in selective laser sintering process," *Rapid Prototyp. J.*, vol. 3, no. 4, pp. 129–136, 1997, doi: 10.1108/13552549710191836.

[53] J. P. Kruth, G. Levy, F. Klocke, and T. H. C. Childs, "Consolidation phenomena in laser and powder-bed based layered manufacturing," *CIRP Ann. - Manuf. Technol.*, vol. 56, no. 2, pp. 730–759, 2007, doi: 10.1016/j.cirp.2007.10.004.

[54] L. Verbelen, S. Dadbakhsh, M. Van Den Eynde, J. P. Kruth, B. Goderis, and P. Van Puyvelde, "Characterization of polyamide powders for determination of laser sintering processability," *Eur. Polym. J.*, vol. 75, pp. 163–174, 2016, doi: 10.1016/j.eurpolymj.2015.12.014.

[55] D. Drummer, K. Wudy, and M. Drexler, "Influence of energy input on degradation behavior of plastic components manufactured by selective laser melting," *Phys. Procedia*, vol. 56, no. C, pp. 176–183, 2014, doi: 10.1016/j.phpro.2014.08.160.

[56] A. E. Jakus, E. B. Secor, A. L. Rutz, S. W. Jordan, M. C. Hersam, and R. N. Shah, "Three-dimensional printing of high-content graphene scaffolds for electronic and biomedical applications," *ACS Nano*, vol. 9, no. 4, pp. 4636–4648, 2015, doi: 10.1021/acsnano.5b01179.

[57] Y. Shi, Z. Li, H. Sun, S. Huang, and F. Zeng, "Effect of the properties of the polymer materials on the quality of selective laser sintering parts," *Proc. Inst. Mech. Eng. Part J. Mater. Des. Appl.*, vol. 218, no. 3, pp. 247–252, 2004.

[58] M. Schmid, A. Amado, K. Wegener, F. Amado, and K. Wegener, "Polymer Powders for Selective Laser Sintering (SLS)," *30th Int. Conf. Polym. Process. Soc.*, pp. S15-377, 2014, doi: 10.1063/1.4918516.

[59] Z. Tian *et al.*, "A review on laser powder bed fusion of inconel 625 nickel-based alloy," *Appl. Sci.*, vol. 10, no. 1, 2020, doi: 10.3390/app10010081.

[60] H. Zarringhalam, C. Majewski, and N. Hopkinson, "Degree of particle melt in Nylon-12 selective laser-sintered parts," *Rapid Prototyp. J.*, vol. 15, no. 2, pp. 126–132, 2009, doi: 10.1108/13552540910943423.

[61] M. Savalani, L. Hao, and R. A. Harris, "Evaluation of CO2 and Nd:YAG lasers for the selective laser sintering of HAPEX," *Proc. Inst. Mech. Eng. Part B J. Eng. Manuf.*, vol. 220, no. 2, pp. 171–182, 2006, doi: 10.1243/095440505X32986.

[62] B. Duan, M. Wang, W. Y. Zhou, W. L. Cheung, Z. Y. Li, and W. W. Lu, "Three-dimensional nanocomposite scaffolds fabricated via selective laser sintering for bone tissue engineering," *Acta Biomater.*, vol. 6, no. 12, pp. 4495–4505, 2010, doi: 10.1016/j.actbio.2010.06.024.

[63] C. E. Majewski, H. Zarringhalam, and N. Hopkinson, "Effects of degree of particle melt and crystallinity in SLS Nylon-12 parts," *19th Annu. Int. Solid Free. Fabr. Symp. SFF 2008*, pp. 45–54, 2008.

[64] H. Zarringhalam, N. Hopkinson, N. F. Kamperman, and J. J. de Vlieger, "Effects of processing on microstructure and properties of SLS Nylon 12," *Mater. Sci. Eng. A*, vol. 435–436, pp. 172–180, 2006, doi: 10.1016/j.msea.2006.07.084.

[65]   M. Vasquez, B. Haworth, and N. Hopkinson, "Optimum sintering region for laser sintered Nylon-12," *Proc. Inst. Mech. Eng. Part B J. Eng. Manuf.*, vol. 225, no. 12, pp. 2240–2248, 2011, doi: 10.1177/0954405411414994.

[66]   L. Hao, M. M. Savalani, Y. Zhang, K. E. Tanner, and R. a. Harris, "Effects of material morphology and processing conditions on the characteristics of hydroxyapatite and high-density polyethylene biocomposites by selective laser sintering," *J. Mater. Des. Appl.*, vol. 220, no. 3, pp. 125–137, 2006, doi: 10.1243/14644207JMDA92.

[67]   Y. Khalil, A. Kowalski, and N. Hopkinson, "Influence of energy density on flexural properties of laser-sintered UHMWPE," *Addit. Manuf.*, vol. 10, pp. 67–75, 2016, doi: 10.1016/j.addma.2016.03.002.

[68]   H. C. H. Ho, I. Gibson, and W. L. Cheung, "Effects of energy density on morphology and properties of selective laser sintered polycarbonate," *J. Mater. Process. Technol.*, vol. 89–90, pp. 204–210, 1999, doi: 10.1016/S0924-0136(99)00007-2.

[69]   J. Bai, B. Zhang, J. Song, G. Bi, P. Wang, and J. Wei, "The effect of processing conditions on the mechanical properties of polyethylene produced by selective laser sintering," *Polym. Test.*, vol. 52, pp. 89–93, 2016, doi: 10.1016/j.polymertesting.2016.04.004.

[70]   R. D. Goodridge, R. J. M. Hague, and C. J. Tuck, "An empirical study into laser sintering of ultra-high molecular weight polyethylene (UHMWPE)," *J. Mater. Process. Technol.*, vol. 210, no. 1, pp. 72–80, 2010, doi: 10.1016/j.jmatprotec.2009.08.016.

[71]   F. E. Wiria, K. F. Leong, and C. K. Chua, "Modeling of powder particle heat transfer process in selective laser sintering for fabricating tissue engineering scaffolds," *Rapid Prototyp. J.*, vol. 16, no. 6, pp. 400–410, 2010, doi: 10.1108/13552541011083317.

[72]   R. D. Goodridge *et al.*, "Processing of a Polyamide-12/carbon nanofibre composite by laser sintering," *Polym. Test.*, vol. 30, no. 1, pp. 94–100, 2011, doi: 10.1016/j.polymertesting.2010.10.011.

[73]   S. Eosoly, N. E. Vrana, S. Lohfeld, M. Hindie, and L. Looney, "Interaction of cell culture with composition effects on the mechanical properties of polycaprolactone-hydroxyapatite scaffolds fabricated via selective laser sintering (SLS)," *Mater. Sci. Eng. C*, vol. 32, no. 8, pp. 2250–2257, 2012, doi: 10.1016/j.msec.2012.06.011.

[74]   H. Zheng, J. Zhang, S. Lu, G. Wang, and Z. Xu, "Effect of core-shell composite particles on the sintering behavior and properties of nano-Al2O3/polystyrene composite prepared by SLS," *Mater. Lett.*, vol. 60, no. 9–10, pp. 1219–1223, 2006, doi: 10.1016/j.matlet.2005.11.003.

[75]   C. Yan, Y. Shi, J. Yang, and J. Liu, "A nanosilica/nylon-12 composite powder for selective laser sintering," *J. Reinf. Plast. Compos.*, vol. 28, no. 23, pp. 2889–2902, 2009, doi: 10.1177/0731684408094062.

[76] S. Ziegelmeier *et al.*, "An experimental study into the effects of bulk and flow behaviour of laser sintering polymer powders on resulting part properties," *J. Mater. Process. Technol.*, vol. 215, no. 1, pp. 239–250, 2015, doi: 10.1016/j.jmatprotec.2014.07.029.

[77] S. Berretta, O. Ghita, and K. E. Evans, "Morphology of polymeric powders in Laser Sintering (LS): From Polyamide to new PEEK powders," *Eur. Polym. J.*, vol. 59, pp. 218–229, 2014, doi: 10.1016/j.eurpolymj.2014.08.004.

[78] M. Drexler, M. Lexow, and D. Drummer, "Selective Laser Melting of Polymer Powder - Part Mechanics as Function of Exposure Speed," *Phys. Procedia*, vol. 78, no. August, pp. 328–336, 2015, doi: 10.1016/j.phpro.2015.11.047.

[79] K. Senthilkumaran, P. M. Pandey, and P. V. M. Rao, "Influence of building strategies on the accuracy of parts in selective laser sintering," *Mater. Des.*, vol. 30, no. 8, pp. 2946–2954, 2009, doi: 10.1016/j.matdes.2009.01.009.

[80] S. Ziegelmeier, F. Wollecke, C. Tuck, R. Goodridge, and R. Hague, "Characterizing the Bulk & Flow Behaviour of LS Polymer Powders Stefan Ziegelmeier," *Solid Free. Fabr. Symp.*, pp. 354–367, 2013.

[81] S. Berretta, O. Ghita, K. E. Evans, A. Anderson, and C. Newman, "Size, shape and flow of powders for use in Selective Laser Sintering (SLS)," *6th Int. Conf. Adv. Res. Virtual Phys. Prototyp.*, no. 2011, pp. 49–54, 2014.

[82] B. Caulfield, P. E. McHugh, and S. Lohfeld, "Dependence of mechanical properties of polyamide components on build parameters in the SLS process," *J. Mater. Process. Technol.*, vol. 182, no. 1–3, pp. 477–488, 2007, doi: 10.1016/j.jmatprotec.2006.09.007.

[83] D. Engstrom, *Powder Bed Fusion, Notes in Introduction to Additive Manufacturing*. Loughborough University, 2016.

[84] S. Yang and J. R. G. Evans, "Metering and dispensing of powder; the quest for new solid freeforming techniques," *Powder Technol.*, vol. 178, no. 1, pp. 56–72, 2007, doi: 10.1016/j.powtec.2007.04.004.

[85] APTIS, "Granuheap as new tool." http://www.aptis.be/application-notes/pharmaceutical-applications/granuheap-new-tool/.

[86] J. C. Nelson, S. Xue, J. W. Barlow, J. J. Beaman, H. L. Marcus, and D. L. Bourell, "Model of the Selective Laser Sintering of Bisphenol-A Polycarbonate," *Ind. Eng. Chem. Res.*, vol. 32, no. 10, pp. 2305–2317, 1993, doi: 10.1021/ie00022a014.

[87] H. Zhang and S. LeBlanc, "Processing Parameters for Selective Laser Sintering or Melting of Oxide Ceramics," in *Additive Manufacturing of High-performance Metals and Alloys - Modeling and Optimization*, IntechOpen, 2018.

[88] A. Kenneth, *Dosage Forms and Their Routes of Administration*, 1st ed. Elsevier Inc., 2009.

[89] M. A. Darji *et al.*, "Excipient Stability in Oral Solid Dosage Forms: A Review," *AAPS PharmSciTech*, vol. 19, no. 1, pp. 12–26, 2018, doi: 10.1208/s12249-017-0864-4.

[90] S. Joshi and H. U. Petereit, "Film coatings for taste masking and moisture protection," *Int. J. Pharm.*, vol. 457, no. 2, pp. 395–406, 2013, doi: 10.1016/j.ijpharm.2013.10.021.

[91] Lieberman HA, *Pharmaceutical dosage forms: Tablets, Vol 1*, 2nd ed. New York, NY: Marcel Dekker Inc, 1989.

[92] M. Jivraj, L. G. Martini, and C. M. Thomson, "An overview of the different excipients useful for the direct compression of tablets," *Pharm. Sci. Technol. Today*, vol. 3, no. 2, pp. 58–63, 2000, doi: 10.1016/S1461-5347(99)00237-0.

[93] G. Thoorens, F. Krier, B. Leclercq, B. Carlin, and B. Evrard, "Microcrystalline cellulose, a direct compression binder in a quality by design environment - A review," *Int. J. Pharm.*, vol. 473, no. 1–2, pp. 64–72, 2014, doi: 10.1016/j.ijpharm.2014.06.055.

[94] A. S. Narang, R. V. Mantri, and K. S. Raghavan, "Excipient compatibility and functionality," *Dev. Solid Oral Dos. Forms Pharm. Theory Pract. Second Ed.*, pp. 151–179, 2017, doi: 10.1016/B978-0-12-802447-8.00006-6.

[95] L. Blecher, "Excipients—the important components," *Pharm Process.*, vol. 12, no. 1, pp. 6–7, 1995.

[96] V. S. Kulkarni and C. Shaw, "Use of Polymers and Thickeners in Semisolid and Liquid Formulations," *Essent. Chem. Formul. Semisolid Liq. Dosages*, pp. 43–69, 2016, doi: 10.1016/b978-0-12-801024-2.00005-4.

[97] A. S. Narang *et al.*, "Wet mass consistency reported by in-line drag force flow sensor compared with powder rheology and shaft amperage," in *Handbook of Pharmaceutical Wet Granulation*, Elsevier Inc., 2018, pp. 651–664.

[98] R. C. Rowe, P. J. Sheskey, W. G. Cook, and and M. E. Fenton, *Handbook of Pharmaceutical Excipients*, 7th ed. London: Pharmaceutical Press, 2012.

[99] T. Horio, M. Yasuda, and S. Matsusaka, "Effect of particle shape on powder flowability of microcrystalline cellulose as determined using the vibration shear tube method," *Int. J. Pharm.*, vol. 473, no. 1–2, pp. 572–578, 2014, doi: 10.1016/j.ijpharm.2014.07.040.

[100] Lamberson RF., Raynor GE., "Tableting properties of microcrystalline cellulose," *Manuf Chem Aerosol News*, vol. 47, no. 6, pp. 55–61, 1976.

[101] Reynir Eyjolfsson, *Design and Manufacture of Pharmaceutical Tablets*. London: Elsevier, 2015.

[102] G. K. Bolhuis and N. A. Armstrong, "Excipients for direct compaction - An update," *Pharm. Dev. Technol.*, vol. 11, no. 1, pp. 111–124, 2006, doi: 10.1080/10837450500464255.

[103] M. Keshavarz and B. Kaffashi, "The ability of retention, drug release and rheological properties of nanogel bioadhesives based on cellulose derivatives," *Pharm. Dev. Technol.*, vol. 19, no. 8, pp. 952–959, 2014, doi: 10.3109/10837450.2013.846371.

[104] O. Luhn, "Dissolution Profile of Novel Composite Pellet Cores Based on Different Ratios of Microcrystalline Cellulose and Isomalt," *J. Pharm. Sci.*, pp. 1–6, 2012, doi: 10.1002/jps.

[105] S. Dhawan, K. Dhawan, M. Varma, and V. R. Sinha, "Applications of Poly (ethylene oxide) in drug delivery systems," *Pharm. Technol.*, vol. 1, no. September, pp. 82–96, 2005.

[106] S. Dhawan, M. Varma, and V. R. Sinha, "High Molecular Weight Poly(ethylene oxide)–Based Drug Delivery Systems- part I : Hydrogels and Hydrophilic Matrix systems," *Pharm Technol*, vol. 29, no. May, pp. 72–74, 76–80, 2005.

[107] J. F. Pinto, K. F. Wunder, and A. Okoloekwe, "Evaluation of the potential use of poly(ethylene oxide) as tablet- and extrudate-forming material.," *AAPS J.*, vol. 6, no. 2, pp. 17–26, 2004, doi: 10.1208/ps060215.

[108] R. Kapil, D. N. Kapoor, and S. Dhawan, "Flow, compressive, and bioadhesive properties of various blends of poly(ethylene oxide)," *Drug Dev. Ind. Pharm.*, vol. 36, no. 1, pp. 45–55, 2010, doi: 10.3109/03639040903037231.

[109] D. Ratna, T. Abraham, and J. Karger-Kocsis, "Thermomechanical and rheological properties of high-molecular-weight poly(ethylene oxide)/novolac blends," *Macromol. Chem. Phys.*, vol. 209, no. 7, pp. 723–733, 2008, doi: 10.1002/macp.200700487.

[110] Dittgen M., "Acrylic polymers: a review of pharmaceutical applications," *STP Pharma Sci.*, vol. 7, no. 6, pp. 403–437, 1997.

[111] M. Adler *et al.*, "Molar mass characterization of hydrophilic copolymers, 1 Size exclusion chromatography of cationic (meth)acrylate copolymers," *E-Polymers*, no. 055, pp. 1–16, 2004.

[112] A. Balogh *et al.*, "Controlled-release solid dispersions of Eudragit® FS 100 and poorly soluble spironolactone prepared by electrospinning and melt extrusion," *Eur. Polym. J.*, vol. 95, pp. 406–417, 2017, doi: 10.1016/j.eurpolymj.2017.08.032.

[113] R. J. Roberts and R. C. Rowe, "The Compaction of Pharmaceutical and Other Model Materials - A Pragmatic Approach," *Chem. Eng. Sci.*, vol. 42, no. 4, pp. 903–911, 1987.

[114] Remon JP., "(Co-)extrusion and injection moulding as manufacturing tools for oral solid dosage forms," *Bull Tech Gattefossé*, vol. 105, pp. 80– 104, 2012.

[115] K. M. Picker-Freyer and T. Dürig, "Physical mechanical and tablet formation properties of hydroxypropylcellulose: in pure form and in mixtures.," *AAPS PharmSciTech*, vol. 8, no. 4, p. E92, 2007, doi: 10.1208/pt0804092.

[116] L. A. Felton and S. C. Porter, "An update on pharmaceutical film coating for drug delivery," *Expert Opin. Drug Deliv.*, vol. 10, no. 4, pp. 421–435, 2013, doi: 10.1517/17425247.2013.763792.

[117] R. P. Dixit and S. P. Puthli, "Oral strip technology: Overview and future potential," *J. Control. Release*, vol. 139, no. 2, pp. 94–107, 2009, doi: 10.1016/j.jconrel.2009.06.014.

[118] S. Bibi, D. H. Bremner, M. Macdougall-heasman, R. Reid, K. Simpson, and A. Tough, "A preliminary investigation to group disparate batches of licit and illicit diazepam tablets using differential scanning calorimetry," *Anal. Methods*, no. 7, pp. 8597–8604, 2015, doi: 10.1039/C5AY01711D.

[119] A. M. Belu, M. C. Davies, J. M. Newton, and N. Patel, "TOF-SIMS characterization and imaging of controlled-release drug delivery systems," *Anal. Chem.*, vol. 72, no. 22, pp. 5625–5638, 2000, doi: 10.1021/ac000450+.

[120] K. Zuurman, K. A. Riepma, G. K. Bolhuis, H. Vromans, and C. F. Lerk, "The relationship between bulk density and compactibility of lactose granulations," *Int. J. Pharm.*, vol. 102, no. 1–3, pp. 1–9, 1994, doi: 10.1016/0378-5173(94)90033-7.

[121] M. Otsuka, H. Ohtani, K. Otsuka, and N. Kaneniwa, "Effect of Humidity on Solid-state Isomerization of Various Kinds of Lactose During Grinding," *J. Pharm. Pharmacol.*, vol. 45, no. 1, pp. 2–5, 1993, doi: 10.1111/j.2042-7158.1993.tb03668.x.

[122] R. Chen, "Characterization of hypromellose acetate succinate by size exclusion chromatography (SEC) using Viscotek triple detector," *Int. J. Polym. Anal. Charact.*, vol. 14, no. 7, pp. 617–630, 2009, doi: 10.1080/10236660903225478.

[123] J. W. McGinity and L. A. Felton, *Aqueous Polymeric Coatings for Pharmaceutical Dosage Forms*, Third. New York: Informa Healthcare Inc., 2008.

[124] Z. Dong and D. S. Choi, "Hydroxypropyl Methylcellulose Acetate Succinate: Potential Drug - Excipient Incompatibility," *AAPS PharmSciTech*, vol. 9, no. 3, pp. 991–997, 2008, doi: 10.1208/s12249-008-9138-5.

[125] L. Martin, R. Mehta, M. Rane, C. Cunningham, and A. Rajabi-siahboomi, "Determination of Processing Window for Hot Melt Extrusion and Milling of Hypromellose Acetate Succinate by Assessing Thermal Degradation," *AAPS*, 2019.

[126] J. Schmidt, M. Sachs, S. Fanselow, K. E. Wirth, and W. Peukert, "New approaches towards production of polymer powders for selective laser beam melting of polymers," *AIP Conf. Proc.*, vol. 1914, 2017, doi: 10.1063/1.5016797.

[127] Leonard C.Thomas, "Use of multiple heating rate DSC and modulated temperature DSC to detect and analyze temperature-time-dependent transitions in materials," no. January, 2001.

[128] F. Technology, "FT4 Powder Rheometer System." http://www.freemantech.co.uk/_powders/ft4-powder-rheometer-universal-powder-tester.

[129] Freeman Technology, "FT4 Powder Rheometer: User Manual."

[130] "EOS GmbH, Electro Optical Systems, Product Information EOSINT P/ PA2200-Pulver."

[131] Q. Fu and W. Sun, "Mie theory for light scattering by a spherical particle in an absorbing medium," *Appl. Opt.*, vol. 40, no. 9, p. 1354, Mar. 2001, doi: 10.1364/AO.40.001354.

[132] U. Ajoku, N. Saleh, N. Hopkinson, R. Hague, and P. Erasenthiran, "Investigating mechanical anisotropy and end-of-vector effect in laser-sintered nylon parts," *Proc. Inst. Mech. Eng. Part B J. Eng. Manuf.*, vol. 220, no. 7, pp. 1077–1086, 2006, doi: 10.1243/09544054JEM537.

[133] J. D. Williams and C. R. Deckard, "Advances in modeling the effects of selected parameters on the SLS process," *Rapid Prototyp. J.*, vol. 4, no. 2, pp. 90–100, 1998, doi: 10.1108/13552549810210257.

[134] A. B. Bashaiwoldu, F. Podczeck, and J. M. Newton, "Application of dynamic mechanical analysis (DMA) to determine the mechanical properties of pellets," *Int. J. Pharm.*, vol. 269, no. 2, pp. 329–342, 2004, doi: 10.1016/j.ijpharm.2003.09.028.

[135] N. Saba *et al.*, "Thermal and dynamic mechanical properties of cellulose nanofibers reinforced epoxy composites," *Int. J. Biol. Macromol.*, vol. 102, pp. 822–828, 2017, doi: 10.1016/j.ijbiomac.2017.04.074.

[136] International and Standard, "ISO 6721-12 Plastics - Determination of dynamic mechanical properties. Part 12: Compressive vibration - Non-resonance method," Switzerland, 2021.

[137] PerkinElmer, "DMA 8000: Dynamic Mechanical Analyzer," 2013.

[138] L. J. Taylor, D. G. Papadopoulos, P. J. Dunn, A. C. Bentham, J. C. Mitchell, and M. J. Snowden, "Mechanical characterisation of powders using nanoindentation," *Powder Technol.*, vol. 143–144, pp. 179–185, 2004, doi: 10.1016/j.powtec.2004.04.012.

[139] S. Chattoraj, L. Shi, M. Chen, A. Alhalaweh, S. Velaga, and C. C. Sun, "Origin of deteriorated crystal plasticity and compaction properties of a 1:1 cocrystal between piroxicam and saccharin," *Cryst. Growth Des.*, vol. 14, no. 8, pp. 3864–3874, 2014, doi: 10.1021/cg500388s.

[140] M. Egart, B. Janković, and S. Srčič, "Application of instrumented nanoindentation in preformulation studies of pharmaceutical active ingredients and excipients," *Acta Pharm.*, vol. 66, no. 3, pp. 303–330, 2016, doi: 10.1515/acph-2016-0032.

[141] B. Govedarica, I. Ilić, R. Šibanc, R. Dreu, and S. Srčič, "The use of single particle mechanical properties for predicting the compressibility of pharmaceutical materials," *Powder Technol.*, vol. 225, pp. 43–51, 2012, doi: 10.1016/j.powtec.2012.03.030.

[142] A. C. Fischer-Cripps, *Nanoindentation*, 2nd ed. N-Y: Springer-Verlag, 2004.

[143] Micro Materials, "NanoTest User Manual: Technical Appendix," 2010. doi: 10.7551/mitpress/8065.003.0009.

[144] S. R. Cohen and E. Kalfon-Cohen, "Dynamic nanoindentation by instrumented nanoindentation and force microscopy: A comparative review," *Beilstein J. Nanotechnol.*, vol. 4, no. 1, pp. 815–833, 2013, doi: 10.3762/bjnano.4.93.

[145] B. Xu and X. Chen, "Determining engineering stress-strain curve directly from the load-depth curve of spherical indentation test," *J. Mater. Res.*, vol. 25, no. 12, pp. 2297–2307, 2010, doi: 10.1557/jmr.2010.0310.

[146] M. Cetin, A. Atila, and Y. Kadioglu, "Formulation and in vitro characterization of Eudragit® L100 and Eudragit® L100-PLGA nanoparticles containing diclofenac sodium," *AAPS PharmSciTech*, vol. 11, no. 3, pp. 1250–1256, 2010, doi: 10.1208/s12249-010-9489-6.

[147] H. M. Tawfeek, A. A. H. Abdellatif, T. J. Dennison, A. R. Mohammed, Y. Sadiq, and I. Y. Saleem, "Colonic delivery of indometacin loaded PGA-co-PDL microparticles coated with Eudragit L100-55 from fast disintegrating tablets," *Int. J. Pharm.*, vol. 531, no. 1, pp. 80–89, 2017, doi: 10.1016/j.ijpharm.2017.08.069.

[148] M. Qiao, L. Zhang, Y. Ma, J. Zhu, and W. Xiao, "A novel electrostatic dry coating process for enteric coating of tablets with Eudragit® L100-55," *Eur. J. Pharm. Biopharm.*, vol. 83, no. 2, pp. 293–300, 2013, doi: 10.1016/j.ejpb.2012.10.006.

[149] S. Hao, B. Wang, Y. Wang, L. Zhu, B. Wang, and T. Guo, "Preparation of Eudragit L 100-55 enteric nanoparticles by a novel emulsion diffusion method," *Colloids Surfaces B Biointerfaces*, vol. 108, pp. 127–133, 2013, doi: 10.1016/j.colsurfb.2013.02.036.

[150] M. J. Alonso, M. L. Lorenzo-Lamosa, C. Remuñán-López, and J. L. Vila-Jato, "Design of microencapsulated chitosan microspheres for colonic drug delivery," *J. Control. release*, vol. 52, pp. 109–118, 1998.

[151] M. Saffari, M. Shahbazi, and M. S. Ardestani, "Formulation and in vitro Evaluation of Eudragit L100 Microspheres of piroxicam," *Nat. Preced.*, pp. 1–5, 2008.

[152] S. Das, P. K. Suresh, and R. Desmukh, "Design of Eudragit RL 100 nanoparticles by nanoprecipitation method for ocular drug delivery," *Nanomedicine Nanotechnology, Biol. Med.*, vol. 6, no. 2, pp. 318–323, 2010, doi: 10.1016/j.nano.2009.09.002.

[153] S. A. Khan and M. Schneider, "Stabilization of gelatin nanoparticles without crosslinking," *Macromol. Biosci.*, vol. 14, no. 11, pp. 1627–1638, 2014, doi: 10.1002/mabi.201400214.

[154] S. Jose, M. T. Prema, A. J. Chacko, A. C. Thomas, and E. B. Souto, "Colon specific chitosan microspheres for chronotherapy of chronic stable angina," *Colloids Surfaces B Biointerfaces*, vol. 83, no. 2, pp. 277–283, 2011, doi: 10.1016/j.colsurfb.2010.11.033.

[155] B. Duan, M. Wang, W. Y. Zhou, W. L. Cheung, Z. Y. Li, and W. W. Lu, "Three-dimensional nanocomposite scaffolds fabricated via selective laser sintering for bone tissue engineering," *Acta Biomater.*, vol. 6, no. 12, pp. 4495–4505, 2010, doi: 10.1016/j.actbio.2010.06.024.

[156] J. Banks, "Adding value in additive manufacturing: Researchers in the United Kingdom and Europe look to 3D printing for customization," *IEEE Pulse*, vol. 4, no. 6, pp. 22–26, 2013, doi: 10.1109/MPUL.2013.2279617.

[157] W.D. Jr. Callister, *Materials Science and Technology*, 5th ed. Jiola, 2004.

[158] L. Szcześniak, A. Rachocki, and J. Tritt-Goc, "Glass transition temperature and thermal decomposition of cellulose powder," *Cellulose*, vol. 15, no. 3. pp. 445–451, 2008, doi: 10.1007/s10570-007-9192-2.

[159] A. Cataldi, A. Dorigato, F. Deflorian, and A. Pegoretti, "Thermo-mechanical properties of innovative microcrystalline cellulose filled composites for art protection and restoration," *J. Mater. Sci.*, vol. 49, no. 5, pp. 2035–2044, 2014, doi: 10.1007/s10853-013-7892-6.

[160] L. P. De Figueiredo and F. F. Ferreira, "The Rietveld Method as a Tool to Quantify the Amorphous Amount of Microcrystalline Cellulose," *J. Pharm. Sci.*, vol. 103, no. 5, pp. 1394–1399, 2014, doi: 10.1002/jps.23909.

[161] I. Gibson, D. W. Rosen, and and B. Stucker, "Rapid Prototyping to Direct Digital Manufacturing," in *Additive Manufacturing Technologies*, 2nd ed., New York: Springer, 2015, pp. 128–145.

[162] F. C. Mayville, R. J. Wigent, and J. B. Schwartz, "Thermogravimetric analysis for the determination of water release rate from microcrystalline cellulose dry powder and wet bead systems," *Pharm. Dev. Technol.*, vol. 11, no. 3, pp. 359–370, 2006, doi: 10.1080/10837450600770064.

[163] A. Crouter and L. Briens, "The effect of moisture on the flowability of pharmaceutical excipients," *AAPS PharmSciTech*, vol. 15, no. 1, pp. 65–74, 2014, doi: 10.1208/s12249-013-0036-0.

[164] A. Kiziltas, D. J. Gardner, Y. Han, and H. S. Yang, "Mechanical Properties of Microcrystalline Cellulose (MCC) Filled Engineering Thermoplastic Composites," *J. Polym. Environ.*, vol. 22, no. 3, pp. 365–372, 2014, doi: 10.1007/s10924-014-0676-5.

[165] A. Kiziltas, B. Nazari, D. J. Gardner, and D. W. Bousfield, "Polyamide 6–Cellulose Composites: Effect of Cellulose Composition on Melt Rheology and Crystallization Behavior," *Polym. Eng. Sci.*, no. 54, pp. 739–746, 2014, doi: DOI 10.1002/pen.23603.

[166] B. Zhao, H. Jiang, Z. Lin, S. Xu, J. Xie, and A. Zhang, "Preparation of acrylamide/acrylic acid cellulose hydrogels for the adsorption of heavy metal ions," *Carbohydr. Polym.*, vol. 224, no. June, p. 115022, 2019, doi: 10.1016/j.carbpol.2019.115022.

[167] Q. Zhang *et al.*, "Improvement on the properties of microcrystalline cellulose/polylactic acid composites by using activated biochar," *J. Clean. Prod.*, vol. 252, p. 119898, 2020, doi: 10.1016/j.jclepro.2019.119898.

[168] T. Vilhelmsen and T. Schæfer, "Agglomerate formation and growth mechanisms during melt agglomeration in a rotary processor," *Int. J. Pharm.*, vol. 304, no. 1–2, pp. 152–164, 2005, doi: 10.1016/j.ijpharm.2005.08.014.

[169] L. H. Gaabour, "Thermal Spectroscopy and Kinetic Studies of PEO/PVDF Loaded by Carbon Nanotubes," *J. Mater.*, vol. 2015, pp. 1–8, 2015, doi: 10.1155/2015/824859.

[170] S. Ibrahim, S. M. M. Yasin, R. Ahmad, and M. R. Johan, "Conductivity, thermal and morphology studies of PEO based salted polymer electrolytes," *Solid State Sci.*, vol. 14, no. 8, pp. 1111–1116, 2012, doi: 10.1016/j.solidstatesciences.2012.05.019.

[171] X. Liu, X. Ma, E. Kun, X. Guo, Z. Yu, and F. Zhang, "Influence of lidocaine forms (salt vs. freebase) on properties of drug–eudragit® L100-55 extrudates prepared by reactive melt extrusion," *Int. J. Pharm.*, vol. 547, no. 1–2, pp. 291–302, 2018, doi: 10.1016/j.ijpharm.2018.06.009.

[172] T. Parikh, S. S. Gupta, M. Anuprabha, and T. M. S. Abu, "Investigation of thermal and viscoelastic properties of polymers relevant to hot melt extrusion - I: Polyvinylpyrrolidone and related polymers," *J. Excipients Food Chem.*, vol. 5, no. 1, pp. 32–45, 2014.

[173] Z. K. Nagy *et al.*, "Solvent-free melt electrospinning for preparation of fast dissolving drug delivery system and comparison with solvent-based electrospun and melt extruded systems," *J. Pharm. Sci.*, vol. 102, no. 2, pp. 508–517, 2013, doi: 10.1002/jps.23374.

[174] C. Strasser, "Improving Process Conditions-Determining the Thermal Stability of Eudragit® by Means of TGA-FT-IR," pp. 1–6, [Online]. Available: www.netzsch.com.

[175] S. Y. Lin, C. M. Liao, and G. H. Hsiue, "A reflectance FTIR/DSC microspectroscopic study of the nonisothermal kinetics of anhydride formation in Eudragit L-100 films," *Polym. Degrad. Stab.*, vol. 47, no. 2, pp. 299–303, 1995, doi: 10.1016/0141-3910(94)00129-V.

[176] F. Zhang, "Melt-Extruded Eudragit® FS-Based Granules for Colonic Drug Delivery," *AAPS PharmSciTech*, vol. 17, no. 1, pp. 56–67, 2016, doi: 10.1208/s12249-015-0357-2.

[177] A. Gómez-Carracedo, C. Alvarez-Lorenzo, J. L. Gómez-Amoza, and A. Concheiro, "Chemical structure and glass transition temperature of non-ionic cellulose ethers DSC, TMDSC®: Oscillatory rheometry study," *J. Therm. Anal. Calorim.*, vol. 73, no. 2, pp. 587–596, 2003, doi: 10.1023/A:1025434314396.

[178] T. G. Rials and W. G. Glasser, "Thermal and Dynamic Mechanical Properties of Hydroxypropyl Cellulose Films," *J. Appl. Polym. Sci.*, vol. 36, pp. 749–758, 1988.

[179] P. Talik and U. Hubicka, "The DSC approach to study non-freezing water contents of hydrated hydroxypropylcellulose (HPC): A study over effects of viscosity and drug addition," *J. Therm. Anal. Calorim.*, vol. 132, no. 1, pp. 445–451, 2018, doi: 10.1007/s10973-017-6889-9.

[180] W. Chen, W. Weng, and M. Fu, "Hydroxypropyl cellulose-based esters for thermal energy storage by grafting with palmitic-stearic binary acids," *J. Appl. Polym. Sci.*, vol. 134, no. 24, pp. 1–11, 2017, doi: 10.1002/app.44949.

[181] G. Loreti, A. Maroni, M. D. Del Curto, A. Melocchi, A. Gazzaniga, and L. Zema, "Evaluation of hot-melt extrusion technique in the preparation of HPC matrices for prolonged release," *Eur. J. Pharm. Sci.*, vol. 52, no. 1, pp. 77–85, 2014, doi: 10.1016/j.ejps.2013.10.014.

[182] M. K. Trivedi, "Influence of Biofield Treatment on Physicochemical Properties of Hydroxyethyl Cellulose and Hydroxypropyl Cellulose," *J. Mol. Pharm. Org. Process Res.*, vol. 03, no. 02, pp. 0–7, 2015, doi: 10.4172/2329-9053.1000126.

[183] J. Chen, J. Wang, R. Li, A. Lu, and Y. Li, "Thermal and X-ray diffraction analysis of lactose polymorph," *Procedia Eng.*, vol. 102, pp. 372–378, 2015, doi: 10.1016/j.proeng.2015.01.165.

[184] Y. Listiohadi, J. A. Hourigan, R. W. Sleigh, and R. J. Steele, "Thermal analysis of amorphous lactose and α-lactose monohydrate," *Dairy Sci. Technol.*, vol. 89, no. 1, pp. 43–67, 2009, doi: 10.1051/dst:2008027.

[185] M. Monschke and K. G. Wagner, "Impact of HPMCAS on the dissolution performance of polyvinyl alcohol celecoxib amorphous solid dispersions," *Pharmaceutics*, vol. 12, no. 6, pp. 1–17, 2020, doi: 10.3390/pharmaceutics12060541.

[186] R. B. Chavan, S. Rathi, V. G. S. S. Jyothi, and N. R. Shastri, "Cellulose based polymers in development of amorphous solid dispersions," *Asian J. Pharm. Sci.*, vol. 14, no. 3, pp. 248–264, 2019, doi: 10.1016/j.ajps.2018.09.003.

[187] D. T. Friesen, R. Shanker, M. Crew, D. T. Smithey, W. J. Curatolo, and J. A. S. Nightingale, "Hydroxypropyl methylcellulose acetate succinate-based spray-dried dispersions: An overview," *Mol. Pharm.*, vol. 5, no. 6, pp. 1003–1019, 2008, doi: 10.1021/mp8000793.

[188] S. Berretta, O. Ghita, and K. E. Evans, "Morphology of polymeric powders in Laser Sintering (LS): From Polyamide to new PEEK powders," *Eur. Polym. J.*, vol. 59, pp. 218–229, 2014, doi: 10.1016/j.eurpolymj.2014.08.004.

[189] G. W. Skinner, W. W. Harcum, P. E. Barnum, and J. H. Guo, "The evaluation of fine-particle hydroxypropylcellulose as a roller compaction binder in pharmaceutical applications," *Drug Dev. Ind. Pharm.*, vol. 25, no. 10, pp. 1121–1128, 1999, doi: 10.1081/DDC-100102278.

[190] R. D. Goodridge, R. J. M. Hague, and C. J. Tuck, "Effect of long-term ageing on the tensile properties of a polyamide 12 laser sintering material," *Polym. Test.*, vol. 29, no. 4, pp. 483–493, 2010, doi: 10.1016/j.polymertesting.2010.02.009.

[191] A. Castellanos, "The relationship between attractive interparticle forces and bulk behaviour in dry and uncharged fine powders," *Adv. Phys.*, vol. 54, no. 4, pp. 263–376, 2005, doi: 10.1080/17461390500402657.

[192] J. Bouffard, F. Bertrand, and J. Chaouki, "PVAm–PIP/PS composite membrane with high performance for CO2/N2 separation," *AIChE J.*, vol. 59, no. 4, pp. 215–228, 2012, doi: 10.1002/aic.

[193] J. Kwon, B. R. Giri, E. S. Song, J. Bae, J. Lee, and D. W. Kim, "Spray-dried amorphous solid dispersions of atorvastatin calcium for improved supersaturation and oral bioavailability," *Pharmaceutics*, vol. 11, no. 9, 2019, doi: 10.3390/pharmaceutics11090461.

[194] A. A. Mousa, "Experimental investigations of curling phenomenon in selective laser sintering process," *Rapid Prototyp. J.*, vol. 22, no. 2, pp. 405–415, 2016, doi: 10.1108/RPJ-12-2013-0132.

[195] K. D. Foster, J. E. Bronlund, and A. H. J. (Tony. Paterson, "Glass transition related cohesion of amorphous sugar powders," *J. Food Eng.*, vol. 77, no. 4, pp. 997–1006, 2006, doi: 10.1016/j.jfoodeng.2005.08.028.

[196] A. H. J. Paterson, G. F. Brooks, J. E. Bronlund, and K. D. Foster, "Development of stickiness in amorphous lactose at constant T-Tg levels," *Int. Dairy J.*, vol. 15, no. 5, pp. 513–519, 2005, doi: 10.1016/j.idairyj.2004.08.012.

[197] J. Mužíková, S. Muchová, A. Komersová, and V. Lochař, "Compressibility of tableting materials and properties of tablets with glyceryl behenate," *Acta Pharm.*, vol. 65, no. 1, pp. 91–98, 2015, doi: 10.1515/acph-2015-0006.

[198] G. Lumay *et al.*, "Effect of relative air humidity on the flowability of lactose powders," *J. Drug Deliv. Sci. Technol.*, vol. 35, pp. 207–212, 2016, doi: 10.1016/j.jddst.2016.04.007.

[199] R. Wallimann, C. Roth, and P. Rudolf von Rohr, "Lactose powder flowability enhancement by atmospheric pressure plasma treatment," *Plasma Process. Polym.*, vol. 15, no. 10, pp. 1–8, 2018, doi: 10.1002/ppap.201800088.

[200] Q. Zhou, B. Armstrong, I. Larson, P. J. Stewart, and D. A. V. Morton, "Improving Powder Flow Properties of a Cohesive Lactose Monohydrate Powder by Intensive Mechanical Dry Coating," *J. Pharm. Sci.*, vol. 99, no. 2, pp. 969–981, 2010, doi: 10.1002/jps.

[201] V. Jannin, V. Bérard, A. N'Diaye, C. Andrès, and Y. Pourcelot, "Comparative study of the lubricant performance of Compritol® 888 ATO either used by blending or by hot melt coating," *Int. J. Pharm.*, vol. 262, no. 1–2, pp. 39–45, 2003, doi: 10.1016/S0378-5173(03)00316-8.

[202] W. Machowski and W. Balachandran, "Dispersion and transport of cohesive lactose powder using travelling wave field technique," *Powder Technol.*, vol. 99, no. 3, pp. 251–256, 1998, doi: 10.1016/S0032-5910(98)00118-1.

[203] T. Uchimoto *et al.*, "A comparative study of glycerin fatty acid ester and magnesium stearate on the dissolution of acetaminophen tablets using the analysis of available surface area," *Eur. J. Pharm. Biopharm.*, vol. 78, no. 3, pp. 492–498, 2011, doi: 10.1016/j.ejpb.2011.01.014.

[204] S. R. Athreya, K. Kalaitzidou, and S. Das, "Processing and characterization of a carbon black-filled electrically conductive Nylon-12 nanocomposite produced by selective laser sintering," *Mater. Sci. Eng. A*, vol. 527, no. 10–11, pp. 2637–2642, 2010, doi: 10.1016/j.msea.2009.12.028.

[205] C. K. Chua, K. F. Leong, K. H. Tan, F. E. Wiria, and C. M. Cheah, "Development of tissue scaffolds using selective laser sintering of polyvinyl alcohol/hydroxyapatite biocomposite for craniofacial and joint defects," *J. Mater. Sci. Mater. Med.*, vol. 15, no. 10, pp. 1113–1121, 2004, doi: 10.1023/B:JMSM.0000046393.81449.a5.

[206] A. E. Tontowi and T. H. C. Childs, "Density prediction of crystalline polymer sintered parts at various powder bed temperatures," *Rapid Prototyp. J.*, vol. 7, no. 3, pp. 180–184, 2001, doi: 10.1108/13552540110395637.

[207] L. Lanzl, K. Wudy, M. Drexler, and D. Drummer, "Laser-high-speed-DSC: Process-oriented thermal analysis of PA 12 in selective laser sintering," *Phys. Procedia*, vol. 83, pp. 981–990, 2016, doi: 10.1016/j.phpro.2016.08.103.

[208] J. Bai, B. Zhang, J. Song, G. Bi, P. Wang, and J. Wei, "The effect of processing conditions on the mechanical properties of polyethylene produced by selective laser sintering," *Polym. Test.*, vol. 52, pp. 89–93, 2016, doi: 10.1016/j.polymertesting.2016.04.004.

[209] B. Mittal, "Formulation Development," in *How to Develop Robust Solid Oral Dosage Forms from Conception to Post-Approval*, Elsevier Inc., 2017, pp. 39–67.

[210] S. Schiermeier and P. C. Schmidt, "Fast dispersible ibuprofen tablets," *Eur. J. Pharm. Sci.*, vol. 15, no. 3, pp. 295–305, 2002, doi: 10.1016/S0928-0987(02)00011-8.

[211] M. Yuan, T. T. Diller, D. Bourell, and J. Beaman, "Thermal conductivity of polyamide 12 powder for use in laser sintering," *Rapid Prototyp. J.*, vol. 19, no. 6, pp. 437–445, 2013, doi: 10.1108/RPJ-11-2011-0123.

[212] A. Wegner and G. Witt, "Correlation of Process Parameters and Part Properties in Laser Sintering using Response Surface Modeling," *Phys. Procedia*, vol. 39, no. December 2012, pp. 480–490, 2012, doi: 10.1016/j.phpro.2012.10.064.

[213] H. J. Fairchild and F. Michel, "Pfizer tablet hardness tester," *J. Pharm. Sci.*, vol. 50, no. 11, pp. 966–969, 1961, doi: 10.1002/jps.2600501119.

[214] D. B. Brook and K. Marshall, "'Crushing-Strength' of Compressed Tablets I," *J. Pharm. Sci.*, vol. 57, no. 3, pp. 481–484, 1968.

[215] J. A. Seitz and G. M. Flessland, "Tablet Hardness and Friability," *J. Pharm. Sci.*, vol. 54, no. 9, pp. 1353–1357, 1965.

[216] A. Abebe, I. Akseli, O. Sprockel, N. Kottala, and A. M. Cuitiño, "Review of bilayer tablet technology," *Int. J. Pharm.*, vol. 461, no. 1–2, pp. 549–558, 2014, doi: 10.1016/j.ijpharm.2013.12.028.

[217] M. Niwa, Y. Hiraishi, N. Iwasaki, and K. Terada, "Quantitative analysis of the layer separation risk in bilayer tablets using terahertz pulsed imaging," *Int. J. Pharm.*, vol. 452, no. 1–2, pp. 249–256, 2013, doi: 10.1016/j.ijpharm.2013.05.010.

[218] M. C. Gohel, R. K. Parikh, B. K. Brahmbhatt, and A. R. Shah, "Improving the tablet characteristics and dissolution profile of ibuprofen by using a novel coprocessed superdisintegrant: A technical note," *AAPS PharmSciTech*, vol. 8, no. 1, pp. 1–6, 2007, doi: 10.1208/pt0801001.

[219] K. Rocksloh *et al.*, "Optimization of crushing strength and disintegration time of a high-dose plant extract tablet by neural networks," *Drug Dev. Ind. Pharm.*, vol. 25, no. 9, pp. 1015–1025, 1999, doi: 10.1081/DDC-100102264.

[220] J. M. Sonnergaard, "Distribution of crushing strength of tablets," *Eur. J. Pharm. Biopharm.*, vol. 53, no. 3, pp. 353–359, 2002, doi: 10.1016/S0939-6411(02)00014-0.

[221] M. H. Fayed, G. M. Mahrous, M. A. Ibrahim, and A. Sakr, "Influence of Carbopol 71G-NF on the release of dextromethorphan hydrobromide from extended-release matrix tablets," *Pharm. Dev. Technol.*, vol. 18, no. 5, pp. 971–981, 2013, doi: 10.3109/10837450.2011.586037.

[222] J. M. Sonnergaard, "Quantification of the compactibility of pharmaceutical powders," *Eur. J. Pharm. Biopharm.*, vol. 63, no. 3, pp. 270–277, 2006, doi: 10.1016/j.ejpb.2005.10.012.

[223] T. Matsumoto, N. Kaneniwa, S. Higuchi, and M. Otsuka, "Effects of Temperature and Pressure During Compression on Polymorphic Transformation and Crushing Strength of Chlorpropamide Tablets," *J. Pharm. Pharmacol.*, no. 43, pp. 74–78, 1991.

[224] C. Caramella *et al.*, "A physical analysis of the phenomenon of tablet disintegration," *Int. J. Pharm.*, vol. 44, no. 1–3, pp. 177–186, 1988, doi: 10.1016/0378-5173(88)90114-7.

[225] H. Vromans, G. K. Bolhuis, C. F. Lerk, and K. D. Kussendrager, "Studies on tableting properties of lactose. VIII. The effect of variations in primary particle size, percentage of amorphous lactose and addition of a disintegrant on the disintegration of spray-dried lactose tablets," *Int. J. Pharm.*, vol. 39, no. 3, pp. 201–206, 1987, doi: 10.1016/0378-5173(87)90217-1.

[226] V. M. Masterson and X. Cao, "Evaluating particle hardness of pharmaceutical solids using AFM nanoindentation," *Int. J. Pharm.*, vol. 362, no. 1–2, pp. 163–171, 2008, doi: 10.1016/j.ijpharm.2008.06.015.

[227] M. Meier, E. John, D. Wieckhusen, W. Wirth, and W. Peukert, "Influence of mechanical properties on impact fracture: Prediction of the milling behaviour of pharmaceutical powders by nanoindentation," *Powder Technol.*, vol. 188, no. 3, pp. 301–313, 2009, doi: 10.1016/j.powtec.2008.05.009.

[228] X. Liao and T. S. Wiedmann, "Measurement of process-dependent material properties of pharmaceutical solids by nanoindentation," *J. Pharm. Sci.*, vol. 94, no. 1, pp. 79–92, 2005, doi: 10.1002/jps.20227.

[229] R. Cabiscol, J. H. Finke, H. Zetzener, and A. Kwade, "Characterization of mechanical property distributions on tablet surfaces," *Pharmaceutics*, vol. 10, no. 4, 2018, doi: 10.3390/pharmaceutics10040184.

[230] Ł. Pawłowski, M. Bartmański, G. Strugała, A. Mielewczyk-Gryń, M. Jazdzewska, and A. Zieliński, "Electrophoretic deposition and characterization of chitosan/eudragit E 100 coatings on titanium substrate," *Coatings*, vol. 10, no. 7, 2020, doi: 10.3390/coatings10070607.

[231] K. Das, D. Ray, N. R. Bandyopadhyay, T. Ghosh, A. K. Mohanty, and M. Misra, "A study of the mechanical, thermal and morphological properties of microcrystalline cellulose particles prepared from cotton slivers using different acid concentrations," *Cellulose*, vol. 16, no. 5, pp. 783–793, 2009, doi: 10.1007/s10570-009-9280-6.

[232] B. V. N. Nagavarma, H. K. S. Yadav, A. Ayaz, L. S. Vasudha, and H. G. Shivakumar, "Different techniques for preparation of polymeric nanoparticles- A review," *Asian J. Pharm. Clin. Res.*, vol. 5, no. SUPPL. 3, pp. 16–23, 2012.

[233] C. J. Martínez Rivas *et al.*, "Nanoprecipitation process: From encapsulation to drug delivery," *Int. J. Pharm.*, vol. 532, no. 1, pp. 66–81, 2017, doi: 10.1016/j.ijpharm.2017.08.064.

[234] N. Mendoza-Munoz, S. Alcala-Alcala, and D. Quintanar-Guerrero, *Polymer Nanoparticles for Nanomedicines*. Springer, 2016.

[235] R. H. Staff, K. Landfester, and D. Crespy, "Recent advances in the emulsion solvent evaporation technique for the preparation of nanoparticles and nanocapsules," *Adv. Polym. Sci.*, vol. 262, no. October, pp. 329–344, 2013, doi: 10.1007/12_2013_233.

[236] H. Fessi, F. Puisieux, J. P. Devissaguet, N. Ammoury, and S. Benita, "Nanocapsule formation by interfacial polymer deposition following solvent displacement," *Int. J. Pharm.*, vol. 55, no. 1, pp. 1–4, 1989, doi: 10.1016/0378-5173(89)90281-0.

[237] S. Pardeshi and S. K. Singh, "Precipitation polymerization: A versatile tool for preparing molecularly imprinted polymer beads for chromatography applications," *RSC Adv.*, vol. 6, no. 28, pp. 23525–23536, 2016, doi: 10.1039/c6ra02784a.

[238] S. Schubert, J. T. Delaney, and U. S. Schubert, "Nanoprecipitation and nanoformulation of polymers: From history to powerful possibilities beyond poly(lactic acid)," *Soft Matter*, vol. 7, no. 5, pp. 1581–1588, 2011, doi: 10.1039/c0sm00862a.

[239] Q. Dong *et al.*, "Engineering size and structure of particles in novel modified-release delivery systems," *J. Pharm. Pharm. Sci.*, vol. 22, no. 1, pp. 150–170, 2019, doi: 10.18433/JPPS30253.

[240] S. Hornig, T. Heinze, C. R. Becer, and U. S. Schubert, "Synthetic polymeric nanoparticles by nanoprecipitation," *J. Mater. Chem.*, vol. 19, no. 23, pp. 3838–3840, 2009, doi: 10.1039/b906556n.

[241] C. P. Azubuike and A. O. Okhamafe, "Physicochemical, spectroscopic and thermal properties of microcrystalline cellulose derived from corn cobs," *Int. J. Recycl. Org. Waste Agric.*, vol. 1, no. 1, pp. 1–7, 2012, doi: 10.1186/2251-7715-1-9.

[242] I. Kouadri and H. Satha, "Extraction and characterization of cellulose and cellulose nanofibers from Citrullus colocynthis seeds," *Ind. Crops Prod.*, vol. 124, no. September, pp. 787–796, 2018, doi: 10.1016/j.indcrop.2018.08.051.

[243] S. Hao, Y. Wang, B. Wang, J. Deng, X. Liu, and J. Liu, "Rapid preparation of pH-sensitive polymeric nanoparticle with high loading capacity using electrospray for oral drug delivery," *Mater. Sci. Eng. C*, vol. 33, no. 8, pp. 4562–4567, 2013, doi: 10.1016/j.msec.2013.07.009.

[244] A. S. Tatavarti, K. A. Mehta, L. L. Augsburger, and S. W. Hoag, "Influence of methacrylic and acrylic acid polymers on the release performance of weakly basic drugs from sustained release hydrophilic matrices," *J. Pharm. Sci.*, vol. 93, no. 9, pp. 2319–2331, 2004, doi: 10.1002/jps.20129.